Thèse

présentée par

Thorsten OHM

pour obtenir le titre de Docteur
de l'Université Joseph Fourier - Grenoble 1

(arrêtés ministériels du 5 juillet 1984 et du 30 mars 1992)

Spécialité: Physique

Effet tunnel quantique de l'aimantation dans un aimant moléculaire, Fe8

Soutenue le 19 octobre 1998

Composition du jury:

G. Chouteau	(Président)
J. M. Hammann	(Rapporteur)
P. C. E. Stamp	(Rapporteur)
C. Paulsen	
R. Sessoli	
J. Souletie	

Thèse préparée au sein du Centre de Recherches sur les Très Basses Températures - CNRS - Grenoble
(Laboratoire associés à l'Université Joseph Fourier - Grenoble)

REMERCIEMENTS

Cette thèse est préparée au CRTBT-CNRS, Grenoble. Je tiens à exprimer ma gratitude à l'ensemble du laboratoire et à ses directeurs, Bernard Hebral et Pierre Monceau, pour m'avoir accueilli en ces lieux.

Je remercie les membres de jury pour leurs présences à la soutenance et leurs soutiens lors de la rédaction de la thèse.

Je remercie mon directeur de thèse Carley Paulsen qui m'a accueilli et proposé un sujet fort intéressant. J'ai apprécié son assistance technique et pragmatique. Le travail avec lui a été très enrichissant.

Le travail n'aurait été possible sans nos collaborateurs du département de chimie de l'Université Florence, Roberta Sessoli et Dante Gatteschi. Je voudrai spécialement exprimer ma gratitude à Claudio Sangregorio qui nous a non seulement fourni des échantillons mais aussi assisté fortement dans nos travaux à Grenoble. J'ai apprécié sa convivialité lors de ses séjours à Grenoble et de notre visite à Florence.

Je remercie Philip C. E. Stamp et Nikolai V. Prokof'ev pour leur soutien théorique important au long de ce travail et pour les nombreuses discussions très profitables que nous avons eu.

Je remercie K. Hasselbach et W. Wernsdorfer pour leur aimable soutien concernant le système de microSQUID et la dilution Sionludi. J'ai apprecié leurs efforts et les nombreuses discussions.

J'ai apprécié la patience et la disponibilité de J. Souletie pour m'avoir répéter mille et une fois la théorie d'exponentielle étirée.

Je présente mes saluts amicaux à nos concurrents F. Lionti et L. Thomas.

Je remercie P. Butaud et R. Melin pour m'avoir permis d'utiliser le système informatique du CRTBT.

Je remercie la fondation de Daimler-Benz pour sa générosité et son soutien financiers pendant la thèse.

Table de Matière

i) Introduction générale 1

ii) Macroscopic Quantum Tunneling of Magnetization 3

iii) Organisation de la thèse 9

I) Experimental Methods 11

I.1) The Magnetometer 13

I.2) The Dilution Refrigerator 19

I.3) SQUID-Technology 21

II) Theory 27

II.1) The Giant Spin 29

II.2) Quantum Tunneling of the Magnetization 31

II.3) Environmental Effects 35

II.4) Coherent and Incoherent Tunneling 41

III) The Molecular Magnet, Fe8 43

IV) Experimental Results 49

IV.1) Theory of Superparamagnetism 51

IV.2) Fe8 55

IV.2.1) The Superparamagnetic regime 55

IV.2.2) The Behavior below 1K 65

IV.2.3) The Quantum Regime 75

IV.2.4) Discrepancies 89

IV.3) Other Molecular Magnets 91

IV.3.1) Fe4 91

IV.3.2) Fe17Fe19 95

IV.3.3) Mn11 99

V) Local Field Effects 103

V.1) Local Field Distribution 103

V.1.1) Numerical Calculations 105

V.1.2) The Initial Local Field Distribution 113

V.1.3) Random Spin Distribution 115

V.2) Experimental Results 123

V.2.1) Square-Root Relaxation 123

V.2.2) The Phenomenological Model 129

V.3) Correlation Effects 135

V.3.1) Correlation Effects 135

V.3.2) Monte-Carlo Simulation 137

V.3.3) Experiments on Correlation Effects 143

Conclusion Générale 147

Annex 151

AI) Spin Levels of Fe8 153

AII) The Magnetization Curve of Fe8 155

AIII) Demagnetizatioin Field 159

AIV) Statistical Local Field Distribution 163

AV) Non-Exponential Relaxation 167

Reférénces 171

Publications 177

i) Introduction générale

La physique mésoscopique est un sujet très actuel de par son intérêt, et est en pleine expansion. Les effets quantiques sur des objets macroscopiques sont très spectaculaires. Par ces recherches on essaie de comprendre la transition entre la physique quantique et la physique classique. Ces études sont liées à la question : « Comment changent les lois de la physique d'un régime classique à un régime quantique en fonction de la taille d'un objet » ? Un des sujets très dynamiques de ces dernières années est la recherche de retournement d'aimantation par effet tunnel quantique (quantum tunneling of the magnetization, **qtm**). D'une façon classique, un vecteur d'aimantation ou un spin géant peut franchir une barrière d'énergie seulement s'il possède assez d'énergie pour passer au-dessus de la barrière. L'effet quantique permet le retournement d'orientation par-dessus la barrière, même si l'énergie est nulle.

En effet, le comportement d'un système mésoscopique est un mélange d'effets classiques et quantiques. L'intérêt de ces études de physique fondamentale est de faire le lien entre le domaine classique de magnétisme en volume (bulk) et le domaine quantique du magnétisme atomique. De plus il peut y avoir des impacts sur la technique. La miniaturisation d'éléments électroniques et de stockage a fait par exemple, que ces 30 dernières années le prix de stockage d'un Mega-octet est passé de 100 000 FF à 5 FF et la taille par bit a diminué d'un facteur 10^7. Aujourd'hui les dispositifs de stockage d'informations et les autres éléments électroniques sont encore de dimensions macroscopiques et contiennent des millions d'atomes. La décroissance de la taille de ces dispositifs est exponentielle et dans le futur, peut être dans 20 ou 30 ans, elle approchera un niveau atomique. A cette échelle l'effet quantique devient important et le comportement physique va changer radicalement. Les études sur les matériaux magnétiques nanoscopiques peuvent donc être importantes pour l'avenir de la technique de stockage.

Etat de l'art

La première interprétation d'une expérience par un effet tunnel quantique d'aimantation a été faite dans les années 50 par Livingston et Bean, mais aucun intérêt théorique n'est apparu à cette époque. Il y a 20 ans environ, Leggett et Caldeira ont fondé la théorie les effets de dissipation sur la physique quantique. La théorie d'effet tunnel quantique d'aimantation a été développée en détail par van Hemmen, Sütö et Schilling il y a 12 ans. Il est étonnant que ce sujet ait été abordé seulement plus de 50 ans après l'effet tunnel quantique sur des particules élémentaires.

L'intérêt expérimental se renouvela vers 1980 par l'étude de petites particules ferromagnétiques et mono-domaines. Le problème était qu'une seule particule mono-domaine était trop petite (~100Å et moins) pour pouvoir être mesurée à cette époque. De ce fait, on a étudié des poudres de particules nanoscopiques. Il est devenu rapidement certain que les distributions en tailles et orientations donnent des effets importants et empêchent une interprétation exacte. Un des problèmes est qu'une distribution de la taille et de l'orientation génèrent des comportements qui ressemble beaucoup à de l'effet tunnel quantique. A basse température, le temps de relaxation devient dans les deux cas indépendant de la température, mais pour des raisons différentes. La distribution de la taille des particules donne également une distribution des hauteurs de barrière dans ce système. Il s'agit donc d'un système mal défini.

Une autre approche réside dans l'étude d'aimants moléculaires. Ces matériaux sont composés de molécules magnétiques entourées par une matrice organique non magnétique. Un des avantages est que les unités magnétiques, les molécules, sont toutes identiques et possèdent la même orientation. Donc il n'y a plus les problèmes de distribution. Un premier succès sur ce sujet fut obtenu lors de études effectuées sur l'échantillon Mn12ac. Il y avait de fortes présomptions que cet échantillon présente un effet tunnel quantique à basse température, mais avec un temps de relaxation de $\tau = 10^8$ sec, c'est-à-dire de 3 années. Un autre indice était l'apparition d'un effet résonant en fonction d'un champ externe à haute température. Cet effet fut interprété comme la signature de croisements des niveaux d'énergie d'une molécule. Dans cette gamme de température il présente un temps de relaxation bien plus court que dans le régime quantique. Il s'agit donc d'un mélange d'effets thermique et quantique.

Nos premières mesures du composé Fe8 ont été effectuées sur un échantillon de poudre. Nous avons observé que ce système montre des effets tunnels quantiques à très basse température. C'était pour la première fois une preuve directe qu'un aimant moléculaire peut présenter un effet quantique. Dans le régime quantique le temps de relaxation est $\tau = 10^4$ sec, c'est-à-dire environ 3 heures. Même si l'effet tunnel quantique était clairement montré, il restait quelques problèmes d'interprétation des données expérimentales :

- Les courbes de relaxation ont une forme d'exponentielle étirée aux basses températures malgré les interactions très faibles entre les molécules.
- Le temps de relaxation mesuré est 10000 fois plus grand que les prédictions théoriques.
- La largeur de la résonance mesurée est également plus grande que prévu, de plusieurs ordres de grandeur.

Ensuite, les chimistes ont réussi à synthétiser de grands monocristaux de Fe8. Nous avons effectué de nouvelles les mesures sur de tels cristaux et trouvé presque les mêmes résultats que sur la poudre. Nous pouvons donc dans cette dernier exclure des effets de distribution.

Nous avons pu résoudre les contradictions ci-dessus en prenant en compte des interactions dipolaires entre des molécules. Même si ces interactions sont très faibles, elles ont une influence très forte sur les effets de relaxation.

ii) Macroscopic Quantum Tunneling of Magnetization

Tunneling effects through an energy barrier are a striking manifestation of quantum mechanics without any equivalent in classical physics. Tunneling of objects on an atomic scale have been known for a long time and well studied (e.g. α–decay (Helium nucleus), Josephson effect (Cooper pairs). Quantum mechanically the tunneling probability p_{qt} is given by $p_{qt} = p_0 \exp(-B)$ with B the Gamov factor, e.g. for a large step barrier of a height U and of thickness a this factor is $B \propto a\sqrt{U-E}$ where $E < U$ is the energy of the particle. As the object becomes bigger and the energy barrier larger (U or a) the tunneling probability decreases exponentially and a tunneling event becomes extremely rare. In a macroscopic system tunneling is completely suppressed due to decoherence effects. The occurrence of decoherence on larger scales is not fully understood even today. On an intermediate scale, often addressed as the mesoscopic scale, quantum effects might occur even though the system is large compared to the microscopic scale.

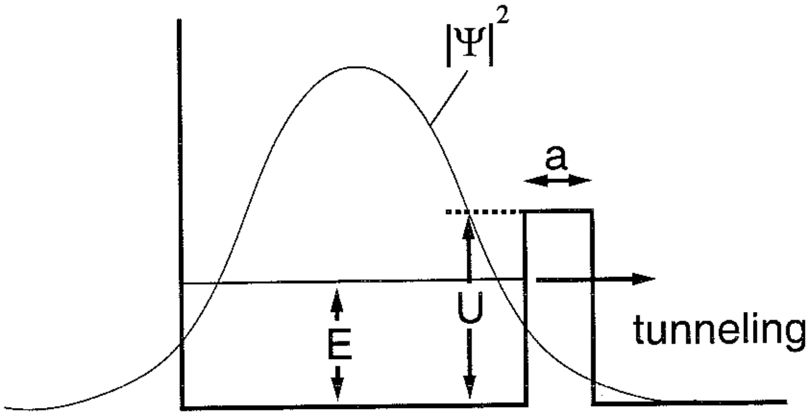

Figure ii.1: Schematic picture of a tunneling process. A particle of energy E tunnels through a barrier of height U and thickness a. The probability distribution $|\Psi|^2$ of the particle's wave function has a finite probability density on the opposite side of the barrier.

The systems we are studying are situated in this regime. We search for a quantum effect, tunneling, of a classical variable, the magnetization vector. Tunneling of the magnetization has, besides the scale effect, some special features when compared to the tunneling of particles. The tunneling of a particle is described by a continuous variable, namely $\vec{r} = (\hat{x}, \hat{y}, \hat{z})$ the particle position in an infinite-dimensional Hilbert space which has a vanishing commutator between their operators ($[\hat{x}, \hat{y}] = 0$ etc.). On the other hand a spin is discrete variable $\vec{\sigma} = (\hat{\sigma}_x, \hat{\sigma}_y, \hat{\sigma}_z)$ with $\hat{\sigma}_i = \hbar s \hat{\tau}_i$ and s integer or half-integer and $\hat{\tau}_i$ the Pauli matrices. A spin is a vector in a finite Hilbert space of dimension $2s+1$ and has a cyclic commutator between their components $[\hat{\sigma}_x, \hat{\sigma}_y] = 2i\hat{\sigma}_z$ etc.

Surprisingly theoretical studies of spin tunneling started more than 50 years after establishment of the quantum mechanical theory of tunneling for particles.

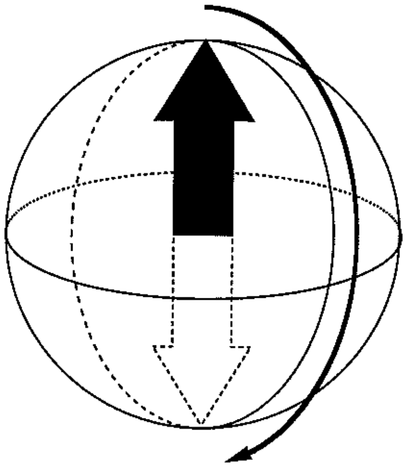

Figure ii.2: In a magnetic system a change in the spin orientation can be though as smooth change in the angle.

In the systems we are studying the variable is the combined spin of a small magnetic molecules. The spins of the individual ions within the molecules are tightly locked up (due to strong internal exchange couplings) and at low temperature the molecule appears as having one single net spin. Such a system whose spin degrees of freedom are reduced to one degree is called a giant spin system. Often is an directional anisotropy associated with a giant spin. If the giant spin is turning, as depicted in figure [ii.2], the system is passing an energy barrier.

Mapping this spin system on a particle picture we imagine the anisotropy barrier as a function of the orientation angle θ and an energy barrier between the orientations $\theta = 0$ "sp in up" and $\theta = \pi$ "spin down" as depicted in figure [ii.3]. The anisotropy potential looks like a two well potential. The two states "up" and "down" are states of minimum energy with a separating energy barrier between them. To overcome this barrier the spin must either have enough energy to jump over the barrier, the classical path, or it might tunnel through the energy barrier.

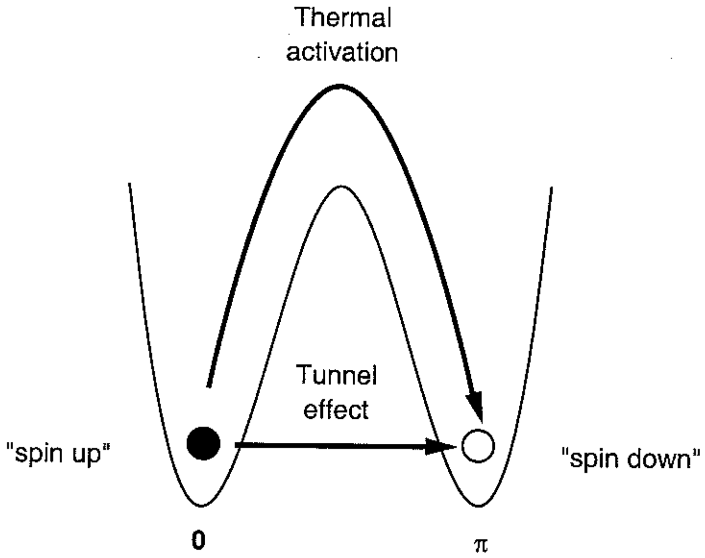

Figure ii.3: A spin flip corresponds to a transition of the orientation from an angle 0 to π. The path can be classical, i.e. over the barrier by thermal activation, or quantum mechanical via tunneling through the barrier.

For the classical path the energy to jump across the barrier comes from thermal activation. Thus the spin is interacts with the phonons of the system. Assume all the (giant) spins in the sample are first placed in the left minimum, "spin up"-orientation, i.e. after saturating in a large enough field. Then the spin system is not in equilibrium according to Boltzmann distribution $p = p_0 \exp(-\Delta / kT)$ where Δ is the height of the energy barrier and T the temperature. Some spins will at some time have enough energy to overcome the barrier and will flip. Until after some time the thermal equilibrium will be established.

For a tunneling process to occur a transverse anisotropy as function of the azimuth angle ϕ must be present. This corresponds to a variation of a potential along the equator in figure [ii.2]. This transverse term breaks the z-symmetry of the system and the z-component of the spin is no longer a good quantum number and the spin might tunnel.

A classical system, say the magnetization of a bulk sample, will never shows tunneling effects. This is not simply due to the fact that the anisotropy might be very high and consequently the tunneling time astronomically large. In a macroscopic system strong decoherence effects suppress any quantum mechanical effects. If we reduce the size and especially the temperature, the decoherence effects will decrease and in a certain range, quantum effects may be present even though the system may be still quite large. By reducing the size further, we approach a mircoscopic level and expect the system to obey only the laws of quantum mechanics. Our main interest is on a system between the border of a pure classical regime and a quantum regime. Leaving aside the problem of decoherence which is strongly related to the temperature and the nature of the interactions in the system, we might still ask to what degree we can call a system "macroscopic", even assuming that quantum tunneling might occur. One criterion is certainly the nature of the energy levels. If the energy levels are continuous we might call the system "macroscopic" while if the levels are discrete with a sizable energy spacing the system is at least on a "mesoscopic" scale if not "microscopic". In this context we might distinguish between systems where quantum tunneling is possible but the energy levels are continuous and a system where the energy spacing between the levels become important. The first case we call "**Macroscopic Quantum Tunneling**" (**MQT**) while in the latter case we prefer to call the quantum effect "**quantum tunneling of the magnetization**" (**qtm**), see figure [ii.4].

A system with continuous energy levels must have a rather large spin say of the order of at least $S \sim 10^4$ or even larger. Such a large spin can be only found in magnetic nano-particles of the order of say 10 – 100Å. So far the search for MQT in a single particle was not successful. On problem is that the signal of these particles are far too small to be measured by current magnetometers. One approach of measuring nano-particles of this size was done by [Wernstorfer 96] using a microSQUID system. Up to today no unambiguous proof of MQT in these system could be given. A similar approach is to use a powder of nano-particles. This way the integrated signal over many nano-particles is large enough to be measured by standard magnetometers. An inevitable problem is the distribution of size and orientation in these kinds of samples. These distribution effects result in a large distribution of relaxation times and effective relaxation time of the sample appears to be temperature independent even in the low temperature range thus showing the same effect as expected for the occurrence of quantum tunneling [Sampaio 94]. In consequence give this approach misleading results that might easily misinterpreted.

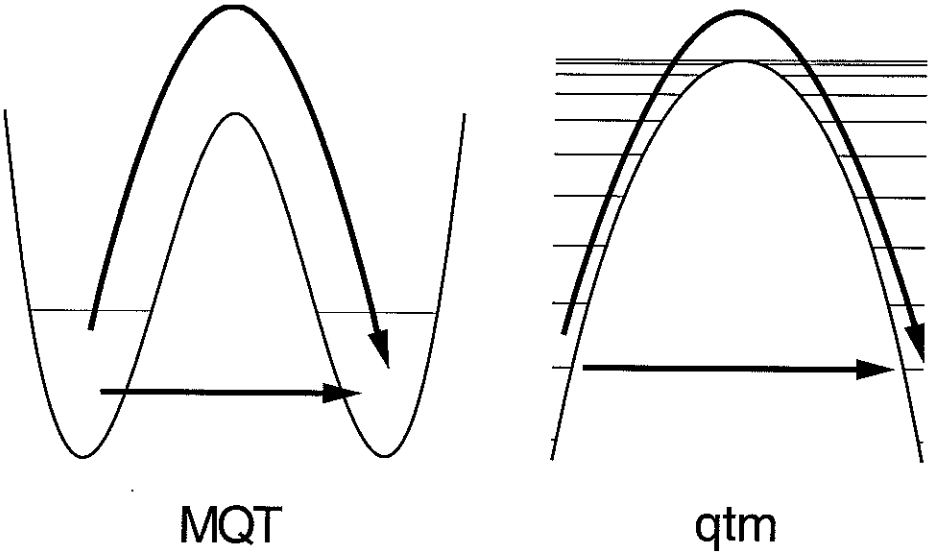

Figure ii.4: In a large system the energy levels will form a continuum. In this case we can talk of **M**acroscopic **Q**uantum **T**unneling, **MQT**. In a smaller mesoscopic system the energy levels are well separated. We will call a tunneling process in such a system **q**uantum **t**unneling of the **m**agnetization, **qtm**.

A further approach in the search of quantum effects of the magnetization is the use of molecular magnets. These materials consist of nano-sized magnetic molecules of transition ions embedded in a non-magnetic organic crystal. This approach eliminates all distribution effects since the magnetic molecules are all identical and due to the embedding crystal all are iso-orientated. A few years before this thesis a first molecular magnet, Mn12ac, has been identified showing quantum effects. During this thesis we identified a second sample, Fe8, which is more appropriate for this kind of studies. Both systems consist of magnetic molecules with a net spin of $S = 10$. For both systems the anisotropy and the energy levels are looking as depicted in figure [ii.5]. This figure shows the energy level splitting of the states $|S, m>$ with $m = +10, +9, ..., -9, -10$. At higher temperatures the spin might overcome the energy barrier by interacting with phonons via thermal activation. At lower temperatures the quantum tunneling occurs between degenerate states, as shown in the figure from $m = +10$ to $m = -10$. One shortcoming is the rather small spin of 10. These spins cannot be claimed to be macroscopic but rather mesoscopic. Due to the moderate spin the energy levels are well separated by an energy of some Kelvin. For example is the level distance between the lowest lying states $m = \pm 10$ and $m = \pm 9$ for Fe8 of the order of 4.6K and for Mn12ac of the order of 11.6K. Though the energy level distance is smaller for higher states in the quantum regime, i.e. at very low temperature, only the lowest lying states are occupied. A consequence is a resonance effect as function of the magnetic field. A magnetic field acting on the spins will shift the states via the Zeemann energy. Since tunneling is only permitted if the initial and the final state are degenerate up to the tunnel splitting a larger energy shift will lift the energy degeneracy and suppress tunneling.

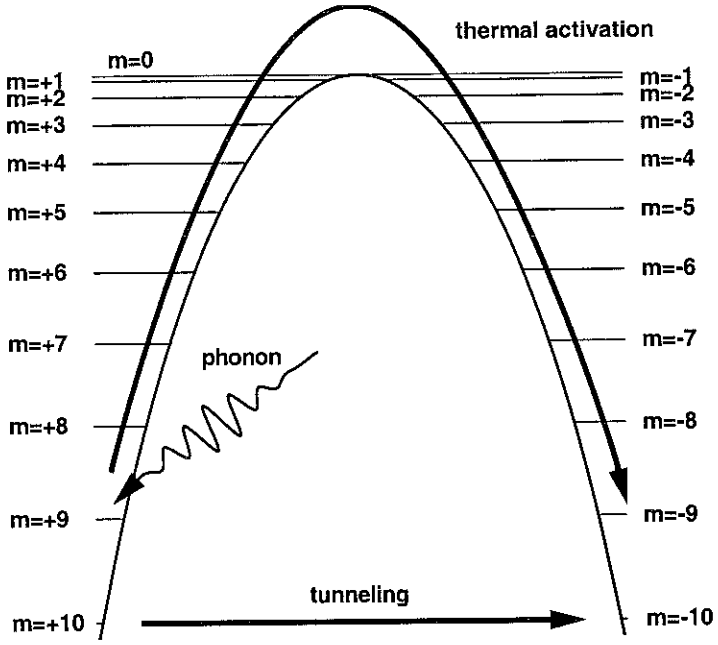

Figure ii.5: Energy levels of a molecule with a net spin of $S = 10$. At low temperatures the spin might tunnel back and forth between the states $m = +10$ and $m = -10$. At higher temperatures the spin might interact with a phonon and gain enough energy to overcome the barrier.

The major problem in the experiments with Mn12ac is the prohibitive long relaxation time at low temperatures. Below 2K the relaxation time of Mn12ac is of the order of 10^8 sec (!), i.e. about 3 years. In a relaxation experiment the magnetization will only change by a few percent even after weeks of experimentation. Such data are difficult to interpret and demand an extreme drift stability of the experiment. Fe8 has a relaxation of 10^4 sec even at the lowest temperatures of the experiment. Such relaxation times are much more appropriate for the study of quantum effects at low temperatures, see figure [ii.6].

We can conclude that our approach of molecular magnetism is appealing and has many advantages over other approaches to study quantum tunneling in magnetic materials, as nanoscopic powders or large mono-domain particles. Nonetheless are still many questions unsolved. The effective relaxation as measured in the experiments is much slower than the theoretical expected tunneling rate for an isolated molecule. During the thesis we found evidence that the mutual dipole interaction between the molecule strongly influence the relaxation behavior.

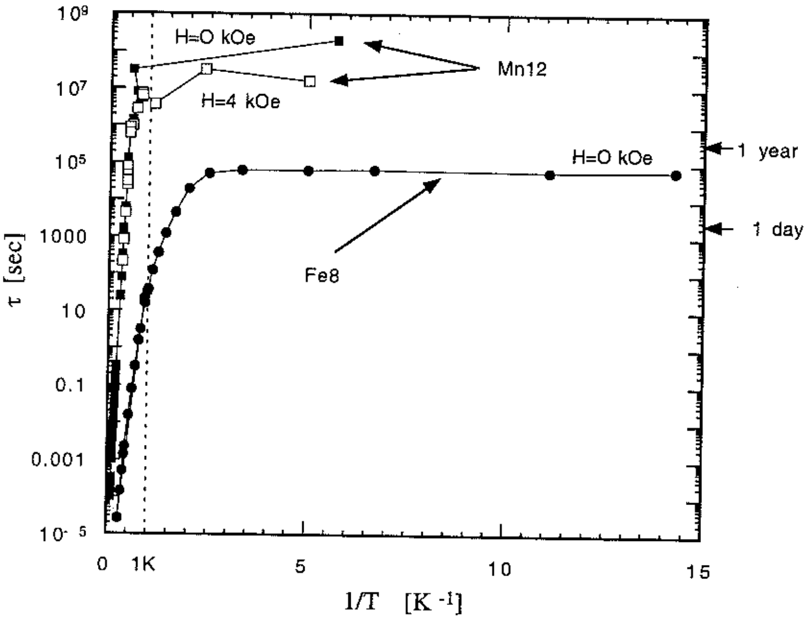

Figure ii.6: Relaxation times τ as function of the inverse temperature $1/T$. Mn12ac and Fe8 show a crossover from a thermal activated regime at high temperatures to a quantum regime at low temperatures where the relaxation time is temperature independent. At low temperature the relaxation time of Mn12ac is of the order of 3 years (~10^8 sec!) and prohibitive large for any experimentation.

iii) Organisation de la thèse

Cette thèse se devise en trois parties. Dans la première partie, qui comprend trois chapitres, nous décrivons en premier lieu les dispositifs expérimentaux et les méthodes de mesures utilisés (chapitre I). Ensuite (chapitre II), nous présentons les théories récentes de l'effet tunnel quantique, tandis qu'au chapitre III nous donnons les caractéristiques du principal échantillon qui nous avons étudié : Fe8. Dans la deuxième partie, chapitre IV, nous présentons nos résultats expérimentaux sur Fe8, mais aussi sur d'autres aimants moléculaires. Chacun d'eux se comporte comme un système superparamagnétique, mais seul Fe8 présente un effet tunnel quantique. Nous constatons des différences entre la théorie de l'effet tunnel quantique à un spin et les expériences. Dans la dernière partie (chapitre V) nous discutons l'influence des champs dipolaires sur la relaxation, ce qui explique bien les différences mentionnées ci-dessus. Nous présentons des calculs numériques et analytiques et nous les comparons avec nos mesures. En résumé nous trouvons des évidences claires que les champs dipolaires gèrent la relaxation dans le système à effet tunnel quantique Fe8.

La plus grande partie de cette thèse a écrite dans la *lingua franca* de physique, l'anglais. Nous pensons que cela permettra aux chercheurs de la communauté internationale qui travaillent sur le sujet, mais peu familiers avec la langue française, de prendre connaissance de ceux de nos résultats qui sont encore préliminaires, et de détails techniques quelquefois cruciaux, que nous n'avons pu faire figurer dans nos publications actuelles.

Chapitre I

Techniques Expérimentales

I.1) Le Magnétomètre 13

I.2) Le Réfrigérateur à Dilution 19

I.3) La Technologie de SQUID 21

Dans ce chapitre nous présentons le dispositif que nous avons utilisé pour les expériences. Nous donnons une introduction brève sur le fonctionnement d'un réfrigérateur à dilution et ensuite nous discutons le principe d'un SQUID. En particulier nous expliquons de manière très détaillé la technique d'un SQUID avec hystérésis.

Pendant la thèse nous avons réalisé des mesures d'aimantation de haute sensibilité à basse température, en champ fort ou en champ alternatif. Nous avions à notre disposition trois magnétomètres. Ils sont tous capables descendre à basse température vers 100 mK ou 50 mK en utilisant un réfrigérateur à dilution et exploitent la technique de SQUID pour les mesures d'aimantation. Ces magnétomètres ont été construits au cours des dernières années au CRTBT-CNRS à Grenoble. Tous leurs détails de construction sont connus et permettent une grande liberté d'utilisation. Nous pouvons changer facilement chaque dispositif pour exécuter une grande variété d'expériences.

Deux magnétomètres sont d'un principe comparable : Il s'agit d'une canne à dilution placée dans un bain de ^{4}He liquide. Un magnétomètre est optimisé pour des mesures en champ fort jusqu'à 8 tesla et l'autre est optimisé pour des mesures en champ alternatif. L'échantillon est placé sur un porte-échantillon de cuivre en contact avec la boîte à mélange. Le système de bobinage et le SQUID se trouvent à l'extérieur du réfrigérateur à dilution dans le bain d'hélium. Les deux magnétomètres ont une sensibilité proche du 10^{-8} uem.

Le troisième magnétomètre, nommé microSQUID, est réalisé selon un principe différent. Le cryostat est de type SionLuDi sans bain d'hélium. A l'intérieur le SQUID, ainsi que l'échantillon et le système de bobinage se trouvent dans le vide. La thermalisation jusqu'à 4,2K est faite par une cascade d'écrans thermalisés par une circulation permanente d'hélium liquide. L'échantillon est placé directement sur un SQUID lithographique qui présente une hystérésis. Le système de contre-réaction est géré par un logiciel. Ce microSQUID permet de mesurer l'aimantation avec un balayage de champ à grande vitesse. Nous avons exploité ce magnétomètre surtout pour les mesures d'hystérésis.

I.1) The Magnetometer

The magnetic measurements where made on three different magnetometers all developed at the CRTBT in Grenoble. All three systems are equipped with a dilution refrigerator and can operate down to temperatures of 50 – 100mK. The signal detection is made using SQUID-technology. Since all magnetometers are constructed and build at the CRTBT they are extremely flexible in their use. They can easily be changed for any kind of measurement.

Features of the magnetometers:

1) *High field SQUID-magnetometer*: Magnetometer equipped with a superconducting coil that can produce magnetic fields up to 8.5 tesla. The system uses a miniature dilution refrigerator ("canne à dilution") that can operate down to 70mK and has a commercial DC-SQUID system. The extraction method is used to obtain measurements in absolute units.

2) *AC–field SQUID-magnetometer*: This magnetometer is optimized for low field and ac-field measurements. The coil system can produce magnetic fields of about $H_{ac} \leq 5$ Oe, $H_{dc} \leq 200$ Oe. This system is equipped with the same miniature dilution refrigerator as 1) but the detection system uses a RF-SQUID. This system also uses the extraction method to obtain absolute values of the signal.

3) *MicroSQUID system*: This system uses lithographic, hysteretic SQUIDs for the measurements. The magnetic field can be changed more rapid than in the other two system but unfortunately only relative measurements can be done. The coil system has 3 coils. Two coils in the *x*- and *y*-direction that can produce fields of the order of 7 kOe and one smaller coil in the *z*-direction that is only used for the feedback. For the cooling a dilution refrigerator of the type "SionLuDi" is used. This system can operate down to 100mK but due to heating effects of the hysteretic SQUID measurements are only possible down to about 200mK.

SQUID-magnetometer

The schematic setup of the high-field SQUID-magnetometer is shown in figure [I.1.1]. The AC-field SQUID-magnetometer is very similar to this system except the superconducting coil and some differences in the control electronics. The low temperature part can be seen on the left hand side of the picture. It consists of a "canne à dilution" that is placed in a liquid helium bath. An important detail is the extractor motor at its top that allows to move the whole dilution refrigerator including the sample while the coils system is fixed. On the right hand side are the electronic components of the analog and digital control units. The whole measurement is controlled by a HP9816 computer. This computer is also responsible for the data acquisition during an experiment. For the further data analyses and storage the data are regularly transferred to a Macintosh computer.

The temperature is controlled by an ORPX system with an independent Epson computer. This unit reads the actual temperature from the thermometers and regulates the temperature by a heater on the sample holder. The regulation is done by a PID-control algorithm (Proportional, Integrated, and Derivative). The applied heating power results from the absolute temperature difference between the actual value and the target value (proportional), the recent change in the temperature

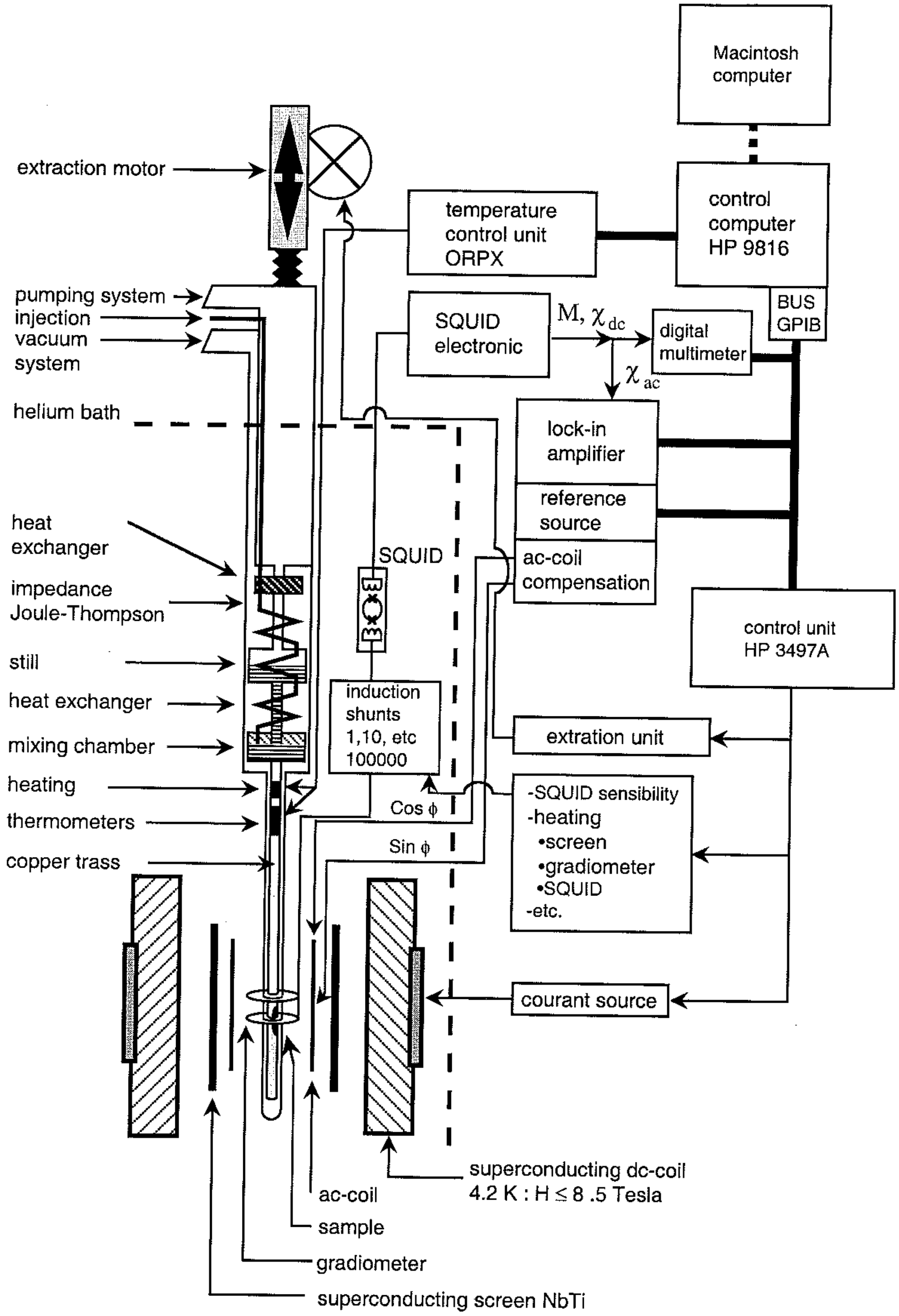
Macintosh computer
extraction motor
temperature control unit ORPX
control computer HP 9816
BUS GPIB
pumping system
injection
vacuum system
SQUID electronic
M, χ_{dc}
digital multimeter
χ_{ac}
helium bath
lock-in amplifier
reference source
heat exchanger
SQUID
ac-coil compensation
impedance Joule-Thompson
control unit HP 3497A
still
heat exchanger
induction shunts 1,10, etc 100000
mixing chamber
extration unit
heating
-SQUID sensibility
-heating
•screen
•gradiometer
•SQUID
-etc.
Cos ϕ
thermometers
Sin ϕ
copper trass
courant source
superconducting dc-coil
4.2 K : H ≤ 8 .5 Tesla
ac-coil
sample
gradiometer
superconducting screen NbTi

Figure I.1.1: Scheme of the high-field SQUID magnetometer.

(derivative), and the recent summed up heat amount (integrated). The Epson computer communicates with the controlling computer by means of a RS232 connection. The thermometers are placed on the copper sample holder and have a distance of a few centimeters to the sample. We are using three resistive thermometers: a Germanium-thermometer that is calibrated to the temperature range of 10K-1K, a RuO_2-thermometer for temperatures below 1K down to the base temperature. The third thermometer is placed on the mixing chamber to control the cooling procedure. Occasionally a forth thermometer are placed on the sample holder, to have a second reference to the existing thermometers, or on the still if problems on the cooling procedure occurs. The thermometers are read out by a resistance-bridge in the ORPX electronics that measures the resistance by extremely small voltages down to 1µV. The ORPX electronic was also developed at the CRTBT and manufactured by Barras-Provence.

The coil system consists of a superconducting dc-coil and a small ac-coil. The dc-coil is supplied via a current source that is voltage controlled by an analog/digital converter connected to the control computer. The ac-signal for the ac-coil comes from the signal generator of the lock-in amplifier or an external reference source also control by the HP computer.

The magnetic signal of the sample is transferred by a superconducting pick-up coil system (a gradiometer) to the SQUID that is placed in a NbTi-tube outside the field created by the main coil. The analog SQUID-output is digitized by a Keithley-multimeter or a lock-in amplifier, depending on the experiment, and recorded by the control computer. For the protection against exterior noise and to stabilize the field a superconducting shield of NbTi is placed between the detection coil and the superconducting dc-coil. For a change in the dc-field this shield has to be heated each time above the critical temperature of T_C=9K. A new measurement can only be done after a certain time (~20 sec) when the shield is cooled down again and possible flux creeps in the shield have settled.

The sensitivity of the SQUID can be reduced by a set of inductive shunts between the gradiometer and the SQUID. This shunt-system reduces the signal by a factor of 10 to 10^6. The sensitivity of the detection system is of the order of 10^{-7}–10^{-9} emu.

Measurements in absolute values

The voltage output of the SQUID-electronics is proportional to the flux in the SQUID and consequently to the magnetization of the sample. The gradiometer of the pick-up system consists of two loops of a superconducting wire wound in opposite directions. Ideally a homogeneous magnetic field will not induce a current in the gradiometer. In reality the gradiometer will of course never be perfectly wound and a small signal will be seen. A more intriguing problem is that for each measurement a unknown amount of flux is trapped within the pick-up loop. Beside the signal of the sample each measurement will a have an arbitrary offset. In order to measure the magnetization in absolute units we use the extraction method. This means that the sample is moved through the two loops of the gradiometer. In our case the whole dilution refrigerator with the sample is moved. A plot of the measured signal versus the displacement gives a function that is flat at the extremities and has at the center a maximum (sample in the upper loop, say) and a minimum (sample in the lower coil). The difference between the maximum and the minimum is proportional to the sample's magnetization and neglects the constant offset that will only shift the whole curve up or down. The HP-computer controls the whole procedure and calculates also the difference between the maximum and the minimum by fitting the curves using a chebychev polynomial. The calibration to convert the voltage output of the SQUID into physical units is done by various samples with a well-known signal like superconductors, paramagnets, or ferromagnets. To calibrate the system lead spheres and a Niobium rod have been used. Below the critical temperature a type I superconductor is a perfect diamagnet, e.g. for a perfect sphere the magnetization is exactly $\chi_{apparent} = -3/8\pi$. In addition a small coil, a Nickel sample and CMN (cerium magnesium nitrate) have been used for the calibration. The later, CMN was also used to check the thermometry. CMN is a perfect paramagnet down to the milliKelviin range and obeys the Curie law. The susceptibility versus $1/T$ must be a straight line with a Curie constant of $C = 0.375$ [emu/mole].

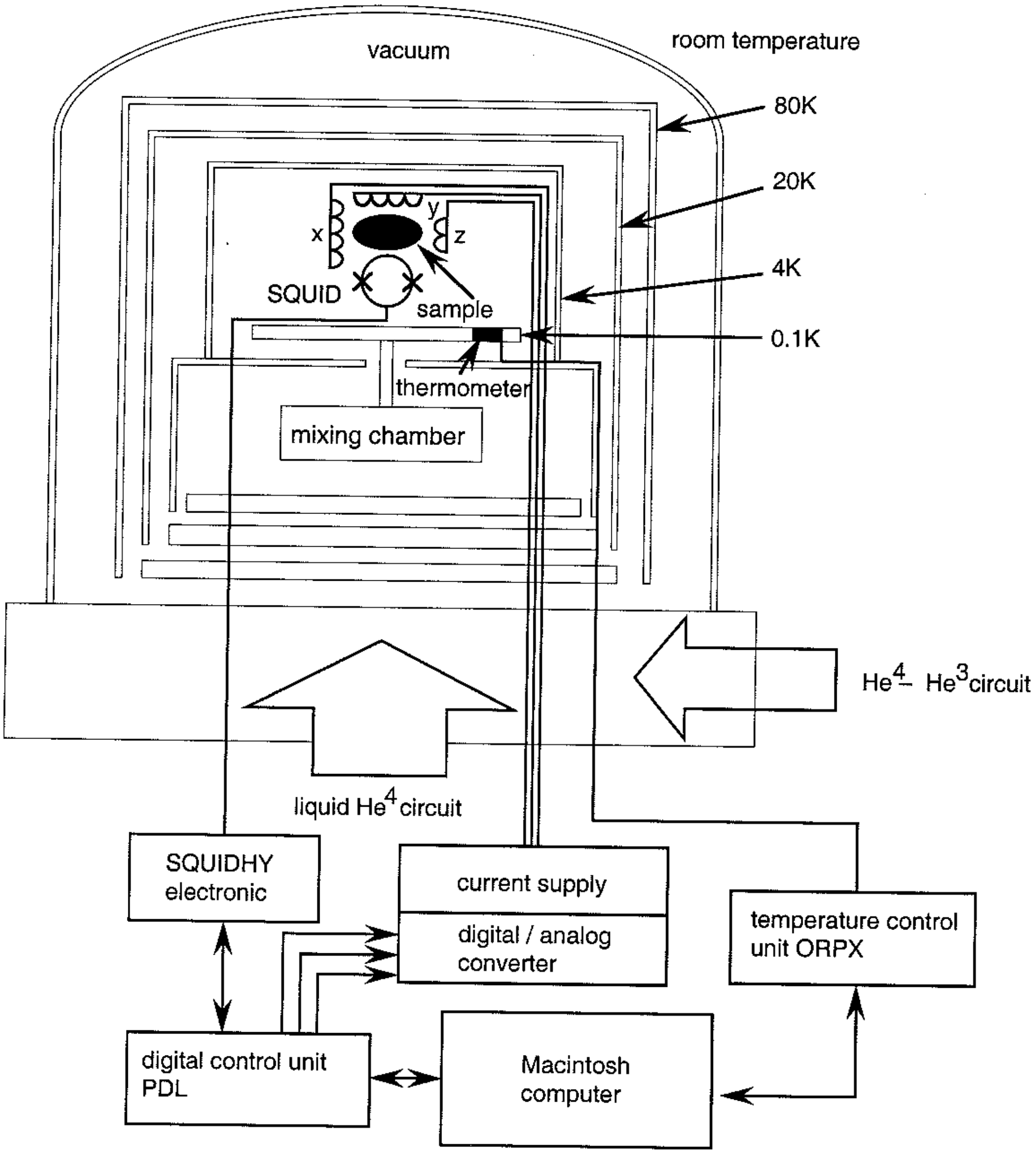
vacuum
room temperature
80K
20K
4K
0.1K
x
y
z
SQUID
sample
thermometer
mixing chamber
He^4- He^{3}circuit
liquid He^{4}circuit
SQUIDHY electronic
current supply
digital / analog converter
temperature control unit ORPX
digital control unit PDL
Macintosh computer

Figure I.1.2: Scheme of the microSQUID system.

The microSQUID system

The setup of the microSQUID is schematically shown in figure I.1.2. The low temperature parts are placed in a vacuum. To maintain the low temperatures in the center of the cryostat 4 screens are used. The outermost screen is made of stainless steel and separates the inner vacuum from the atmosphere. The inner thermal screens consist of copper and are thermalized by a constant flow of liquid helium ^{4}He through a tube system. The temperature is decreasing from room temperature at the outermost shield over 3 screens at 80K and 20K to the innermost thermal screen at 4.2K around the center of the cryostat. The dilution refrigerator is placed in the interior shielding and the experiment table cools down to 100mK. The coils are connected to the 4.2K-screen and the sample holder to the experiment table. Like in the other system the temperature is controlled by a independent ORPX-unit with an Epson computer. The thermometers and the heater is placed on the experiment table.

The sample holder carries the silicon wafer with the lithographic niobium or aluminum SQUID on it. One wafer contains 2 or 4 motives each containing 12 lithographic SQUIDs. For the measurements on Fe8 we used niobium SQUIDs. For the production of the SQUIDs a thin layer of niobium was evaporated on a silicon wafer and the SQUID motives were etched into this layer using lithographic methods. The SQUIDs were produced at the laboratory L2M of Dominique Mailly in Bagneux. The sample is placed directly on this wafer close to the SQUIDs.

Ideally the SQUIDs with the sample and the thermometers are at the same temperature. However, during a measurement parts of the SQUID become normal and in consequence give up heat and the temperature of the system increase. In fact the temperature during a measurement increasing by about 100mK. It is possible that due to the continuous heating of the SQUID, a temperature gradient builds up between the SQUID, the sample and the thermometers. The problem is more acute when the samples are very small and placed close to the micro-bridges of the SQUID [Wernstorfer 96]. In our case the samples were relatively large, in fact larger than the SQUID itself and were placed far from the SQUID. We observed no temperature differences between measurements made with the conventional magnetometers and the microSQUID indicating that the heating problem of the SQUIDs has in our case only a minor effect.

The SQUIDs are directly connected via a selection switch to the analog control electronic "SQUIDHY". The SQUID electronic is connected to a digital control unit "PDL" that contains a programmable digital signal processor. Both systems were recently developed at the CRTBT [Cernicchiaro 97]. The measurement procedure is controlled by a Macintosh-computer that communicates with the PDL-unit. The electronics "SQUIDHY" applies the current to the SQUID and measures continuously its state. The PDL-unit is responsible for the timing and initialization of the electronics. The measurement software on the Macintosh-computer is written in C using some high-level functions of the software library MANIP, also developed at the CRTBT. A detailed measuring procedure of the hysteretic SQUID is described in the section I.3.

I.2) Dilution Refrigerator

Most measurements were made at very low temperatures, below 1K down to 70 mK. These temperatures were created by the technique of a dilution refrigerator.

The central unit of a dilution refrigerator consists of a closed circuit of a mixture of ^{3}He and ^{4}He. The low temperature part of this setup is made of two chambers, the mixing chamber and the still. A schematic view is presented in figure [I.2.1]. It shows the two chambers with heat exchangers and two Joule-Thomson impedances. This central unit is placed in a high vacuum and is shielded against the thermal radiation entering from the exterior. A sealed pumping system maintains a continuous flow of the mixture.

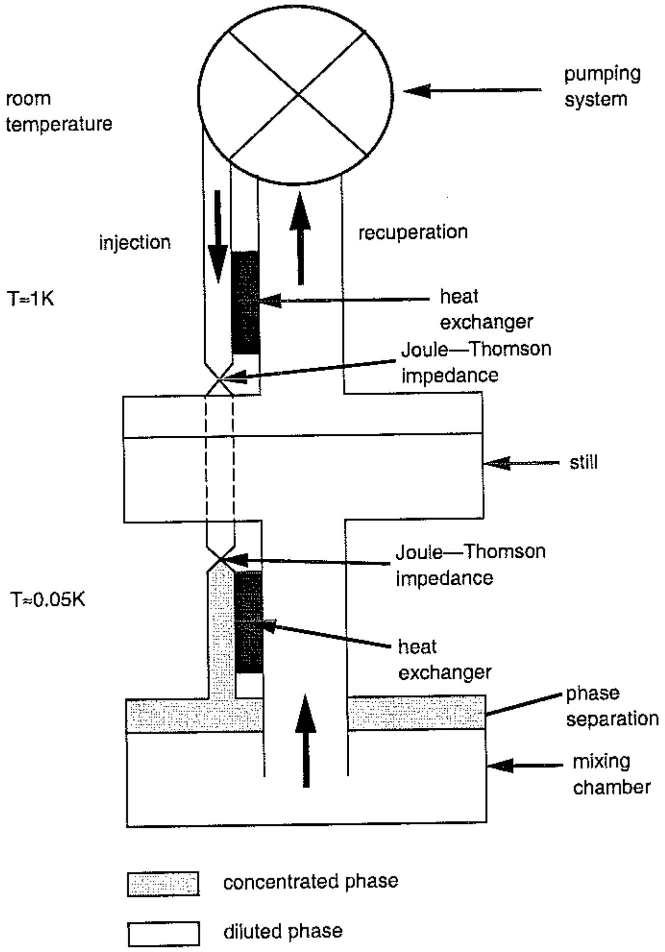
room temperature
pumping system
injection
recuperation
T≈1K
heat exchanger
Joule—Thomson impedance
still
Joule—Thomson impedance
T≈0.05K
heat exchanger
phase separation
mixing chamber
concentrated phase
diluted phase

Figure I.2.1: Schematic figure of the close ^{3}He^{4}He-circuit of a dilution refrigerator.

The physical cooling principle is to lower the temperature of a liquid by reducing the vapor pressure upon the surface. In this system ^{3}He is pumped through an inert layer of superfluid ^{4}He into vacuum. Below 0.8K a phase separation occurs in the helium mixture into a ^{3}He-rich phase floating on a ^{4}He-rich phase. This phase separation takes places in the mixing chamber. The still is kept at a higher temperature of about 1.1K thus the mixture has no phase separation. In the still the mixture has a surface with a vacuum and an augmented vapor pressure due to the higher temperature. The vacuum in the still is maintained by the pumping system. ^{3}He-atomes first diffuse from the ^{3}He-rich phase into the ^{4}He-rich phase in the mixing chamber and than diffuse in the still into the vacuum. Then the ^{3}He gas is then re-injected by the pumping system through a heat exchanger system and two Joule-Thomson impedances into the mixing chamber. By this technique the effective diffusion of ^{3}He through two surfaces at different temperatures is more effective than by simply pumping on a ^{3}He-vacuum or ^{4}He-vacuum surface and consequently lower temperatures are achieved.

The sample is placed on a copper tress that is in thermal contact with the mixing chamber. The temperature is regulated by an Epson digital computer with an analog interface ORPX. Several thermometers and a resistive heater placed on the sample holder are connected to the control unit. The temperature is permanently measured and corresponding to the predetermined target temperature an appropriate current is applied to the heater.

I.3) Principle of a SQUID

SQUID is an acronym for " **S**uperconducting **Qu**antum **I**nterference **D**evice ". A SQUID consists of a superconducting ring with one or two Josephson junctions. SQUID are certainly amongst the most sensitive devices for physics. Indeed, some SQUIDs have been made that are close to the quantum limit in energy resolution [Awschalom 89]. In this section we will discuss the physical principle of a SQUID by the example of a DC-SQUID which has two Josephson junctions. A SQUID with only one Josephson junction is called a RF-SQUID, see for example the reference [Gallop 91]. We also give details of the hysteretic SQUIDs.

– The superconducting state

A superconducting state can be described by a complex order parameter $\Psi(\vec{r})$ as in the theory of Ginzburg and Landau. This function is related to an energy gap of 2Δ in the density of states via $\Delta = |\Psi|^2$. The complex order parameter $\Psi(\vec{r}) = \Psi_0 \exp(i\phi(\vec{r}))$has an amplitude Ψ_0 and an imaginary phase of $i\phi(\vec{r})$. The superconducting current is related to the gradient of the phase and the amplitude by

$$\vec{j} = -\left[\frac{2e^2}{mc}\mathbf{A} + \frac{e\hbar}{m}\vec{\nabla}\phi(\vec{r})\right]\Psi_0^2 \quad (1, \mathrm{I.3})$$

where $\mathbf{A}$ is the vector potential of the magnetic induction $\vec{B} = \vec{\nabla} \times \mathbf{A}$. A direct consequence of a superconducting current in a ring is the quantization of the magnetic flux $\Phi = area \times B$ through the hole of the ring $\Phi = n\Phi_0$ with n = 0,1,2... and $\Phi_0 = hc/2e = 2.0679 \times 10^{-7}$ [gauss cm^2] the flux quantum. The total flux Φ is the sum of the flux induced by the external field Φ_{ext} and the flux induced by the superconducting current in the ring Φ_{int} thus

$$\Phi = \Phi_{ext} + \Phi_{\mathrm{int}} = n\Phi_0. \qquad (2, \mathrm{I.3})$$

For a given Φ_{ext} there are many possible internal states of the superconducting ring $\Phi'_{\mathrm{int}} - \Phi_{\mathrm{int}} = m\Phi_0$ with m = 0,1,2, ... which satisfy the quantization condition (2, I.3).

– The Josephson Effect

The carrier of the superconducting current, the Cooper pairs, can tunnel through an isolating barrier (the Josephson junction) between two superconductors. There exist a DC Josephson effect and an AC Josephson effect depending on the presence of a potential difference V across the isolating barrier.

The total current through a Josephson junction is directly related to the phase difference

$$\delta_0 = \phi_1 - \phi_2 \quad (3, \mathrm{I.3})$$

between the two superconductors on both sides. The phase of the order parameter is arbitrary but fixed thus the phase difference is also arbitrary but fixed. The Josephson current is given by

$$I(\delta_0) = I_0 \sin(\delta_0). \qquad (4, \mathrm{I.3})$$

In the presents of an electrical potential $V(t)$ across the Josephson junction, the phase difference will change in time

$$\delta(t) = \delta_0 + 1/\Phi_0 \int_0^t V(t')\, dt'. \quad (5, \mathrm{I.3})$$

If the potential is zero $V(t) = 0$ a current $I(\delta)$ can pass the barrier without any resistance as given by equation (4, I.3). This effect is called the DC Josephson effect, see e.g. [Gallop 61]. If the current surpasses the critical current $I(\delta)$ the junction will have a measurable resistance.

This dc-current disappears if a constant tension is present $V(t) = V_0$ over the junction. This voltage drop generates an alternating supercurrent at a frequency ω proportional to the voltage $\omega = V_0 / \Phi_0$. This is called the AC Josephson effect [Feynman 66].

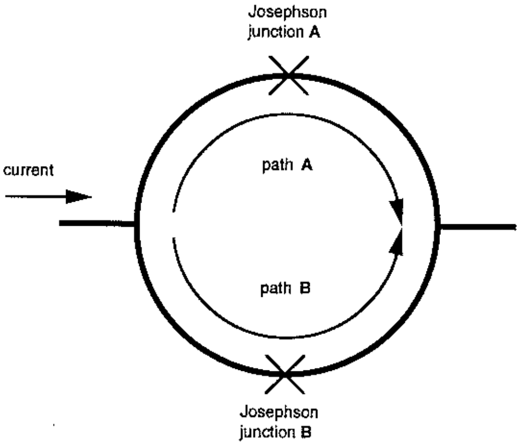

Figure I.3.1: A DC-SQUID consist of a superconducting ring with two Josephson junctions.

- The DC-SQUID

A DC-SQUID is a superconducting ring with two Josephson junctions as schematically shown in figure [I.3.1]. The DC-SQUID exploits quantum inferences that occur between the two pathways that enclose an area with a magnetic flux. For the two paths through the ring **A** and **B** the phase difference is

$$\Delta\phi = \delta_{\mathbf{A}/\mathbf{B}} + 1/\Phi_0 \int\limits_{\mathbf{A}/\mathbf{B}} \mathbf{A}(\vec{s})\, d\vec{s}\,.(6, \mathrm{I}.3)$$

The index indicates whether the current is passing through the Josephson junction by the path **A** or **B**. $\mathbf{A}(\vec{s})$ is the vector potential along a path $\vec{s}$. The gauge invariance in a superconductor force the total phase difference to be zero or a integer multiple of 2π, equation (2, I.3). The induced flux in the SQUID area by the external field is

$$\Phi_{ext} = \oint\limits_{ring} \mathbf{A}(\vec{s})\, d\vec{s}\,. \qquad (7, \mathrm{I}.3)$$

Due to Stoke's theorem this is equivalent to the more common definition of flux $\Phi = B \times ring\ area$ with B the magnetic induction. The critical current through a DC-SQUID is therefore given by

$$I_C = I_0 \left| \cos\left(\frac{\pi\Phi_{ext}}{\Phi_0} \right) \right|. \qquad (8, \mathrm{I}.3)$$

Thus the critical current that can pass through a DC-SQUID is modulated by the flux induced in the ring area by an external magnetic field. The critical current is maximal if the external flux Φ_{ext} itself satisfy the quantization condition $\Phi_{ext} = n\Phi_0$, compare equation (2, I.3). An ideal example of a SQUID-characteristic, i.e. the critical current I_C vs. the flux, is shown in figure [I.3.2].

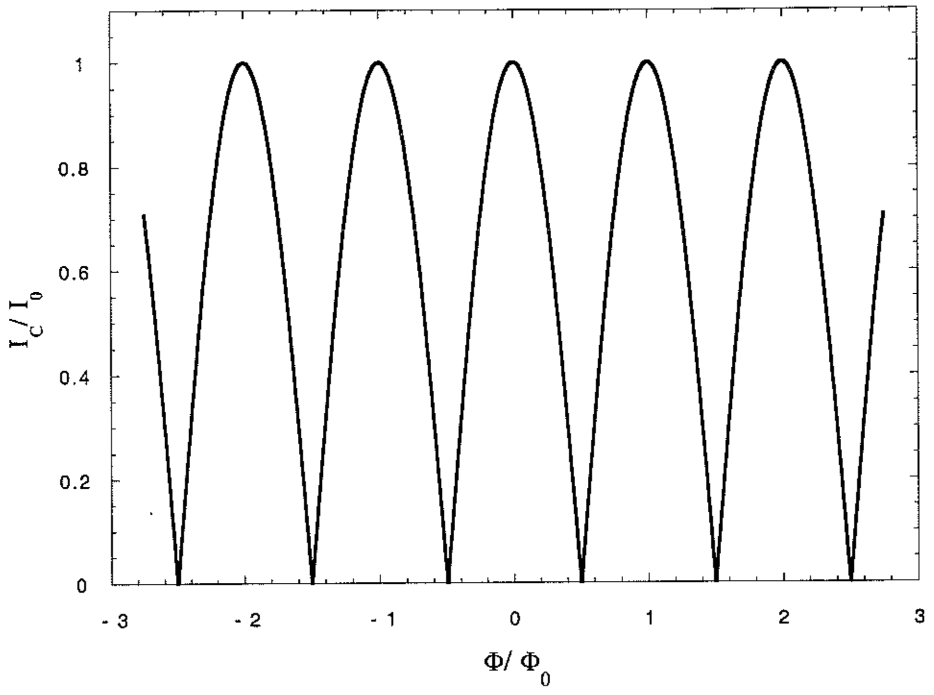

Figure I.3.2: Characteristic of a DC-SQUID: The critical current is a periodic function of the total flux.

– *Feedback technique for a shunted DC-SQUID*

In a common practical usage of a DC-SQUID, the Josephson junctions are accompanied with a capacitance C and an ohmic resistance R in parallel to the Josephson junction. Therefore the *VI*-characteristics of the DC-SQUID is modified as shown by the dashed line in figure [I.3.3]. Up to the critical current I_{C1} the SQUID has no resistance. For a slightly larger current, up to I_{C2} the SQUID has a non-ohmic resistance until the current surpasses I_{C2} and the resistance of the SQUID becomes ohmic. A SQUID with such a *VI*-characteristic is called a shunted SQUID. The value of I_{C1} and I_{C2} change with the flux as described by equation (8,I.3).

For magnetic measurements the SQUID is exposed to two sources of a magnetic field. One component comes from the sample and the other from a small feedback-coil close to the SQUID that is used by the electronic control unit and does not effect the sample. The DC-SQUID electronics provides a magnetic feedback field that keeps the SQUID at the same point in the non-ohmic region between I_{C1} and I_{C2}, the working point. Thus if the induced flux from the sample is changed the control unit keeps track of the change by a counterbalancing field of the feedback-coil. This counterbalancing field is proportional to the signal of the sample. For the high-field magnetometer and the ac-field magnetometer commercial SQUID-systems of the type B.T.I and S.H.E. cooperation are used including the control electronics.

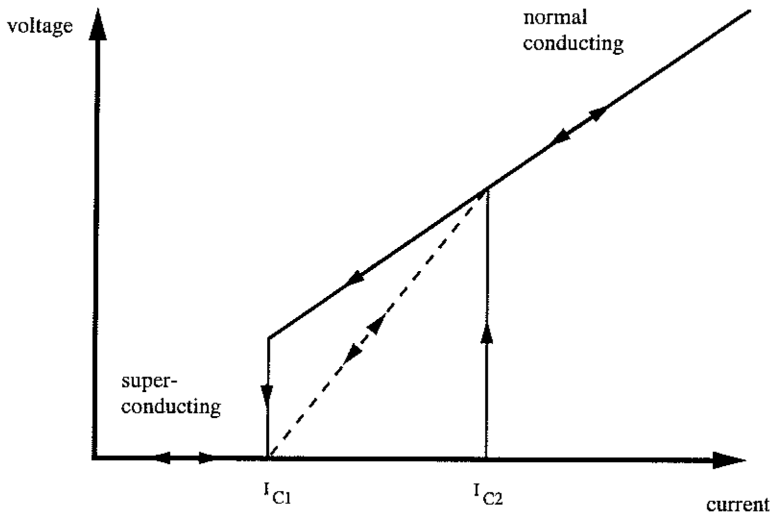

Figure I.3.3: *VI*-characteristic of a hysteretic SQUID (solid line). The dashed line is an examplary curve for a shunted SQUID. We call the dashed part "non-ohmic" region because it doesn't extrapolate to zero.

– *Measurement technique of a hysteretic SQUID*

A microSQUID-system using hysteretic SQUIDs was developed at the CRTBT over the recent years, see the thesis of Wolfgang Wernsdorfer [Wernsdorfer 96]. The Josephson junctions of a hysteretic SQUID doesn't have an isolating layer between two superconductors but a microbridge that acts as a weak link between them. The underlying physics of the Josephson junction remains essentially the same as described above but the *VI*-characteristic of a hysteretic SQUID is different from that of a shunted SQUID. The characteristic does not have a non-ohmic regime. If the current reaches the critical value of I_{C2} the micro-bridges become normal and have an ohmic resistance. In order to reinstall the SQUID into a superconducting state the applied current has to be reduced to a much lower value than I_{C2}. It is therefore not possible for a control unit to hold the SQUID on one working point as for the shunted SQUID.

To measure a magnetic signal with a hysteretic SQUID, the control electronics continuously measures the critical current. The electronic ramps up the current passing through the SQUID until a resistance is detected, i.e. the micro-bridges become normal. Then the current is immediately cut and the superconducting state is reinstalled. To follow the change in a magnetic signal a feedback signal is applied as for the shunted SQUID. The control unit is connected to a small coil that counterbalances the signal of the sample, thus the critical current I_{C2} remains constant.

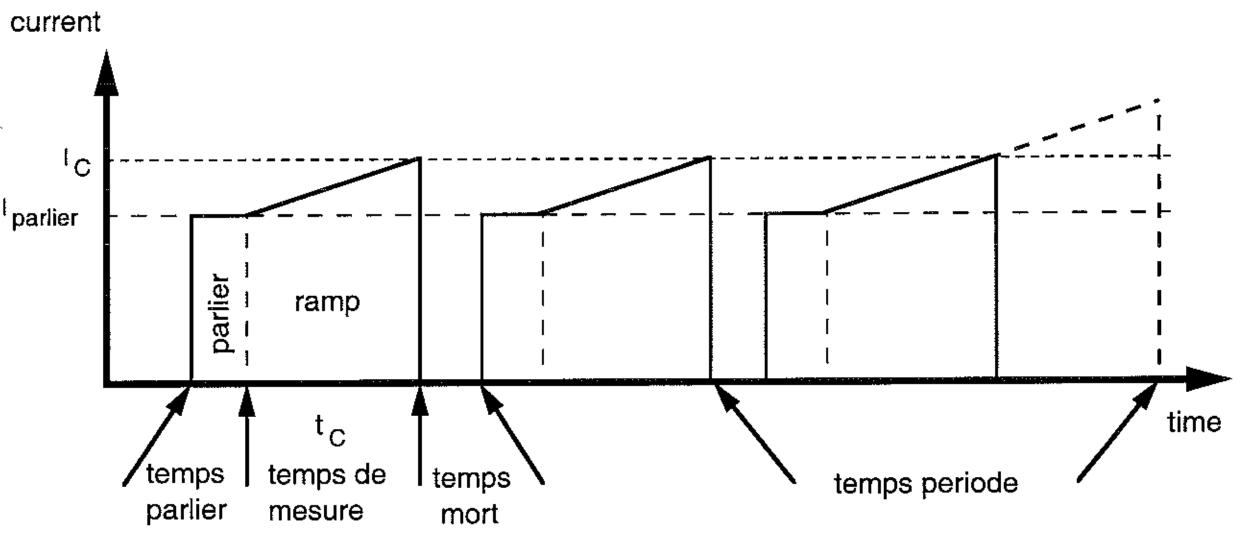

Figure I.3.4: Schema of the ramping procedure measuring the critical current of a hysteretic SQUID.

– The technical realization of the feedback procedure for a hysteretic SQUID

The setup of the microSQUID system is shown in figure [I.1.2]. The control unit consists of an analog device that applies a current to the SQUID and measures is resistance and a digital unit PDL that takes care of the timing and drives the analog device. The feedback is regulated by software on a Macintosh-computer. The Macintosh-computer communicates with the PDL unit and calculates the feedback signal. The calculated value of the feedback signal is communicated to an digital-analog converter that drives the feedback coil via a voltage controlled current supply.

The measurement protocol is depicted in figure [I.3.4]. Each of the three ramps represents one measurement of the critical current of the hysteretic SQUID. One measurement cycle consists of three steps:

- At the beginning of a measurement cycle a constant current $I_{parlier}$ is applied. This current should be chosen slightly below the expected critical current. During a certain time "temps parlier" this current is kept constant to give the analog electronic some time to stabilize. A typical value for this time duration is about 100 µsec.

- Afterwards the current is ramped at a constant rate v [A/sec]. As long as the current is still below the critical current I_{C2} the micro-bridges stays superconducting and the electronic will measure no resistance. As soon as the critical current is reached the micro-bridges become normal conducting and the electronic measures a resistance over the SQUID and the current is immediately cut. When the ramp begins a counter is initialized that measures the time t_C until the critical current is reached "temps de mesure".

- The control system wait some time after the critical current is reached "temps mort". During this time the micro-bridges will cool down and become superconducting again.

The measured time t_C is proportional to the critical current of the $I_{C2} = I_{parlier} + vt_C$. Typical values for the critical current of the hysteretic SQUID we have used are of the order $I_C \approx 1$ mA. Occasionally the electronic doesn't detect a transition of the SQUID. In this case the ramp will be stopped after some time "time periode" and a new measurement cycle initialized. This time period also determines the speed of the feedback. For our experiments we chose a measurement time (temps periode) of about 0.5 msec sec to 1 msec. Thus the feedback can at maximum work at a rate of 1–2 kHz. The feedback was controled by a Quadra Macintosh computer. The program compares the former critical current I_{C2}^{former} with the recent value I_{C2}^{new}. The applied feedback signal is then changed proportional to difference between these values.

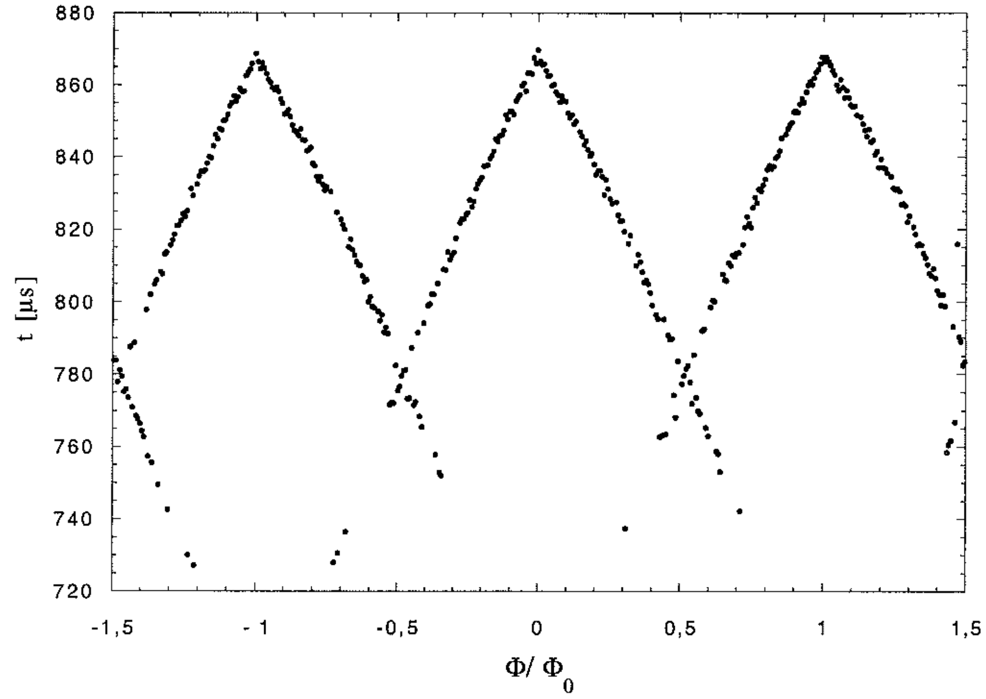

Figure I.3.5: Characteristic of a hysteretic niobium SQUID.

Besides the very rare occasions that the electronics does not detect a transition in the SQUID, the use of niobium SQUIDs has some problems. The SQUID-characteristic of a niobium SQUID is far from the ideal case as depicted in figure [I.3.2]. Often the characteristic of a niobium SQUID is double-valued as shown in figure [I.3.5]. This figure shows the characteristic of an empty niobium SQUID we have used. For more details see [Wernsdorfer 96]. The measured critical current will jump between to branches and will strongly destabilize the feedback. We therefore used a software filter to ignore useless measurements. This filter program takes three measurement values of the critical current and calculates the average value of the two values that are the closest to each other and neglects the third value. This way we have obtained good results and misleading values for the feedback software are omitted. This filter will of course only work if at least two third of the measurements are correct. We obtained by this method satisfying results but on the cost of the feedback speed which was in our case not critical.

Chapitre II

Aperçu Théorique

II.1) Le Spin Géant 29

II.2) L'Effet Tunnel Quantique d'Aimantation 31

II.3) Les Effets d'Environnement 35

II.4) L'Effet Tunnel Cohérent et Incohérent 41

Dans ce chapitre nous donnons un aperçu de la théorie de l'effet tunnel quantique d'aimantation. Dans la section II.1 nous discutons le concept de spin géant. Une molécule qui se compose de plusieurs spins est décrite par un Hamiltonien complexe et peut avoir une grande variété d'états excités. A basse température seules les excitations de basse énergie sont possibles et la structure interne de la molécule est négligeable. Sous cette condition, l'Hamiltonien peut être simplifié, c'est-à-dire ramené à celui d'un système à un seul spin, le spin géant. La molécule apparaît donc comme une entité avec un spin S unique. Dans la section II.2, nous décrivons l'effet tunnel quantique d'un tel spin géant. En présence d'une barrière d'anisotropie uni-axiale un axe facile est déterminé et les $2S+1$ états m d'un spin sont séparés. Il ne reste que la dégénérescence entre les états $\pm m$. Pour l'effet tunnel quantique il faut des termes dans l'Hamiltonien qui brisent la symétrie en direction de l'axe facile. Ces termes perpendiculaires déterminent une amplitude tunnel quantique. Le spin peut seulement franchir la barrière d'énergie si la différence entre l'état initial et final est plus petite que cette amplitude tunnel quantique. A haute température, le spin peut franchir la barrière par activation thermique. Le spin interagit avec des phonons et selon la distribution thermique de Boltzmann il peut franchir la barrière d'anisotropie avec une certaine probabilité. Dans la section II.3 nous discutons quelques détails relatifs aux effets d'environnement sur un spin géant. Il s'agit d'un aperçu des théories récentes sur un bain de spins nucléaires et un bain de phonons et leur effet sur le spin géant. La dernière section II.4 décrit comment les effets d'environnement peuvent détruire la cohérence quantique dans ce système.

II.1) Giant Spin Model

The idea of a giant spin is to represent a magnetic entity, e.g. a single domain particle or a molecular nano-magnet or molecule, by a single spin degree of freedom $\hat{S}$. That is to represent all internal electronic spin degrees $\hat{s}_i$ by a single, central spin $\hat{S} = \sum_{i=1}^{N} \hat{s}_i$. This concept is only appropriate for the low temperature regime with small dissipation effects of the environment and on an energy scale well below a typical excitation of an internal degrees of freedom.

A theoretical approach to describe its motion is to use semi-classical methods on a giant spin S in the limit $\lim_{\hbar \to 0} \hbar S = const.$ thus implying $S \to \infty$ [Hemmen 86a, Hemmen 86b, Enz 86]. Another method is to truncate a comprehensive, "high energy" Hamiltonian to a low energy, effective Hamiltonian. It turns out [Stamp 98] that for a large class of high energy Hamiltonians the truncated, effective Hamiltonian shows some universal properties, i.e. a single effective Hamiltonian describes well the low energy properties of a variety of different high energy Hamiltonians. Including an environment a general Hamiltonian has the form

$$\hat{H} = \hat{H}_0(\hat{S}) + \sum \hat{H}_{\text{int}} + \hat{H}_{env} \quad (1, \text{II}.1)$$

where $\hat{H}_{env}$ is the Hamiltonian of an environment, like e.g. an oscillator bath (phonons) or a spin bath (nuclear spins), with its interaction via $\hat{H}_{\text{int}}$ to the central spin $\hat{H}_0(\hat{S})$. The summation symbol should just indicate that the central spin might couple to several environmental influences, like phonons, nuclear spins, electromagnetic fields etc. Thus for an organo-metallic molecular magnet each magnetic molecule containing a number of electronic spins $\{\hat{s}_i\}$ is mapped on central, giant spin surrounded by a non-magnetic, organic matrix.

The Giant Spin

For the giant spin Hamiltonian a quite general form can be given as

$$\hat{H}_0(\hat{S}) = \sum_{l=1}^{N} K_l^{\|} \hat{S}_z^l + \frac{1}{2} \sum_{r=1}^{N} K_r^{\perp} \left(\hat{S}_+^r + \hat{S}_-^r \right) \quad (2, \text{II}.1)$$

acting on a Hilbert space of the dimension $D\left[\hat{H}_0(\hat{S})\right] = 2S + 1$. This form separates the diagonal components $\hat{H}_0^{\|}(\hat{S}_z)$, conserving the S_z–states, from the off-diagonal components $\hat{H}_0^{\perp}(\hat{S}_+, \hat{S}_+)$, which breaks the z-symmetry and allow tunneling between the S_z–states. The coefficient $K_2^{\|}$ represents the uni-axial anisotropy and formally $K_1^{\|} = g\mu_B H_{\|}$ is the Zeemann-term for an applied longitudinal magnetic field $H_{\|}$. $K_r^{\perp}$ is the in-plane anisotropy.

This giant spin Hamiltonian results from the truncation of a high energy, microscopic Hamiltonian like

$$\hat{H}_0\left(\{\hat{s}_i\}\right) = \frac{1}{2} \sum_{<i,j>} J_{ij}^{\alpha\beta} \hat{s}_i^{\alpha} \hat{s}_j^{\beta} + \frac{1}{2} \sum_{j} K_j^{\alpha\beta} \hat{s}_j^{\alpha} \hat{s}_j^{\beta} \quad (3, \text{II}.1)$$

acting on a much larger Hilbert space of the dimension $D\left[\hat{H}_0\left(\{\hat{s}_i\}\right)\right] = \prod_{i=1}^{N} 2\hat{s}_i + 1$. This Hamiltonian takes into account explicitly the internal electronic spin degrees of freedom including their exchange or super-exchange interactions. A truncation of this kind is only meaningful if the internal excitations of $\hat{H}_0\left(\{\hat{s}_i\}\right)$ are negligible on the energy scale of the giant spin Hamiltonian. For example internal excitations like magnons can lower their energy by spreading over the whole sample. As the sample (i.e. also S) becomes larger, these "internal magnons" can interfere with the $2S$+1 low energy states of the giant spin.

A Giant Spin in an Environment

For the molecular nano-magnet systems under consideration the most important environmental influences come from the surrounding nuclear spins of a molecule and at "higher" temperatures from phonons of the crystal lattice. Both effects can be described in terms of an environmental bath (spin bath, oscillator bath) and its interaction with the central spin. In general a mapping between the oscillator bath description and the spin bath description is not possible [Prokef'ev 96]. A crucial difference between these models is that the oscillators are only very weakly affected by the central system whereas the spins in the spin bath model change the spectra and dynamics completely [Stamp 98].

– Nuclear Spins

For the spin bath of the nuclear spins the Hamiltonian for the spin bath and the interaction can be written as [Stamp 98]

$$\hat{H}_{int}^{nuclear} + \hat{H}_{bath}^{nuclear} = \frac{1}{S}\sum_{k=1}^{N}\vec{\omega}_k \hat{S}\hat{\sigma}_k + \sum_{k=1}^{N}\sum_{k'=1}^{N} V_{k,k'}^{\alpha\beta}\hat{\sigma}_k^{\alpha}\hat{\sigma}_{k'}^{\beta} \qquad (4, \text{II}.1)$$

where $\hat{\sigma}_k$ represents the nuclear spins, $\vec{\omega}_k$ the coupling constants, and $V_{k,k'}^{\alpha\beta}$ the dipole inter-nuclear interaction within the bath. A separation of the interaction term into a longitudinal and a transverse component gives

$$\hat{H}_{int}^{nuclear}\left(\hat{S},\{\hat{\sigma}_k\}\right) = \frac{1}{S}\sum_{k=1}^{N}\omega_k^{\parallel}\hat{S}_z\sigma_z^{(k)} + \sum_{k=1}^{N}\omega_k^{\perp}\left(\hat{S}_+\hat{\sigma}_+^{(k)} + \hat{S}_-\hat{\sigma}_-^{(k)}\right) \qquad (5, \text{II}.1)$$

with $\omega_k^{\parallel}$, $\omega_k^{\perp}$ the longitudinal and transversal coupling constants respectively. The dynamics of the nuclear spin system is governed by longitudinal T_1–processes and by transversal T_2–processes. At low temperatures T_1 increases dramatically while T_2 is of the order of 10^{-4}–10^{-5} sec [Prokof'ev 97a, Stamp 98]. The inter-nuclear interaction $V_{k,k'}^{\alpha\beta}$ are of the order of $\sim T_2^{-1}$ and this dynamics will still be present at low temperatures [Prokof'ev 96].

– Phonons

At temperatures where phonons become relevant an additional pair $\hat{H}_{int}^{phonon} + \hat{H}_{bath}^{phonon}$ comes into play. Their effects can be well described in terms of an oscillator bath as first studied by Feynman and Vernon [Feynman 63] and Caldeira and Leggett [Caldeira 81, Caldeira 83]. Using the "spin–boson" model the Hamiltonian is given by [Stamp 98]

$$\hat{H}_{int}^{phonon} + \hat{H}_{bath}^{phonon} = \frac{\Omega_0}{S}\hat{S}_x\hat{S}_y\left(\frac{m_e}{M_{molecule}}\right)^{1/4}\sum_{\vec{q}}\sqrt{\frac{\omega_q}{\Theta_D}}\left[b_{\vec{q}} + b_{\vec{q}}^{+}\right] + \sum_{\vec{q}}\left(b_{\vec{q}}^{+}b_{\vec{q}} + \frac{1}{2}\right) \qquad (6, \text{II}.1)$$

where Ω_0 is the low energy cut-off, m_e the electron mass, $M_{molecule}$ the mass of the molecule, ω_q the phonon energy, Θ_D the Debye temperature, and $b_{\vec{q}}, b_{\vec{q}}^{+}$ the phonon annihilation and creation operators.

II.2) Quantum Tunneling of the Magnetization in Molecular Magnets

In a molecular system with a sizable anisotropy the spin might flip via under barrier tunneling. Given a giant spin S of a molecule with an anisotropy of $\hat{H}^{\|} = -K^{\|}\hat{S}_z^2$, i.e. S is not too large and the anisotropy not too small the eigenvalues E_m of the eigenstates $|S,m\rangle$ are well separated with a remaining degeneracy between the states of same modulus of $|m|$ and opposite sign $\pm m$. The level spacing ΔE_m between the energies E_m and E_{m-1} is $\Delta E_m = K^{\|}(2m-1)$ and is of the order of a few Kelvins for the systems under consideration. See the schematic level scheme in figure [II.2.1].

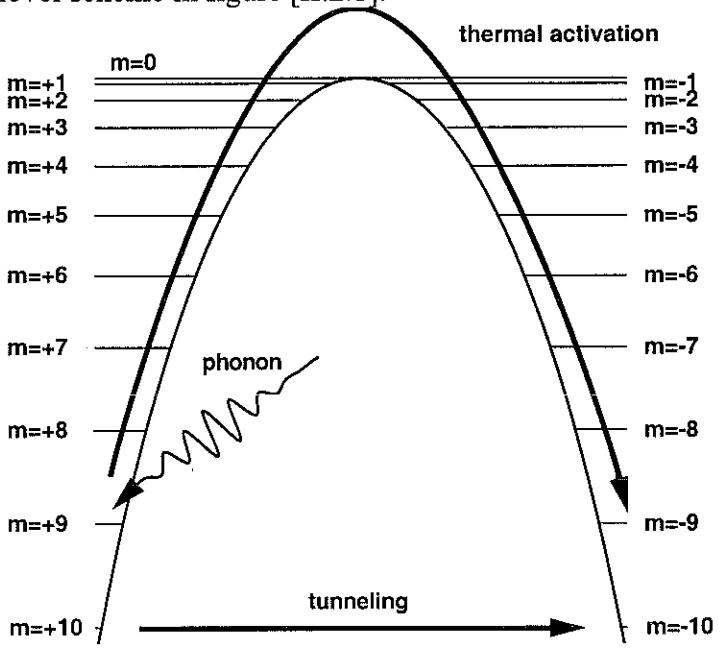

Figure II.2.1: Level scheme for S=10. The spin might gain energy by a phonon and overcome the barrier or it might tunnel directly through the barrier. Quantum tunneling through the barrier is only permitted if the initial and the final state have the same energy up to the tunnel splitting Δ_{tunnel}.

– *thermal activation*

The states are populated following the Boltzmann distribution $p_m(T) \propto \exp(-E_m / kT)$. At high temperatures the probability of a spin to be near the top of the energy barrier is large thus a thermal activated transition is probable with the rate of the Arrhenius law $\tau_{TA}^{-1}(T) = \tau_{0\_TA}^{-1} \exp(-\Delta_{Barrier} / kT)$. The prefactor τ_{0_TA} for molecular magnets can vary from 10^{-12} to 10^{-7} sec and the relaxation at higher temperatures can be quite rapid. At low temperatures $T << K^{\|}S^2$ a thermal activated transition over the barrier is extremely unlikely, since the relaxation time becomes astronomically large, the molecule is most likely to be found only in the lowest states.

– *quantum tunneling*

If an off-diagonal term $H^{\perp}(\hat{S}_+, \hat{S}_-)$ is present S_z is no longer a good quantum number, i.e. S_z is not conserved, and transitions via tunneling are possible. The off-diagonal terms give rise to a tunnel splitting Δ_{tunnel}. Tunneling is only permitted if the initial state E_m and the final state E_{-m} are in resonance $|E_m - E_{-m}| \leq \Delta_{tunnel}$. The ratio of the level splitting to the resonance width depends of course on the ratio of the diagonal to the off-diagonal terms in the Hamiltonian. For the systems of interest, Fe8 and Mn12, the resonance width is much smaller than the level spacing $\Delta_{tunnel} << \Delta E_m$. The relaxation rate τ_{qtm}^{-1} in resonance in this quantum regime is temperature independent. In consequence a molecular tunneling system will show a crossover from a thermal activated behavior with a relaxation time $\tau_{TA}^{-1}(T)$ at higher temperatures to a temperature independent relaxation time τ_{qtm}^{-1} at lower temperatures. The crossover temperature T_c can be estimated from the Arrhenius law. At the crossover temperature $\tau_{qtm} = \tau_{TA}(T_C)$ thus

$$kT_C = \Delta_{Barrier} / \ln\left(\tau_{qtm} / \tau_{0\_TA}\right). \qquad (1, \mathrm{II}.2)$$

Resonant Quantum Tunneling

An applied external field H shifts the energy of the eigenstates according to the Zeemann term. Neglecting the off-diagonal terms, the Hamiltonian is

$$\hat{H} = -K^{\|}\hat{S}_z^2 + g\mu_B \hat{S}_z H. \qquad (2, \mathrm{II}.2)$$

A degeneracy between the states m and $-(m-n)$ will regularly occur for the "resonance" fields

$$H_n = n\frac{K^{\|}}{g\mu_B}, n = 0,1,...S. \qquad (3, \mathrm{II}.2)$$

Including the off-diagonal $\hat{H}^{\perp}\left(\hat{S}_+, \hat{S}_-\right)$ elements complicates the situation since the states $|S,m\rangle$ are no longer eigenstates, and the wave function must be written as a mixture of states $|S,m'\rangle = \sum_m \alpha_{m,m'} |S,m\rangle$. In particular if the off-diagonal term has the form

$$\hat{H}^{\perp}\left(\hat{S}_+, \hat{S}_-\right) = K_r^{\perp}\left(\hat{S}_+^r + \hat{S}_-^r\right) \qquad (4, \mathrm{II}.2)$$

with $K_r^{\perp} << K^{\|}$ the states $|S, m \pm nr\rangle$ with $n = -S, -S+1, ..., S-1, S$ will mix. As a consequence the resonance field will differ from H_n in equation [2, II.2] and depend also on m. Level crossing occurs at the field values $H'_{n,m} = nK^{\|}/g\mu_B + \Delta H_{n,m}$ with $\Delta H_{n,m} << K^{\|}/g\mu_B$. The energy levels will not coincide at the same field value but for each pair of states $\pm m$ the resonance field is systematically shifted with m, see e.g. [Thomas 97].

An exception are second order off-diagonal terms, i.e. $r = 2$ in equation (4, II.2). In this case the off-diagonal term becomes $\hat{H}^{\perp}|S,m\rangle = K^{\perp}(m(m+1) + m(m-1)) = 2K^{\perp}m^2$ and the resonance field is $H'_n = n\left(K^{\|} + 2K^{\perp}\right)/g\mu_B$, $n = 0,1,...S$ and the crossover field remains equidistant and all pairs $\pm m$ will coincide at the same field value.

It has been shown experimentally that the relaxation time varies strongly with the external field. DC-relaxation measurements in the quantum regime show appreciable relaxation only within a small range of the resonance fields and almost no relaxation between these fields. A hysteresis cycle at low temperatures shows a periodic change of the slope, with a strongly enhanced slope at the resonance fields.

Theoretical Results

In this section a short summery of existing theories and their results will be given. These pioneering theories are based on isolated spins and neglect any environment or interaction between the spins. Different methods have been chosen to solve the tunneling problem for different situations, but some features are common in their solutions:

- Suppression of quantum tunneling for half-integer spin S
- Tunneling rate $\tau_{qtm}^{-1} \approx \tau_0^{-1}x^S$ with $x \propto K^{\perp}/K^{\|}$
- A transverse magnetic field $H_{\perp}$ enhances tunneling
- Estimates vary over a wide range but it seems improbable that the tunnel splitting for Fe8 exceeds 10^{-8}K (~200Hz) and for Mn12 10^{-10}K (~2Hz)

The possible methods for calculating the tunneling amplitude of an isolated giant spin are:

1) WKB-Method:
   Solving the semi-classical problem $S \rightarrow \infty$ by mapping the spin system on a particle system and using the WKB-formalism [Hemmen 86a, 86b, 88].
2) Perturbation Theory:
   Can be applied when the off-diagonal elements are small compared to the anisotropy barrier [Korenblit 78, Garanin 91].
3) Instanton formalism:
   Using the path integral formalism and integrating over the classical paths [Enz 86, Ioselevich 87].
4) Diagonalization:
   If the Hamiltonian is simple enough a direct diagonalization may be possible, see annex I for an example.

– *Examples of detailed solutions*

- Van Hemmen and Sütö [Hemmen 86a, 86b, 88, 94] start from the quite general Hamiltonian

$$\hat{H}_0(\hat{S}) = -K^{\|}\left|\hat{S}_z\right|^l - \frac{1}{2}\sum_{r=1}^{N} K_r^{\perp}\left(\hat{S}_+^r + \hat{S}_-^r\right) \quad (5, \text{II.2})$$

with $K_l^{\|}$ and $K_r^{\perp}$ positive and assuming a strong parallel anisotropy $K^{\|}S^l >> \sum_{r=1}^{N} K_r^{\perp} S^r$ where $S >> 1$ is the total spin. They suggest that spin tunneling could be described as a hopping process of a particle on the spectrum of $\hat{S}_z$. Assuming only one coefficient $K_r^{\perp}$ is non-zero ($r = N$) their semi-classical treatment yields for low energies $E \leq -K^{\|}S^l$ a tunneling amplitude Δ_{tunnel} of

$$\Delta_{tunnel} = \tau_0^{-1}\left(\frac{K_N^{\perp}S^N}{2|E|}\right)^{2S/N} \qquad (6, \text{II.2})$$

with a quantum mechanical attempt frequency of

$$\tau_0^{-1} = lK^{\|}S^{l-1}/2\pi. \qquad (7, \text{II.2})$$

- Garanin [Garanin 91] has chosen a perturbative approach to calculate the tunnel splitting for a system described by the Hamiltonian

$$\hat{H} = -D\hat{S}_z^2 + B\hat{S}_y^2 \qquad (8, \text{II.2})$$

and found a tunnel splitting for $B<<D$ of

$$\Delta_m = \frac{8D}{[(m-1)!]^2}\frac{(S+m)!}{(S-m)!}\left(\frac{B}{16D}\right)^m. \quad (9, \text{II.2})$$

This result can for the ground state and $S >> 1$ be simplified to

$$\Delta_S = \frac{8DS^{3/2}}{\sqrt{\pi}}\left(\frac{B}{4D}\right)^S. \qquad (10, \text{II.2})$$

II.3) Environmental Effects

Nuclear Spins

The effects of a bath of nuclear spins can be discussed in terms of an additional magnetic field a central spin experiences [Stamp 98]. In this chapter we take only the hyperfine interaction into account and neglect any further interaction, e.g. the dipole fields of the electronic spins. The nuclear spins within and around a giant spin in a molecular magnet give rise to a hyperfine field acting on the central spin and vice versa, the central spin will act via its dipole field on the magnetic moment of the nuclei. The energy bias of a spin bath of N nuclear spins on a two level system, i.e. the giant spin is either up or down (compare equation 5, II.1), is given by

$$\varepsilon = \sum_{k=1}^{N} \omega_k^{\parallel} \sigma_z^{(k)} \quad (1, \mathrm{II}.3)$$

where we have neglected the transverse term $\omega_k^{\perp} = 0$. The polarization of the nuclear spin bath is $\vec{P} = \sum_k \vec{\sigma}_k$ and several nuclear spin configuration $\{\vec{\sigma}_k\}_{k=1,N}$ can result in the same polarization, i.e. they are in the same polarization group. The values of $\omega_k^{\parallel}$ are spread around a ω_0 in a way that $\sqrt{\sum_k (\omega_k^{\parallel} - \omega_0)/N} \equiv \delta\omega$. A measure of the distribution width within one polarization group is $\xi_0 \sim \sqrt{N}\delta\omega_0$. It has been argued in [Stamp 98] that in a real system the polarization groups are overlapping thus in a sample the hyperfine fields are varying over a range of $E_0 \sim \sqrt{N}\omega_0$.

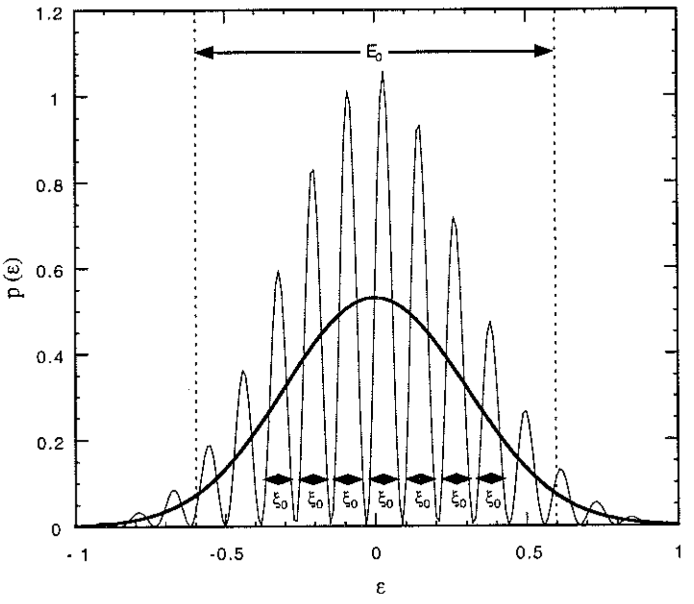

Figure II.3.1: The hyperfine energy spreads ξ_0 per polarization group sum up over the whole sample to a much broader distribution E_0.

In addition to this energy bias spread, the magnetic moments of the nuclei vary strongly from element to element. Manganese $^{55}_{25}Mn$ has a strong hyperfine field with a nuclear spin of I=5/2. In contrast natural iron consist mainly (~97%) of the isotope $^{55}_{26}Fe$ which has no magnetic moment since I=0. The hyperfine field does not just originate from the ion nuclei of the magnetic cluster but also from e.g. the hydrogen nuclei of the organic ligands around and within the molecule. In Fe8 for example there are about ~100 hydrogen atoms within each unit cell. Therefore an exact evaluation of the hyperfine field is impossible. Estimates for Mn12 give an average hyperfine spread of $E_0 \sim 0.4$–0.5K (~300–400 gauss) and for Fe8 the spread might be only of the order of about $E_0 \sim 10^{-3}$K (~1 gauss, although these values are not certain but at least the spread for Fe8 is much smaller than for Mn12). These fields are much larger than the estimated tunnel amplitude for these systems $\Delta_{tunnel} \sim 10^{-8}$–$10^{-10}$K. Prokof'ev and Stamp argue [Prokof'ev 96 & 97, Stamp 98] that a static nuclear spin bath will block the relaxation while taking the dynamics of the nuclei into account give rise to incoherent tunneling.

– *static effect*

The spread of the hyperfine fields within the molecules of a sample is much larger than the tunnel amplitude, $E_0 >> \Delta_{tunnel}$, and most giant spins in the sample are off resonance. Only a very small fraction of the molecules can tunnel where the initial and the final state of the giant spin are accidentally in the range of the tunnel amplitude Δ_{tunnel}. The system is essentially blocked.

– *dynamic effect*

The inter-nuclear interaction $V_{k,k'}^{\alpha\beta}$ gives rise to a dynamics within the spin bath, see equation (5, II.1). $V_{k,k'}^{\alpha\beta}$ is of the order of the T_2-processes ($V_{k,k'}^{\alpha\beta} \sim T_2^{-1}$). At low temperatures the T_2-processes are the only dynamics in the nuclei system since T_1 will become very large [Prokef'ev 96 & 97]. The hyperfine field will wander on average over the whole range of ξ_0 within a time T_2 [Prokef'ev 96, Stamp 98]. T_2^{-1} is typically of the order of 10–100 kHz even in the milliKelvin range. This rapid fluctuation will destroy the coherence in the central spin system but sweeps it continuously through the small tunneling window of Δ_{tunnel}. Prokof'ev and Stamp have shown that the central spin system will remain long enough within the resonance window to allow tunneling. They derived in the limit of no nuclear spin co-flipping with the central spin the incoherent tunneling rate for a single, isolate molecule is

$$\tau_0^{-1} = \frac{2\Delta_{tunnel}^2}{\sqrt{\pi}\xi_0}. \quad (1, \text{II.3})$$

In this formula the nuclei spin bath effects are summed in the denominator. Any additional bias ξ will alter the relaxation rate exponentially as

$$\tau_N^{-1}(\xi) = \tau_0^{-1} \exp\left(-|\xi| / \xi_0\right). \quad (2, \text{II.3})$$

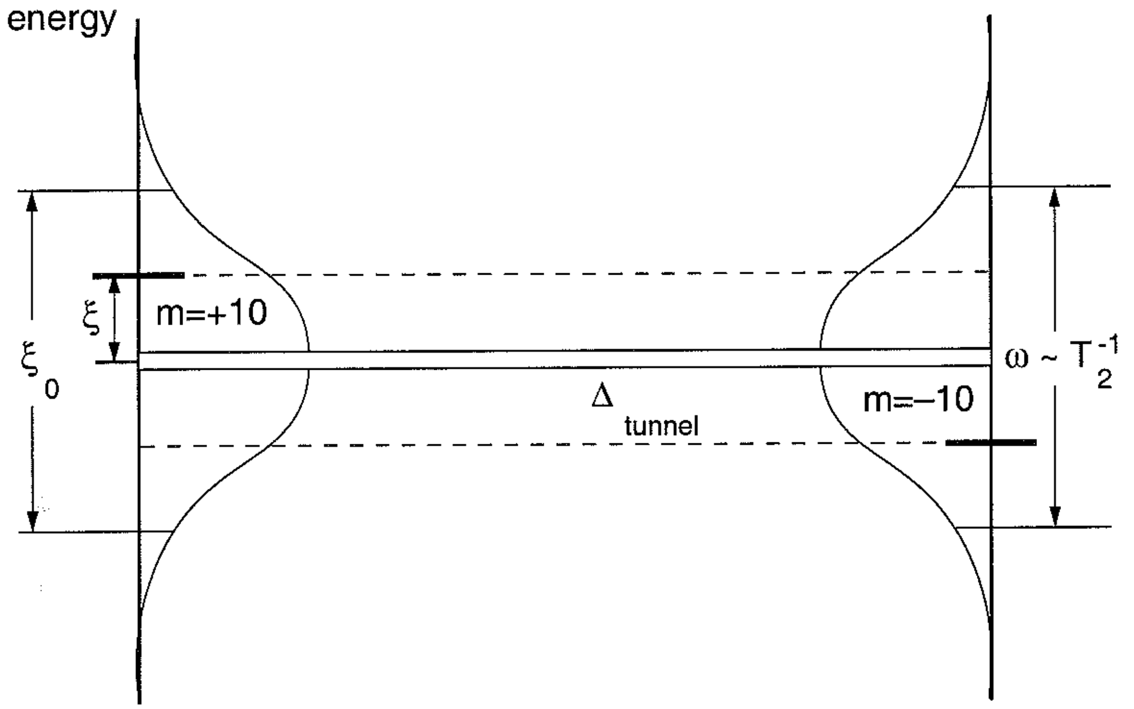

Figure II.3.2: Effect of the hyperfine field on the lowest lying levels $m = \pm 10$ within one polarization group. A static hyperfine field that shift the energy level by ξ larger than Δ_{tunnel} will block the system. Within a polarization group the hyperfine fields are distributed over a width ξ_0. Nuclear T_2-processes might shift the energy levels over the whole range ξ_0 and will eventually open a tunneling window for some time while sweeping through Δ_{tunnel}.

Phonons

At not too low temperature phonons can influence the relaxation dynamics in various ways. In the thermal activated regime phonons govern the relaxation rate in an ideal case as given in the Arrhenius law $\tau^{-1} = \tau_0^{-1} \exp(-\Delta_{Barrier} / kT)$. Beside this net effect, single phonons can influence the relaxation. In a theoretical description phonons couple to the spin via the matrix element $\langle m | V_{\sigma,q} | m' \rangle$ of the spin-phonon interaction, which are not quantified for these kinds of systems but can be assumed as small. We will outline here some recent ideas that may be of importance near the crossover temperature between the thermal activated regime and the quantum regime.

– thermal activated cascade

Neglecting any tunneling effects, the population of the spin levels as function of temperature follows the Boltzmann distribution $p_m^{thermal}(T) = p_0^{thermal} \exp(-E_m / kT)$. The barrier for an anisotropy of $-DS_z^2$ is $\Delta_{Barrier} = DS^2$ with the unperturbed eigenstates $E_m = -Dm^2$ and $m = -S,\ldots,+S$. Thus the population of a higher state is exponentially small. The energy difference ΔE_m between the levels m and m–1 is $\Delta E_m = D(2m-1)$. A phonon of this energy can lift the system from one state to the next higher state, and this energy is much smaller than the energy difference to the top of the barrier. Therefore a cascade process might be possible where a system is lifted in a sequence from one state to the next until it reaches the top of the barrier, see figure [II.3.3]. Afterwards the system may cascade down on the other side. Villain *et al.* [Villain 94] calculated that a thermal activated cascade has a relaxation time of

$$\tau_{casc}^{-1} = \tau_{0\_casc}^{-1} \frac{\exp\left(-\Delta_{Barrier} / kT\right)}{1-\exp\left(-\Delta_{Barrier} / S^2 kT\right)} \qquad (1, \mathrm{II}.3)$$

with

$$\tau_{0\_casc}^{-1} = \frac{3}{2\pi} \frac{\left|V_S\right|^2}{\rho c_{phonon}^5} \frac{\Delta_{Barrier}^3}{S^6}. \quad (2, \mathrm{II}.3)$$

c_{phonon} is the phonon velocity, ρ the specific mass, and V_S the matrix element of the spin–phonon interaction. Comparison with experiments are difficult because the spin–phonon interactions are not known. A tentative estimate indicates that $\tau_{0\_casc}^{-1}$ is much larger than obtained by experiment [Villain 94].

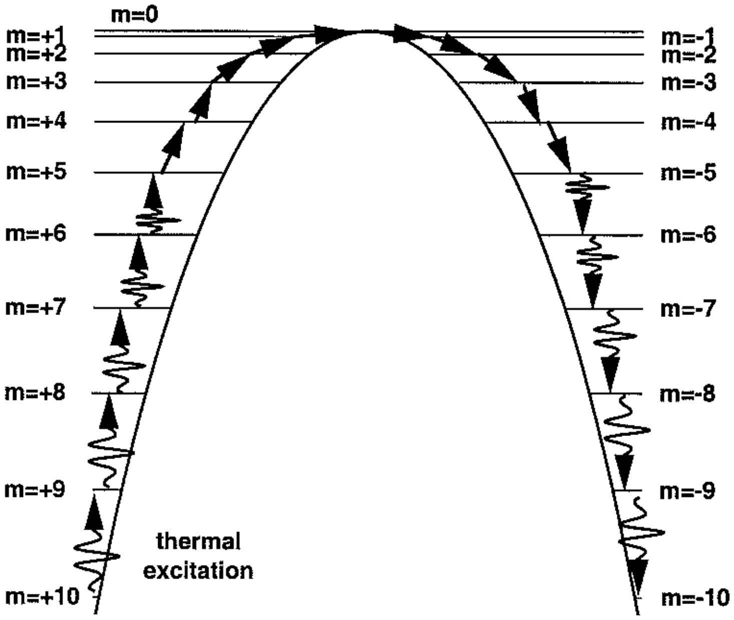

Figure II.3.3: A thermal activated cascade can result in a inversion of the spin direction without absorbing a phonon that has the energy of the barrier height. The system is absorbing low energy phonons that are just sufficient to jump from the state $m = +10$ to $m = +9$, then from $m = +9$ to $m = +8$, and so on. After the top of the barrier is reached the spin will relax to the unpopulated states of opposite spin orientation.

– thermal activated tunneling

The closer the levels are to the top of the barrier the larger is the tunnel amplitude Δ_m, see e.g. [Garanin 91] and consequently the relaxation rate. Very vaguely $\tau_m^{-1} \sim \Delta_m \sim x^m$ and $x \propto K^{\perp} / K^{\parallel}$. The tunnel rate of a system can therefore be enhanced if it is thermally lifted to a higher state and then tunnels, see figure [II.3.4]. This effect might become important in an intermediate temperature range where a thermal activated transition to a next level is probable but a thermal activated transition to overcome the whole barrier is improbable.

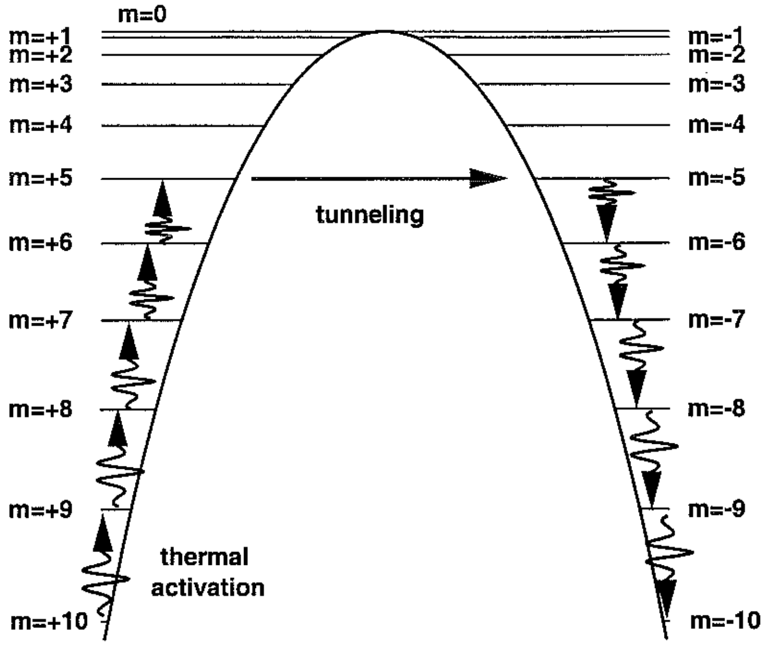

Figure II.3.4: The tunneling can be thermally activated. The higher the energy state the larger is the tunneling rate. Phonons can lift the system in a sequence up to a higher state. If the tunneling rate for this level is larger than the probability to be lifted to the next higher state by a phonon the system will shortcut the cascade and tunnel through the barrier.

– *thermal assisted tunneling*

A phonon can add or dissipate the energy bias between the initial and the finial state even if they are not in resonance, see figure [II.3.5]. As mentioned in the chapter on incoherent tunneling, equation (4, II.3), the tunneling rate will change by a factor $(coupling\ constant)^2 \times (density\ of\ states)$ thus here $V_{m,m'}^2 \times (\hbar\omega_{phonon})^3$. Politi *et al.* [Politi 95] analyzed in detail the tunnel rate for phonon assisted tunneling and found

$$\tau_{pat}^{-1} = \frac{12}{\pi\hbar^3 c_{phonon}^3 \rho} |V_S|^2 (h_z S)^3. \quad (3, \mathrm{II}.3)$$

c_{phonon} is the phonon velocity, ρ the specific mass, and V_S the matrix element of the spin–phonon interaction. $h_z S = g\mu_B H_\parallel S$ is the energy shift due to a magnetic field $H_\parallel$ along the easy axis thus giving the energy bias between the unperturbed eigenstates $m=\pm S$. In equation (3, II.3), the quantum coherence rate of the isolated system τ_{qc}^{-1} is included in the matrix element V_S [Politi 95].

Note that this mechanism gives a minimum of the relaxation rate τ_{pat}^{-1} for $H_\parallel = 0$ [Burrin96]. This is in contrast to experiments which show a maximum of the relaxation rate τ_{pat}^{-1} around zero-field [Paulsen 95a]. In addition, a non-monotone resonant behavior was observed as function of the external field.

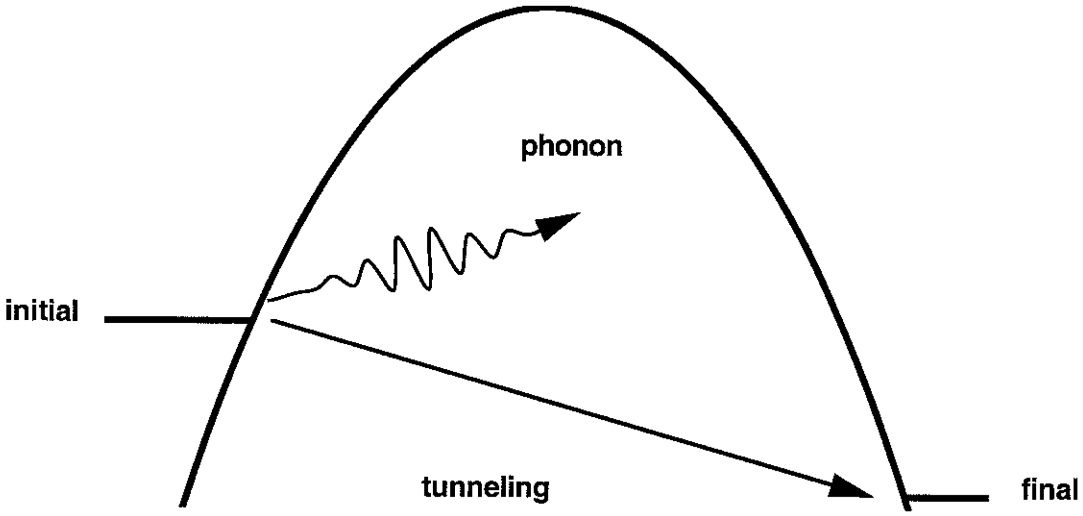

Figure II.3.5: If the spin-phonon coupling is large enough the tunneling can be thermally assisted. Without any environment a spin can only tunnel if the initial and the final state have the same energy within Δ_{tunnel}. By coupling to an environmental bath the energy difference between the initial and the final state of the spin can be gained from or dissipated to the environment.

II.4) Coherent and Incoherent Tunneling

According to quantum mechanics, under certain conditions a system can be prepared in a state that is a superposition of several eigenstates. For example, a system may be described in terms of the un-perturbed eigenstates states and an additional symmetry breaking contribution that gives rise to a tunnel splitting. If the system is isolated, a transition between its states can occur in a coherent way, i.e. the complete information of the initial quantum state will be preserved during each transition. However, including an environment which is usually associated with dissipation the transition will become incoherent, thus after every transition the information of the former states will be lost. In this case each transition would have the same effect as a measurement process on a quantum system and no superposition is present after a transition.

Quantum Coherence

Assume an isolated system with two degenerate levels (± 1) and a tunnel amplitude or tunnel splitting of Δ between these states: If the system is at the time t=0 prepared in the state +1, it will for later times oscillate coherently between the states +1 and –1 at a frequency

$$\nu_{qc} = \Delta / 2\pi\hbar. \qquad (1, \text{II}.4)$$

If an energy bias of ε is present this quantum coherence rate will change. Supposing the system is prepared at $t = 0$ in the eigenstates a, then $p_{ab}(t)$ is the probability to find the system in the eigenstate b at the time t, e.g. $a = +1$ and $p_{+1,+1}(t) = 1 - p_{+1,-1}(t)$ then $p_{+1,-1}(t) = \Delta^2 / E^2 \sin^2(Et)$ with $E = \sqrt{\Delta^2 + \varepsilon^2}$. If ε becomes large $\varepsilon >> \Delta$ the coherent oscillations will stop. The frequency will increase but the amplitude will reduce as $\sim \Delta^2 / E^2$, see figure [II.4.1]. The isolated system has no possibility to dissipated or gain energy from the environment thus energy conversation suppresses the transition. In consequence, coherence occurs only within a very narrow range where the bias is of the order of the tunnel amplitude. Since the tunnel amplitude in molecular magnets is very small the experimental observation of a coherence effect (magnetic quantum coherence, MQC) is very difficult to obtain. See the experimental findings of Awshalom on ferritin [Awshalom92a & 92b] and the theoretical criticisms in [Garg93a, 93b, 95, 96, Stamp 92a, Prokof'ev 93a, 94].

Incoherent Tunneling

If the quantum system is coupled to an environment, a transition between two states is accompanied with an excitation to the environment. The consequence depends strongly on the coupling. Certainly if the dissipation due to the environment is strong, i.e. strong coupling, then any quantum effects will be suppressed and the system behaves classically. A weak coupling to a dissipative environment will allow quantum effects like tunneling but might make the transitions incoherent. Thus the information of the former quantum state will be destroyed and the system appears after the transition, as it had been recently prepared in this state. For example if the system is weakly coupled to an oscillator bath the tunnel rate is given by

$$\tau_{tunnel}^{-1}(\varepsilon) = \Delta(\varepsilon)\gamma_{env}(\varepsilon) \qquad (3, \text{II}.4)$$

including an energy bias ε where $\Delta(\varepsilon) = \Delta^2 / E^2$ and the influence of the environment enters by

$$\gamma_{env}(\varepsilon) = (\text{coupling constant})^2 \times \rho_{bath}(\varepsilon). \qquad (4, \text{II}.4)$$

The environment is assumed as a bath that couples to the spin and $\rho_{bath}(\varepsilon)$ is the density of states of the bath at the energy bias ε. Thus if the density of states of the environment has for example a gap at ε the quantum system is in the same dilemma as an isolated system that it cannot dissipate the energy for the transition and the resonance width is as small as for a system without an environment.

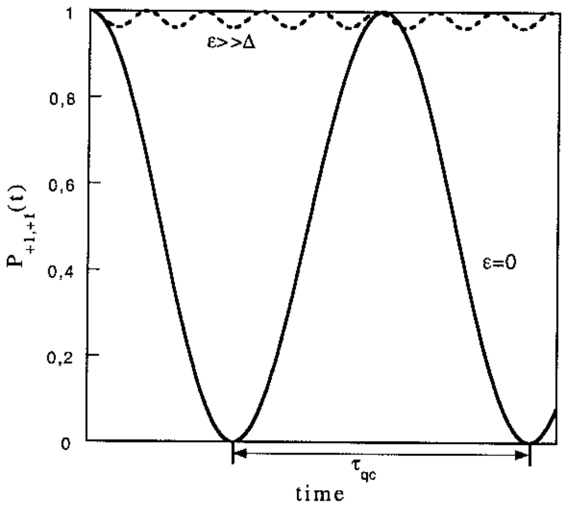

Figure II.4.1: Coherent oscillation between the up and the down state. The plot shows the time evolution of the probability to find a spin in an up state after it has been initialized in the up state. If the energy bias ε is small the probobolity oscillates with a rate of τ_{qc}^{-1} between the up and down state. If the energy bias is much larger than the tunnel splitting ε>>Δ the fluctuations are faster than τ_{qc}^{-1} but the change in the probability amplitude is very small and spin flipping is almost impossible.

Chapitre III

L'Aimant Moléculaire Fe8

Le système principal que nous avons étudié est un composant organique contenant des ions de fer désigné par simplification sous le vocable « Fe8 ». Ce système est composé d'une molécule de 8 ions de fer entourés par un cristal organique non-magnétique. La symétrie cristallographique est triclinique avec une seule molécule par cellule. Dans une molécule les ions de fer interagissent fortement par des liens de superéchange. L'état de base a un spin total de 10 avec 6 spins ioniques parallèles et 2 spins ioniques antiparallèles. La molécule a une barrière d'anisotropie uni-axiale de largeur 27 K et les mesures de RPE indiquent une anisotropie transversale d'ordre 2. Cette anisotropie transversale brise la symétrie en direction de l'axe facile et permet l'effet tunnel quantique.

III) The octanuclear iron nanomagnet, Fe8

A large part of my study was devoted to the Fe8-system. This work was done in close collaboration with the chemistry department of the university of Florence, D. Gatteschi, R. Sessoli, and C. Sangregorio. The synthesis of this compound was part of the thesis of C. Sangregorio [Sangregorio 98].

– Molecular Structure

The Fe8-sample was first synthesized by Wieghardt *et al.* [Wieghardt 84]. The Fe8 sample contains iron ion complexes of equal valence, Fe^{3+}, each ion carrying an electronic spin of s=5/2. The skeleton of the iron complex is shown in figure [III.1]. The molecule has a butterfly shape and is relatively flat in the crystallographic a-direction. Six iron ions placed at the exterior of the complex are bound to an amine ligand FeN_3O_3, depicted as rings in figure [III.1] and the two central Fe^{3+}-atoms are surrounded by an octahedral array of six O-atoms. The iron ions in the complex are coupled together by 12 μ_3-hydroxo bridges and 2 μ_2-oxo bridges. The ionic charge of +8 of the complex is almost compensated by 7 Br^- ions bound by electrostatic forces and hydrogen bonds to the complex. The space group of the complex is P1, thus triclinic. The charge excess of +1 is balanced by the charge of –1 of a $[Br \cdot 8H_2O]^{(-)}$ molecule. The complete structure formula reads

$$\left\{\left[(tacn)_6 Fe_8(\mu_3 - O)_2(\mu_2 - OH)_{12}\right]Br_7 \cdot H_2O\right\}^{(+)}\left[Br \cdot 8H_2O\right]^{(-)}$$

where *tacn* stands for 1,4,7-triazacyclononane. The positive charged iron-complex and the counterbalancing Br-molecule form a cation-anion lattice, corresponding to a distorted NaCl structure of triclinic symmetry.

The crystal structure was analyzed by X-ray-defraction [Wieghardt 84]. The relative positions of the iron ions to center of the molecule are given in table [III.1]. The positions of the 8 ions were used for the calculation of the local field, see section V.1, assuming that the individual 5/2 spins orientated along the a-axis.

	X/a	Y/b	Z/c	Spin
1	–0.1573	+0.2031	+0.1569	+5/2
2	–0.2364	–0.0195	–0.1305	–5/2
3	–0.1717	–0.2111	–0.0060	+5/2
4	+0.1714	+0.2115	–0.0063	+5/2
5	+0.2365	+0.0226	+0.1326	–5/2
6	+0.1563	–0.1992	–0.1563	+5/2
7	+0.0046	+0.1054	+0.0453	+5/2
8	–0.0031	–0.1029	–0.0392	+5/2

Table III.1: Relative positions of the iron ions and their spin ground state

– Hyperfine field

Natural iron consists to 97% of the isotope ${}^{55}_{26}Fe$ which carries no nuclear magnetic moment (I = 0) only the isotope ${}^{56}_{26}Fe$ has a nuclear magnetic moment (I = 1/2) which has a natural abundance of about 3%. Although the hyperfine field due to the iron ions is small, a realistic estimate of the hyperfine field must include the nuclei of the surrounding organic matter. It is difficult to give an exact value but estimates are of the order of 10^{-3} K, see [Prokof'ev 98, Abragam 70]. In addition the hyperfine field is very inhomogeneous because many molecules will consists only of ${}^{55}_{26}\mathrm{Fe}$-ions where a small hyperfine field is caused only by the nuclei the organic ligands. In the other molecules containing iron isotopes with a nuclear magnetic moment the hyperfine field will be considerably larger.

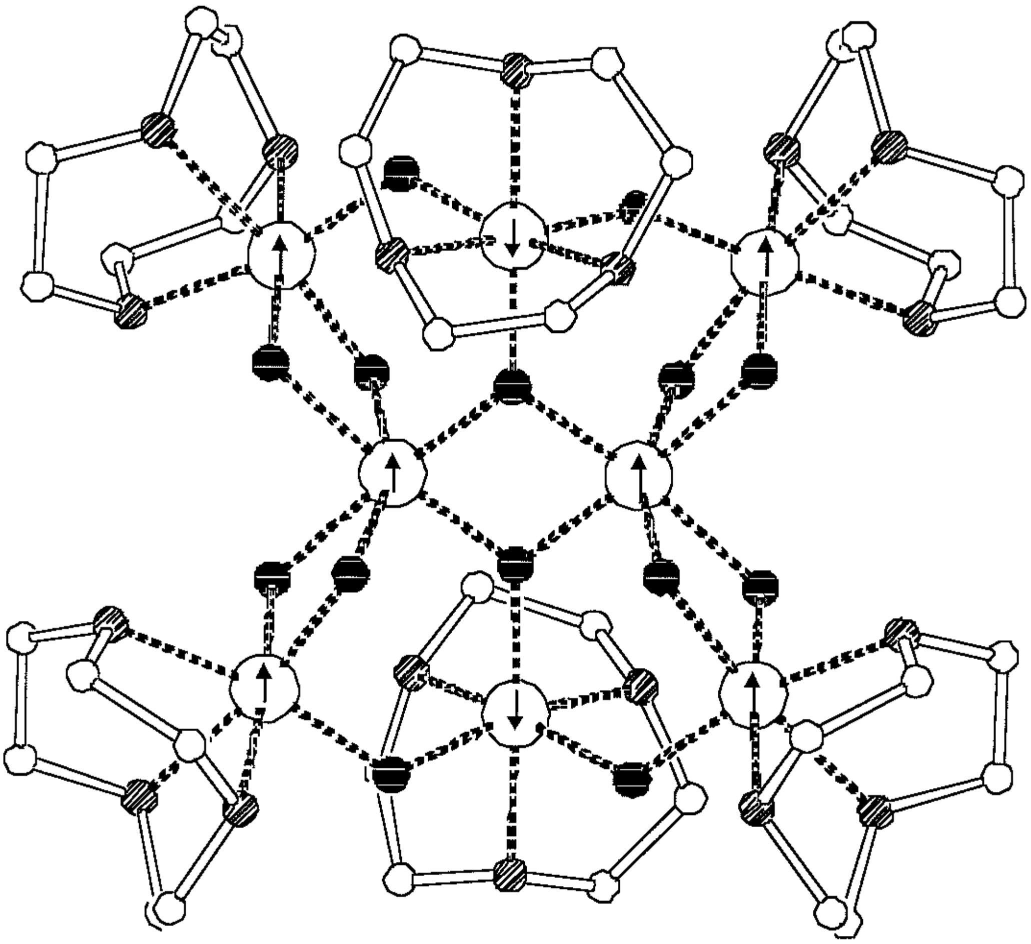

Figure III.1: Schematic view of a Fe8-molecule (PLUTON image). The large empty circles represent the iron-ions, the small black circles hydrogen-atoms, empty small circles oxygen-atoms, and the hashed circles nitrogen-atoms.

– *Bonds and the Ground State*

The iron ions interact by superexchange forces via the oxo-bridges. Their strenght have been discussed in [Delfs 93]. The authors have applied the spin Hamiltonian formalism to calculate all $(2s+1)^8$ = 1679616, s = 5/2, energy eigenstates of the molecule. The spin Hamiltonian of the molecule was solved numerically. From these energy level scheme the susceptibility has been calculated and fit to measured data in a temperature range from 4.2K to 300K. Due to the complexity of the problem, they simplified the molecule structure to have a D_2-symmetry. In this approach only 4 different bonds are remain. A schematic view of the bonds and the ionic spin states in the ground state is shown in figure [III.2]. All couplings between the iron ions are antiferromagnetic and frustration effects are present in the triangle couplings in the wings of the butterfly shape. The coupling strength of the bonds have been estimated to be: J_1~25–35 K, J_2~130–170 K, J_3~J_4~20–50 K, with J_3<J_4. The presence of frustration within the molecule might result in canting of the electronic spin of the iron ions.

The calculated total spin of the ground state is S=10 with 6 iron spins parallel and two spins anti-parallel. This ground state configuration was confirmed by elastic neutron scattering experiments [R. Sessoli, private communication]. The energy difference to the next exited state of total spin S=9 has been estimated to be 32K [Sangregorio 98].

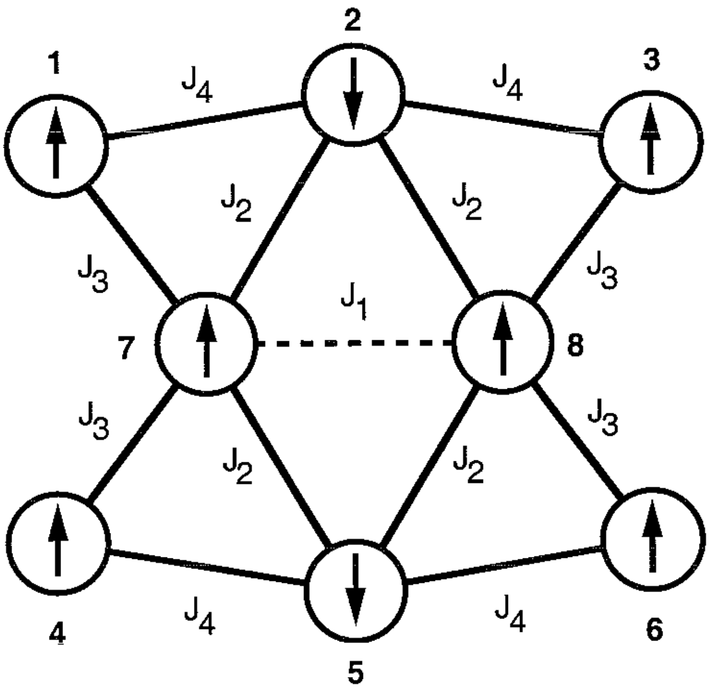

Figure III.2: Simplified interaction scheme of Fe8.

– *The Fe8-Hamiltonian*

The giant spin Hamiltonian for Fe8 is give by

$$\hat{H} = -D\hat{S}_z^2 + E/2\left(\hat{S}_+^2 + \hat{S}_-^2\right). \quad (1, \mathrm{III})$$

The height of the anisotropy barrier is DS^2 and the second order off-diagonal terms give rise to the tunnel splitting. The parameters D and E have been evaluated by EPR measurements [Barra 96] and are recently confirmed by inelastic neutron scattering [Caciuffo 98]. The EPR measurements give D=0.27K and E=0.046K in reasonable agreement with the results of the neutron scattering measurements D=0.29K and E=0.047K. In the neutron scattering experiment forth order terms of combinations of $\hat{S}_z, \hat{S}_+, \hat{S}_-$, and $\hat{S}$ have also been estimated. The prefactors for these terms are of the order of 10^{-6} K.

– *The unit cell*

The Fe8-lattice is triclinic and the unit cell is defined by:

a=10.522(7)Å	α=89.90(6)°
b=14.05(1) Å	β=109.65(5)°
c=15.00(1)Å	γ=109.27(6)°

One molecules per unit cell Z=1, molar mass m=2250, density ρ=1.92 g/cm^3, unit cell volume V=1956 Å^3. A schematic view of the unit cell is presented in figure [III.3].

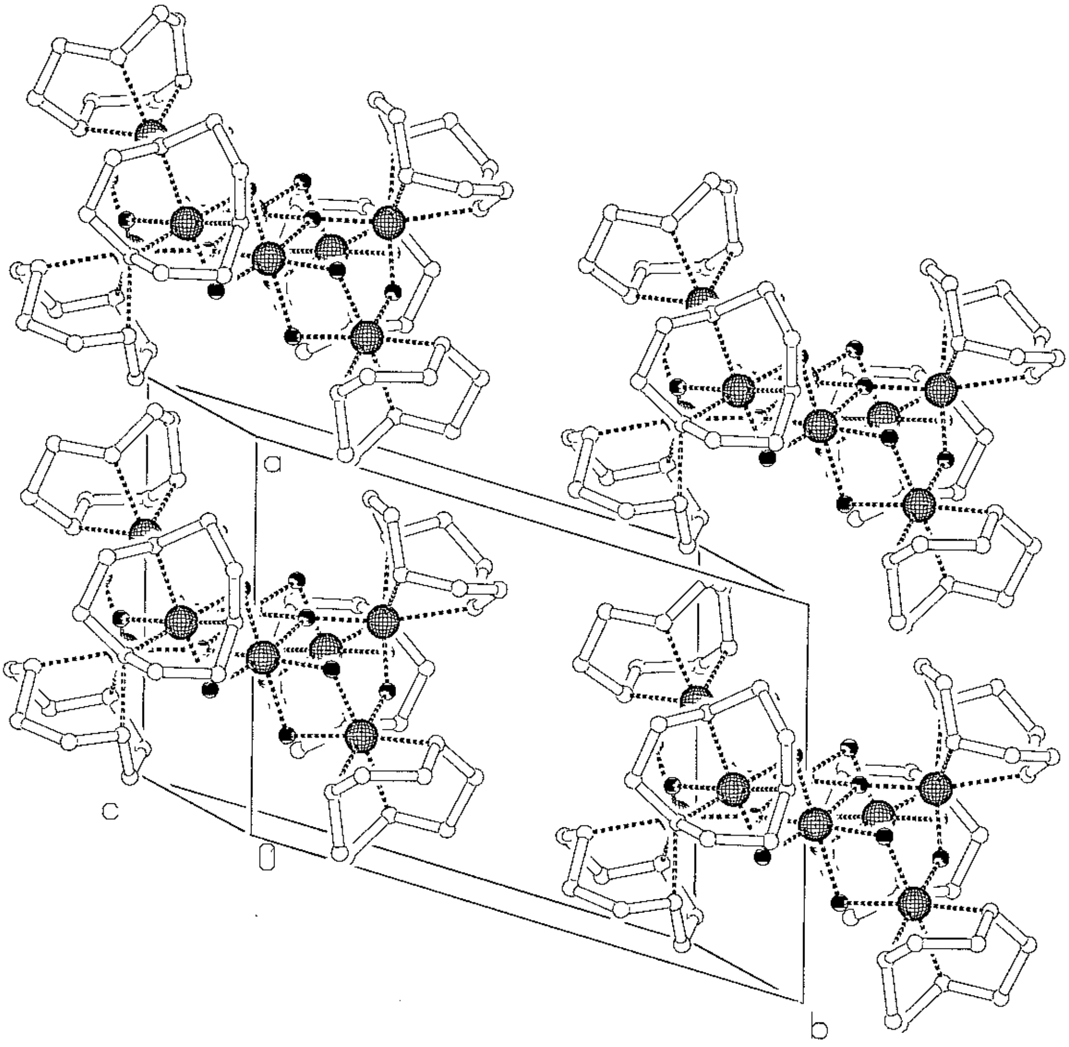

Figure III.3: Schematic view of a Fe8-unit-cell. This image shows the relative positions of the Fe8-molecules with respect to each other (PLUTON image).

Chapitre IV

Résultats Expérimentaux

IV.1) Théorie de l'Aimant Superparamagnétique 51

IV.2) Résultats sur Fe8 55
IV.2.1) Régime Superparamagnétique 55
IV.2.2) Régime Intermédiaire, au-dessous de 1K 65
IV.2.3) Régime Quantique 75
IV.2.4) Contradictions entre les Expériences et la Théorie 89

IV.3) Autres Aimants Moléculaires 91
IV.3.1) Fe4 91
IV.3.2) Fe17+Fe19 95
IV.3.3) Mn11 99

Dans ce chapitre nous présentons des résultats expérimentaux sur le principal système étudie au cours de cette thèse, Fe8, mais également des résultats sur d'autres aimants moléculaires, Fe4, Fe17+Fe19 et Mn11. Nous avons mesuré l'aimantation en fonction de la température et du champ et la susceptibilité en fonction de la fréquence et de la température.

Dans la première section, IV.1, nous donnons un rappel de la théorie classique du paramagnétisme et du superparamagnétisme.

Dans la section IV.2 nous présentons les résultats obtenus sur Fe8. Ce système montre un comportement superparamagnétique à haute température et un effet tunnel résonant à basse température.

A haute température la courbe d'aimantation de Fe8 ne suit pas la fonction de Brillouin d'un système paramagnétique simple mais une fonction qui prend en compte la barrière d'anisotropie. La constante de Curie de la susceptibilité en champ faible est plus élevée que pour un système paramagnétique : elle correspond à la valeur que nous avons calculée pour un système superparamagnétique. La partie imaginaire de la susceptibilité satisfait le modèle de Debye et le système est donc géré par un seul temps de relaxation. La courbe de relaxation vers 1 K est exponentielle comme prévu pour un système régulier et sans interactions. Le temps de relaxation à haute température suit la loi d'Arrhenius avec une valeur de la barrière de 24 K et un préfacteur $\tau_0 \sim 10^{-7}$ s, bien plus grand que pour un spin libre. Dans cette gamme de température, Fe8 relaxe donc par activation thermique. Nous avons obtenu les mêmes temps de relaxation pour un échantillon en poudre et un monocristal.

Au-dessous d'une température de 0,4 K la relaxation est indépendante de la température. La courbe de relaxation est non-exponentielle, bien décrite par une exponentielle étirée. Le temps de relaxation varie fortement avec le champ externe. La variation n'est pas monotone et montre un effet résonant : le temps de relaxation est plus court à des valeurs de champ équidistantes de 2 kOe. Dans la première résonance, le temps de relaxation a une valeur de $\tau \sim 10^4$ s et hors résonance une valeur de 10^8 s. La courbe d'hystérésis présente des sauts aux valeurs du champ résonant et l'aimantation reste presque constante hors résonance. La première résonance a une largeur d'environ 100 Oe et la deuxième résonance a une largeur de 500 Oe. Comme dans le régime superparamagnétique nous avons mesuré les mêmes temps de relaxation pour un échantillon en poudre et un monocristal. Cependant nous avons observé une influence de la forme du monocristal. Nous avons fait des mesures sur des échantillons de forme allongée, sphérique et aplatie. La courbe de relaxation varie avec la forme mais les paramètres de l'exponentielle étirée ont presque la même valeur. Nous avons observé par contre que la position de la première résonance change beaucoup avec la forme de l'échantillon. Pour l'échantillon long, après la saturation dans un champ positif, la première résonance se trouve à une valeur de +80 Oe à +100 Oe. L'échantillon sphérique a sa première résonance à +230 Oe et l'échantillon plat à une valeur de +200 Oe, également après une saturation en champ positif.

Dans la section IV.3 nous présentons les résultats expérimentaux sur 3 autres aimants moléculaires, Fe4 (IV.3.1), Fe17+Fe19 (IV.3.2) et Mn11 (IV.3.3). Tous se comportent comme un système superparamagnetique avec une barrière d'anisotropie. Dans aucun de ces systèmes nous n'avons observé d'effet tunnel quantique :
soit il n'existe pas dans ces échantillon
soit la barrière d'anisotropie est trop petite (Fe4 : $\Delta_{\text{barrière}} = 2{,}4$ K, Mn11 : $\Delta_{\text{barrière}} = 6{,}2$ K) et nous n'observons que de la relaxation par activation thermique
soit le système se compose de deux molécules différentes (Fe17+Fe19) que nous n'avons pas pu distinguer dans les expériences.

IV.1) Paramagnetism

In this chapter we recall some aspects of classical paramagnetism and superparamagnetism. In a paramagnet the spins do not interact and have no preferred direction. In a superparamagnet many individual spins can be replaced by a large collective spin and often anisotropy is present.

– *Curie law*

A paramagnet contains say N magnetic ions of spins $\vec{S}$ and orbital moment $\vec{L}$ thus the total angular moment is $\vec{J}=\vec{L}+\vec{S}$. In a weak magnetic field H the susceptibility $\chi = dM/dH$ will obey the Curie law

$$\chi = \frac{C}{T} \qquad (1, \text{IV}.1)$$

with

$$C = \frac{g^2\mu_B^2 J(J+1)}{3k} \qquad (2, \text{IV}.1)$$

the Curie constant. g is the Landé factor, $\mu_B = e\hbar/2m = 9.27410\times10^{-21}$ [erg/gauss] is the Bohr magneton, and $k_B = 1.38062\times10^{-16}$ [erg/Kelvin] the Boltzmann constant. If the orbital moment is zero $\vec{L}=0$ then $\vec{J}=\vec{S}$ and the Landé factor is simply the g-factor of a bare spin g=2. In cgs-units the Curie constant then becomes simply $C = 0.5\ S(S+1)$ [emu/mole]. The Curie constant are often also expressed in units of emu/mass or emu/volmue.

If there are interactions between the spins as in a ferromagnet of antiferromagnet the Curie law no longer holds. However, in good approximation, these interactions give rise to a uniform shift of the Curie law on a $1/\chi$ versus T plot as describe by the Curie-Weiss law

$$\chi = \frac{C}{T-\Theta}. \qquad (3, \text{IV}.1)$$

The Curie-Weiss temperature Θ is proportional to the magnitude of the interactions. In general interactions will have more subtle effects. The Curie-Weiss law represents the effect of an interaction that give rise to a mean field interaction proportional to the magnetization $\Theta = c_{mean}M$ where c_{mean} is a constant factor.

– *Debye model*

The dynamics of a paramagnet may be described by the phenomenological model of Debye. It assumes that the dynamics is given by one characteristic time τ and the change in the magnetization is proportional to the magnetization at each instant like in a natural decay process. Thus the time evolution of the magnetization is given by the differential equation

$$\frac{dM(t)}{dt} = -\frac{M(t)-M_\infty}{\tau} \qquad (3, \text{IV}.1)$$

with an exponential solution for the time evolution of $M(t)$

$$M(t) - M_\infty = (M_0 - M_\infty)\exp(-t/\tau). \quad (4, \text{IV}.1)$$

M_∞ is the equilibrium magnetization of the system and depends on the external field, temperature, etc.

For an alternating magnetic field $H(t) = H_0 \exp(i\omega t)$ the system will follow with the same frequency ω but a difference in the amplitude and phase. The complex susceptibility $\chi = \chi' + i\chi''$ in this case has a real and imaginary part as

$$\chi'(\omega) = \frac{\chi_T - \chi_S}{1+\omega^2\tau^2} + \chi_S \qquad (5, \text{IV}.1)$$

$$\chi''(\omega) = \frac{(\chi_T - \chi_S)\omega\tau}{1+\omega^2\tau^2}. \qquad (6, \text{IV}.1)$$

$\chi_S = \chi_{\omega\to\infty}$ is the adiabatic susceptibility and $\chi_T = \chi_{\omega\to 0}$ the isothermal susceptibility, following the Curie-law $\chi_T(T) = C/T$.

Superparamagnetism

The behavior of a paramagnet changes when an anisotropy barrier is present. In this case the system is no longer isotropic but an energy potential $V(\phi,\theta)$ as function of the angles ϕ and θ breaks the symmetry. The origin of the anisotropy energy may be due to the crystalline field or surface effects [Morrish 65, Aharoni 96].

A classical example is the *Stoner-Wohlfarth* model describing a situation of isolated, non-interacting grains having a uniaxial anisotropy. In this case the energy of a single grain is given by

$$E = K_{\|}\sin^2(\phi-\theta) - \mu H\cos(\theta). \qquad (7, \text{IV}.1)$$

In the simplified case where the anisotropy axis is parallel to external field H, $\theta = 0$, the energy has two minima at $\phi = 0$ and $\phi = \pi$ with the energy $E_1 = -\mu H$ and $E_2 = +\mu H$ respectively. The maximum in between occurs at $\cos\phi = -\mu H / 2K_{\|}$. Substituting this in equation (7,IV.1) gives for the maximum $E_{\max} = K_{\|}(1+(H/H_S)^2)$ with $H_S = 2K_{\|}/\mu$. Thus in effect an energy barrier

$$\Delta(H) = K_{\|}(1-(H/H_S))^2 \qquad (8, \text{IV}.1)$$

occurs between the minima.

Arrhenius law

The presence of an energy barrier Δ changes the characteristic time. It is no longer constant but depends on the temperature T and also on the magnetic field H. Applying the Boltzmann law for thermal transition probability we end up with the Arrhenius law

$$\tau^{-1} = \tau_0^{-1}\exp(-\Delta/kT)(9, \text{IV}.1)$$

where the energy barrier Δ may vary with the field $\Delta(H)$ as mention above for the Stoner-Wohlfarth model, see [Aharoni 96] for a detailed discussion. The prefactor τ_0 was first determined by Néel [Néel 49] and later refined by Brown [Brown 63]. Typical values in the literature for τ_0 are 10^{-7}–10^{-12} sec a free spin usually has a value of $\tau_0 \sim 10^{-10}$–10^{-12} sec.

If the system is not govern by a single relaxation time τ, for example when a distribution in size or orientation of particles is present or if there are interacting spins, then deviations from the Arrhenius law will be observed. For these situations a large variety of phenomenological formulas are given in the literature. One example is the Fulcher law

$$\tau^{-1} = \tau_0^{-1}\exp\left(-\Delta/k(T-T_0)\right) \ (10, \text{IV}.1)$$

where T_0 is a phenomenological fitting parameter related to the magnitude of an interaction between the spins.

Blocking temperature

The blocking temperature T_B is defined as the temperature where the characteristic time of the system $\tau(H,T)$ is of the same order as the time scale of the experiment τ_{exp}. Below T_B the system appears as frozen. Note that the blocking temperature depends on the kind of the experiment an depends in general on the frequency. Thus the blocking temperature T_B may vary from experiment to experiment like dc measurements, ac measurements or mössbauer experiments.

To give an example we will discuss a typical ac-measurement. In the experiment we measure the ac-susceptibility at a constant frequency ω as function of the temperature T. The characteristic time of the sample $\tau(T)$ is increasing with lower temperatures monotonically as e.g. given by the Arrhenius law (9, IV.1). The experimental time scale is given by $\tau_{\mathrm{exp}} = 1/\omega$. Lets for simplicity assume the adiabatic susceptibility is zero then the real and the imaginary part of the susceptibility as function of the temperature is given by

$$\chi'(T) = \frac{1}{1+\tau^2(T)/\tau_{\mathrm{exp}}^2}\frac{C}{T} \qquad (11, \mathrm{IV}.1)$$

$$\chi''(T) = \frac{\tau(T)/\tau_{exp}}{1+\tau^2(T)/\tau_{exp}^2}\frac{C}{T} \qquad (12, \mathrm{IV}.1)$$

As long as $\tau_{exp} >> \tau(T)$, i.e. at high temperatures, the real part is dominated by the Curie-law and the imaginary part is almost zero. At very low temperatures where $\tau_{exp} << \tau(T)$ the real part and the imaginary part are vanishing. In the intermediate range where $\tau_{exp} \sim \tau(T)$ the real part is diminishing and starts deviating from the Curie-law and the imaginary part has a maximum at $\tau_{exp} = \tau(T)$. We can thus determine the blocking temperature $T_B(\tau)$ from the maximum of the imaginary part of the susceptibility

$$\tau_{exp} = \tau(T_B).$$

If we want to do a dc-relaxation measurement to determine the characteristic time we have to fix the temperature T and resolve the characteristic time, in this case called relaxation time, by a fit to the relaxation curve, e.g. by a exponential function equation (4, IV.1).

Since for both cases the dynamic is determined by the differential equation (3, IV.1), the relation between the characteristic time τ and the temperature T is the same. It doesn't matter if we determine it by ac-measurement $T_B(\tau)$ or dc-measurements $\tau(T)$.

IV.2.1) Fe8, Superparamagnetic Regime

In this chapter we discuss the magnetic properties of Fe8 at higher temperatures, that is in our case in a range between 1K and 10K. We will shown that in this temperature range Fe8 behaves as a superparamagnet with a spin of $S = 10$. We estimate that the interactions between the molecules are very small and shouldn't exceed 0.1K.

We present measurements on a single crystal as well as on a powdered sample. We measured the dc-magnetization as function of the field up to 8 tesla and the ac-susceptibility for frequencies in the range of 0.005Hz up to 6kHz.

The inverse dc–susceptibility of Fe8 obeys the Curie–Weiss law in a temperature range from 2K to 5K. At 4.2K the magnetization curve for a single crystal is close to saturation for fields larger than about 2 tesla and at saturation we found a value of about 20 μ_B indicating a spin of $S = 10$. The magnetization curve deviates strongly from the Brillouin-function of a simple paramagnet. The data can be fit by a magnetization curve calculated for a superparamagnet with an Ising-like energy barrier. The characteristic time of the system follows roughly the Arrhenius law thus showing the behavior of a classical thermal activated system. From these data we derived a barrier height of 24K in reasonable agreement with previous EPR-measurements. The time constant τ_0 of the Arrhenius law is of the order of 10^{-7} sec which is considerably larger than that of a free spin.

Field dependence

The magnetization curve of on Fe8 single crystal measured at 4.2K and for a field up to 8 tesla is presented in figure [IV.2.1.1]. The sample starts saturating for fields larger than about 2 tesla. This field is about of the order of the anisotropy energy[1] of Fe8. The magnetization continuous to increase, reaching a plateau above approximately 6 tesla. This increase is most likely due to a small miss-alignment of the crystal (~5° – 10°). If all spins are already parallel to the easy axis but not aligned to the external field, an increasing field will force the spin to align with the field against the anisotropy energy. The magnetization achieves a value of $20\mu_B$ as expected for $S = 10$ and $g = 2$, $M_{sat} = 2\,S\,\mu_B = 20\,\mu_B$.

In figure [IV.2.1.2] three magnetization curves are presented for 3 different sample shapes at a temperature of 4.2K. The aspect ratio of the long sample is 1.0 x 0.5 x 0.7 and of the flat sample 1.0 : 2.9 : 3.6. The three curves are different for small fields but the curves for the spherical sample and the long sample tend toward the same saturation value. One reason for the differences in the beginning of the curves is due to different demagnetization factors N. We expect that $N^{flat} > N^{sphere} = 4\pi/3 > N^{long}$. The internal field is then given by $H^{shape}_{internal} = H_{applied} - N^{shape}M$. Another reason might be a misalignment of the easy axis along the external field. The spherical sample and the flat sample are especially difficult to orientate.

---

[1] A field of 2 tesla corresponds to an energy of about 25K for a spin $S = 10$ system.

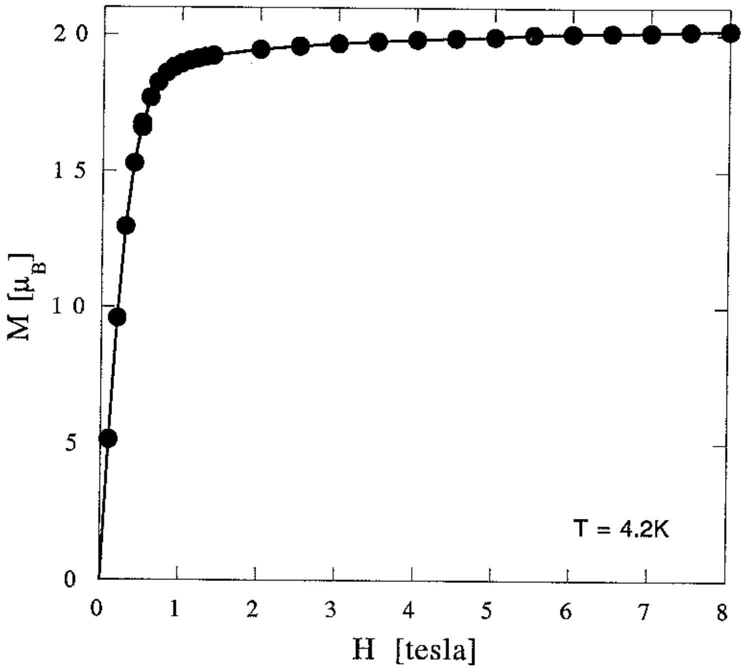

Figure IV.2.1.1: Magnetization curve of a single crystal (long1) up to 8 tesla. The sample has an aspect ratio of about 1.0 x 0.5 x 0.7 and was measured along the longest axis of the sample, which corresponds roughly to the easy axis.

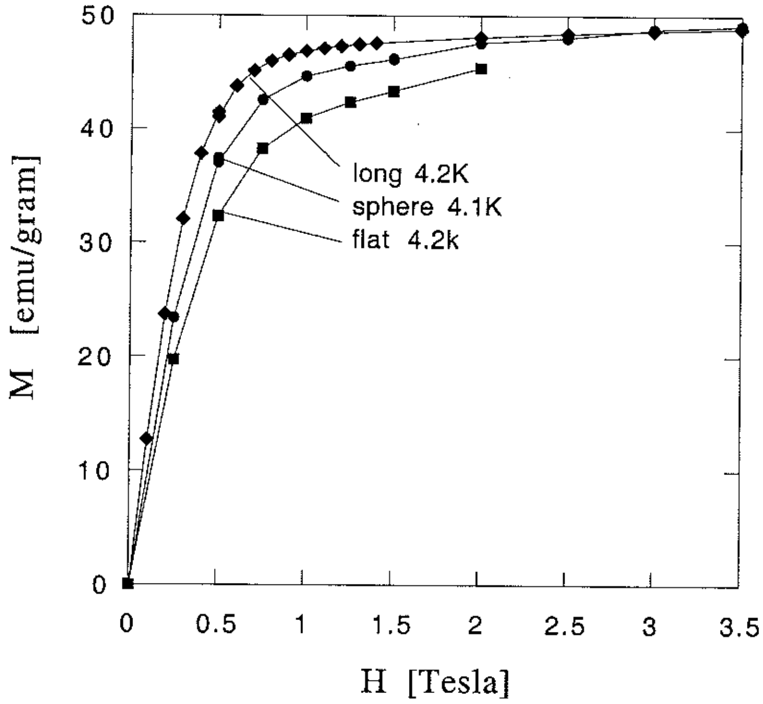

Figure IV.2.1.2: Magnetization curve for single crystals of different shapes. The difference in the magnetization comes from different demagnetization fields due to the sample shapes and from a mis-alignment in the setup of the experiment.

In the annex II we calculated the magnetization curve for a Hamiltonian of Fe8

$$\hat{H} = -D\hat{S}_z^2 + E/2\left(\hat{S}_+^2 + \hat{S}_-^2\right) + g\mu_B \hat{S}_z H. \qquad (1, \text{IV}.2.1)$$

We show there that the contribution of the tunneling term $E/2\left(\hat{S}_+^2 + \hat{S}_-^2\right)$ to the magnetization curve is negligible but we keep it for completeness. In figure [IV.2.1.3] a fit of this theoretical curve to the data is shown for a temperature of 4.2K and a field up to 1 tesla. We see that the Brillouin function doesn't fit the data at all. The theoretical curve matches well the data if we assume a demagnetization correction. In this case the internal field is given by

$$H_{internal} = H_{applied} - NM \qquad (2, \text{IV}.2.1)$$

with a demagnetization factor of $N = 2.5$. See annex III for a detailed discussion on the demagnetization field.

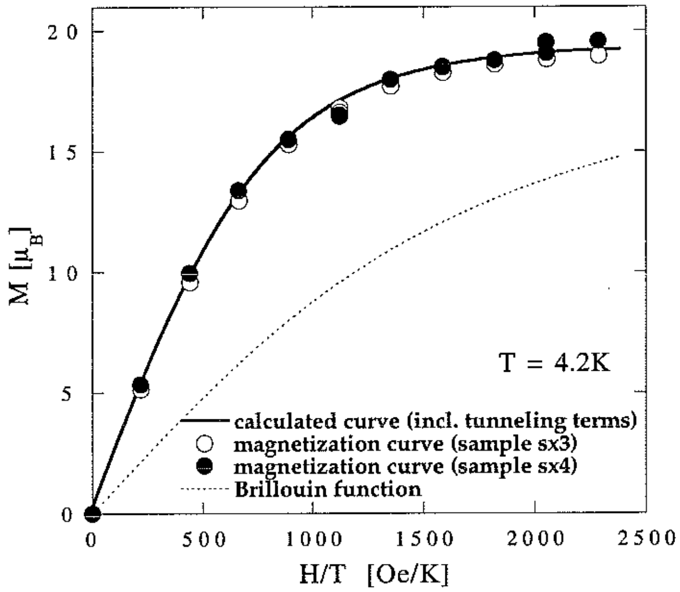

Figure IV.2.1.3: Magnetization curve of two single crystals and a fit to a theoretical function. The Brillouin-function (dashed line) doesn't match the data. The calculated function (solid line) takes into account the anisotropy term as well as the second order tunneling term in the Hamiltonian. To fit the data we have assumed a demagnetization factor of $N = 2.5$.

Temperature dependence

The temperature dependence of the magnetization is shown in figure [IV.2.1.4]. The experiment was made on a Fe8-single crystal (sx4) approximately 2.5mm x 0.6mm x 1.0mm in a field of $H_{applied} = +830$ Oe. In this figure we present the internal dc-susceptibility $\chi_{intern} = M/H_{intern}$ in the temperature range of 1K to 18K. To calculate the internal susceptibility we have taken into account that the internal field is different from the external applied field due to the demagnetization field, equation (2, IV.2.1). We approximate $N = 1.25$ from the reference [Brailsford 66] where the demagnetization factors are listed for a variety of aspect ratios. In addition the ac-susceptibility (the real part $\chi'(T)$) is shown for a frequency of 2Hz. The curves superimpose at high temperatures but deviate slightly at low temperatures. Below 2K the ac-susceptibility shows a blocking effect and decreases to zero.

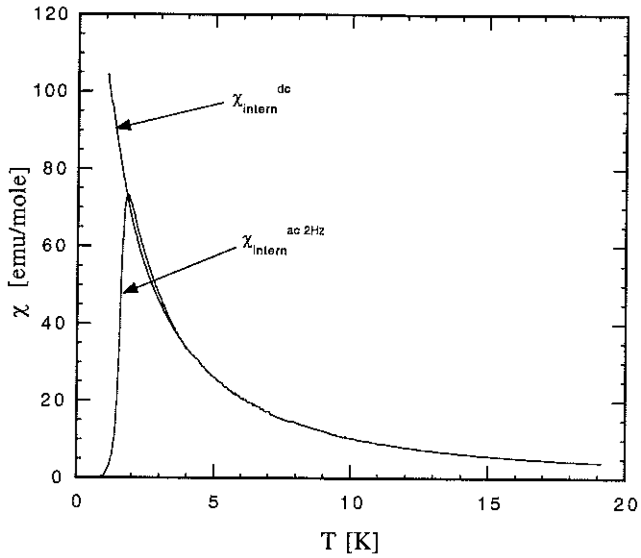

Figure IV.2.1.4: Internal susceptibility of a Fe8 single crystal. The dc-susceptibility was measured in a field of $H_{applied}$ = +830 Oe. To estimate the internal field we have used a demagnetization factor of N = 1.25. The ac-susceptibility was measured at a frequency of 2Hz.

To fit this data to a Curie-Weiss law, we must restrict the temperature range. This is because at too high a temperature, the system is no longer in a pure $S = 10$ state, but will mix with the $S = 9$ state. On the other hand at low temperatures saturation effects will occur and also time effects. In figure [IV.2.1.5] the inverse susceptibility is shown for a temperature range from 2K to 5K. In this temperature range the dc-susceptibility and the ac-susceptibility are both linear and superimpose. We obtain from this plot a Curie constant of $C = 134$ [emu/mole K^{-1}] for the dc-susceptibility and $C = 132$ [emu/mole K^{-1}] for the ac-susceptibility. The theoretical value of the Curie constant for a spin $S = 10$ system and without an anisotropy is $C = 55$ [emu/mole K^{-1}]. However, we have shown in the annex II that the susceptibility of Fe8 for small fields at 4.2K is about 2.4-times larger than of a simple paramagnet due to the Ising like anisotropy (see table [AII.1]). Including the anisotropy leads to a theoretical value of 132 [emu/mole K^{-1}] in excellent agreement with the measurement. From extrapolations of the fit to the Curie-Weiss law to the $1/\chi = 0$ axis, we can estimate that the intermolecular interaction in the Fe8-system should be very small of about $\Theta \leq 100$mK.

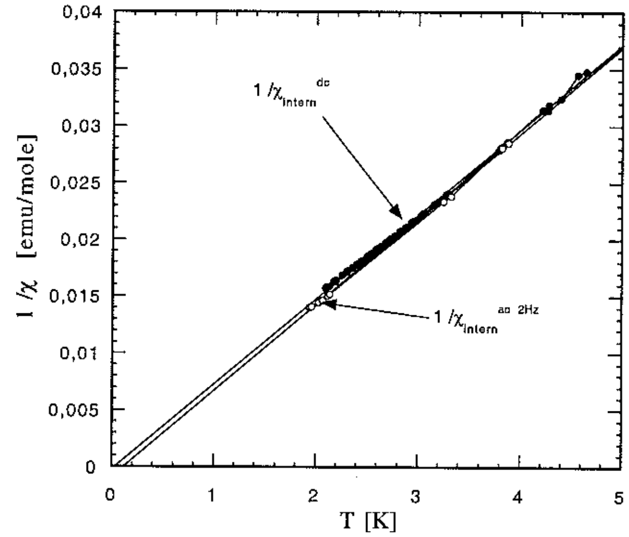

Figure IV.2.1.5: Inverse susceptibility in a temperature range from 2K to 5K.

Characteristic time

In the high temperature regime $T \geq 1\text{K}$ we can determine the characteristic time of the system by ac-susceptibility measurements. A sequence of ac-measurements for different frequencies on a powdered sample is show in the figures [IV.2.1.6] and [IV.2.1.7] and on a single crystal in figure [IV.2.1.9]. In figure [IV.2.1.6] the real and the imaginary part are plotted together. It can be seen that the maximum of $\chi''(T)$ occurs at the inflection point of the real part of $\chi'(T)$.

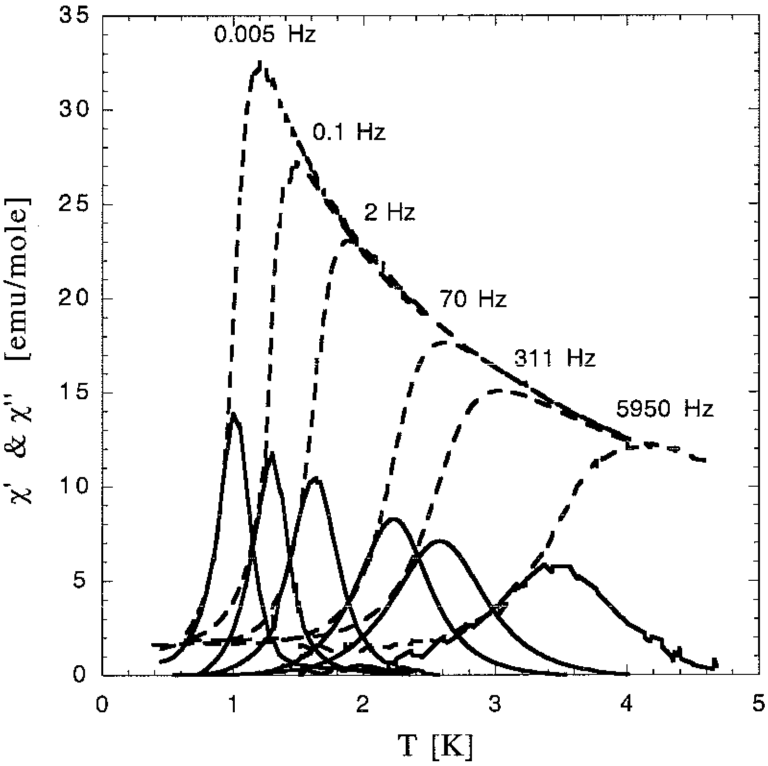

Figure IV.2.1.6: χ'(T) and χ''(T), the real and imaginary part of the ac-susceptibility of a powdered sample. The maximum of χ''(T) is about at the inflection point of χ'(T).

This comes as follows: The Curie-law in equation (11, IV.1) is monotonous increasing and the "step" in $\chi'(T)$ comes from the term $1/(1+\omega^2\tau^2)$. The inflection point of this function is the zero-point of its second derivation, the first derivation is everywhere none-zero. The second derivation of this function is

$$\frac{d^2}{dT^2}\frac{1}{1+\omega^2\tau^2(T)} = -\frac{2\omega^2}{\left(1+\omega^2\tau^2(T)\right)^2}\left[\left(\frac{d\tau(T)}{dT}\right)^2\left(1-4\frac{\omega^2\tau^2(T)}{1+\omega^2\tau^2(T)}\right)+\tau(T)\frac{d^2\tau(T)}{dT^2}\right].$$

If we assume that $\tau(T)$ has an exponential form and $d\tau(T)/dT = c\tau(T)$ the expression in the bracket on the right hand side only vanishes if $\omega\tau = 1$. This corresponds to the maximum of $\chi''(T)$. Even though this is only a simplified argument we will see that this is almost the case in all ac-measurements we have made and present in this thesis.

In the figures [IV.2.1.7] and [IV.2.1.9] the real and the imaginary part are plotted separately. For higher temperatures, above the blocking temperature, the real parts of the susceptibility $\chi'(T)$ for all frequencies superimpose and follow the Curie-Weiss law. The agreement with the Curie-law is shown in figure [IV.2.1.8].

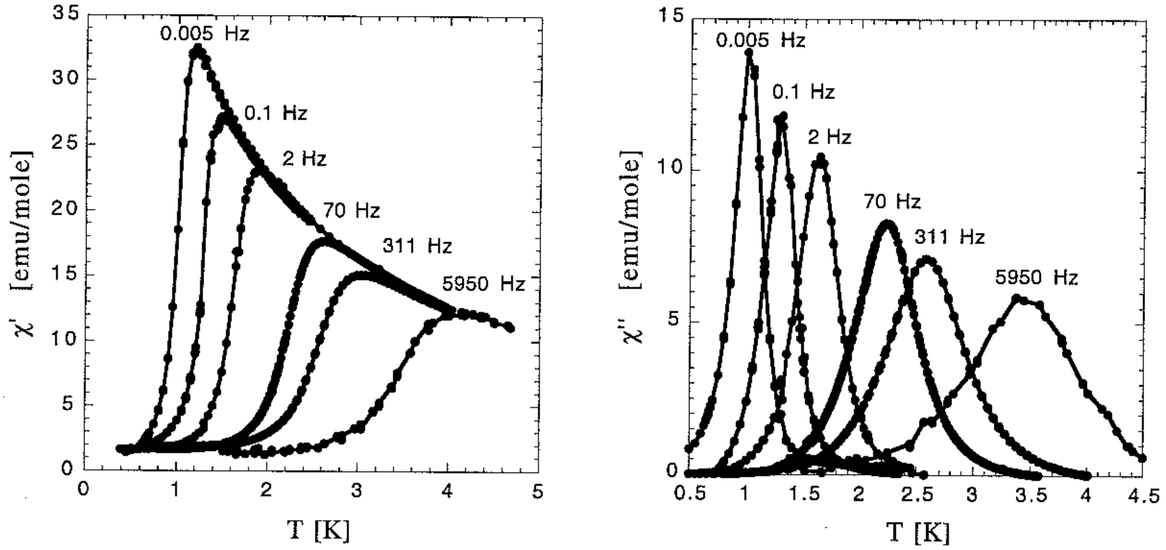

Figure IV.2.1.7: χ'(T) and χ"(T) of a powdered sample.

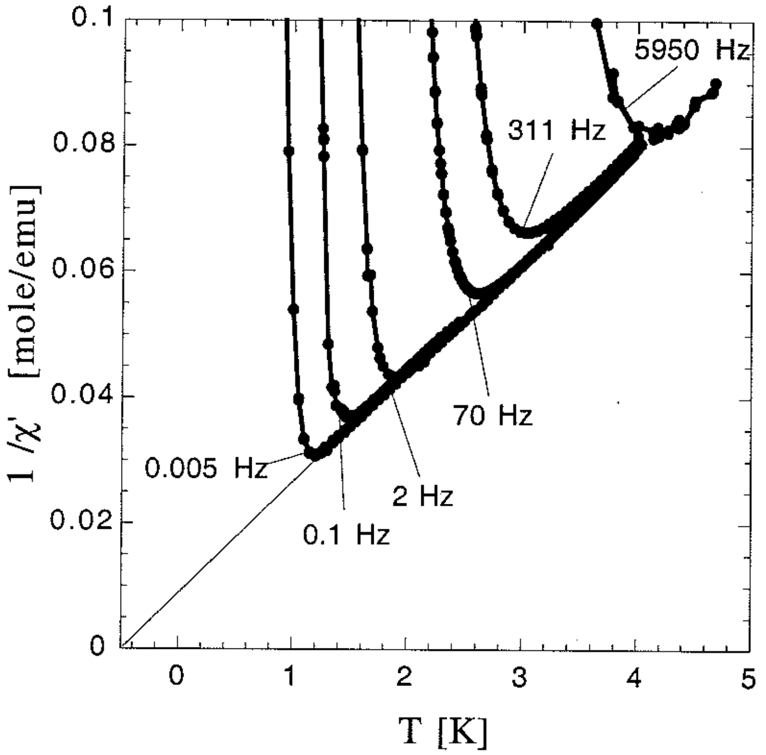

Figure IV.2.1.8: Inverse susceptibility 1/χ'(T) of the powdered sample. For temperatures above the blocking temperature the ac-susceptibility follows the Curie-Weiss law.

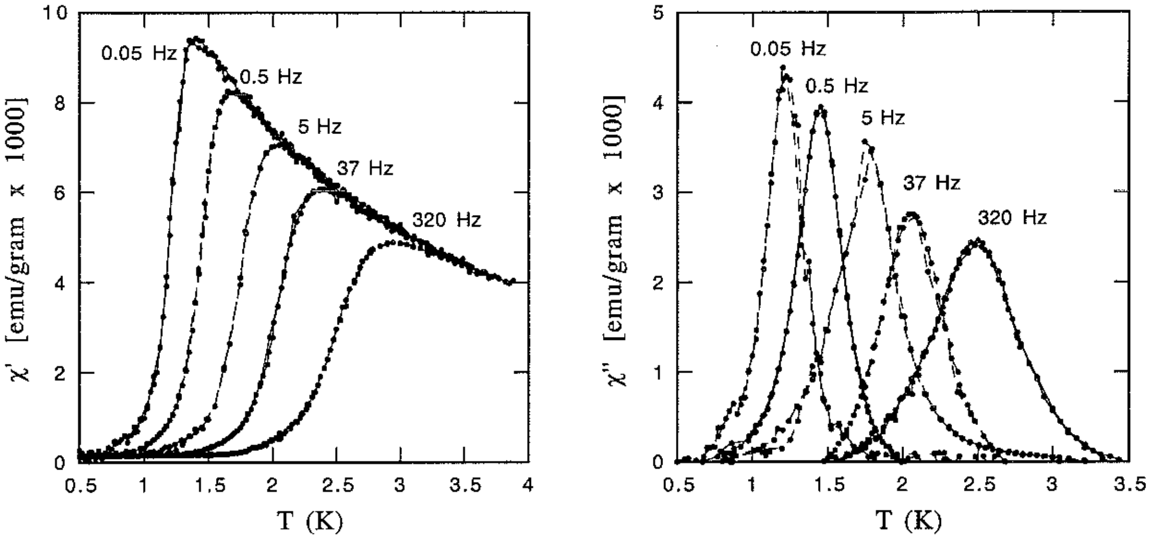

Figure IV.2.1.9: $\chi'(T)$ and $\chi''(T)$ of a single crystal.

In figure [IV.2.1.10] we fit the ac-susceptibility data of a single crystal to the theoretical curve that results from the Debye-model. For the temperature dependence we used the Arrhenius law thus

$$\chi''(T)=\frac{\omega\tau_0\exp(\Delta/T)}{1+\left(\omega\tau_0\exp(\Delta/T)\right)^2}\frac{C}{T}. \qquad (1, \mathrm{IV}.2.1)$$

This fit confirms that their is only one characteristic time present in the system.

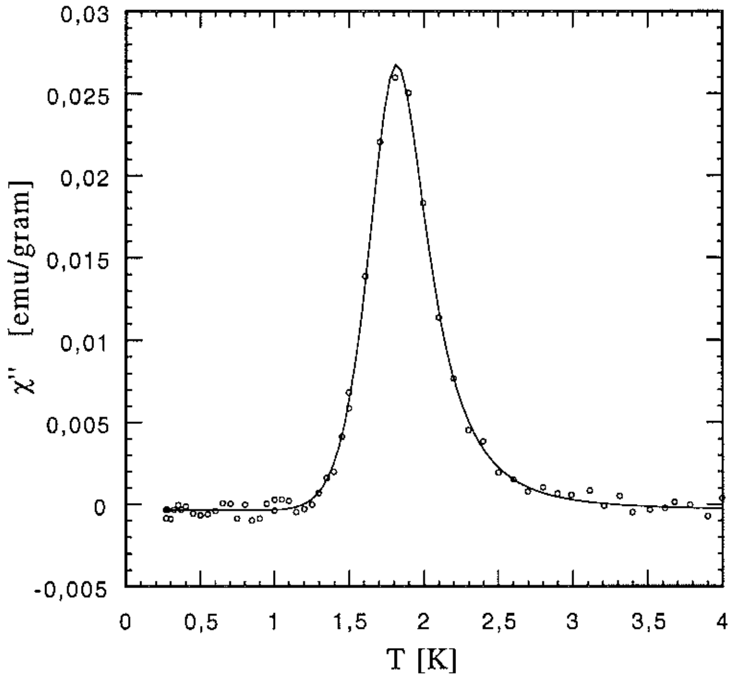

Figure IV.2.1.10: Imaginary part of the ac-susceptibility for a frequency of 2Hz measured on a single crystal. The data points are fit with the theoretical function for $\chi''(T)$ due to the Debye-model including the temperature dependence of the characteristic time, equation (1, IV.2.1).

The imaginary parts $\chi''(T)$ have the same behavior for the powdered sample and the single crystal. For lower frequencies the maximum shifts to lower temperatures and the peak becomes larger and narrower. For a given frequency f, the peak in $\chi''(T)$ occurs when $\omega\tau = 1$ with $\omega = 2\pi f$. This defines the blocking temperature T_B for for the characteristic time $\tau = 1/\omega$. The results are plotted in figure [IV.2.1.11]. We see that the temperature dependence of the characteristic time is the same for the powdered sample and the single crystal. In this plot the data do not lie on a straight line but show a slight curvature. Since we expect that the deviation from an Arrhenius law is growing at lower temperatures, as we are approaching the quantum regime, we used only the data point at higher temperatures for a fit to the Arrhenius law. On a semi-logarithmic plot the Arrhenius law is a straight line $\ln(\tau) = \ln(\tau_0) - (\Delta / k)\ 1/T$ where the intercept corresponds to τ_0 and the slope to the energy barrier height Δ. The fit gives a value of $\tau_0 \approx 10^{-7}$ sec and $\Delta = 24$K. The barrier height is in reasonable agreement with EPR-measurements [Barra 96], $\Delta = 27$K. The prefactor τ_0 is much larger than the value of a free spin which is typically of the order of $\tau_0 = 10^{-9} - 10^{-12}$ sec.

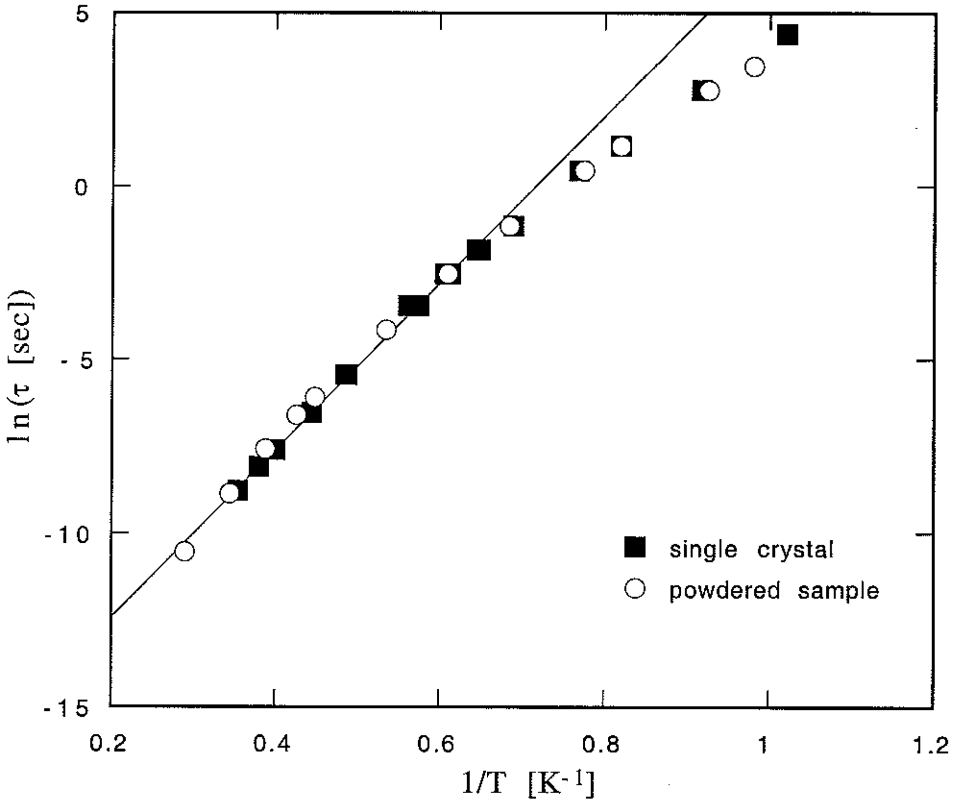

Figure IV.2.1.11: The characteristic times of a powdered sample and a single crystal as a function of the temperature. The data at high temperature are fit to the Arrhenius law.

It is interesting to note that the data may be fit to a Fulcher law. On a semi-logarithmic scale the Fulcher-law reads $\ln(\tau) = \ln(\tau_0) + (\Delta / k)/(T - T_0)$. The fit is shown in figure [IV.2.1.12]. This function matches better the data, but an extra parameter T_0 has been introduced. The obtained values for this fit are very different to the values of an Arrhenius fit. One problem is that the fit is very sensitive to the fitting parameters Δ and T_0 and the temperature range is too small to obtain a reliable fit of this kind with unique parameters.

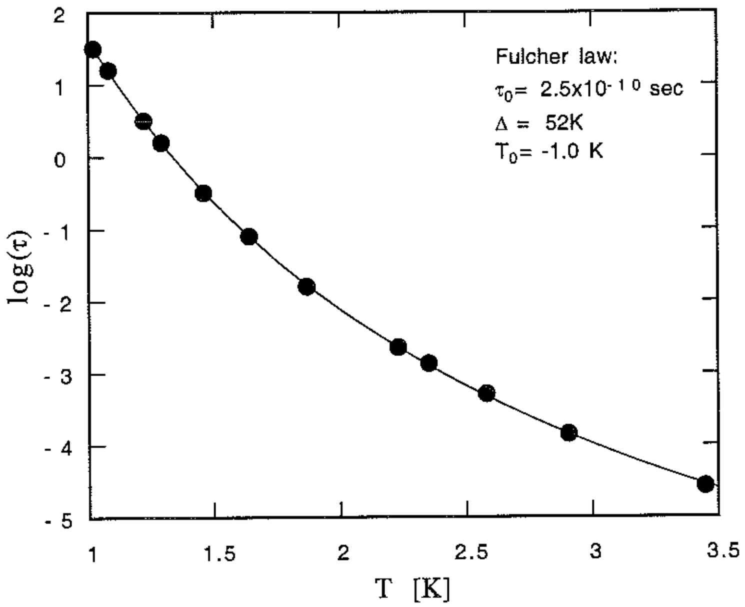

Figure IV.2.1.12: Characteristic times of the powdered sample fit to the Fulcher law. (Same data as in figure [IV.2.1.11])

IV.2.2) Fe8, Behavior below 1K

Below 1K we found that the magnetization deviates from superparamagnetic behavior. The characteristic relaxation time is faster than expected for a pure thermal activated process. Below 0.4K the relaxation behavior becomes temperature independent. We interpret this as a signature of quantum tunneling process. The relaxation is surprisingly not single exponential as expected for an ordered system with only weak interactions. The data are best fit by a stretched exponential function. A stretched exponential relaxation is ubiquitous in physics and especially well studied for spin glass systems. Beside the shape of the relaxation curve we will see that a stretched exponential fit is not perfect and variations of fitting parameters are possible.

Relaxation measurements

For lower temperatures the characteristic time becomes slower, effectively too small to make ac-measurements. We therefore used dc-relaxation measurements to determine the relaxation behavior below 1K.

The dc-relaxation measurements were done at a constant temperature. The measurement protocol is shown in figure [IV.2.2.1]. We first saturate the sample in a sufficiently high field. Afterwards the field is changed to a predetermined value. When the field is stabilized[2] a timer is set to zero and the magnetization decrease is measured continuously as function of the time. The magnetization was measured using the extraction method, thus we are able to measure the magnetization in absolute units.

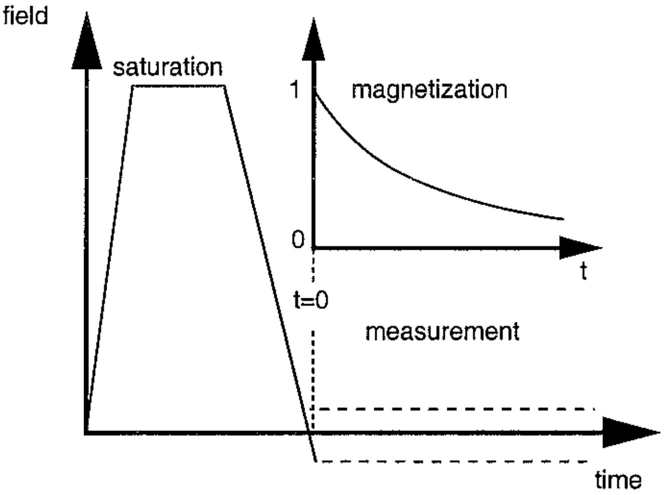

Figure IV.2.2.1: Measurement of the relaxation curve. First the sample is saturated in a large, positive field. Afterwards the field is changed to a predetermined field value and the magnetization decrease is measured as function of the time.

A series of relaxation measurements on a powdered sample in zero field is shown in figure [IV.2.2.2]. Figure [IV.2.2.3] shows a similar series of measurements on a single crystal and in an external field of H_{extern} = +100 Oe. These measurements where made in temperatures from 1K down to 0.07K. It can be seen that the relaxation becomes slower for lower temperatures. For temperatures below 0.4K the relaxation curves are identical. For higher temperatures $T \leq 0.7$K the magnetization approaches within about 3 hours (~10^4 sec) the equilibrium value M_∞. For the measurements in zero field $M_\infty = 0$ and for H_{extern} = +100 Oe the equilibrium value is about $M_\infty = M_{sat}/10$.

---

[2] That means the current is constant and the superconducting shield cooled again.

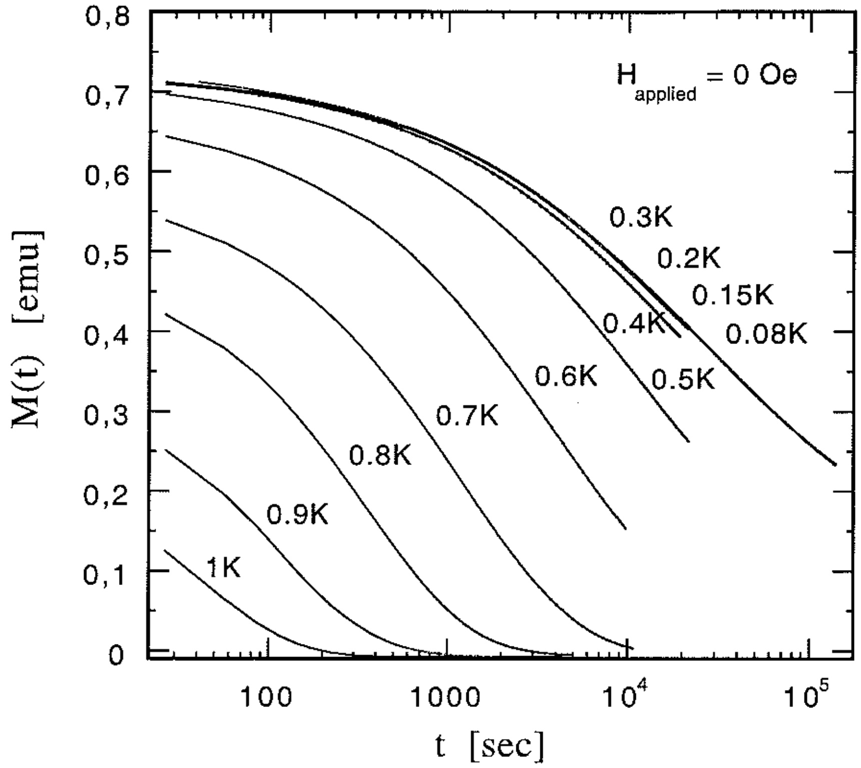

Figure IV.2.2.2: A series of relaxation measurements on a powdered sample in zero field. For lower temperatures the relaxation becomes slower. For temperatures below 0.4K the relaxation curves are superimposing, i.e. the relaxation is temperature independent.

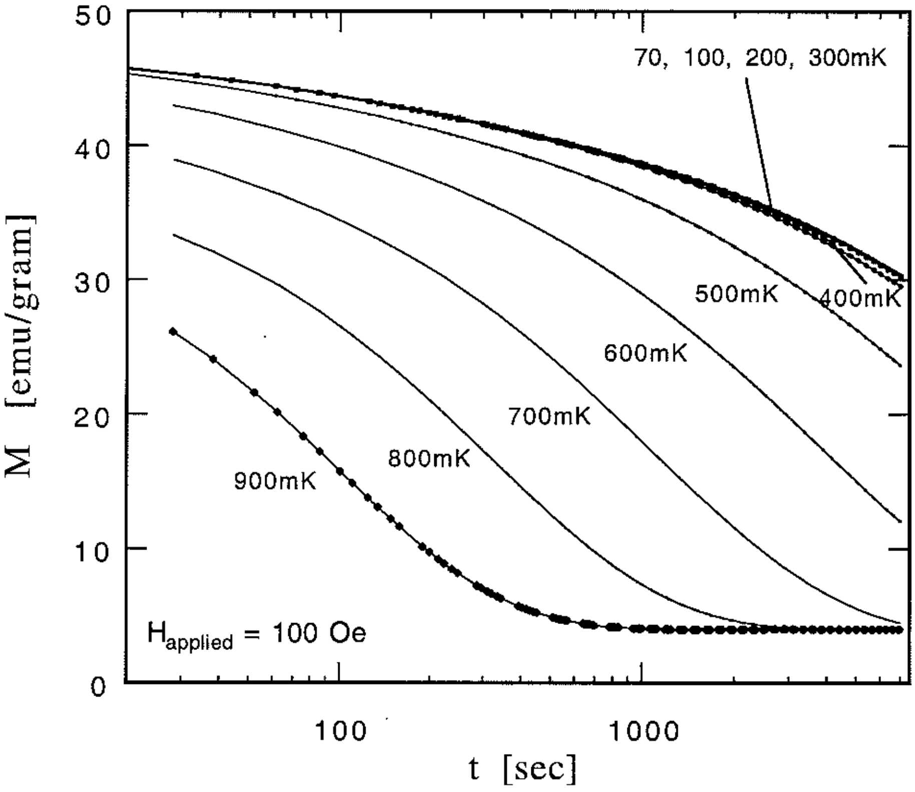

Figure IV.2.2.3: A series of relaxation curves of a single crystal in an external field of +100 Oe.

The figure [IV.2.2.4] show both sets of relaxation curves in one plot from 0.5K to 0.9K. Beside the offset in the equilibrium value due to the external field the relaxation curves look very similar and are in fact well fit by the same functions with similar fitting parameters.

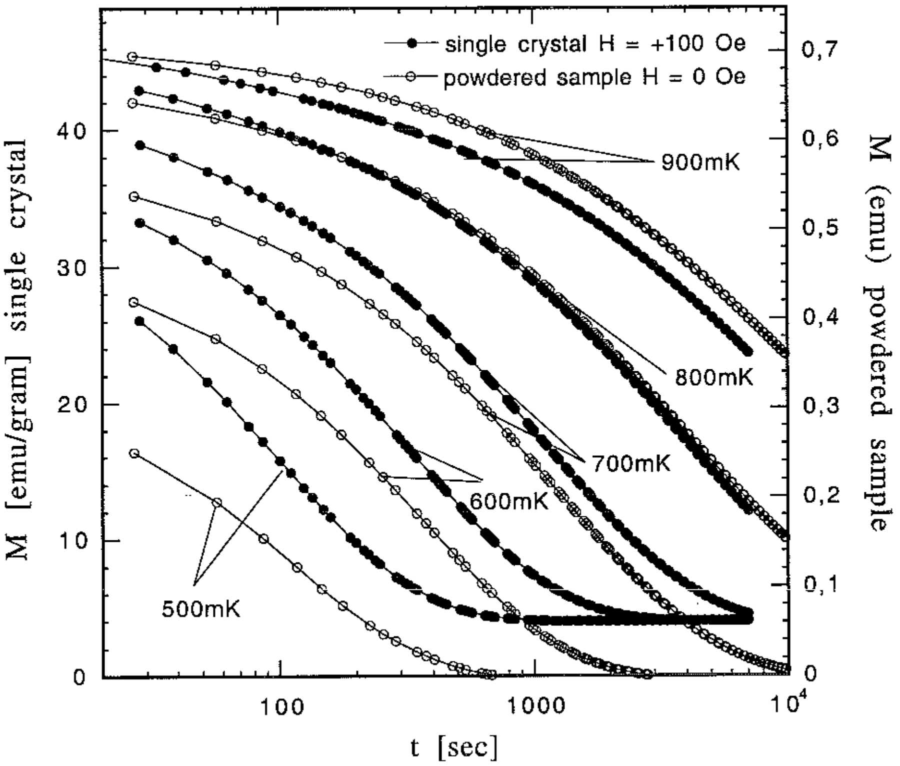

Figure IV.2.2.4: A comparison between the relaxation curves of a powdered sample and a single crystal. Besides the scaling and the offset due to the external field the relaxation curves are very similar.

The relaxation curve for 1K and 0.9K can be well fit by a single exponential function

$$M(t) = M_0 \exp(-t/\tau). \qquad (1, \mathrm{IV}.2.2)$$

For lower temperatures this function doesn't fit the data anymore. The relaxation curves below 0.8K are reasonably well fit by a stretched exponential

$$M(t) = M_0 \exp\left(-(t/\tau)^\beta\right) \qquad (2, \mathrm{IV}.2.2)$$

where $\beta \leq 1$is a new dimensional-less fitting parameter. In the figures [IV.2.2.5] and [IV.2.2.6] fits of the data to a stretched exponential function are presented. Figure [IV.2.2.5] shows that the fit works reasonably well but doesn't fit perfectly the data. We can improve the fit for longer times by including the equilibrium value M_∞ to the fitting function

$$M(t) = M_\infty + (M_0 + M_\infty)\exp\left(-(t/\tau)^\beta\right). \qquad (3, \mathrm{IV}.2.2)$$

We can see that the fit is much improved by this additional parameter and that the parameters are changing slightly. The relaxation time τ is changing by a factor of 2 and the exponent β by 20% to 30%. Figure [IV.2.2.6] show the fit on a log M vs. t -plot.

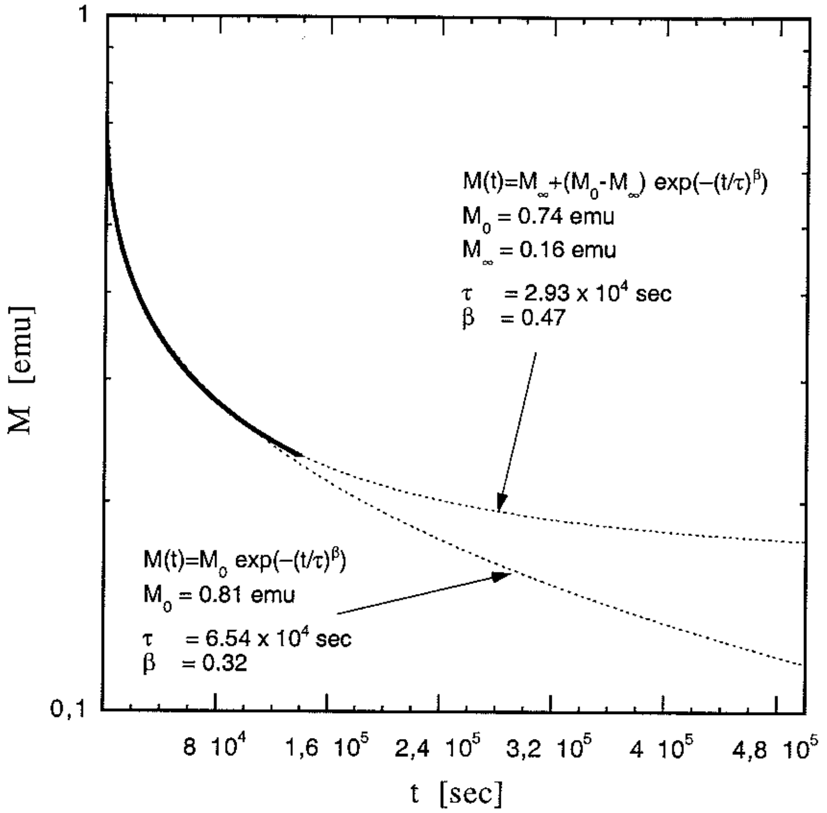

Figure IV.2.2.5: Semi-logarithmic plot of two stretched exponential fits to a relaxation curve of a powdered sample at 70mK. The fit that takes into account a none-zero equilibrium value M_∞ matches better the data.

The relaxation series show also that we are always missing the beginning of the relaxation. This comes because the first measurement can only be done some time after the external field has been settled, typically ~ 20 – 30 sec. In addition, the relaxation may start before the target field is reached, i.e. during the change in the magnetic field. These effects are especially pronounced at high temperatures. If we fit the relaxation curves with a single or a stretched exponential function, we find that for the extrapolation to $t = 0$, the initial magnetization M_0 is not the same. The temperature dependence of M_0 and M_∞ is show in figure [IV.2.2.7]. These data are for the powdered sample in zero field. This figure shows that for temperatures below 0.5K the relaxation curve extrapolates to the same initial magnetization value M_0. For higher temperatures the relaxation starts even before we are beginning with the measurements and M_0 is constantly decreasing for higher temperatures. The equilibrium value M_∞ is zero for temperatures higher than 0.7K as we expect.

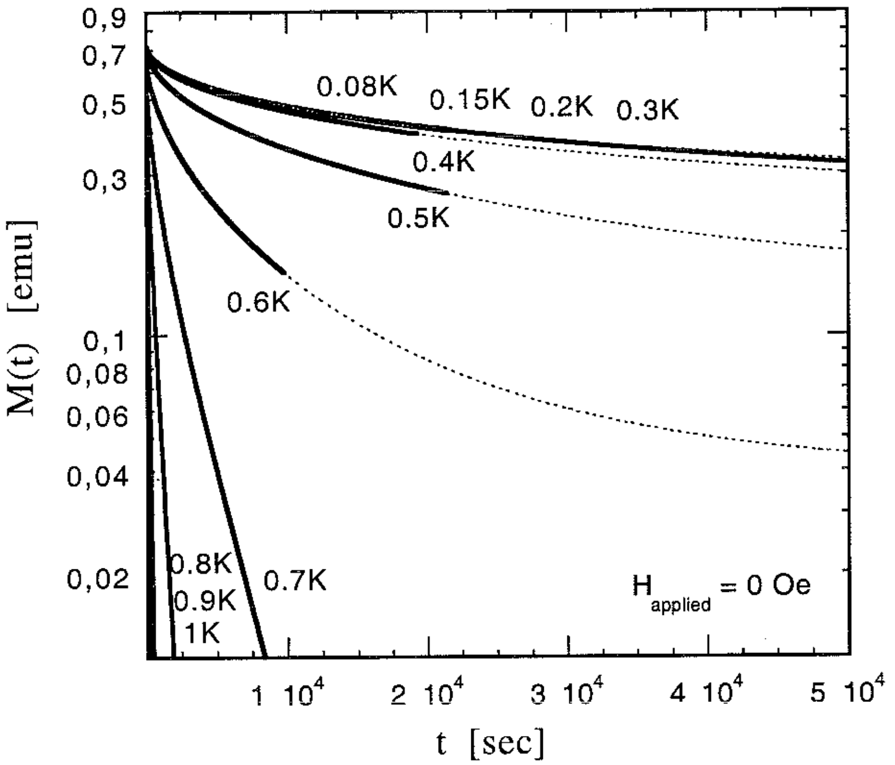

Figure IV.2.2.6: Semi-logarithmic plot of a series of relaxation curves of a powdered sample in zero field. The dashed lines are fits of stretched exponential functions to the data with $M_\infty \neq 0$.

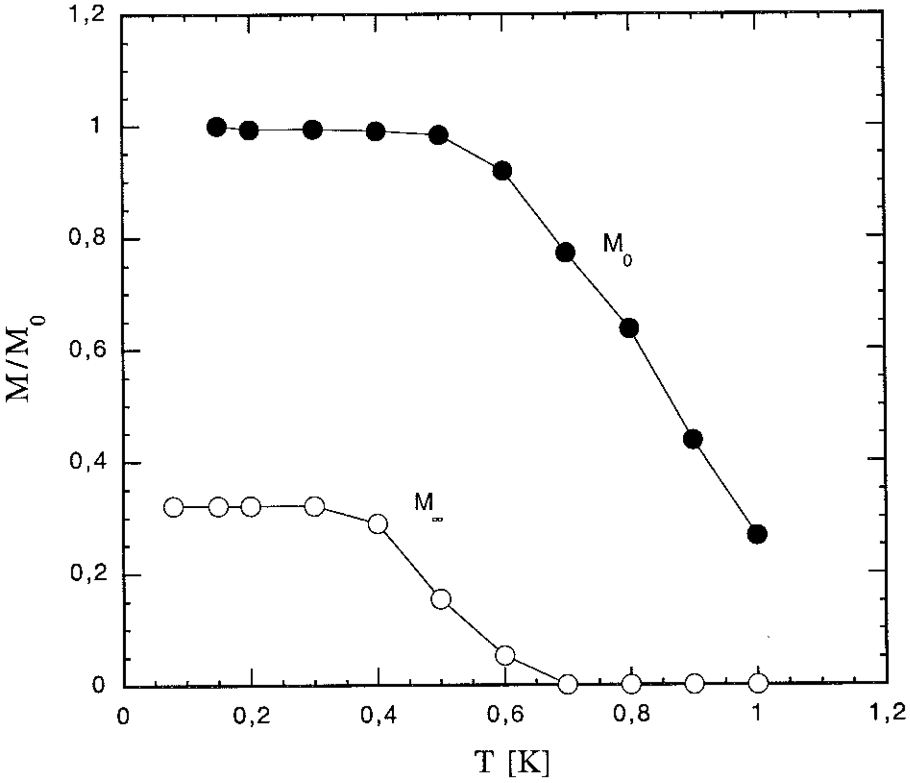

Figure IV.2.2.7: The fitting parameters M_0 and M_∞ as function of the temperature for a powdered sample in zero field.

The relaxation time resolved by fitting the data to a stretched exponential with $M_\infty = 0$ are shown in figure [IV.2.2.8]. In this plot we present only the data down to 0.4K (=2.5 K^{-1}), i.e. the region where the relaxation is still temperature dependent. For high temperatures we have added the ac-data as discussed before. We see that the determined relaxation times for both methods match perfectly and have the same values[3] in the small overlapping region around 1K.

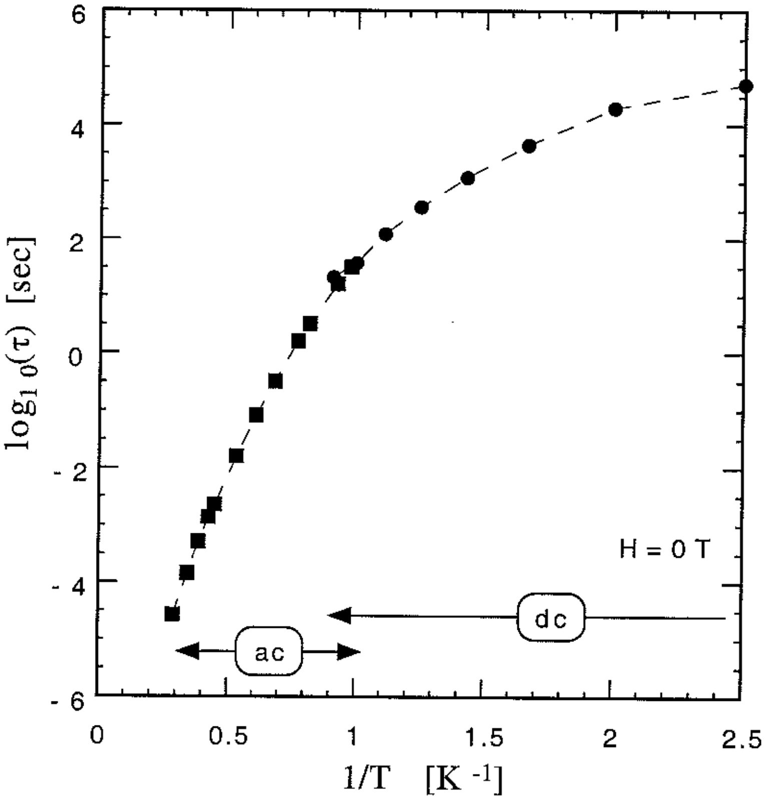

Figure IV.2.2.8: The relaxation time τ versus the inverse temperature $1/T$. The characteristic times obtained by ac-methods match the relaxation times obtain by dc-relaxation measurements in a small temperature range around 1K.

The temperature dependence of β is shown in figure [IV.2.2.9]. For high temperatures we expect $\beta = 1$ as we have observed at 1K and 0.9K for the powdered sample.. This means that the relaxation curve is single exponential in this temperature range. For temperatures below 0.4K the parameter $\beta = 0.4$ is constant as is the relaxation time, $\tau = 10^4$ sec.

---

[3] Note that for the dc-data τ_{dc} is the fitting parameter of the stretched exponential and for the ac-data $\tau_{ac}=2\pi/f$ with f the frequency of the measurement.

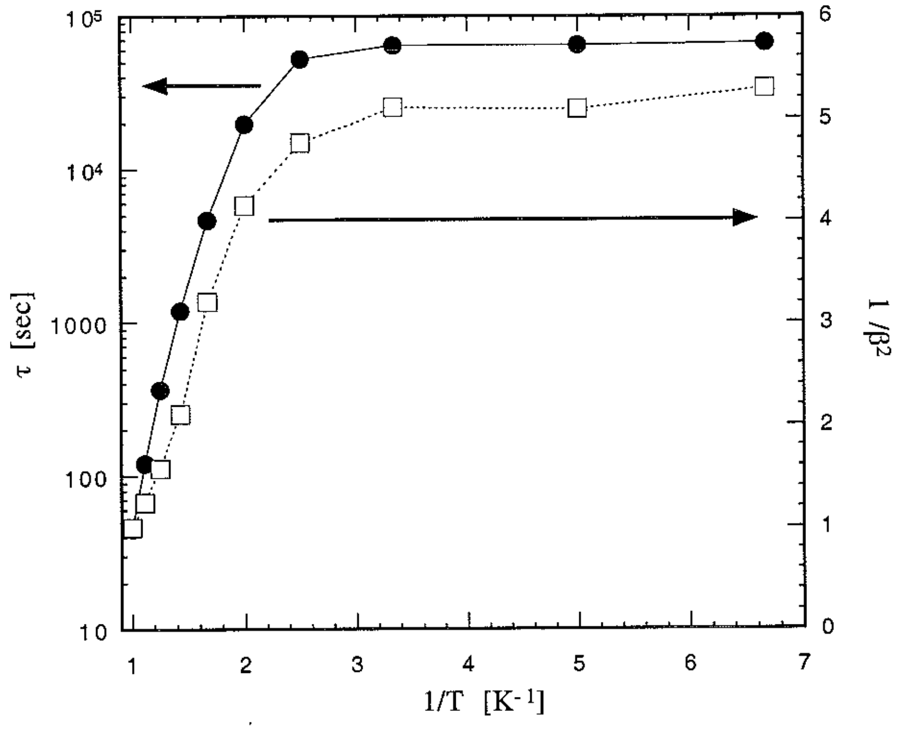

Figure IV.2.2.9: The relaxation time τ and the parameter β versus the inverse temperature $1/T$. At high temperatures we expect that $\beta = 1.0$ as observed for 1.0K and 0.9K while the relaxation time is roughly following the Arrhenius law. At temperatures below 0.4K β and τ stay constant with $\beta \approx 0.4$ and $\tau = 6\times10^4$ sec. In a small intermediate temperature range $\ln \tau \sim 1/\beta^2$.

Magnetic Viscosity

The magnetic viscosity is a helpful tool to study the relaxation data. The magnetic viscosity is defined as

$$S(t) = \frac{dM(t)}{d\ln(t)}. \quad (1, \text{IV.2.2})$$

We calculated the magnetic viscosity of the relaxation data of the powdered sample, figure [IV.2.2.2]. The resulting plot of $S(t)$ is plotted in figure [IV.2.2.10].

The relation between the relaxation curve $M(t)$ and $S(t)$ is comparable to the relation between $\chi'(\omega)$ and $\chi''(\omega)$. Assuming the Debye model, i.e. only one single relaxation time is present in the sample, the equation for the real and imaginary part of the susceptibility as function of the frequency is give by

$$\chi'(\omega) = \frac{1}{1+\omega^2\tau^2}\chi \quad (2, \text{IV.2.2})$$

$$\chi''(\omega) = \frac{\omega\tau}{1+\omega^2\tau^2}\chi. \quad (3, \text{IV.2.2})$$

In general the relation between the real and the imaginary part of the susceptibility is given by the Kramers–Kronig–Relation. In this simple case the relation can be given by

$$\frac{d\chi'(\omega)}{d\ln\omega} = -2\chi''^2(\omega). \qquad (4, \text{IV.2.2})$$

This equation is equivalent to the definition of the magnetic viscosity taking into account that $\chi'(\omega)$ as given in equation (2, IV.2.2) is the Fourier-transform of an exponential function.

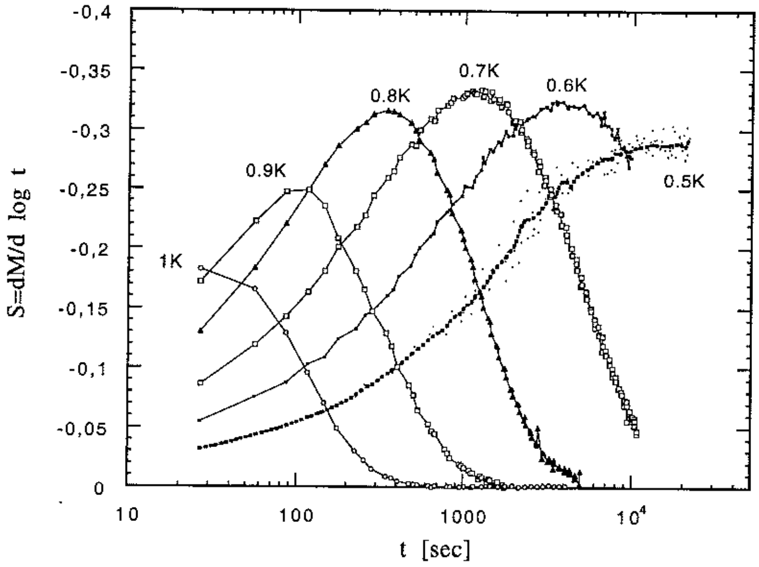

Figure IV.2.2.10: Magnetic viscosity of the relaxation curves for the powdered sample in zero field. The maximum of $S(t)$ in this plot corresponds roughly to the inflexion point of the relaxation curves.

We can thus argue that a kind of analogy exists in terms of frequency (ac-measurements) and time evolution (dc-measurements, thus the relation between

$$M(t) \leftrightarrow S(t) \qquad (5, \text{IV}.2.2)$$

is comparable to the relation between

$$\chi'(\omega) \leftrightarrow \chi''^{2}(\omega). \qquad (6, \text{IV}.2.2)$$

As for the ac-susceptibilities, see section [IV.2.1], is the maximum of $S(t)$ near the inflection point of $M(t)$. If we compare the maxima of the curves in figure [IV.2.2.10] ($\tau_{visc}(T)$) to the relaxation times obtained by fitting the relaxation curves to a stretched exponential function ($\tau_{stretch}(T)$) we find that they are identical, see figure [IV.2.2.11].

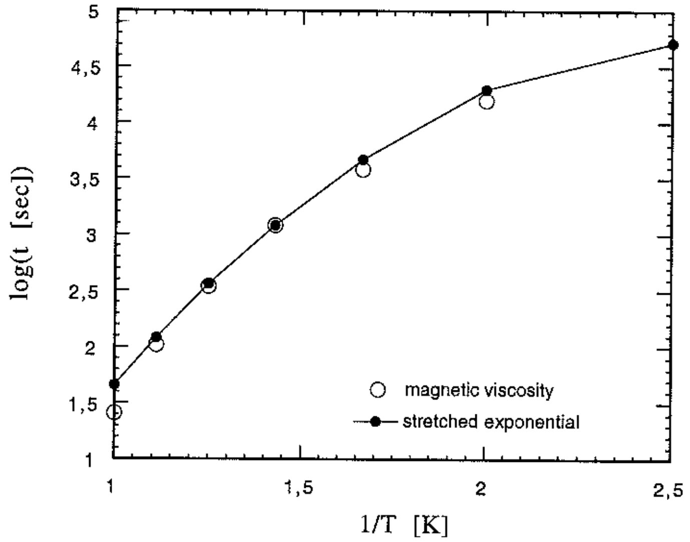

Figure IV.2.2.11: A comparison between the relaxation times obtained by fitting the relaxation curves to a stretched exponential function with $M_\infty = 0$ and the maxima of the magnetic viscosity. In this small intermediate temperature range both methods give the same result.

Field dependence

The field dependence of the relaxation time is shown in figure [IV.2.2.12] for the temperature range of 4.2K to 0.4K. The field effects are only shown for the dc-relaxation measurements. It is remarkably that the field dependence of the relaxation time is not monotone. The sample is saturated in a positive field of a few tesla. If we let the sample relax in an external field of $H_{extern} = -1$ kOe the relaxation is orders of magnitude slower than in zero field. If we further increase the field in which the relaxation takes place to a value $H_{extern} = -2.35$ kOe the relaxation is orders of magnitude *faster* compared to the relaxation in zero field or in a field of –1 kOe.

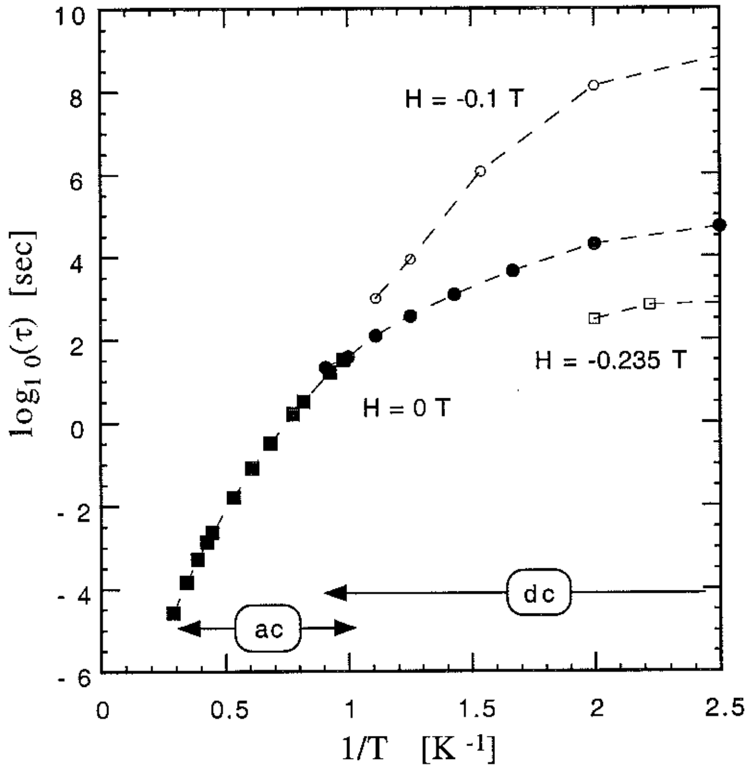

Figure IV.2.2.12: Field dependence of the relaxation time for temperatures below 1K. The relaxation time changes with the field by orders of magnitude. The field dependence is not monotonic. If we change the field to –1 kOe the relaxation becomes slower for a even larger negative field (-2.35 kOe) the relaxation time becomes faster than for zero field.

For higher temperatures we observe the same effect in the hysteresis curve. The hysteresis curve for a temperature of 1K is presented in figure [IV.2.2.13]. This figure shows two hysteresis curves at the same temperature but measured with different sweeping rates of the field, 1.4 Oe/sec and 48.5 Oe/sec. First we see clearly a superparamagnetic hysteresis effect: The area of the hysteresis curve depends on the sweeping rate. At a fixed temperature the relaxation time of a superparamagnet is $\tau(T,H)$ as e.g. given by the Arrhenius law. Thus if the sweeping rate of the field is fast compared to the time scale of the relaxation time at this temperature the sample cannot follow the field change and stays during the whole hysteresis curve in a non-equilibrium state. In this case the hysteresis curve has a large area as for example the curve for a sweeping rate of 48.5 Oe/sec. The slower the sweeping rate the more time the system has to approach equilibrium and consequently the area of the hysteresis curve is smaller. In the theoretical case of an infinitely slow sweeping, rate the system can reach the equilibrium and the hysteresis curve will be closed and reversible.

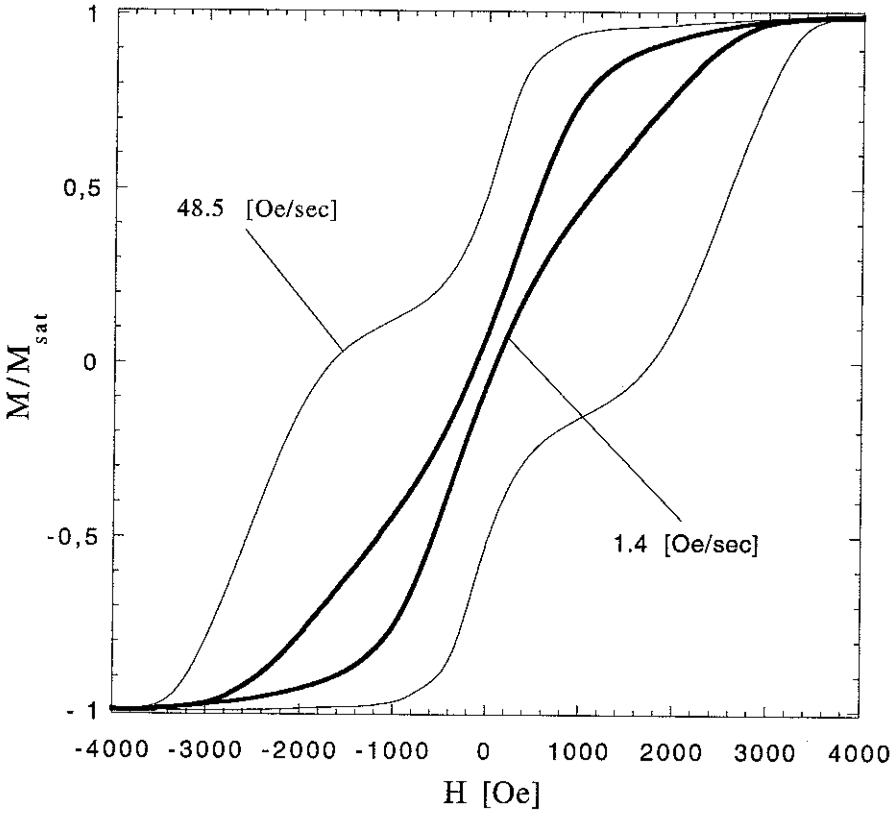

Figure IV.2.2.13: Hystersis curves at 1K. The hysteresis shows a typical superparamagnetic effect. The area of the hysteresis depends on the sweeping rate. The faster the field is changing, the larger is the area. The slope of the hysteresis curve is modulated. Fast relaxation at 0 kOe and around –2 kOe, slow relaxation at –1 kOe.

The modulation of the slope of the hysteresis curve is remarkable. Starting with a flat slope near the positive saturation field the slope becomes steeper around zero field. Afterwards, around a field of –1 kOe the slope flattens meaning that the relaxation time becomes slower compared to the relaxation in zero field. At a field value of about –2 kOe the slope again becomes steeper thus the relaxation rate is increasing. This is the same effects as discussed for figure [IV.2.2.12]: fast relaxation around $H = 0$ kOe and $H = -2$ kOe, slow relaxation at $H = -1$ kOe. This resonant effect is related to crossing energy levels in the spin system. We discuss this in more detail in the next section on the quantum effects.

IV.2.3) Fe8, Quantum regime

In the quantum regime, i.e. below a temperature of 400mK, the relaxation is independent of the temperature and relaxation only occurs via tunneling of the magnetization. In this regime and at the first resonance the relaxation time is $\tau = 6 \times 10^4$ sec and the stretched exponential parameter $\beta = 0.4$. The relaxation curve varies with the shape of the sample but the parameters of the stretched exponential fit remain approximately the same.

The field effects in the quantum regime are tremendous. The relaxation time change by 4 orders of magnitudes between a measurement at 0 kOe and –1 kOe! The field dependence is not monotone but modulated in such a way that we find fast relaxation at equidistant fields of 2 kOe starting from zero and extremely slow relaxation starting from –1 kOe. This resonant behavior is explained by the energy crossing of the spin levels due to the Zeemann shift of an external field. If the levels are degenerate tunneling is permitted and the measured rate is about 10^{-5} Hz, i.e. a relaxation time of 10^4 sec. If the levels are not degenerate the system is off-resonance and tunneling is suppressed. In this case this system can still relax via thermal activation but at these temperatures the probability is extremely low, thus at these field values the systems has a relaxation time of about of about 10^8 sec!

Sample shape effects

The sample shape has an influence on the relaxation curve as shown in figure [IV.2.3.1]. We measured a long sample[4], a spherical sample, and a flat sample. Since the relaxation curve of the long sample resembles the one of the powdered sample, it seems that most of the micro-crystals in the powder have the same shape as the long sample. The long sample was measured as grown and had basically smooth surfaces, while the flat sample is cut from a long sample, and the spherical sample was obtained from milling a large single crystal. The spherical sample and the flat sample have rough surfaces due to their production process. We believe that this will have an effect on the relaxation behavior since the local field distribution governs the relaxation process and a rough surface gives rise to strong inhomogeneities in the demagnetization field.

The fitting parameters to the curves in figure [IV.2.3.1] are presented in table [IV.2.3.1]. It can be seen that the parameters vary slightly from shape to shape.

shape	M_0 / [emu/gram]	M_∞ / M_{sat}	τ / 10^4 sec	β	$H_{applied}$ / [Oe]	*angle* α	$H_{corrected}$ / [Oe]
long	48.1	0.15	3.19	0.46	110	14°	107
sphere	45.1	0.25	2.22	0.35	300	25°	272
flat	39.5	0.20	2.09	0.43	260	37°	208
powder	47.0	0.22	2.93	0.47	0	–	0

Table IV.2.3.1: Parameters for a stretched exponential fit to the relaxation curve of samples with different shapes. The measurements where done in the quantum regime but for different external fields $H_{applied}$. The fields were chosen to have the fastest relaxation after saturation in a strong positive field, i.e. at the center of the first resonance.

---

[4] The long sample has an aspect ratio of 1.0 : 0.5 : 0.7.
The flat sample has an aspect ratio of 1.0 : 2.9 : 3.6.

The expected value for the saturation is $M_{sat} = 49.6$ [emu/gram]. The fact that we measure a smaller saturation value may be due to mis-alignment of the sample and no corrections have been made for diamagnetic contributions. We estimate the angle α by $M = M_{\text{sat}} \cos(\alpha)$. Due to this mis-alignment the applied field is not the same as that parallel to the easy axis. We have therefore corrected the field value by the same amount $H_{\text{corrected}} = H_{\text{applied}} \cos(\alpha)$. The equilibrium value of the relaxation is non zero for all sample shapes even for different field values at a value of about $M_\infty \approx 0.2\ M_{sat}$. The relaxation time is of the order of $\tau \approx 3\times10^4$ sec compared to $\tau \approx 6\times10^4$ sec if we set $M_\infty = 0$ for the stretched exponential fit. The parameter β of the exponent is in all cases about $\beta \approx 0.4$.

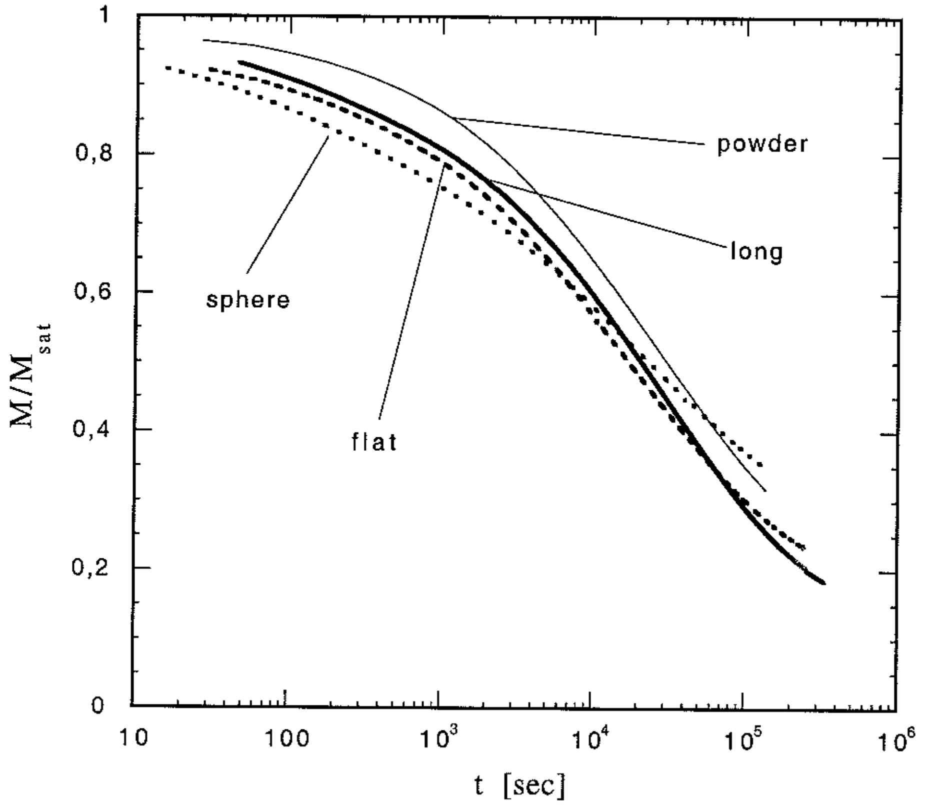

Figure IV.2.3.1: Relaxation curves in the quantum regime for different sample shapes. The curves are slightly different but the fitting parameters of a stretched exponential function do not vary appreciably, see table [IV.2.3.1].

In figure [IV.2.3.2] one of the main result of our studies is presented. It shows the dependence of the relaxation time as a function of the temperature and the external field for a powdered sample. For the dc relaxation measurement the sample was first saturated in a positive field > +3 tesla. At high temperatures the data lie roughly on a straight line indicating that the relaxation is thermally activated and obeys the Arrhenius law. For lower temperatures the relaxation deviates from the Arrhenius law and becomes gradually faster than expected for a thermal activated process. Below about 0.4K the relaxation time is independent of temperature but depends strongly on the external field. At –1 kOe the relaxation time is slower by 4 orders of magnitude compared to the relaxation in zero field. If we increase further the field to about –2 kOe the relaxation time becomes faster again. At this field value the relaxation time is faster by 2 orders of magnitude compared to a relaxation in zero field and 6 orders of magnitude faster compared to a relaxation in a field of –1 kOe!

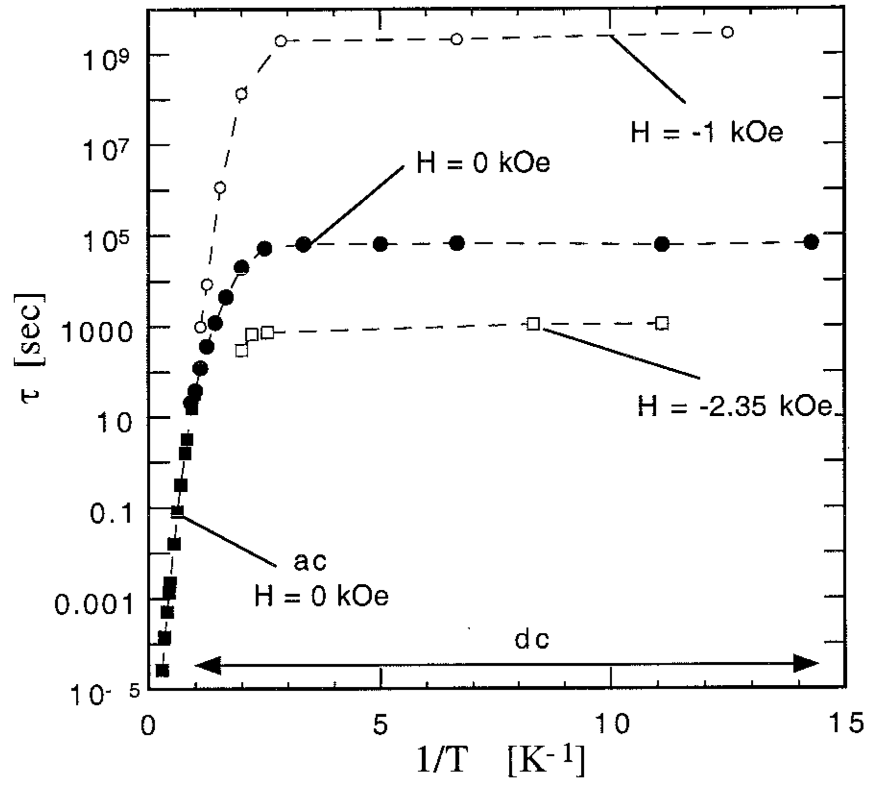

Figure IV.2.3.2: Relaxation time survey for a powdered Fe8 sample as function of temperature and field. Below 0.4K the relaxation time becomes temperature independent. In this quantum regime the relaxation time varies strongly and non-monotonically with the field.

Three examples of relaxation curves taken with different fields in the quantum regime are presented in figure [IV.2.3.3]. These curves are from measurements on a single crystal at a temperature of 150mK. The fit to a stretched exponential function gives the following parameters: $\tau = 3.1 \times 10^4$ sec, $\beta = 0.47$ in +100 Oe, $\tau = 10^8$ sec in a field of –1 kOe, and $\tau = 4.5 \times 10^3$ sec, $\beta = 0.42$ in a field of –2 kOe. Thus the relaxation time varies strongly with external field and the parameter β also varies slightly with field. Due to general difficulties of fitting a stretched exponential function the variation in β might be artificial due to the fitting algorithm. The fit to the curve at –1 kOe is not reliable because the change in the magnetization is too small and we set $\beta = 1$. The relaxation times of the single crystal sample are about the same as for the powdered sample with $M_\infty \neq 0$. The interaction between the crystals in the powder and their arbitrary orientation does not change appreciably the behavior.

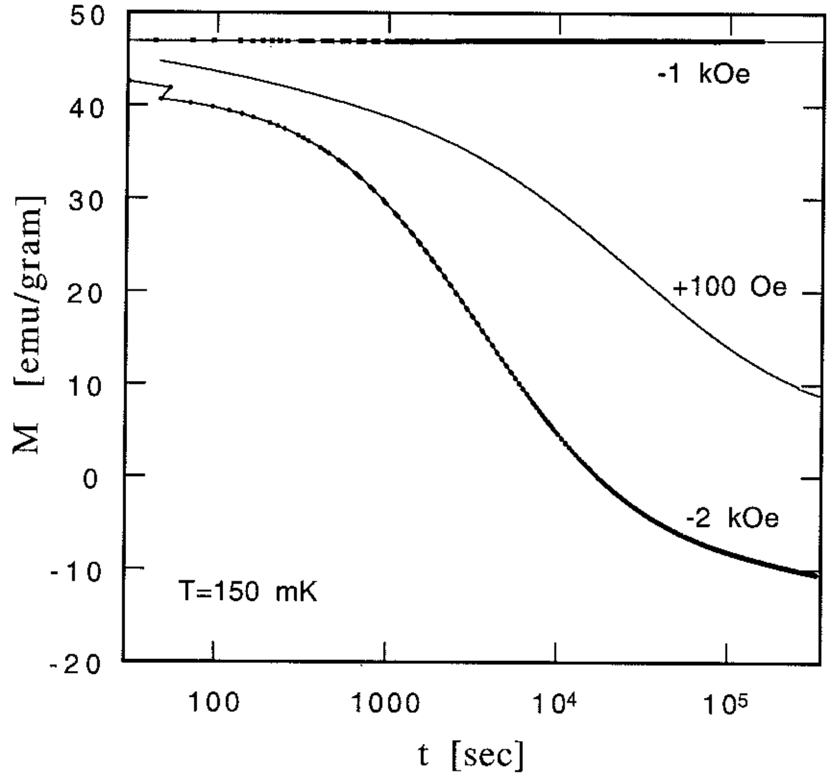

Figure IV.2.3.3: Relaxation curves of a single crystal for different field values at a temperature of 150mK.

If we look closer at the field dependence of the relaxation around zero field we find that the relaxation is faster at a field of +80 Oe compared to a relaxation in 0 Oe after saturating the sample in a strong positive field. For a field value that is slightly larger, +180 Oe, the relaxation becomes slower again. This result is surprising since the internal field of the sample including the demagnetization field is always positive, see annex III. Thus we would expect that we need a negative external field to counterbalance the effect of the demagnetization field to bring the system into resonance, contrary to what we observe.

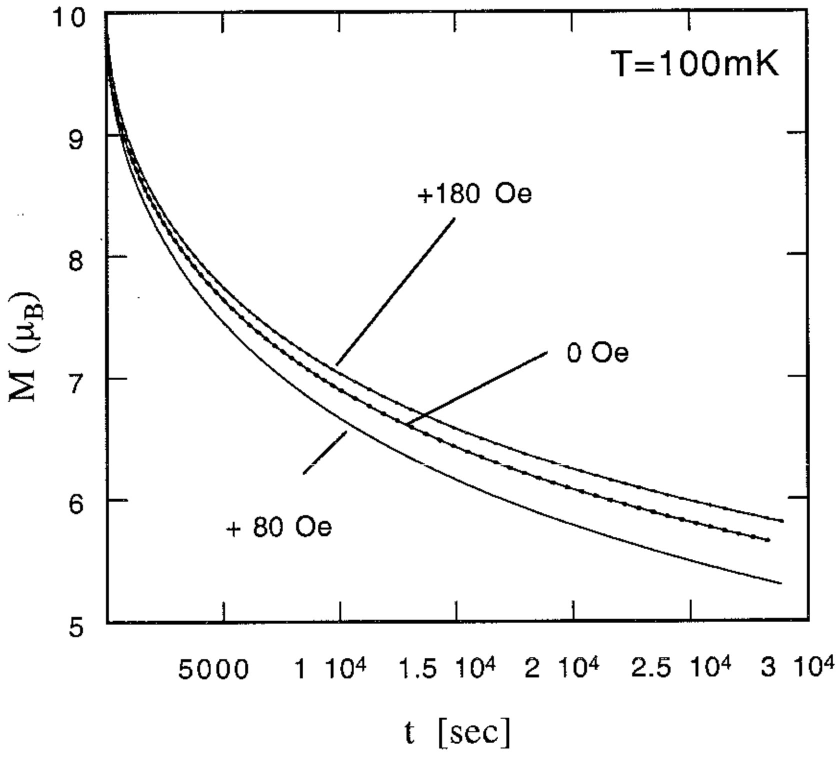

Figure IV.2.3.4: Relaxation curves of a powdered sample at different small field values around zero.

Resonant Quantum Tunneling

In figure [IV.2.3.5] we present a schematic view of the resonance effect in this system. This general idea was first proposed by M. Novak based on high temperature measurements on the Mn12ac-system [Novak 95b]. On the left hand side the level scheme of a molecule in zero field is shown. All of the levels are in resonance and tunneling is permitted between any of the states. If the molecule experience a magnetic field the energy levels will shift due to the Zeeman energy as shown on the right hand side of the figure. If the energy levels are not degenerate then tunneling between them is strongly supressed. The natural resonance width is given by the tunnel splitting of degenerate levels. From the theories, e.g. of van Hemmen and Sütö, we can estimate that the resonance width should not exceed 10^{-5} Oe! That means any field larger than this value will suppress tunneling effects and block the system.

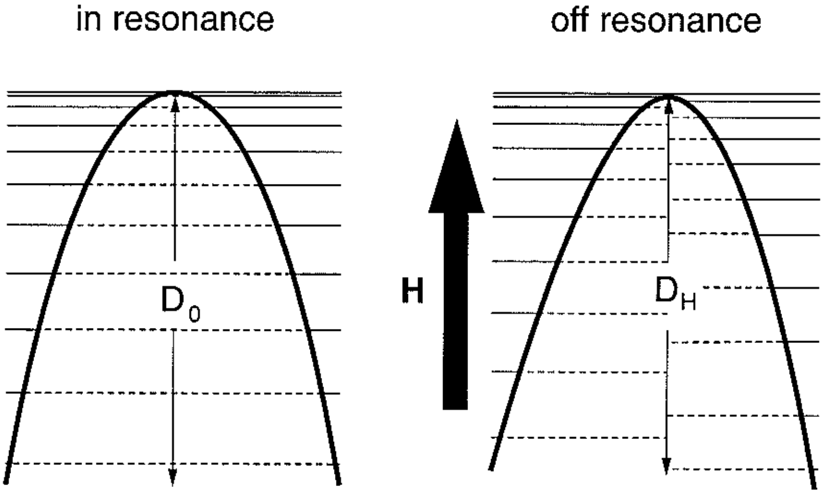

Figure IV.2.3.5: Scheme of resonance effects. If the spin states are degenerate tunneling is permitted. In the presence of a magnetic field the levels shift. If the levels are not degenerate tunneling is suppressed.

The dependence of the energy levels of Fe8 on the magnetic field is shown in figure [IV.2.3.6]. These energy levels have been calculated for a Hamiltonian of the form

$$\hat{H} = -D\hat{S}_z^2 + E/2\left(\hat{S}_+^2 + \hat{S}_-^2\right) - g\mu_B\hat{S}_zH. \qquad (1, \text{IV.2.3})$$

The technical details are discussed in the annex I. In zero field all levels of same modulus $|m|$ are degenerate (up to the tunnel splitting Δ) and tunneling is permitted. If the field is increased levels of different signs separate and tunneling is suppressed if the energy difference is larger than the tunnel splitting. At a field value of about 2 kOe the levels cross again but this time between the states m and $-(m-1)$. If the field is further increased the levels separate again until the field reaches a field of 4 kOe and so on. The system thus shows a resonance as a function of field, at values separated equidistantly by $\Delta H = 2$ kOe. At each resonance field, *all* states are degenerate, and in resonance, see section II.2.

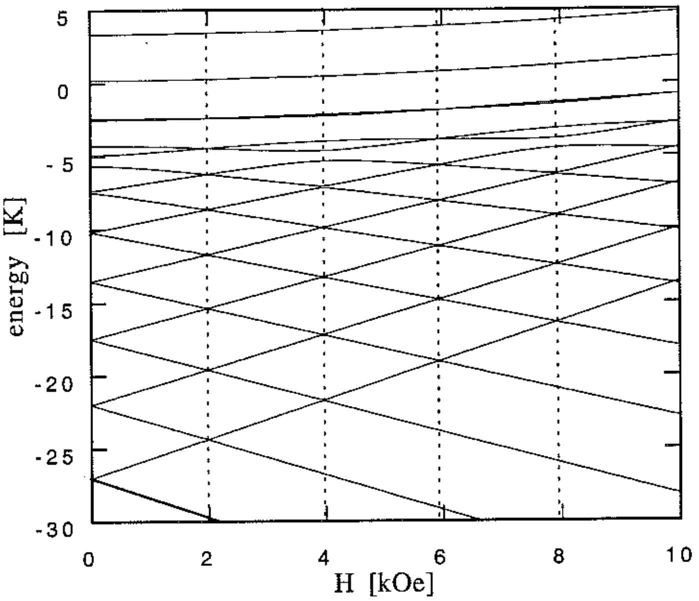

Figure IV.2.3.6: Dependence of the Fe8 spin levels on the magnetic field. The levels cross at field values of 0 kOe, 2 kOe, 4 kOe etc. At these field values tunneling is permitted within $\pm\Delta_{tunnel}$, the tunnel splitting. Between these values the system is blocked, see annex I.

Figures [IV.2.3.7] and [IV.2.3.8] show hysteresis curves at different temperatures. The hysteresis curves in figure [IV.2.3.7] were taken at a sweeping rate of 48 Oe/sec and for fields in the range of ±7 kOe. This field is not sufficient to saturate the sample. We therefore had to apply a field of +7 kOe and heat the sample to about 1.5K and field cool the sample in order to saturate. For the same reason, these curves only present minor hysteresis curves.

It can be seen that the hysteresis curve opens with lower temperature and is not closed even at a temperature of 1.3K at this field sweeping rate. The opening of the relaxation curve reflects the increase of the relaxation time and the system is not in equilibrium at any point of the curve. Below 0.4K the hysteresis curves superimpose due to the temperature independence in the quantum regime.

At every temperature the hysteresis curve shows a non-monotonic modulation of the slope. The slope is flat at fields of about 1 kOe and 4 kOe and steep at fields of about 3 kOe and 5 kOe. In the region with a steep slope the system is in resonance and the tunneling rate high. In the region with a flat slope the system in off resonance and blocked. These field values do not correspond to the theoretical values or to the measured field values from the previous discussed relaxation in the relaxation measurements because of a mis-alignment of the crystal. Since the easy axis is not exactly along the field direction (but off by an angle α) only a fraction of the field value is contributing to the Zeeman energy shift $H_{parallel} = H_{field} \cos(\alpha)$.

In figure [IV.2.3.8][1] the hysteresis curve was measured at a higher sweeping rate of 140 Oe/sec. The setup used for these measurements is capable of reaching field values of 14 kOe. In this figure 5 steps in the hysteresis curve can be seen. Again the curves for temperatures below 0.4K are identical and the resonance steps are present at all measuring temperatures.

---

[1] These hysteresis curves where made in collaboration with Wolfgang Wernsdorfer at the Laboratory Louis Néel.

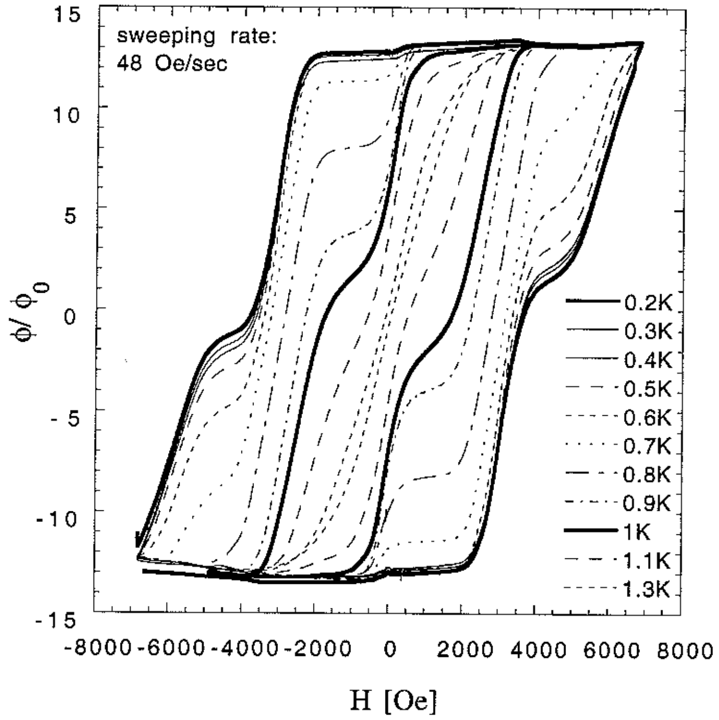

Figure IV.2.3.7: Hysteresis curves of a micrometer sized single crystal. At all temperatures resonance effects can be observed. These measurements were made using a microSQUID system.

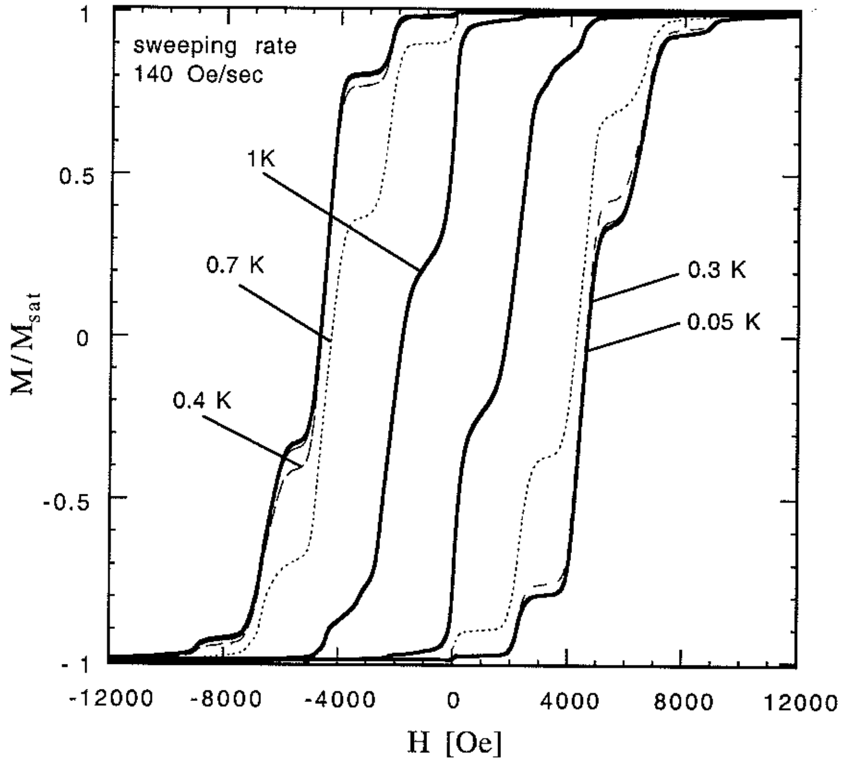

Figure IV.2.3.8: Hysteresis curves of a micrometer sized single crystal. In the quantum regime 5 resonance steps can be seen.

The derivative of one branch of the hysteresis curves dM / dH is roughly proportional to the relaxation time. During the short time of $t_{measure}$ the field can be assumed as being fixed. If the relaxation is stretched exponential

$$M(t) = M_0 \exp\left(-(t/\tau(H))^{\beta(H)}\right). \qquad (2, \mathrm{IV}.2.3)$$

the derivative with respect to the field H gives

$$\frac{dM}{dH} = \left(\frac{\beta(H)}{\tau(H)}\frac{d\tau(H)}{dH} - \ln\left(\frac{t_{measure}}{\tau(H)}\right)\frac{d\beta(H)}{dH}\right)\left(\frac{t_{measure}}{\tau(H)}\right)^{\beta(H)} M(t_{measure}). \ (3, \mathrm{IV}.2.3)$$

Assuming that the variation with field of $\beta(H)$ is rather small we can conclude that

$$\frac{dM}{dH} \sim \left(\frac{1}{\tau(H)}\right)^{\beta(H)+1}\frac{d\tau(H)}{dH}. \quad (4, \mathrm{IV}.2.3)$$

In the figures [IV.2.3.9], [IV.2.3.10], and [IV.2.3.11] the derivation is shown for different sweeping rates for a powdered sample and a single crystal respectively. In figure [IV.2.3.9] we can see three peaks equidistantly spaced by 2 kOe corresponding to 3 resonances. In figure [IV.2.3.11] the numerical derivative of a measurement on a microSQUID is shown. In this figure we can see 5 resonances almost equidistantly spaced. From figure [IV.2.3.10] taking only account of the first resonance we can estimate the width of the first resonance to be 200 Oe to 300 Oe. The faster the sweeping rate the more pronounced is the peak and in all cases the peaks are skewed to the left, i.e. towards the direction of the field sweeping. This resonance width is orders of magnitude larger than expected from the theory.

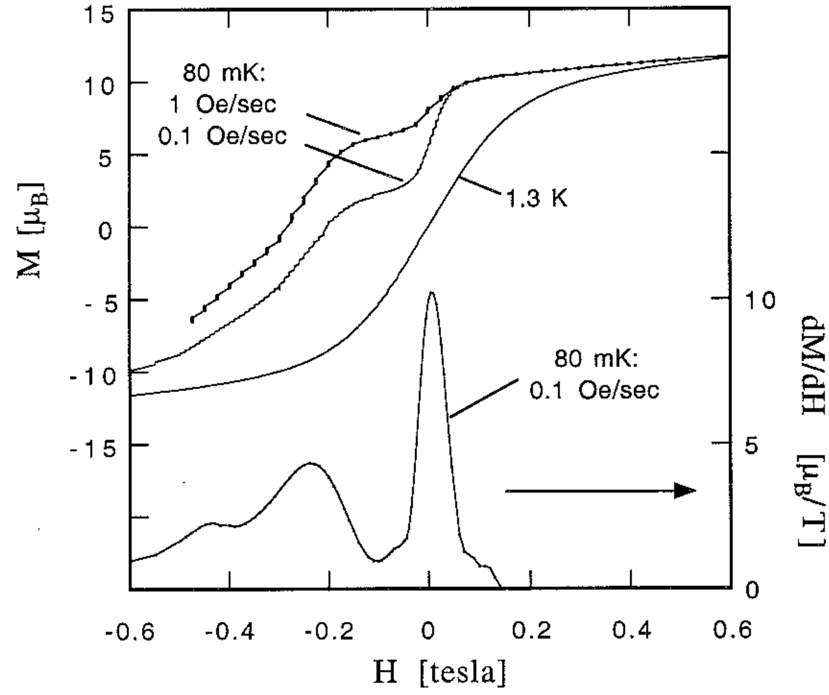

Figure IV.2.3.9: One branch of a hysteresis curve and its derivative with respect to the field. The derivative shows 3 resonance peaks.

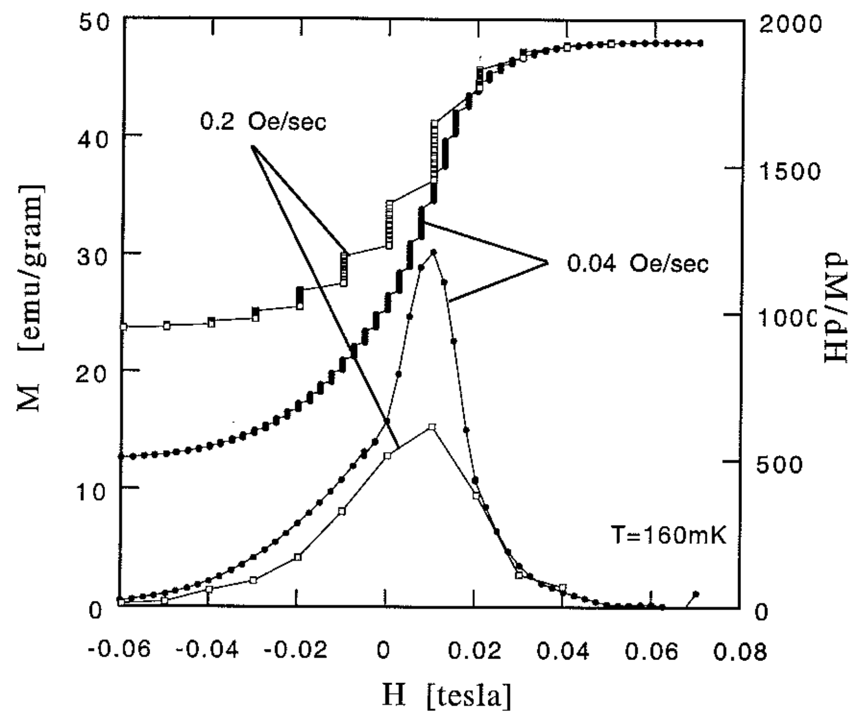

Figure IV.2.3.10: One branch of a hysteresis curve made at different sweeping rates on a single crystal. The derivative shows the first resonance. The resonance has a width of about 200 Oe to 300 Oe.

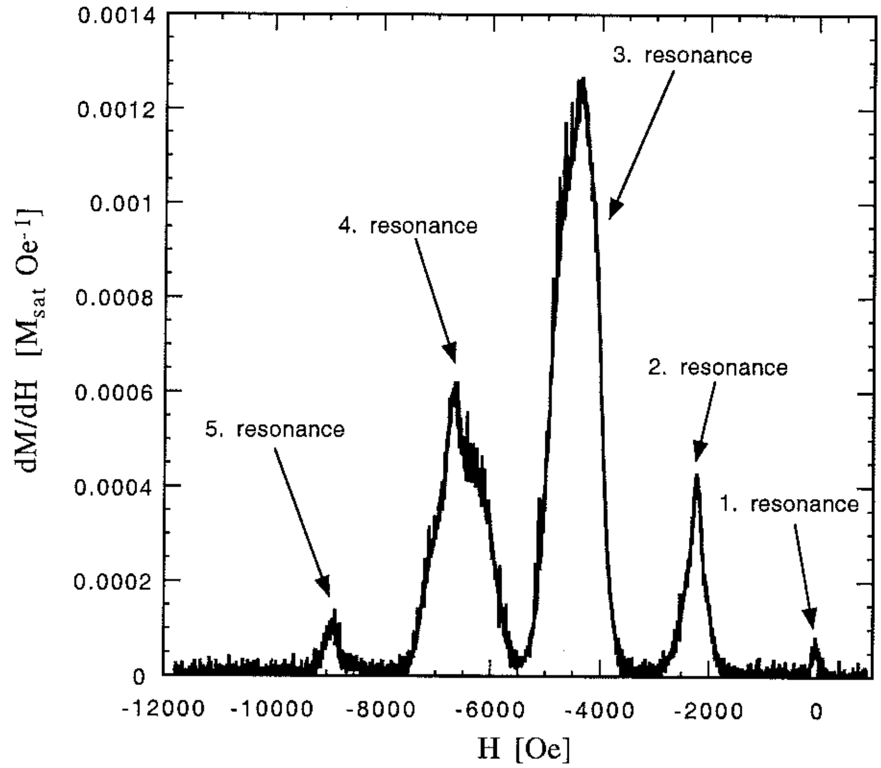

Figure IV.2.3.11: Numerical deviation dM/dH of a branch from a hysteresis curve measured in the quantum regime at 50mK and a sweeping rate of 140 Oe/sec, see figure [IV.2.3.8]. The figure clearly shows 5 resonances that are equidistantly spaced by about 2200 Oe. The measurement was made with a microSQUID on a micrometer sized single crystal.

One problem with estimating the resonance by this method is that the sample relaxas continuously during the field sweep of the resonance. Thus when we are reach for example the center of the resonance, a major fraction (depending on the sweeping rate) of the spins are already turned. In a way by this method we are "summing up" the relaxation within a resonance while passing through it.

A much better and more quantitative method to measure the resonances in shown in the 4 figures [IV.2.3.12], [IV.2.3.13], [IV.2.3.14], and [IV.2.3.15]. The measurement method for these plots is the same as for our relaxation measurements. We first saturate the sample in a large field and after a fast field change we let the sample relax for 180 seconds in the predetermined field H. We repeat this procedure many times for different field values from $H = +0.8$ kOe to $H = -4$ kOe. The field differences between these measurement is about $\Delta H = 50$ Oe. Every vertical line in these figures represent one relaxation measurement and the points of the line are the measured values of the magnetization. If the sample is in resonance the relaxation is fast and the magnetization changes a lot. If the sample is off resonance the relaxation is slow and the magnetization stays almost constant during the 180 sec of the measurement.

At the first resonance and especially at the second resonance we can see that the first measurement is not at the saturation value. Before the target field is reached starting from the saturation field and the first measurement can be done some time is needed. During this time the sample might already start relaxing especially in the center of a resonance.

The difference between these figures is the shape of the single crystal. The sample for the figures [IV.2.3.12] and [IV.2.3.13] are two different long single crystals as grown. The sample of the figure [IV.2.3.14] is spherical, and for the figure [IV.2.3.15] flat. The 4 figures clearly show the first two resonances and figure [IV.2.3.12] also a part of the third resonance. All samples have a first resonance around zero but with different maxima, i.e. the center of the resonance, depending on the shape. The field values for the centers are: long1 $H_{center} = +80$ Oe, long2 $H_{center} = +100$ Oe, spherical $H_{center} = +230$ Oe, and flat $H_{center} = +200$ Oe. This is not in the order we would expect due to the demagnetization field. The demagnetization factor orders as $N_{long} < N_{sphere} < N_{flat}$. The field values of the centers orders as $H_{long} < H_{flat} < H_{sphere}$. The center of the second resonance is at about –2 kOe as expected. The second center for the spherical sample at about –2.5 kOe and for the flat sample at about –2.8 kOe. The large deviation of the center of the second resonance from the expected value was due to misalignment of these samples. When we correct the resonance fields by the angles we have estimated in table [IV.2.3.1] we get: long1 $H_{center} = +78$ Oe, long2 $H_{center} = +97$ Oe, spherical $H_{center} = +208$ Oe, and flat $H_{center} = +160$ Oe.

Even with this more elaborate method, the samples have about the same resonance width as derived above. For all samples the first resonance has a width of 100 Oe and the second resonance of about 500 Oe up to almost 1 kOe for the spherical and the flat sample. Again the fact that the last two samples were not well aligned give rise to an apparently larger resonance. It is therefore reasonable to assume the second resonance has a resonance width of roughly 500 Oe.

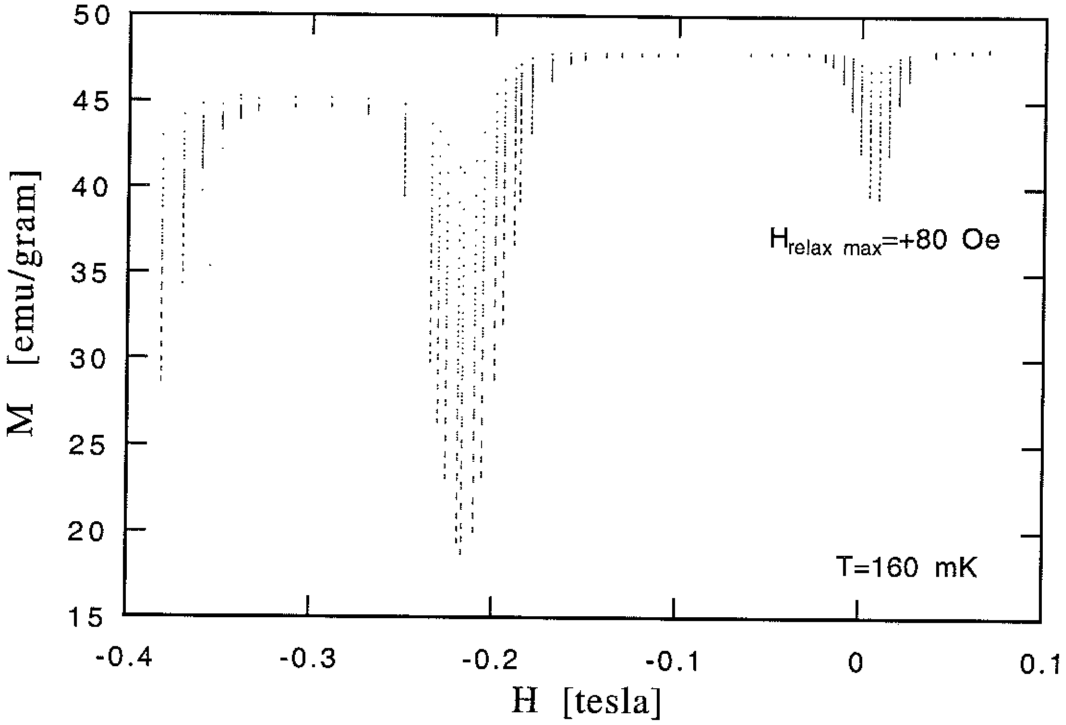

Figure IV.2.3.12: Multi-Relaxation-Scan at different field values in the quantum regime. The sample is a single crystal with a long shape (long1).

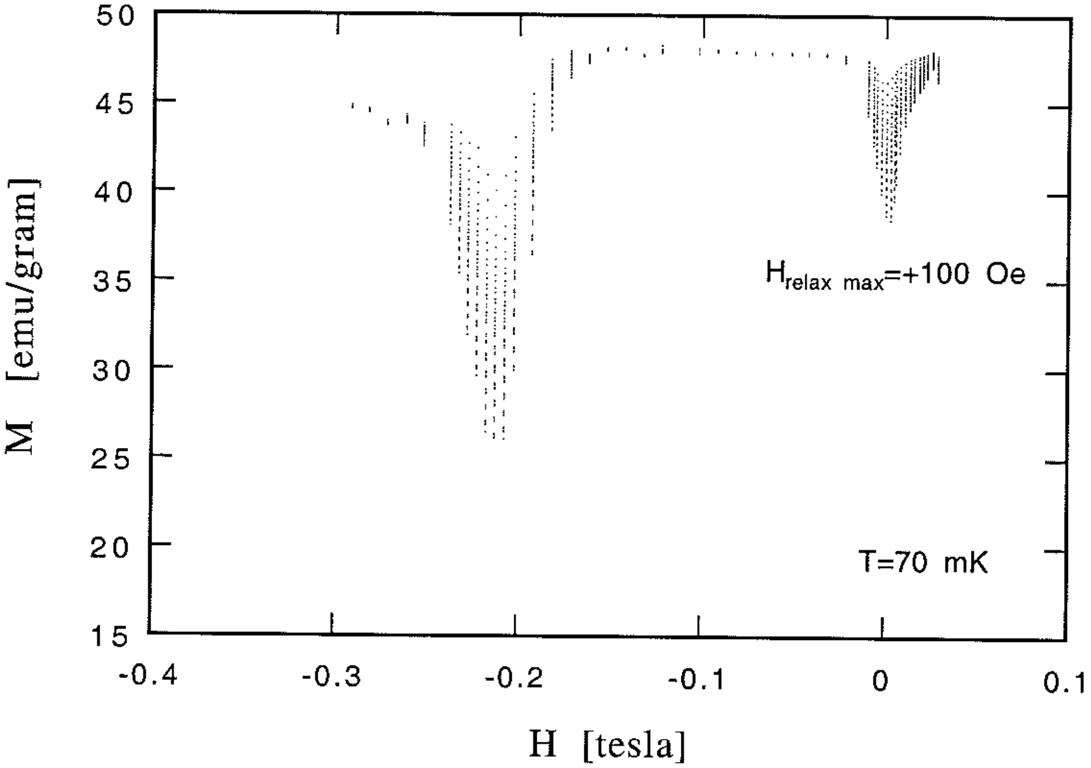

Figure IV.2.3.13: Multi-Relaxation-Scan at different field values in the quantum regime. The sample is a another single crystal with a long shape (long2).

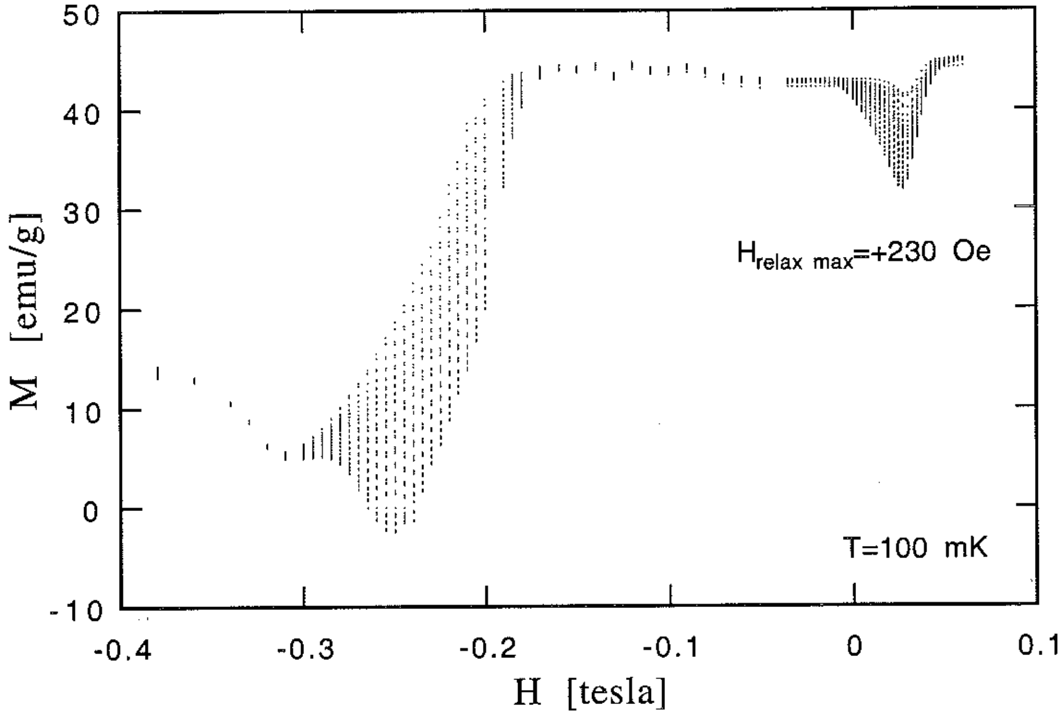

Figure IV.2.3.14: Multi-Relaxation-Scan at different field values in the quantum regime. The sample is a single crystal with a spherical shape.

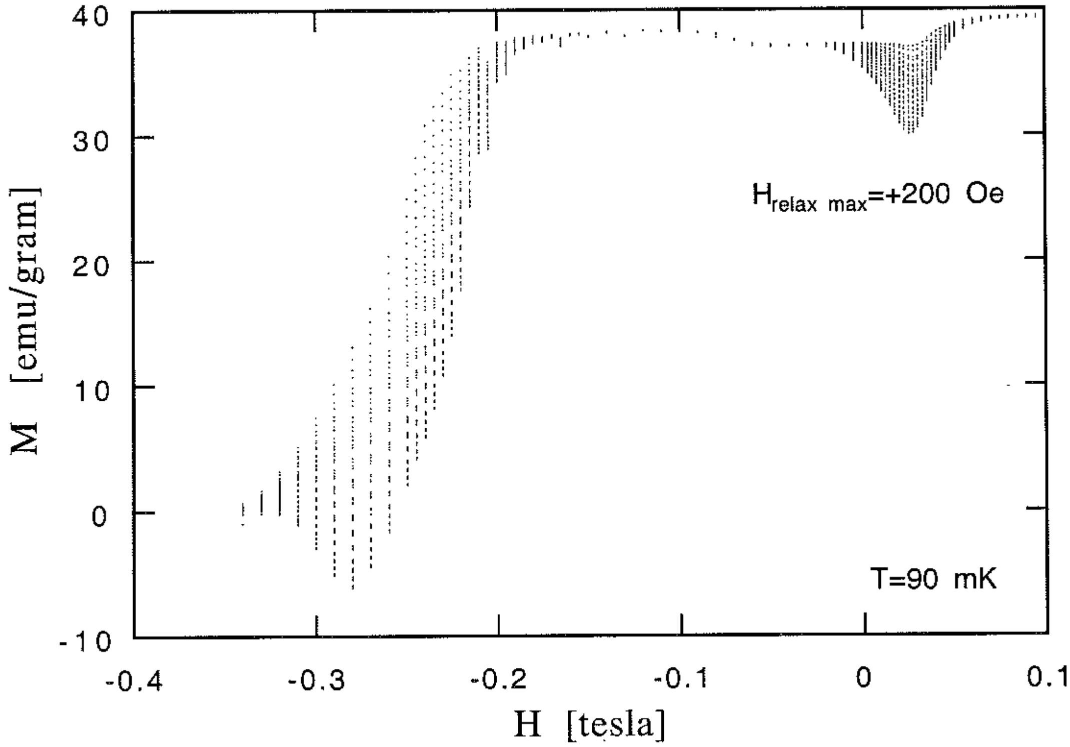

Figure IV.2.3.15: Multi-Relaxation-Scan at different field values in the quantum regime. The sample is a single crystal with a flat shape.

IV.2.4) Fe8, Discrepancies

Pioneering theories for magnetic quantum tunneling based on isolated giant spins have been proposed during the last 20 years or so [Korenblit 78, Hemmen 86a, Enz 86, Ioselevich 87, Garanin 91]. (Very recently theories have been developed which include environmental effects, such as phonons [Villain 94] and nuclear spin interactions [Prokof'ev 98]). In comparison to an isolated giant spin several experimental facts are not in agreement with theory.

We believe that taking into account the dipole fields generated by the molecular spins can solve these discrepancies. The local field distribution is of the order of 100 Oe to 500 Oe, thus the same as the observe resonance width in the experiments, see chapter [V.1]. The non-exponential relaxation can be understood in the same terms as discussed in chapter [V.2] , see also [Prokof'ev 98]. Finally, the long relaxation time is also discussed in the chapter [V.2].

Three Discrepancies:

– *The observed resonance width is too large*

Existing theories, e.g. [Hemmen 86a, Enz 86, Garanin 91, Dobrovitski 97], give rise to an estimated tunnel splitting of the order of 10^{-8}K corresponding to a resonance width of 10^{-5}–10^{-4} Oe. Such a small resonance width would make experimentation very difficult. The effect of hyperfine fields can give rise to an effective broadening of the resonance of Fe8 [Prokof'ev 98] but still the resulting resonance width shouldn't exceed a few Oersted for Fe8. All measurements show a resonance width of the order of about 100 Oe and .

– *The relaxation curve is non-exponential*

The relaxation for non-interacting, identical particles should be single exponential $M(t) \propto \exp(-t/\tau)$ (which is the case at high temperature). However, for Fe8 the data in the low temperature regime are best fit by a stretched exponential $M(t) \propto \exp\left(-(t/\tau)^{\beta}\right)$ [Sangregorio 97], which poses the problem of interpreting what τ corresponds to (at best it may be considered as an effective or average relaxation time).

A stretched exponential fit is typical for disordered systems such as spin-glasses or a system with a distribution in the size or orientation of the magnetic particles, see annex V, and at first seems a surprising result for Fe8. Distribution effects can be ruled out because molecular magnetic crystals are spatially ordered. In addition, the essential ingredients for spin glass behavior, such as strong interactions and frustration are not present in Fe8.

– *The measured relaxation times are too long*

Theories of quantum tunneling give an estimate for the quantum tunneling frequency ν for Fe8 of the order of 1 Hertz, e.g. for the Hamiltonian of Fe8, the predicted quantum tunneling frequency due to the theory of van Hemmen and Sütö [Hemmen 86b] reads

$$\nu = \tau_0^{-1}\left(\frac{E}{2D}\right)^{S} \quad (1, \mathrm{IV}.2.4)$$

with $\tau_0^{-1} = 2DS/2\pi$. Thus for Fe8 we get $\tau_0 \sim 10^{-11}$ sec and $\nu \sim 1$ Hz. Their theory assumes a single, isolated giant spin where the WKB-formalism is applied in a semi-classical limit. In a more recent theory, Prokof'ev and Stamp [Prokof'ev 98] estimate the relaxation time for a molecule in resonance ($\xi = 0$) as

$$\tau_N^{-1}(\xi = 0) \approx \frac{2\Delta_{10}^2}{\sqrt{\pi}\Gamma_2} \quad (2, \text{IV}.2.4)$$

where an environment of nuclear spins is taken into account and ξ is the energy bias due to a magnetic field acting on the molecule. Γ_2 is the energy scale of the nuclear T_2 processes, typically $T_2^{-1} \sim 10^{-7} - 10^{-5}$ K. The tunnel splitting of the lowest states $|S_z| = 10$ is estimated to be of the order of $\Delta_{10} \sim 10^{-8}$ K. Thus the relaxation time for Fe8 is in the range of $\tau_N \sim 0.1 - 10$ sec. The measured relaxation times are of the order of 10^4 seconds for Fe8 [Sangregorio 97] thus off by 4 orders of magnitude.

Chapitre IV Section 3

Autres Aimants Moléculaires

IV.3.1) Fe4 91

IV.3.2) Fe17+Fe19 95

IV.3.3) Mn11 99

In the following sections [IV.3.1], [IV.3.2], and [IV.3.3] we take a small diversion. During the course of my thesis work, I had the opportunity to measure many different molecular magnetic systems. We show here that Fe8 is quite extraordinary (as well as Mn12ac which is not a subject of my studies). Most compounds for various reasons do not show clear quantum effects. The following are three examples (Fe4, Fe17Fe19, and Mn11) of molecular magnets that we have measured.

IV.3.1) Fe4

The structure of a Fe4 molecule is presented in figure [IV.3.1.1]. A central Fe-ion is bond to three peripherial Fe-ions via μ-OMe double bridges. The sample has a small anisotropy barrier of 2.6K. Due to the small energy barrier the observed characteristic time is rather short even below 1K. In the accessible temperature range only thermal activation was observed roughly following the Arrhenius law. The ac-susceptibility as function of the temperature has two peaks. One peak indicates a superparamagnetic behavior the second peak is frequency independent over 3 decades. We can give no interpretation of the second peak.

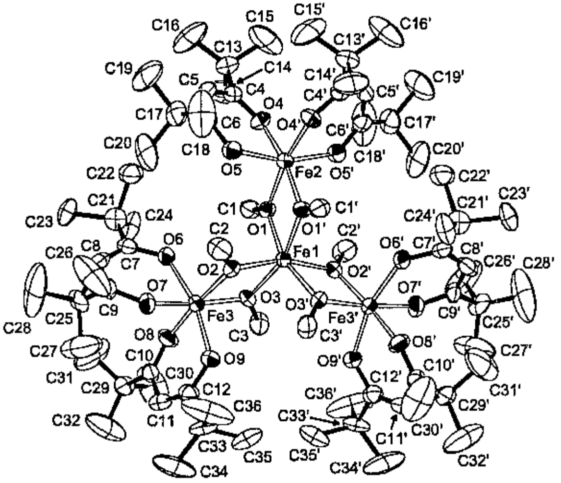
C15'
C16
C15
C16'
C13
C13'
C19
C14
C14'
C19'
C5
C4
C4'
C5'
O4
C17
C6
O4'
C6'
C17'
C20
C18
C18'
C20'
O5
Fe2
O5'
C22
C22'
C21
C1
C1'
C21'
C23'
C23
C24
C24'
C2
O1
O1'
C2'
C26
C8
O6
Fe1
O6'
C7'
C8'
C7
O2
O2'
C26'
C28'
O7
O7'
O3
O3'
C9
C9'
C28
C25
Fe3
Fe3'
C25'
O8
C3
C3'
O8'
C27
C10
O9
O9'
C27'
C31
C29
C30
C12
C12'
C10'
C31'
C36'
C29'
C32
C11
C36
C33'
C33
C35
C35'
C11'
C30'
C34
C34'
C32'

Figure IV.3.1.1: Schematic view of the Fe4-molecule. 3 Fe-ion are bond via μ-OMe double bridges to the central Fe-ion, Fe1.

The magnetization curve of Fe4 is shown in figure [IV.3.1.2]. At low temperatures the sample starts saturating at about 1 kOe. These measurements where done with the μSQUID-system and only relative measurements are possible. We therefore can not determine the total spin of the molecule from this measurement. In the inset we can see that the magnetization does not scale with H/T as would be for a paramagnet.

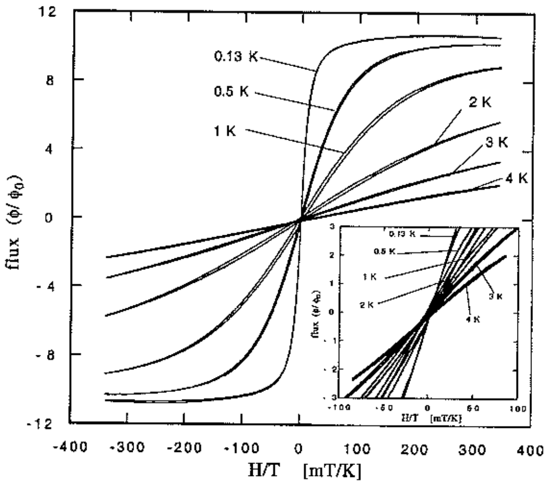

Figure IV.3.1.2: Magnetization curves for different temperatures of a Fe4 micrometer-sized sample. The inset show that the magnetization curve is not scaling with *H/T*.

AC-susceptibility measurements at a very low frequency shows that the Curie-Weiss law is obeyed even below 1K (down to about 0.3K) though the inverse susceptibility is slightly curved. Below a temperature of 0.3K the inverse susceptibility starts deviating from the Curie-Weiss law. From this small temperature range we can roughly estimate a Weiss temperature of $\Theta \leq 0.1$K. These measurements were made using the low field ac-SQUID-magnetometer.

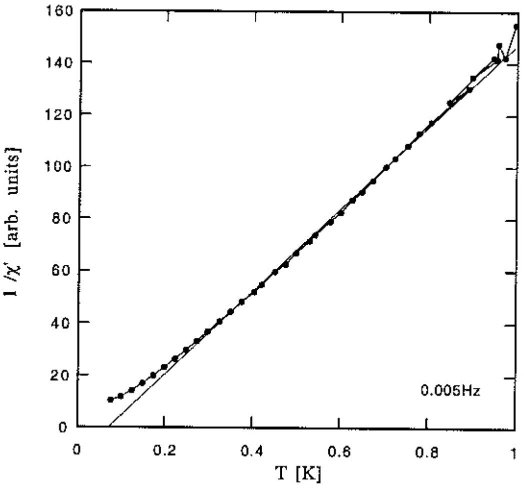

Figure IV.3.1.3: Temperature dependence of the ac-susceptibility for a frequency of 0.005 Hz. The inverse susceptibility is slightly curved but down to 0.3 K the Curie-Weiss law is obeyed. Below 0.3 K the deviation is growing.

The ac-susceptibility for different frequencies is presented in the figures [IV.3.1.4] and [IV.3.1.5]. It is remarkable that we observed two peaks in the real part and the imaginary part of the susceptibility. One of the peaks shifts with lower frequencies to lower temperatures as expected for a superparamagnet. The second peak in almost frequency independent over 3 decades, 0.5Hz – 500Hz. At a frequency of 0.005Hz we did not observe the second peak in our temperature range.

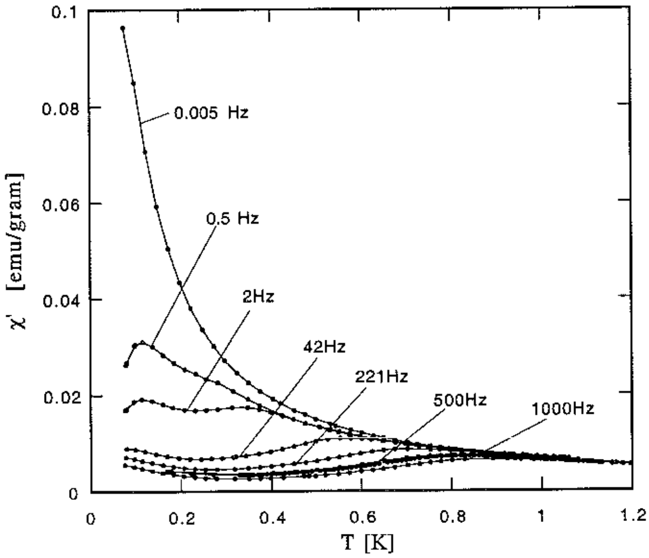

Figure IV.3.1.4: Real part of the ac-susceptibility of a powdered Fe4-sample. The susceptibility has two peaks, one that is shifting to lower temperatures for lower frequencies and one that doesn't shift at all.

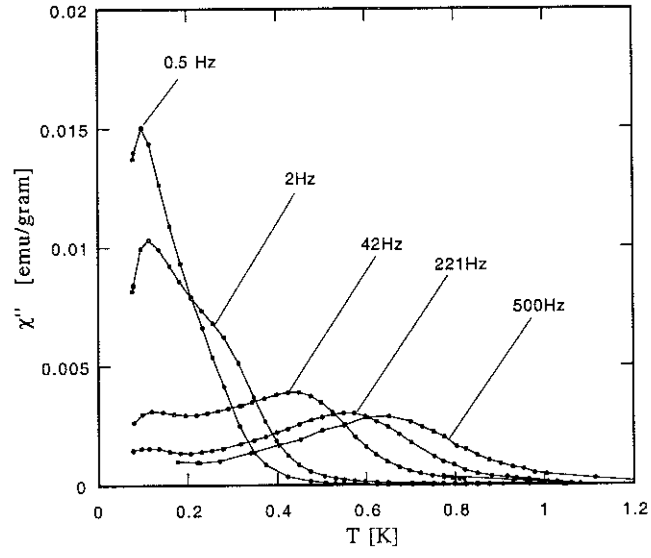

Figure IV.3.1.5: Imaginary part of the ac-susceptibility of a powdered Fe4-sample. The imaginary part has two peaks: One is frequency dependent and the other is almost frequency independent over 3 decades.

The temperature dependence of the first peak is shown in figure [IV.3.1.6]. It is difficult to determine the exact value of the peak because of interference with the second peak. The data obeys the Arrhenius law in good approximation. From the Arrhenius law we found a barrier height of $\Delta = 2.6$K and a prefactor of $\tau_0 = 6 \times 10^{-6}$ sec. The value of τ_0 is surprisingly large.

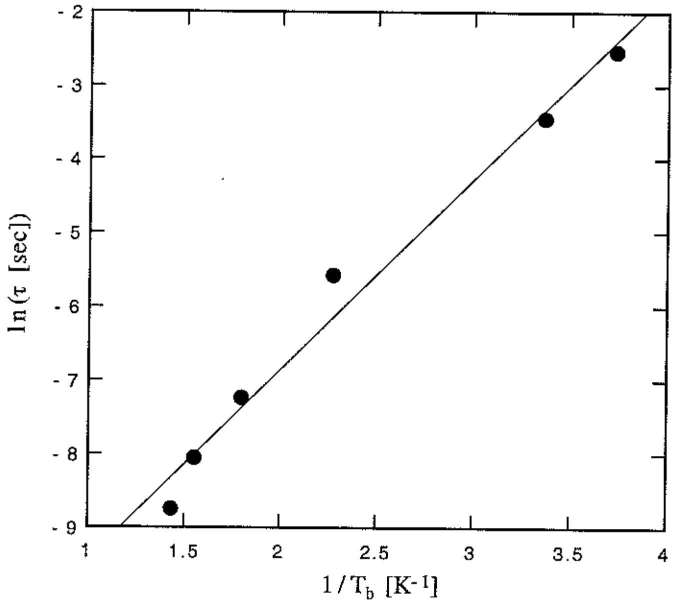

Figure IV.3.1.6: Temperature dependence of the first peak. The Arrhenius law is obeyed in good approximation. We found an energy barrier of $\Delta = 2.6$K and a prefactor of $\tau_0 = 6 \times 10^{-6}$ sec.

IV.3.2) Fe17Fe19

The system Fe17Fe19 consists of two different molecules of 17 and 19 iron-ions that are relativly close to each other. A plateau in the ac-susceptibility is observed which complicate the interpretation of the data.

The hysteresis curve is shown in figure [IV.3.2.1]. The measurement was done on a powdered sample at 100mK. The sample starts saturating at about 3 tesla with a saturation magnetization of 70μ_B per unit cell. The total spin per unit cell is thus $S = 35$. Since each unit cell contains two molecules of different size we cannot determined the net spin of the individual molecule Fe17 and Fe19 respectively. The sample shows hysteretic behavior with a coersive field of about 600 Oe and a remnant magnetization of about 18μ_B.

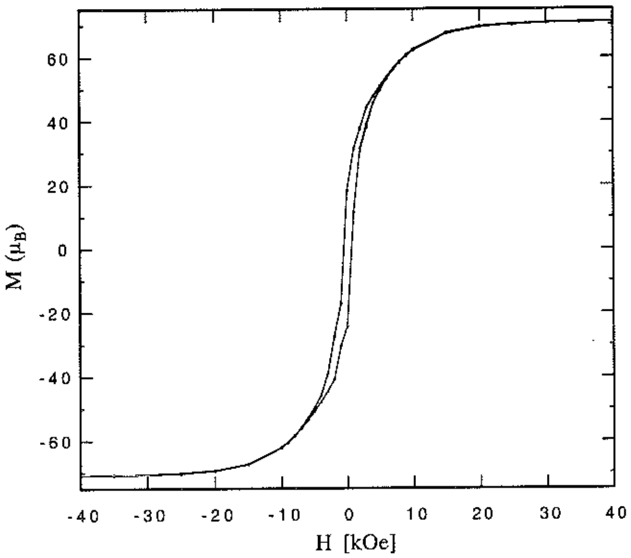

Figure IV.3.2.1: Hysteresis curve of a powdered Fe17Fe19-sample at 100mK.

The zero field cooled / field cooled (ZFC/FC) measurement are shown in figure [IV.3.2.2]. The measurement was done in a field of 25 Oe. It is noteworthy that the zero field cooled curve is peaked at 1K.

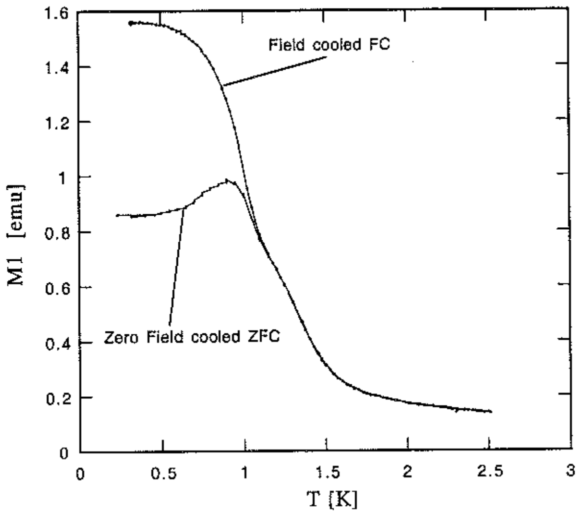

Figure IV.3.2.2: Zero field cooled / field cooled measurement on a powdered sample in a field of 25 Oe.

The inverse susceptibility in figure [IV.3.2.3] is curved and then constant below 1K. The positive intercept on the *T*-axis of the high temperature data indicates the presence of ferromagnetic interactions.

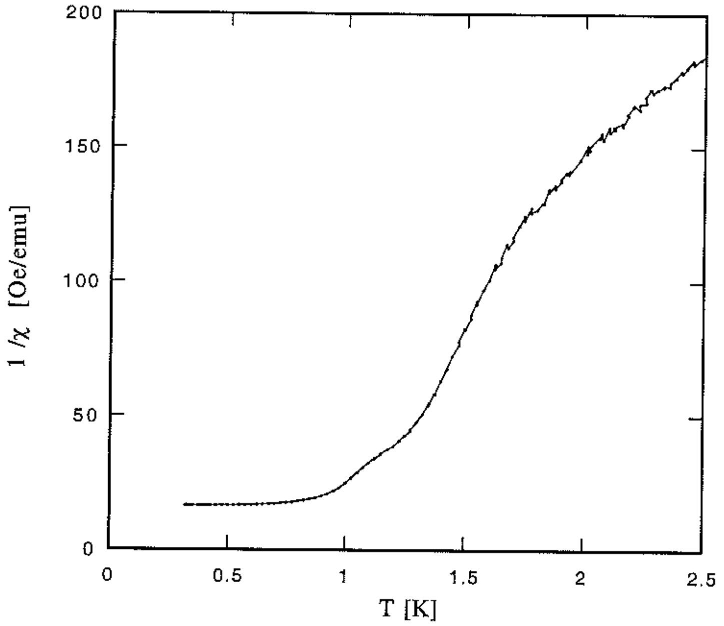

Figure IV.3.2.3: Inverse susceptibility of a powdered sample measured in a field of 25 Oe.

In figure [IV.3.2.4] ac-measurements are presented. The peak is smeared out to a plateau that might be interpreted as one peak fixed at a temperature of about 1.5K that superimpose with a peak that is shifting with decreasing frequencies to lower temperatures. However such a plateau in the susceptibility complicates further analyses.

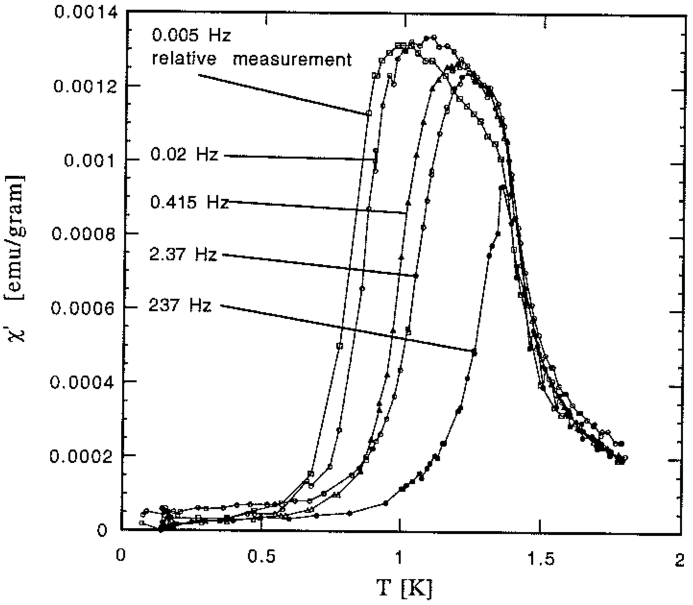

Figure IV.3.2.4: Real part of the ac-susceptibility of a powdered sample.

The maximum position of the susceptibility versus the frequency (the corresponding characteristic time) is shown in figure [IV.3.2.5]. These data are not well fit by a Arrhenius law but by the Fulcher-law

$$\tau(T) = \tau_0 \exp\left(\frac{\Delta}{T - T_0}\right). \qquad (1, \text{IV}.3.2)$$

From the fit we found a barrier height of $\Delta = 4.8\text{K}$, a prefactor of $\tau_0 = 6 \times 10^{-8}$ sec, and a $T_0 = 0.7\text{K}$.

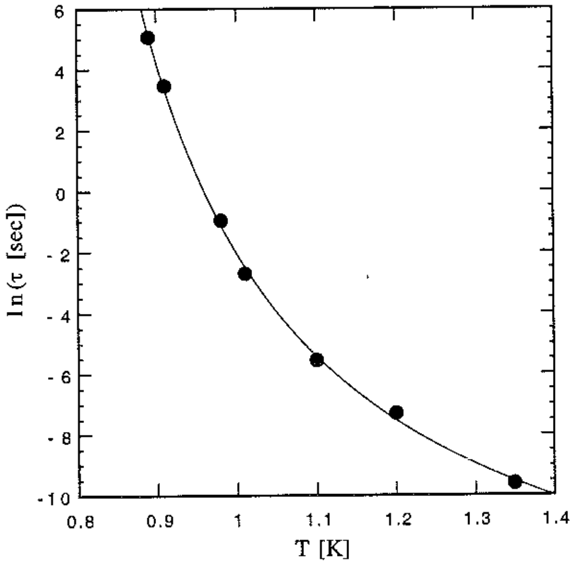

Figure IV.3.2.5: Temperature dependence of the characteristic time fit by a Fulcher law.

IV.3.3) Mn11

The Mn11 sample consist of a Mn10 molecule, with 10 manganese ions tightly coupled, and an additional uncoupled manganese ion.

The magnetization curve up to 1 tesla is plotted in figure [IV.3.3.1]. This measurement was make on a single crystal at a temperature of 80 mK. The crystal had to be stored in a solvent to prevent it from decomposition. The sample is almost saturated at 1 tesla with a saturation value of 30 μ_B. The uncoupled manganese ion ($S = 5/2$) contributes a magnetization of $5\mu_B$ thus leaving $25\mu_B$ for the Mn10 molecule, i.e. $S = 12.5$; see [Goldberg 95, Canschi 98]. Due to the solvent an error in the mass of some percent is possible thus a spin of $S = 12$ as reported in [Canschi 98] is possible. The hysteresis curve has a coersive field of about 250 Oe and a remnant magnetization of about 16 μ_B.

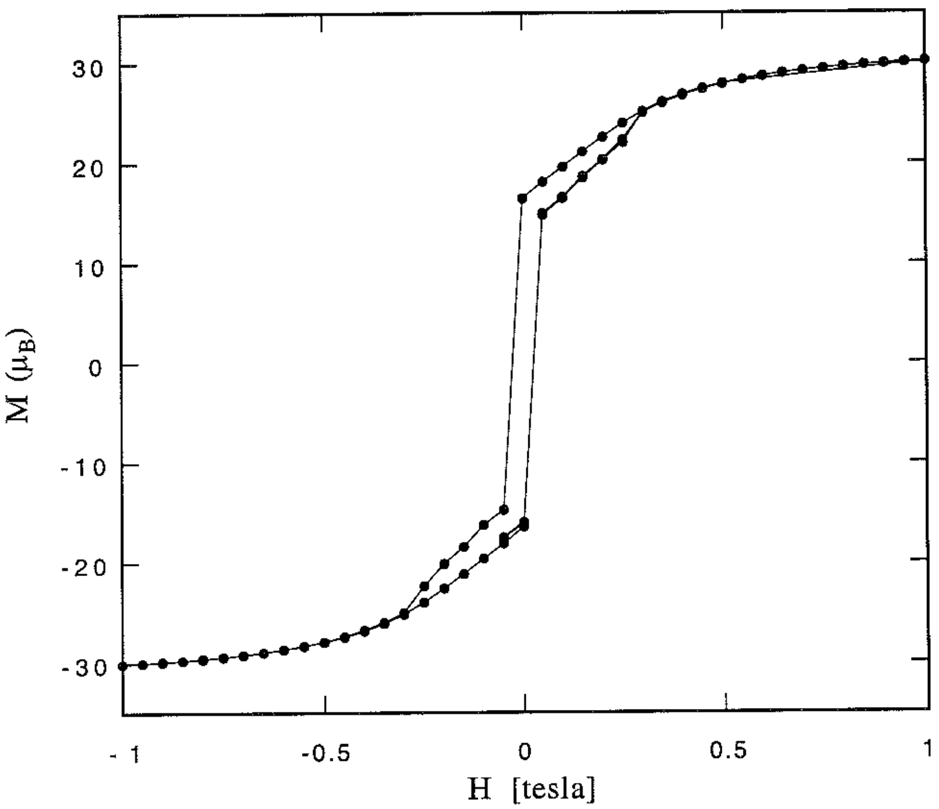

Figure IV.3.3.1: Hysteresis curve at 80mK of a powdered Mn11-sample.

The zero field cool / field cool (ZFC/FC) measurement are shown in figure [IV.3.3.2]. The measurements were done in a field of 30 Oe.

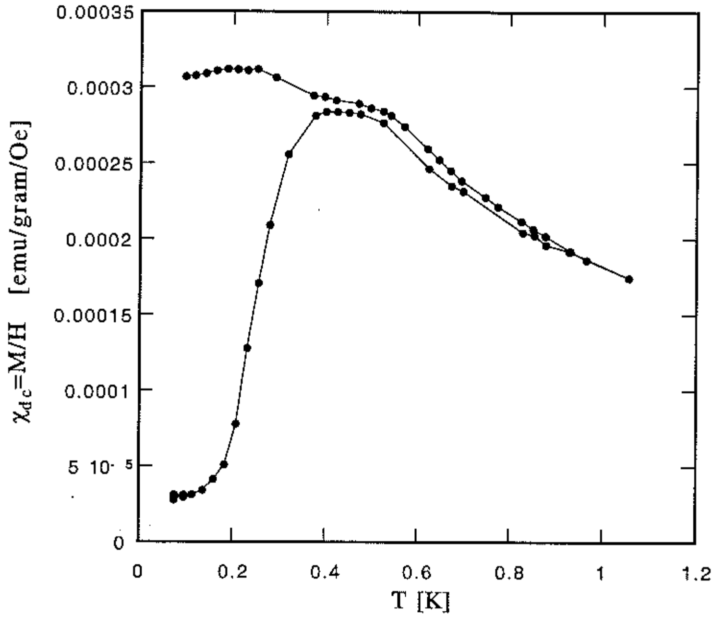

Figure IV.3.3.2: Zero field cooled / field cooled measurement on a powdered Mn11-sample in a field of 30 Oe.

An extrapolation of the linear part of the inverse susceptibility, i.e. the part that obeys the Curie-Weiss law, is pointing to a negative Weiss temperature, which implies the presence of antiferromagnetic interactions.

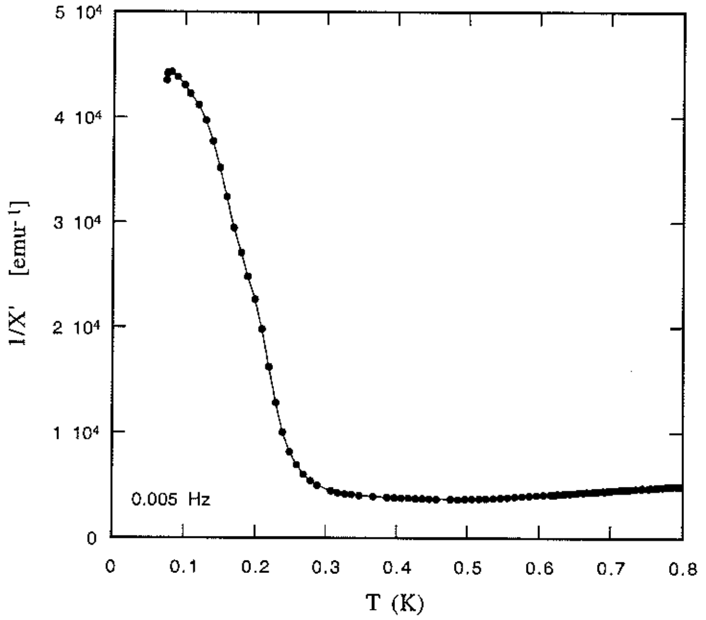

Figure IV.3.3.3: Inverse susceptibility at a very low frequency of 0.005Hz. The measured curve is typical for the presence of an antiferromagnetic interaction below 0.3K.

In the figures [IV.3.3.4] and [IV.3.3.5] measurements of the ac-susceptibility are shown for frequencies from 0.005Hz to 525Hz. As expected the blocking temperature decreasing for lower frequencies but surprisingly the height of the peak of the imaginary part also decrease, figure [IV.3.3.5]. It seems also that for the lower frequencies the peak of the imaginary part is not symmetric as for high frequencies.

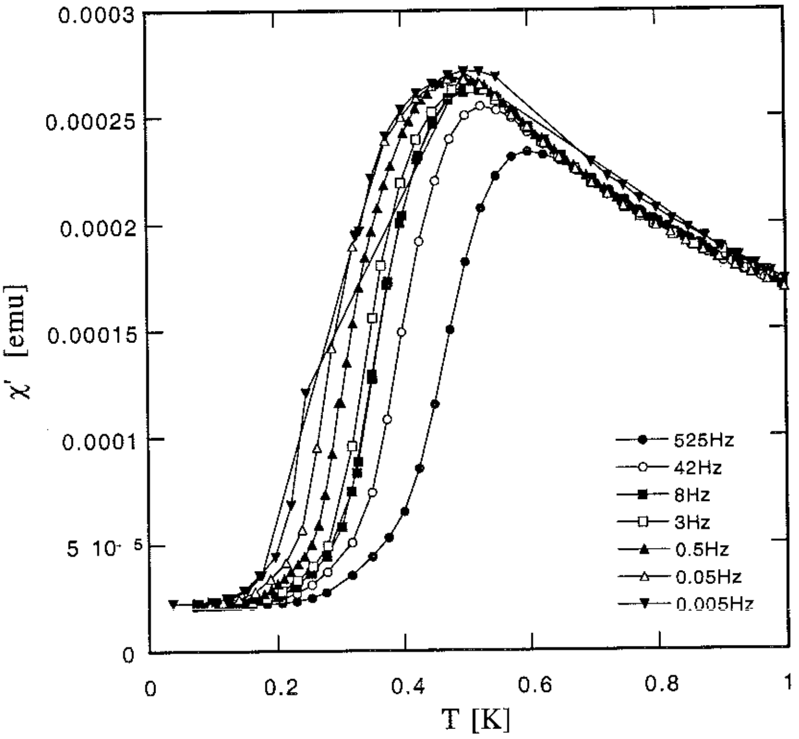

Figure IV.3.3.4: Real part of the ac-susceptibility on a powdered Mn11-sample.

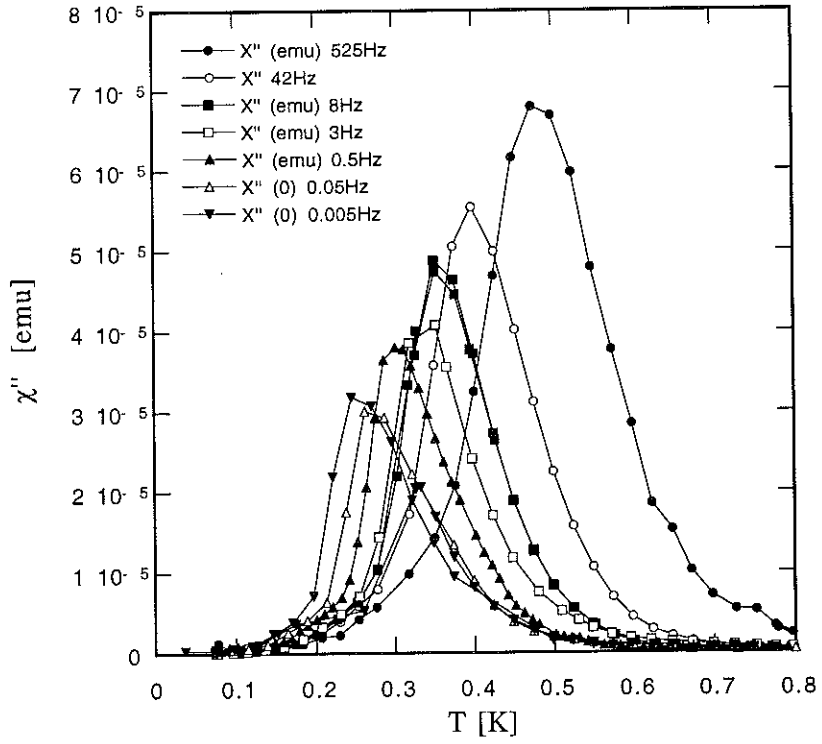

Figure IV.3.3.5: Imaginary part of the ac-susceptibility. Surprisingly the peaks decrease in size for lower frequencies.

The temperature dependence of the peak is shown in figure [IV.3.3.6]. The data are reasonably well fit by a Arrhenius law and we found a barrier height of $\Delta = 6.2$K and a prefactor of $\tau_0 \approx 8 \times 10^{-10}$ sec.

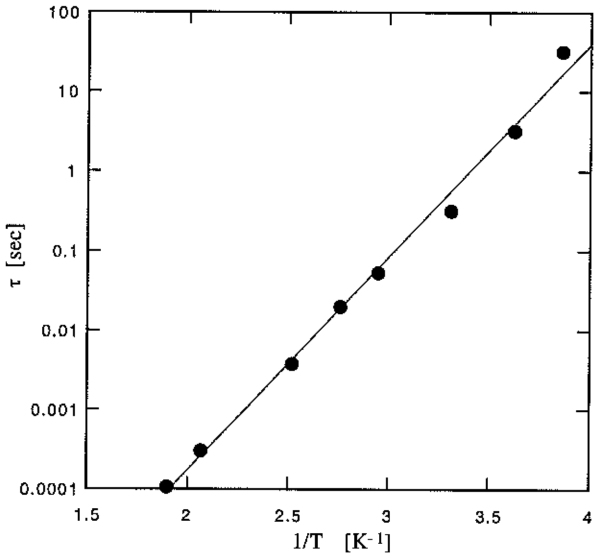

Figure IV.3.3.6: Temperature dependence of the imaginary part of the ac-susceptibility obeys reasonably well the Arrhenius law. The barrier height is $\Delta = 6.2$K and the prefactor $\tau_0 = 8 \times 10^{-10}$ sec.

Chapitre V

Le Champ Local

V.1) Distribution du Champ Local 103

V.1.1) Calculs Numériques 105

V.1.2) Distribution Initiale 113

V.1.3) Distribution des Spins Retournés Aléatoires 115

V.2) Résultats Expérimentaux 123

V.2.1) Relaxation en Racine Carrée 123

V.2.2) Modèle Phénoménologique 129

V.3) Effet de Corrélation 135

V.3.1) Effet de Corrélation 135

V.3.2) Simulations Monte-Carlo 137

V.3.3) Mesure de l'Effet des Corrélations 143

Afin de mieux comprendre l'influence de la distribution du champ local nous avons effectué des calculs numériques. Dans ce chapitre nous présentons principalement des calculs sur le système Fe8 et quelques-uns sur le système Mn12ac.

Dans la section V.1 nous présentons les détails techniques de ces calculs. Il est nécessaire de faire une distinction entre le champ dipolaire et le champ local. Le champ dipolaire est le champ magnétique créé par tous les spins dans un échantillon ; il varie de position à position et même à l'intérieur d'une molécule. Le champ local est directement lié au décalage d'énergie d'un spin géant. Ce champ est seulement défini par rapport à une molécule et les positions de ses spins ioniques.

Nous avons calculé la distribution du champ local pour un échantillon dont tous les spins sont parallèles, ce qui correspond à la distribution initiale d'une expérience de relaxation. Ensuite nous avons étudié la distribution dans un cas où les spins sont retournés de manière aléatoire. Nous observons une forte influence du réseau triclinique sur la distribution du champ local.

Dans la section V.2 nous présentons des résultats expérimentaux qui montrent l'influence du champ local sur la relaxation. Le début d'une courbe de relaxation suit une loi en racine carrée du temps. Ce comportement est prédit par la théorie de Prokov'ef et Stamp prenant en compte l'interaction dipolaire entre les molécules et les effets hyperfins à l'intérieur d'une molécule. Ensuite nous présentons un modèle phénoménologique simple qui décrit bien la courbe de relaxation sur 4 décades en temps. Dans ce modèle nous supposons que la résonance quantique d'une molécule est très étroite, de 4 à 5 ordres de grandeur plus petite que la largeur de la distribution du champ local. En conséquence, seule une petite fraction des spins est en résonance. La plupart des molécules sont hors résonance et ne peuvent pas participer à la relaxation. Nous supposons que la distribution du champ local évolue pendant la relaxation. Le nombre de molécules en résonance diminue au cours du temps, avec pour effet que la relaxation se ralentit. Pour cette raison, la courbe de relaxation ressemble à une fonction exponentielle étirée. Une autre conséquence de cet effet est que nous n'observons pas le taux d'effet tunnel quantique τ_{tunnel} dans les expériences mais un temps de relaxation effectif $\tau_{effectif}$. Le rapport entre le taux effectif de relaxation et le taux d'effet tunnel quantique $\tau_{effectif} / \tau_{tunnel} \sim \sigma / \Delta_{tunnel}$ a le même ordre de grandeur que le rapport entre la largeur de la distribution du champ local σ et la résonance quantique d'une seule molécule Δ_{tunnel} : $\sigma / \Delta_{tunnel} \sim 10^4 - 10^5$. De cette façon nous pouvons également comprendre pourquoi nous observons dans les expériences une résonance avec une largeur de 100 Oe et plus.

Dans la dernière section, V.3, nous discutons l'apparition de corrélations inhabituelles dans un système d'effet tunnel résonant. Autour de la résonance moléculaire, ces corrélations changent la distribution du champ local. Dans cette région elles diminuent l'amplitude de la distribution en comparaison avec une distribution aléatoire et encore moins de molécules sont en résonance que dans un modèle statistique. Un spin qui tourne change le champ local dans son environnement proche. Dans une certaine région le changement du champ local est plus grand que la résonance moléculaire et les molécules dans cette région sont bloquées. Un autre spin qui tourne dans la proximité d'une telle région va bloquer également des spins voisins, mais dans une région en commun, si les champs s'opposent, quelques molécules vont peut-être se débloquer. Donc le champ local ne détermine pas l'orientation d'un spin, il permet ou supprime le retournement d'un spin par effet tunnel quantique. Pour une simulation de la relaxation dans le régime quantique nous utilisons une méthode de Monte-Carlo. A la fin du chapitre, nous présentons une expérience qui montre clairement les effets des corrélations sur le champ local. Nous mesurons les temps de relaxation dans la première résonance d'un échantillon demi-démagnétisé pour des champs différents. Pour ces mesures nous préparons l'échantillon de deux manières différentes. Dans un cas l'échantillon est démagnétisé par activation thermique et dans l'autre cas l'échantillon est démagnétisé par effet tunnel quantique. Nous observons que la variation du temps de relaxation en fonction du champ dans la première résonance, est très différente dans les deux cas. D'après la théorie, l'inverse du temps de relaxation correspond à la distribution du champ local. Cette mesure prouve que la distribution du champ local est fortement influencée par l'effet tunnel résonant.

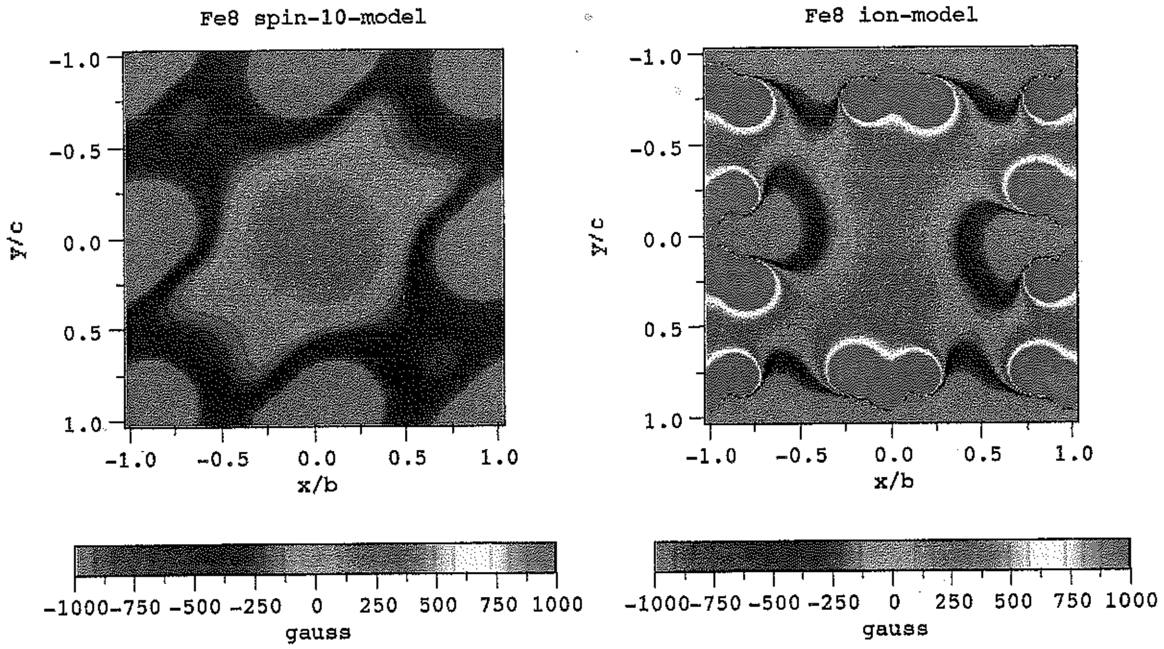

a) Fe8 spin-10-model
$B_{\parallel}$ cut along the *bc*-plane

b) Fe8 ion-model
$B_{\parallel}$ cut along the *bc*-plane

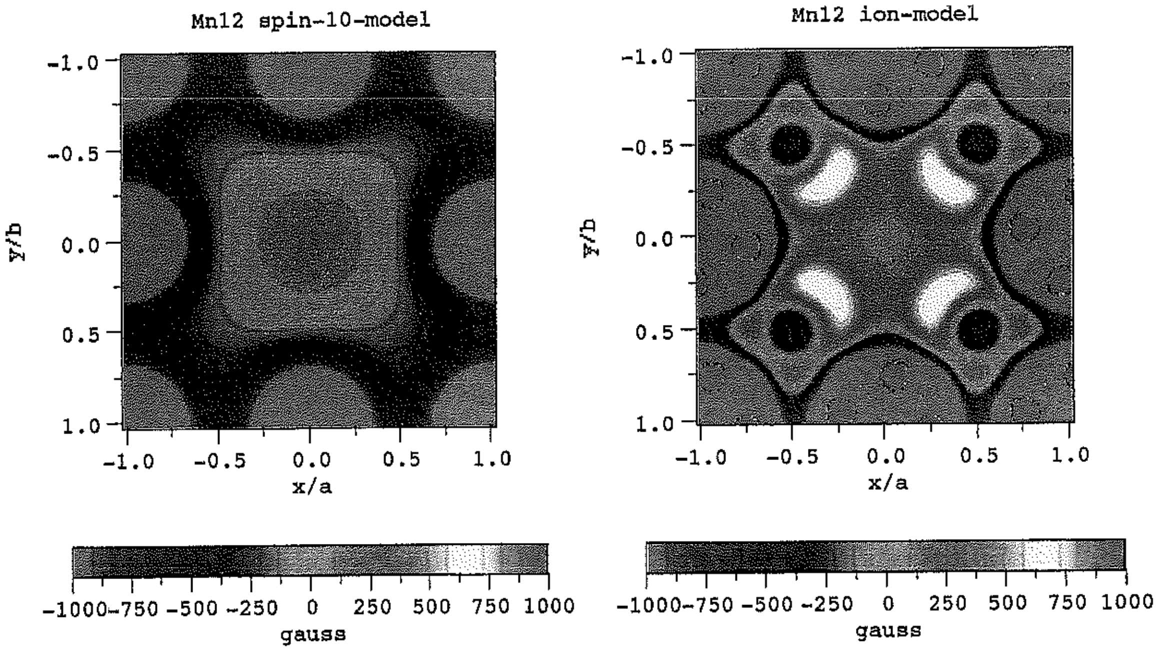

c) Mn12ac spin-10-model
$B_{\parallel}$ cut along the *ab*-plane

d) Mn12ac ion-model
$B_{\parallel}$ cut along the *ab*-plane

Figure V.1.1.2: Density plots of the parallel component $B_{\parallel}$ of the dipole field within one unit cell. The plane is cut perpendicular to the easy axis. The calculation was done for the central unit cell of a spherical sample of 200Å diameter. The central molecule/spin itself has been omitted.

V.1.1)Numerical Calculations

Dipole field

We calculated the dipole field that is created by the molecular spins. We assume that the spins are point dipoles. The well-known result from magneto-static gives a dipole field for a spin:

$$\vec{B}(\vec{r}) = \frac{3\vec{r}(\vec{r}\cdot\vec{m})}{|\vec{r}|^5} - \frac{\vec{m}}{|\vec{r}|^3} \quad (1, \text{V.1.1})$$

where $\vec{r}$ is the spatial vector pointing at the spin and $\vec{m} = g\mu_B s_z \vec{u}$ is the magnetic moment of the spin. The z-component of the spin is s_z and pointing along the unit vector $\vec{u}$. A molecule that consist of several ion spins creates a dipole field of

$$\vec{B}(\vec{r}) = \sum_{i=1}^{N} \frac{3(\vec{r}-\vec{r}_i)((\vec{r}-\vec{r}_i)\cdot\vec{m}_i)}{|\vec{r}-\vec{r}_i|^5} - \frac{\vec{m}_i}{|\vec{r}-\vec{r}_i|^3} \quad (2, \text{V.1.1})$$

where N is the number of ion spins in the molecule and $\vec{m}_i = g\mu_B s_z^{(i)}\vec{u}$ are the individual magnetic moments of the ion spins. We neglect any possible canting within the molecule. The spatial vectors $\vec{r}_i$ are the relative positions of the ion spins to the center of the molecule at $\vec{r}$. The relative positions of the ions of Fe8 for example are given in the table [III.1].

Our main interest is the dipole field distribution in the quantum regime at low temperatures. In this case the molecule ($S = 10$) is in its ground state $|S_z| = 10$. (We will write the net molecular spin as capital S and the ion spins as minuscule s). The ion spin configuration for the ground state of Fe8 is shown in figure [V.1.1.1]. For the up state of the molecule $S_z = +10$ two ion spins are pointing down ($s_z = -5/2$) and six ions spins are pointing up ($s_z = +5/2$). For the down state $S_z = -10$ the ions spins are reverse, i.e. six ion spins are pointing down and two are pointing up.

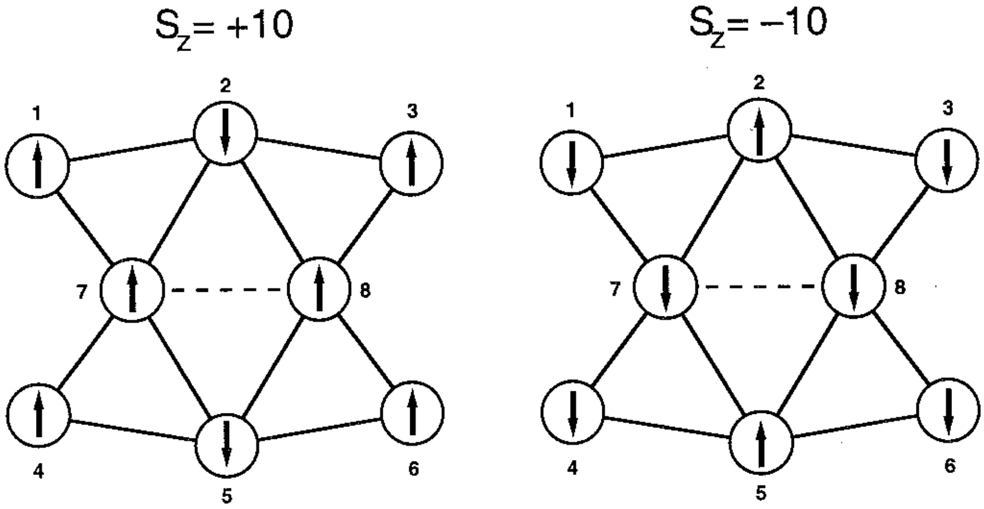

Figure 1: V.1.1.1: Schematic figure of the up state, $S_z = +10$, and the down state, $S_z = -10$, of a Fe8-molecule.

To calculate the dipole field at the position of a particular molecule we have to sum up the contributions of all the molecules inside the sample, except the molecule under consideration

$$\vec{B}(\vec{r}) = \sum_{\substack{k,l,m \\ \text{except one}}} \vec{B}(\vec{r}_{k,l,m} - \vec{r}) \qquad (3, \text{V.1.1})$$

where $\vec{r}_{k,l,m}$ points at a molecule and k, l, m are the indices of the molecule on the lattice, i.e. $\vec{r}_{k,l,m} = k\vec{a} + l\vec{b} + m\vec{c}$. The lattice vectors $\vec{a}$, $\vec{b}$, and $\vec{c}$ for the triclinic lattice of Fe8 can be found in chapter [III]. For Mn12ac the procedure is of course the same but one has to take into account that the lattice of Mn12ac is body-centered and has two molecules per unit cell.

We made such calculations for Fe8 and Mn12ac for the case that molecular spins are pointing up and the sample has a spherical shape, see figure [V.1.1.2]. In these images only the parallel component

$$B_{\|}(\vec{r}) = \vec{B}(\vec{r}) \cdot \vec{u} \qquad (4, \text{V.1.1})$$

along the easy axis is shown in a density plot. The easy axis of Fe8 is almost parallel to the $\vec{a}$-axis thus is this case the unit vector is given by $\vec{u} = \vec{a}/|\vec{a}|$. The Fe8-images display a cut through the *bc*-plane of the unit cell for the central molecule of the sphere. The easy-axis of Mn12ac is along the crystallographic $\vec{c}$-axis thus in this case $\vec{u} = \vec{c}/|\vec{c}|$ and the cut is through the *ab*-plane. In all images the central molecule itself has been omitted and the next neighbors in the images are placed at the corners, and at the half of each sideline.

For both molecules we have calculated the dipole field for the case that we take all 8 iron-ions or 12 manganese-ions for Fe8 and Mn12ac, respectively, into account corresponding to equation (2, V.1.1). We will call this the **ion-model**. The other two images represent calculations where we have neglected in inner structure of the molecule and replace the molecules by one single spin of $S = 10$ as in a giant spin model. This calculation uses the equation (1, V.1.1) with $S_z = +10$, we call this the **spin-10-model.**

The difference between the two models is remarkable. The dipole field is not only different at the corners of the image close to neighboring molecules but also in the center of the image. In the case of the spin-10-model the spin of the omitted central molecule is simply at the center of the images and will not notice the dipole field distribution. This will change for the ion-model. The molecules have a diameter of about 5Å that corresponds to 0.2 in the displayed units of the images. Even over this range the dipole field distribution is varies and therefore each ion in the molecule will experience a different field value. Thus at first view it is no longer evident what value the Zeemann energy shift of the molecular giant spin state has, e.g. some ion-spins are pointing down and have a negative energy shift while other ion-spins that are pointing up and will result in a positive energy shift.

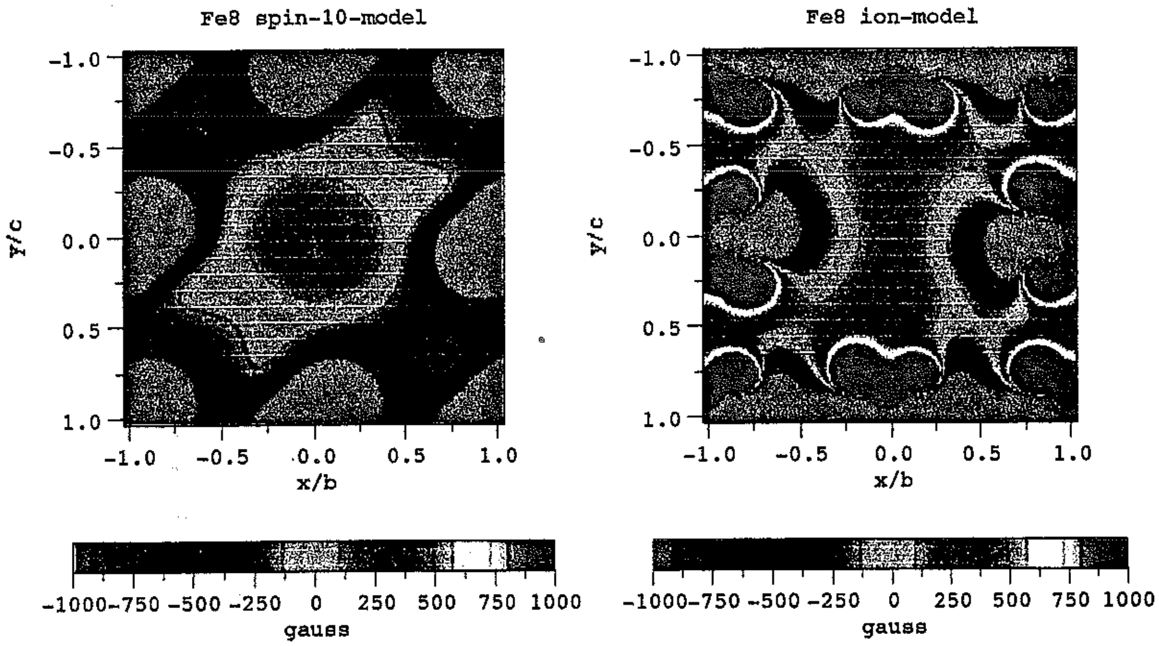

a) Fe8 spin-10-model
$B_{\parallel}$ cut along the *bc*-plane

b) Fe8 ion-model
$B_{\parallel}$ cut along the *bc*-plane

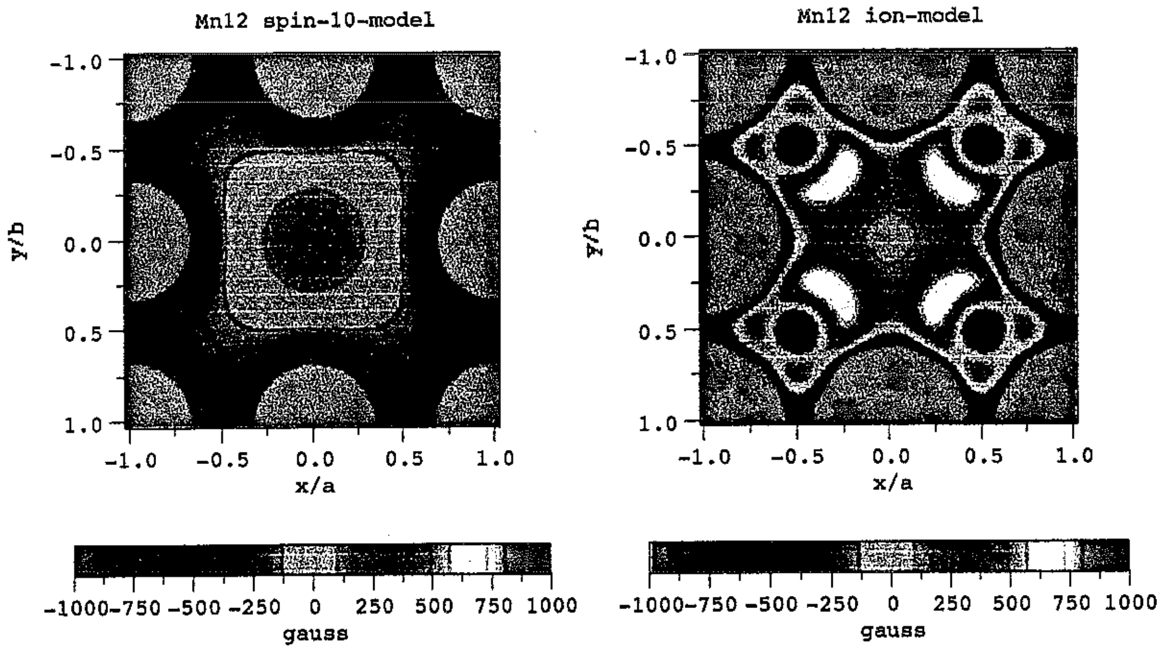

c) Mn12ac spin-10-model
$B_{\parallel}$ cut along the *ab*-plane

d) Mn12ac ion-model
$B_{\parallel}$ cut along the *ab*-plane

Figure V.1.1.2: Density plots of the parallel component $B_{\parallel}$ of the dipole field within one unit cell. The plane is cut perpendicular to the easy axis. The calculation was done for the central unit cell of a spherical sample of 200Å diameter. The central molecule/spin itself has been omitted.

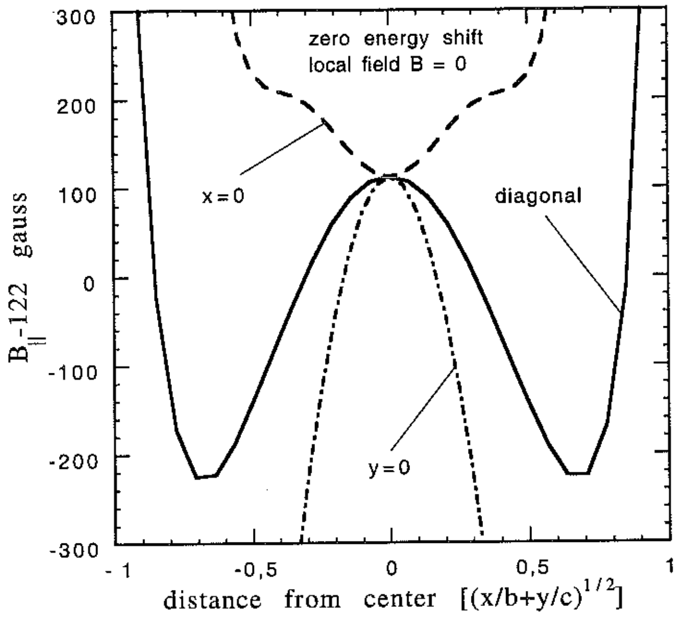

Figure V.1.1.3: Three cuts through the parrallel dipole field $B_{\|}$ distribution within a Fe8-molecule for zero local field in the ion-model. These curves show the variation of the dipole field along three lines in the *bc*-plane in the unit cell as shown in figure V.1.1.2b, compare figure table [V.1.1.2].

Local field

For a single giant spin in the state S_z the energy shift due to a magnetic field H is given by the Zeemann term

$$\varepsilon = g\mu_B S_z H. \quad (5, \text{V.1.1})$$

For a molecule with several ion-spins $s_z^{(i)}$ tightly locked up the total energy shift of the molecule is given by the sum

$$\varepsilon = \sum_{i=1}^{N} g\mu_B s_z^{(i)} H(\vec{r}_i). \quad (6, \text{V.1.1})$$

Now we have to take into account that the magnetic field $H(\vec{r}_i)$ is different at each ion position $\vec{r}_i$.

Because we want to discuss the energy shift of the giant spin state in terms of a magnetic field we introduce the following definitions:

- The **parallel dipole field** $B_{\|}(\vec{r})$ is defined as in equation (4, V.1.1), that is the parallel component of the summed dipole field of all giant spin or ion-spins within the sample, except the giant spin or ion-spins of the molecule under consideration.

- The **local field** B is defined as the magnetic field that must act on a giant spin S to result in the same energy shift due to the Zeemann term as defined in equation (5, V.1.1) or (6, V.1.1), respectively. Thus the local field is only defined in connection with the molecule, it is the field acting *on* a molecule. For the spin-10-model the local field is simply the parallel dipole field

$$B = B_{\|}(\vec{r}_{giant\ spin}) \qquad (6, \text{V.1.1})$$

at the giant spin position $\vec{r}_{giant\ spin}$. For the ion-model the local field is defined as

$$B = \frac{\sum_{i=1}^{N} s_z^{(i)} B_\parallel(\vec{r}_i)}{S_z}. \qquad (7, \text{V}.1.1)$$

Again $\vec{r}_i$ are the positions of the ion-spins that are in a state $s_z^{(i)}$ and S_z is the state of the net spin of the molecule, i.e. $S_z = \sum_{i=1}^{N} s_z^{(i)}$.

According to these definitions, a local field value corresponds to the same energy shift regardless of which model, ion or spin-10, we have employed. In the case of a giant spin of $S = 10$ a local field of 744.4 gauss corresponds to an energy shift of 1K.

For Fe8 and Mn12ac we have calculated the parallel dipole field for the spin-10-model and for the ion-model. The values are shown in table [V.1.1.1]. It is surprising by how much the dipole field values vary within the molecule in the ion-model. In addition, the difference in the local field calculation between the two models is a factor of 3. For Fe8 the local field and consequently the energy shift for the ion-model is about three times smaller than for the spin-10-model, which accidentally for Mn12ac is vice versa.

Note that if we subtract of the local field values, the molecule has no energy shift. For the spin-10-model the field will in this case be exactly zero, while for the ion-model non of the ions will see zero field (!) but fields that are varying by 100 gauss and more, see table [V.1.1.2].

	Fe8				**Mn12ac**			
	spin-10-model		ion-model		spin-10-model		ion-model	
spin n°	$B_\parallel$ [gauss]	spin S_z	$B_\parallel$ [gauss]	spin s_z	$B_\parallel$ [gauss]	spin S_z	$B_\parallel$ [gauss]	spin s_z
1	381	10	224	+5/2	107	10	49	-3/2
2	—	—	224	+5/2	—	—	49	-3/2
3	—	—	89	+5/2	—	—	49	-3/2
4	—	—	185	-5/2	—	—	49	-3/2
5	—	—	116	+5/2	—	—	153	+2
6	—	—	116	+5/2	—	—	263	+2
7	—	—	187	-5/2	—	—	153	+2
8	—	—	91	+5/2	—	—	263	+2
9	—	—	—	—	—	—	153	+2
10	—	—	—	—	—	—	263	+2
11	—	—	—	—	—	—	153	+2
12	—	—	—	—	—	—	263	+2
B	**381**	**+10**	**122**	**+10**	**107**	**+10**	**303**	**+10**

Table V.1.1.1: Dipole field values $B_\parallel$ and local field B of Fe8 and Mn12ac for the spin-10-model and the ion-model. These calculations were made for a spherical sample of 200Å diameter with all spins up, i.e. all giant spins are in the state $S_z = +10$. The sphere contain 2237 molecules and 2148 molecules for Mn12ac and Fe8, respectively.

spin n°	Fe8 $B_\parallel$ [gauss]	 spin S_z	Mn12ac $B_\parallel$ [gauss]	 Spin S_z
1	+102	+5/2	–254	-3/2
2	+102	+5/2	–254	-3/2
3	–36	+5/2	–254	-3/2
4	+63	-5/2	–254	-3/2
5	–6	+5/2	–150	+2
6	–6	+5/2	–40	+2
7	+65	-5/2	–150	+2
8	–31	+5/2	–40	+2
9	—	—	–150	+2
10	—	—	–40	+2
11	—	—	–150	+2
12	—	—	–40	+2
B	**0**	**+10**	**0**	**+10**

Table V.1.1.2: The parallel dipole field $B_\parallel$ at the ion positions for zero energy shift ($B = 0$) in the ion-model. Even though the local field is zero the parallel dipole field values $B_\parallel$ at the ion positions are always different from zero and varies from ion to ion.

V.1.2) Initial field distribution

In this section we will present the calculated local field distribution in the Fe8 system with all spins parallel, i.e. pointing in the same direction along the easy axis (the *a*-axis). This is the initial configuration for a relaxation experiment after the sample has been saturated in a strong magnetic field. We will discuss the effect of the sample geometry and differences that are due to the model we have used, i.e. if we are replacing every molecule by one single spin (spin–10–model) or if we take the inner structure of the molecule into account (ion–model).

In the first figure [V.1.2.1] we compare the local field distribution for three different sample shapes calculated using the ion-model. One sample has a spherical shape of 200Å diameter, one sample is a flat cubes of 15 x 31 x 51 sites (corresponding to an aspect ratio of 1.0 x 2.8 x 4.9), and finally a long cube of 49 x 17 x 25 sites (corresponding to an aspect ratio of 1.0 x 0.46 x 0.61).

The local field distribution of the spherical sample is a very narrow peak centered at 122 gauss. The value of the center is of course the same as in the table [V.1.1.1]. The small distribution width is due to finite size effects of the numerical calculation. In particular, the field values at the surface can vary significantly from fields in the center, though we expect ideally a uniform field due to the homogeneous demagnetization field.

The local field distribution for the long sample is shifted to a positive field at about 360 gauss and strongly skewed to the left side. The reason for the shift to a more positive field is that more neighboring spins are stacked along the *a*–direction and contribute to a more positive field.

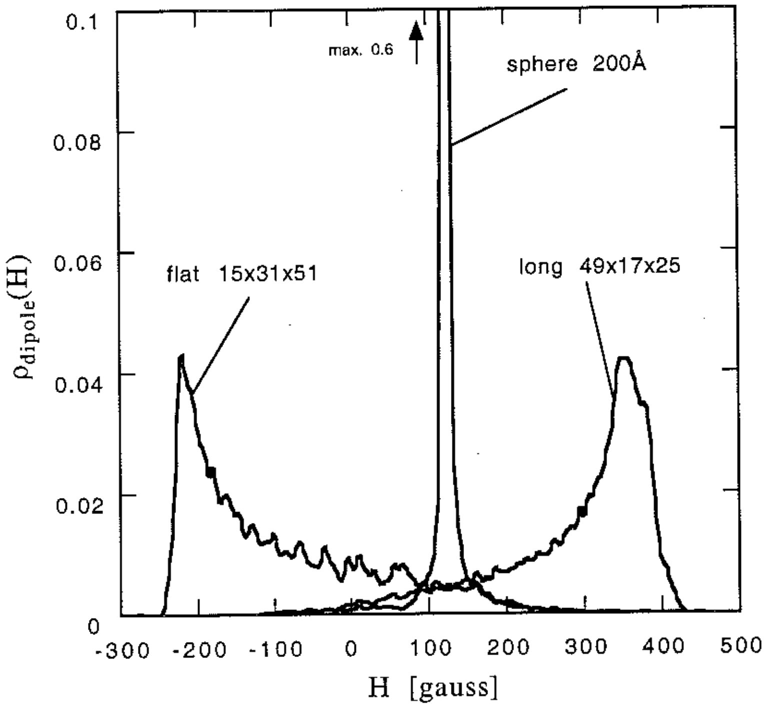

Figure V.1.2.1: The local field distribution of Fe8 with all spins up for three different sample shapes using the ion-model.

The local field distribution for the flat sample is shifted in the opposite direction, i.e. to a negative field value of –220 gauss and is strongly skewed to the right hand side. The reason for the shift in this case is that neighboring spins in the *b*– or *c*–direction contribute an antiparallel field thus a negative field. In the flat sample the spins in the *b*– or *c*–direction are more numerous and dominate the local field distribution.

An interesting technical aspect is how the local field distribution depends on the model we used for the calculation (ion-model/spin-10-model). We therefore calculated the initial local field distribution for the same sample shapes in the ion-model and the spin-10-model. In addition we did the same calculation for a simple cubic (sc) lattice for spins $S = 10$. For this "reference" calculation we assumed that the unit cell has the measures 13Å x 13Å x 13Å.

For a spherical sample the local field is uniform. In the numerical calculation the local field distribution is extremely narrow and the observed width is due to the finite size effects. We made the calculation on spheres of diameter 200Å and 400Å. The difference in the local field between the two spheres is smaller than 1 gauss. The local field in a sc-sphere is zero, as expected. Using the ion-model the local field has a value of +122 gauss and in the spin-10-model a value of +381 gauss.

The local field distributions for a cubic sample are presented in figure [V.1.2.2]. These calculations were made on a cube of 55 x 19 x 27 sites (= 28215 sites). Using the Fe8 triclinic lattice this corresponds to a sample of 577.5Å x 266.95Å x 405Å. The aspect ratio of this sample is 1.0 x 0.46 x 0.70 and about the same of a Fe8 sample we have used in the experiments (long1). We can see in the figure that the only difference between the models is a shift of about 220 gauss. Beside this shift the local field distributions for both model resemble each other. The local field distribution for the sc-cube has also the same shape but is even more shifted. The shift between the Fe8 spin-10-model and the sc spin-10-model is about 350 gauss. This is of the same order as the difference between the Fe8-sphere in the spin-10-model and the sc-sphere. An additional field shift for the sc-cube comes from the slightly different aspect ratio compared to the Fe8-cube. Using the same number of sites in the cube the sc-cube has the measures 715Å x 247Å x 351Å thus an aspect ration of 1.0 x 0.35 x 0.57. The difference in the aspect ratio results in a change in the demagnetization field and gives a further shift in the local field.

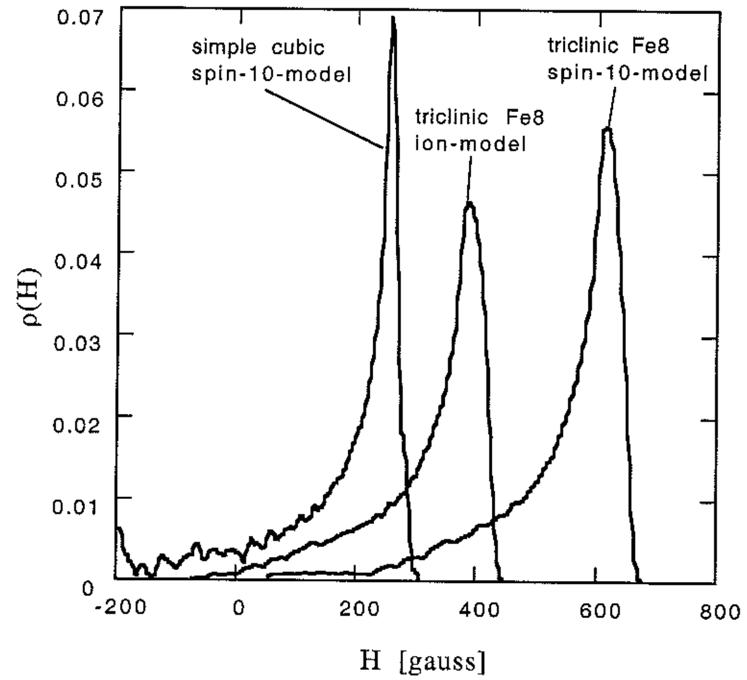

Figure V.1.2.2: Comparison of the initial field distribution of a cube with 19x27x55 sites. The local field has been calculated using 3 different models.

V.1.3) Random spin orientation

So far we have only calculated the local field distribution for a configuration where all spins are parallel and pointing in the same direction. In the following we want to discuss how the local field distribution changes if some spins are turned. In this section we calculate the local field distribution for spherical samples where the spins are turned by random. This corresponds to an Ising-system of spins $S = 10$ with a magnetization different from the saturation value. If the fraction n_{-} of spins are turned, the magnetization of the sample is $M = 1-2n_{-}$. We will see that the triclinic lattice of Fe8 has a strong influence on the local field distribution and result in a rather complicated shape. First some calculations of the spin-10-model are presented because the lattice effects are very pronounced. Afterwards the same calculations are presented for the ion-model of Fe8 where the same effects occur but less pronounced.

First we will discuss the spin-10-model. The initial distribution for the sphere was shown in the previous chapter, the local field distribution of a sphere is extremely narrow and centered at 381 gauss. The local field distribution for 10% of the spins turned by random is shown in figure [V.1.3.1]. This corresponds to a system with a magnetization of $M = 0.8$. In this figure we see three peaks. The largest one is centered at about +400 gauss (peak 3) the next is centered at –200 gauss (peak 2), and the third is very small and centered at about –800 gauss (peak 1). The reason for the occurrence of three distinct peaks comes from the triclinic lattice of Fe8. The nearest neighbors in the easy-axis direction (*a*-axis) are closer to the centeral molecule (10.5Å) than the neighbors in the *b*- or *c*-direction (14.05Å and 15.0Å, respectively) and thus have a considerably stronger field contribution to the local field at a molecule. The difference in the field strength ($\sim 1/r^3$) is of the order of a factor 3 – 4. The 3 peaks therefore correspond to 3 different spin configurations of the nearest neighbors in the *a*-direction. All molecules in the peak 3 have two neighbors in the *a*-direction that are both parallel to *M*. The molecules in peak 2 have neighbors where one is parallel and one is antiparallel, and finally the molecules in peak 1 have neighbors that are both down. For the following discussion we define the configurations with respect to the next neighbors in the *a*-direction:

- **configuration 1**: both neighbors in *a*-direction are antiparallel
- **configuration 2**: one neighbor is parallel and one neighbor is antiparallel
- **configuration 3**: both neighbors in *a*-direction are parallel

In the figures [V.1.3.2] and [V.1.3.3] the local field distribution are presented for the case that 25% of the spins are turned by random and 50% are turned, respectively.

From these three figures we can conclude that each peak shifts to larger local field values as more and more spins are turned, and the number of molecule in the peaks changes. The number of molecules in the peaks is proportional to the area of the peaks. Peak 3, which is the closest to the initial distribution, decreases while the other peaks increase. If half of the spins are turned peak 1 and 3 are of the same size and half as large as the central peak 2. For this situation, half of the spins have nearest neighbors (along *a*-axis) that are pointing up and down (configuration 2) while one quarter have only up nearest neighbors (configuration 1) and the last quarter have only down neighbors (configuration 3).

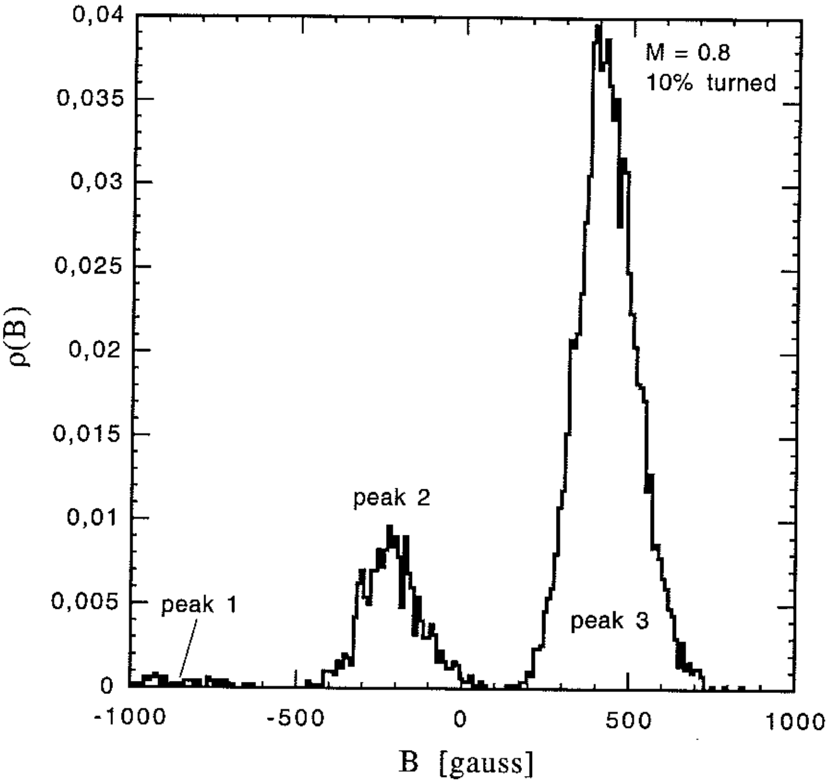

Figure V.1.3.1: Local field distribution of a spherical Fe8-sample in a spin-10-model with 10% of the spins turned randomly. The 3 peaks correspond to 3 different configurations of the nearest neighbors along the *a*-axis.

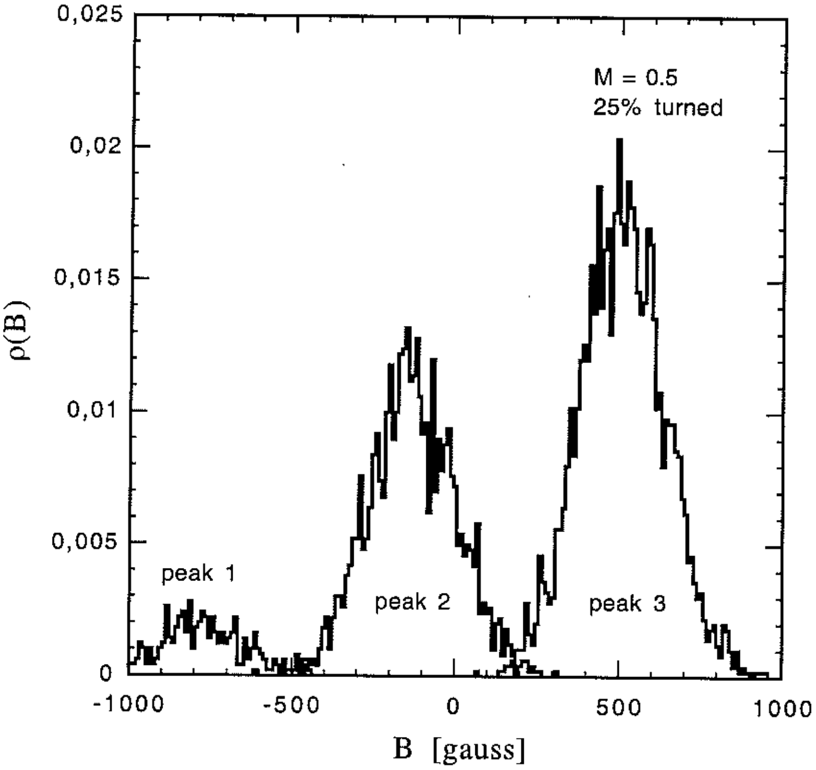

Figure V.1.3.2: Local field distribution of a spherical Fe8-sample in a spin-10-model with 25% of the spins turned randomly.

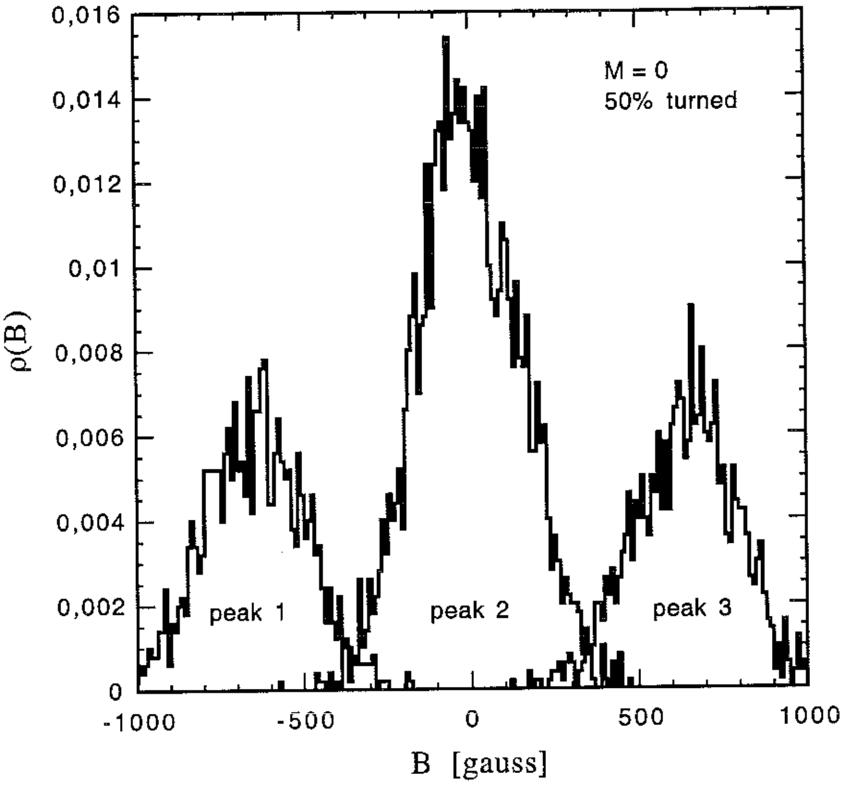

Figure V.1.3.3: Local field distribution of a spherical Fe8-sample in a spin-10-model with 50% of the spins turned ramdomly.

The resulting effect of the change in the peak size is that even though each individual peak is shifting to larger local field values, the overall center (the mean value) is shifting to smaller value. The overall mean value of the local field distribution is +381 gauss if all spin are up and zero if half of the spins are turned, as expected.

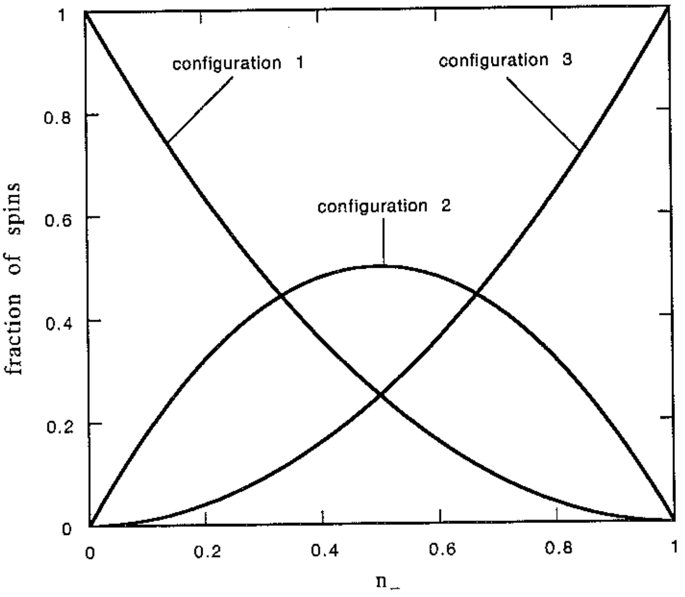

Figure V.1.3.4: Fraction of spins corresponding to the 3 configuration of next neighbors in the a-direction as function of the fraction of turned spins.

In figure [V.1.3.5] the mean values of the 3 peaks and the overall mean value is presented. The figure shows that the three peaks are moving linearly to larger field values until the 2nd peak reaches zero when half of the spins are turned. The overall mean value shifts linearly in the opposite direction until it also reaches zero when the magnetization is zero.

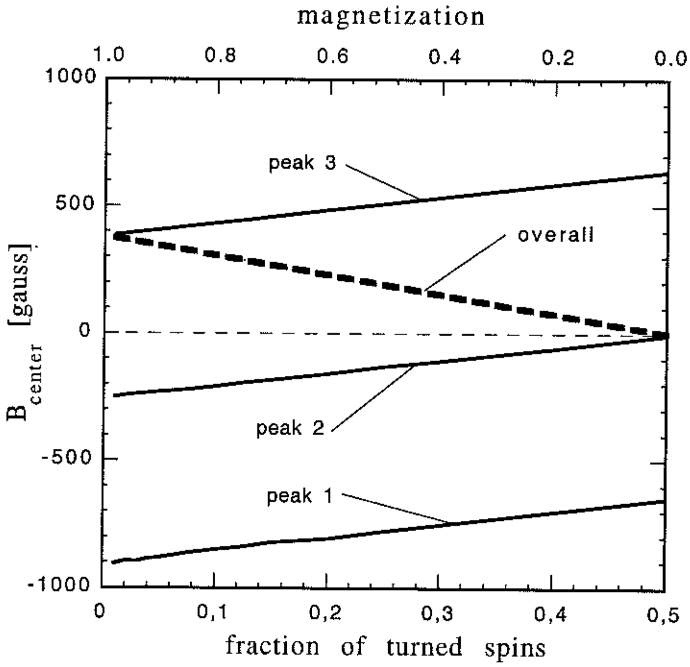

Figure V.1.3.5: Center value of the 3 peaks and the center value of the overall distribution in the spin-10-model for a spherical Fe8-sample. The spins are turned at random.

The standard deviation σ of the three peaks is plotted in figure [V.1.3.6] for the randomly turned spin configurations. The standard derivations for all the three peaks are identical. It increases linearly for a small number of turned spin and then roughly follows the equation $\sigma^2 = \sigma_0^2 n_-$ where n_- is the fraction of turned spins. The standard deviation reaches a maximum at $n_- = 0.5$, i.e. $M = 0$, and decreases again if we turn even more spins. Near the maximum $\sigma(n_-)$ deviates from $\sigma^2 = \sigma_0^2 n_-$. We have extrapolated the curve to a negative magnetization $M = -1$. In this region the order in the system is increasing thus the standard deviation decreases as can be see.

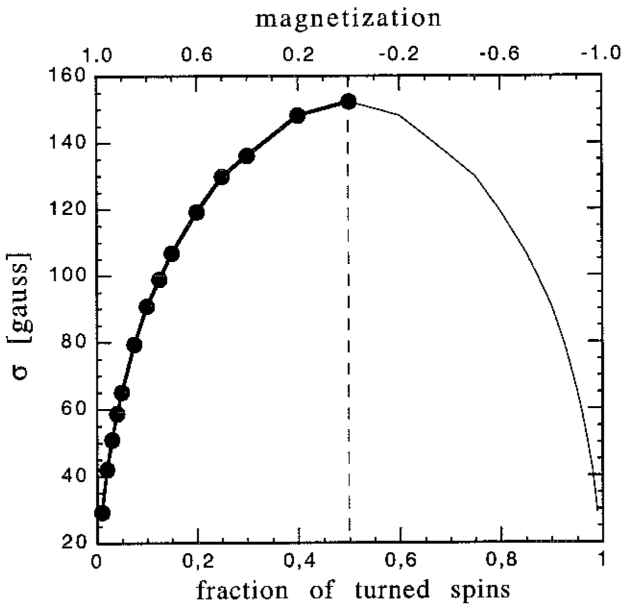

Figure V.1.3.6: Standard deviation of the 3 peaks in the local field distributions in the spin-10-model for Fe8.

In figure [V.1.3.7] a series of local field distributions are shown for several percentages of turned spins where we have taken into account the individual ions within the molecules (ion-model). The distributions have a quite complicated shape for the same reason as in the above calculation, the triclinic lattice of Fe8.

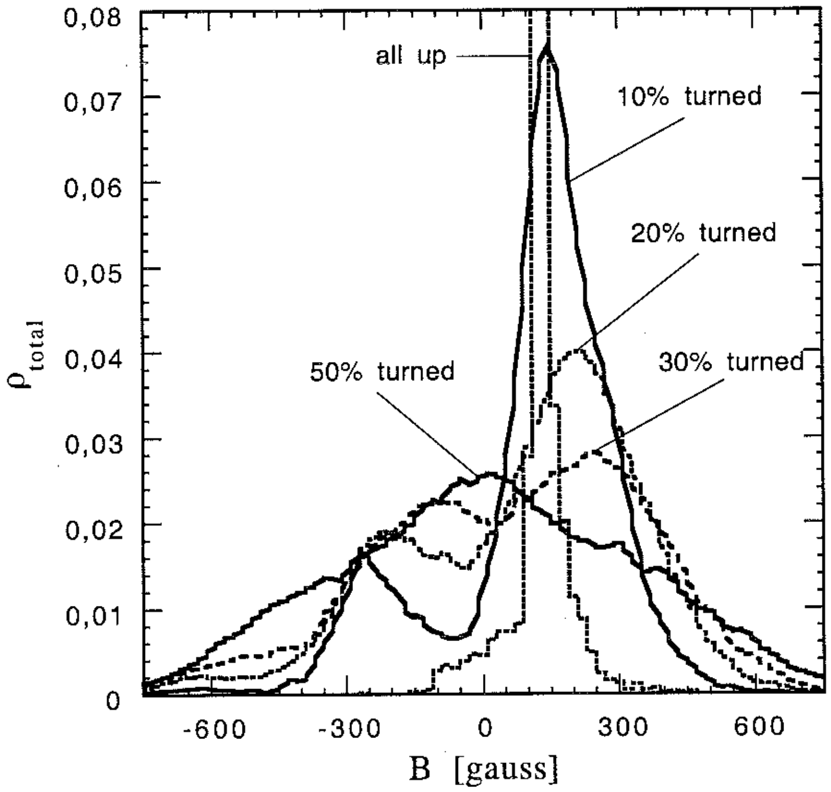

Figure V.1.3.7: Series of local field distributions for a spherical Fe8-sample in the ion-model. The spins are turned at random

The distribution for the initial state is very narrow with some finite size effects and centered at +122 gauss. In contrast to the spin-10-model, the 3 peaks although still present, are not well separated if some spins are turned. The peaks for the three different configurations overlap as can be seen in the figures [V.1.3.8] and [V.1.3.9]. These figures show the local field distribution for 20% and 50% of the spins turned, respectively. The bold line is a smoothed curve of the overall local field distribution. The thin lines are the distributions corresponding to the three configurations as before.

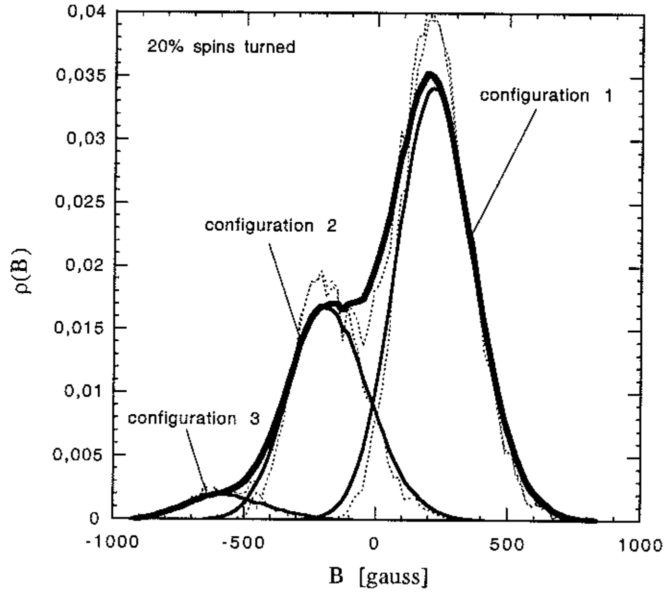

Figure V.1.3.8: Local field distribution in the ion-model of a spherical Fe8-sample with 25% of the spins turned at random. The distribution shape is strongly influenced by the 3 different configurations of the nearest neighbors along the *a*-axis.

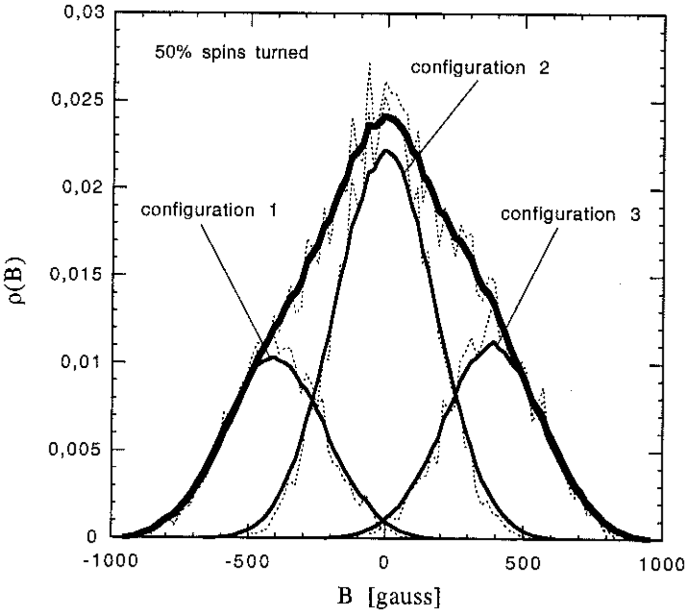

Figure V.1.3.9: Local field distribution in the ion-model for 50% of the spins turned at random with the 3 distributions due to different nearest neighbor configurations.

The mean values for the ion-model are shown in figure [V.1.3.10]. The mean values of the peaks due to the three configurations shift linearly to higher field values while the overall mean value goes to zero for $M = 0$.

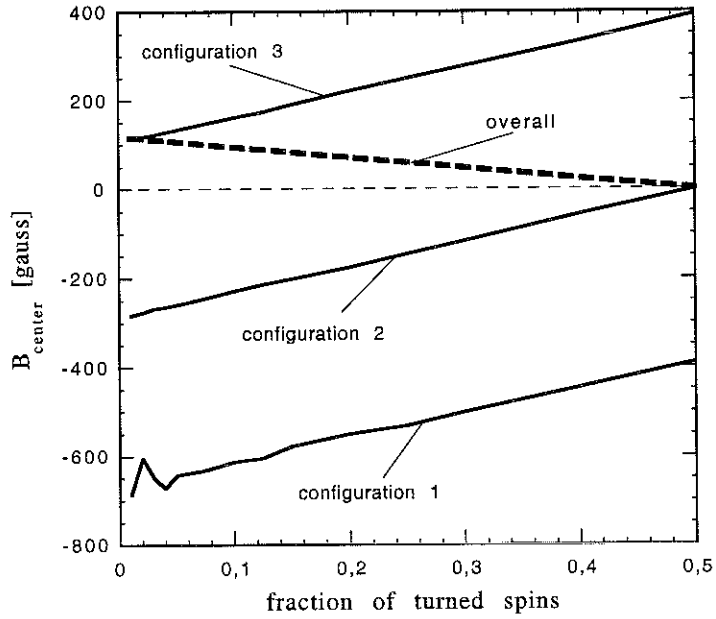

Figure V.1.3.10: Center value of the 3 peaks and the overall distribution for a spherical Fe8-sample in the ion-model as function of the fraction of turned spins. The spins are turned at random.

In figure [V.1.3.11] the standard deviation of the three peaks and the overall standard deviation is shown. The standard deviations of the peaks corresponding to the three different configurations are identical. As in the spin-10-model, the standard deviation has a maximum when 50% of the spin are turned, afterwards it will decrease again.

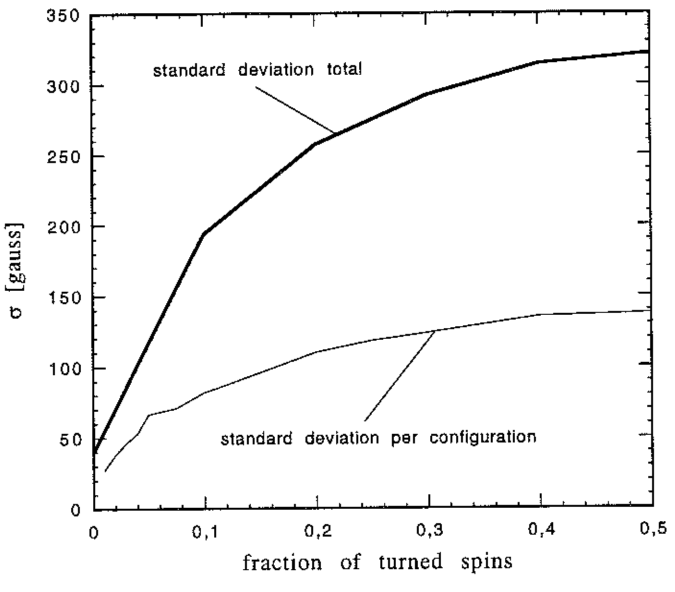

Figure V.1.3.11: Standard deviation of the 3 peaks and the overall distribution for a spherical Fe8-sample in the ion-model.

V.2.1) Square-root relaxation

The combined effects of fluctuating hyperfine fields and the local field distribution has been taken into account in a theory proposed by Prokof'ev and Stamp (P&S). In the quantum regime, P&S predict that for short times, i.e. for the beginning of the relaxation the magnetization decreases as the square root of time. We found that for the first 100 sec of the relaxation, the magnetization curve is square root like for all external fields within the first resonance. The inverse of the square-root relaxation time is proportional to the initial local field distribution.

[Prokof'ev 98] predict that due to fluctuating hyperfine fields within a molecule, the relaxation time is given by

$$\tau_N^{-1}(\xi) \approx \tau_0^{-1} \exp\left(-|\xi|/\xi_0\right) \qquad (1, \text{V.2.1})$$

where ξ is an energy bias and ξ_0 is the average strength of the hyperfine field, see chapter [II.3]. P&S estimated that $\xi_0 \sim T_2^{-1}$ where T_2^{-1} is the fluctuation rate of the hyperfine field, typically $T_2^{-1} \sim 10^{-7} - 10^{-5}$ sec. Expressed in units of a magnetic field acting on a spin $S = 10$ this energy corresponds to $\xi_0 \sim 10^{-4} - 10^{-2}$ gauss. The relaxation rate between the ground states $m = -10$ and $m = +10$ of a single molecule in resonance, i.e. $\tau_0^{-1} = \tau_N^{-1}(\xi = 0)$ is given by

$$\tau_0^{-1} \approx \frac{2\Delta_{10}^2}{\sqrt{\pi}\Gamma_2} \qquad (2, \text{V.2.1})$$

where Δ_{10}^2 is the tunnel splitting between the ground states and Γ_2 of the order of T_2^{-1}. P&S estimated that Δ_{10} shouldn't exceed 10^{-8}K. Thus the tunneling rate of a single isolated molecule in resonance should be of the order of

$$\tau_0 \sim 0.05 - 5 \text{ sec.} \qquad (3, \text{V.2.1})$$

This relaxation time is of the same order as the inverse frequency ν_{qc}^{-1} given by the theory of van Hemmen and Sütö. This coincidence may be due to the fact that accidentally the small hyperfine fields in Fe8 is (very roughly) of the order of the tunnel splitting, i.e. $\Delta_{10} \sim \Gamma_2$ thus $\tau_0^{-1} \sim \Delta_{10}$ as based on the theory of van Hemmen and Sütö. However, a major difference between these theories is that due to the hyperfine interaction the tunneling should be incoherent while in the theory of van Hemmen and Sütö the tunneling is coherent.

P&S also include dipole interactions between molecules. They argue that after saturation of the sample, and at the beginning of the relaxation the local field distribution is an evolving Lorentzian distribution. The center and the width are changing linearly with the magnetization. For a short times in the range

$$\tau_0 \frac{\xi_0}{E_D} < t < \tau_0 \frac{E_D}{\xi_0} \qquad (4, \text{V.2.1})$$

the relaxation curve should follow a square-root law

$$M(t) \approx 1 - \sqrt{t/\tau_{sqrt}} \,. \qquad (5, \text{V.2.1})$$

E_D is the total dipolar coupling from the nearest neighbors and roughly of the order of $100 - 500$ gauss. The square-root behavior should be observable in a time range from fractions of a milliseconds up to at least 100 sec or even longer. The predicted experimental relaxation rate in their theory is give by

$$\tau_{sqrt}^{-1} = \tau_0^{-1} \frac{\xi_0}{E_D} c \ (6, \text{V.2.1})$$

where c is a geometrical factor that depends on the sample shape and is roughly of the order of $0 - 100$.

To verify the theoretical predicted square-root time dependence, we analyzed the relaxation curves in the quantum regime using the Multi-Relaxation-Scan data as presented in the section [IV.2.3] figures [IV.2.3.12] to [IV.2.3.15]. The relaxation curves in the first resonance are shown in figure [V.2.1.1]. Each vertical line represents a relaxation measurement of 180 sec. These measurements were made on a long single crystal (long1). Before each measurement (one vertical line) the sample was first saturated in a strong positive field of ≥ 3 tesla. The field was then rapidly decreased to a predetermined field as can be seen in the figure.

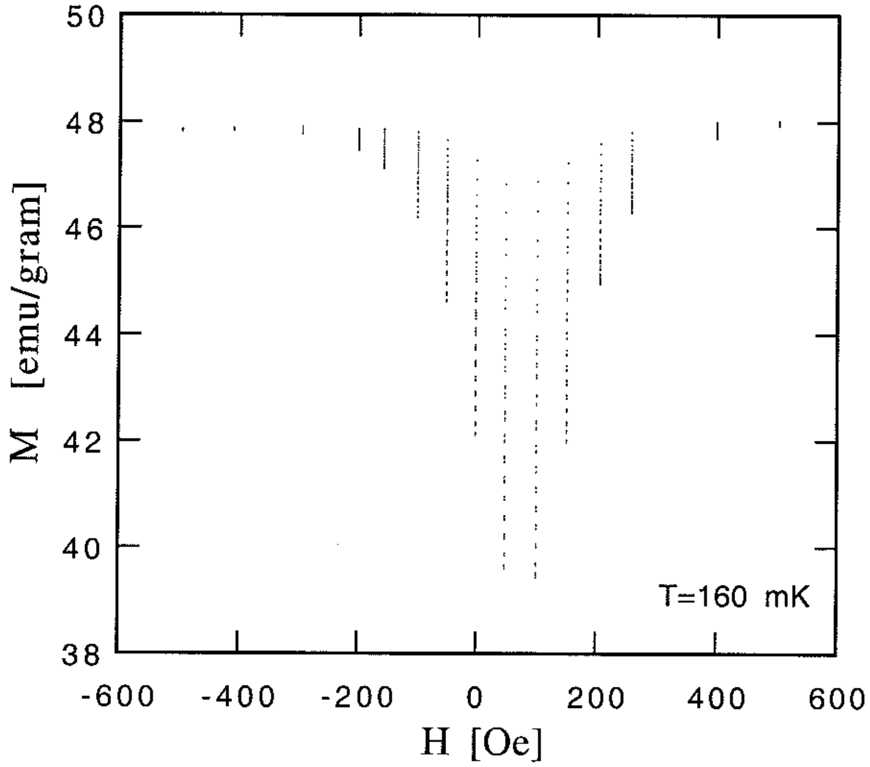

Figure V.2.1.1: Relaxation curves for different field values. Each vertical line represents one relaxation measurement. For every measurement the sample was first saturated in a strong positive field. The measurements were done on a long single crystal (long1).

From the vertical lines in this figure the relaxation of the magnetization for the fields of +400 Oe to –200 Oe are plotted versus the square root of time in figure [V.2.1.2]. The figure shows that for the first 100 seconds, all fields the data are on a straight line in this plot and can be well fit by a square-root law (solid line). For longer times the data begin to deviate from the square-root law. The duration of the square-root behavior is of the order of what we expect from the theory but rather short compared to the typical relaxation time (≥ 10^4 sec) at this temperature. One might therefore presume that the fit is just an expansion of the stretched exponential function that fits the data over a much longer time range. A first order expansion of the stretched exponential function is given by

$$M(t) \approx 1-(t/\tau)^{\beta} \qquad (7, \text{V}.2.1)$$

with $\beta = 0.4$. A fit of this kind (dashed line) doesn't match the data very well as can be see in the figure. Another important restriction is that all fitted curves when extrapolated to zero time should coincide at the saturation value $M(t=0) = M_{sat}$. With this restriction we see that the best fit in this region is by a square-root law. For larger times the relaxation behavior must change otherwise it would not be fit by a stretched exponential function with $\beta = 0.4$.

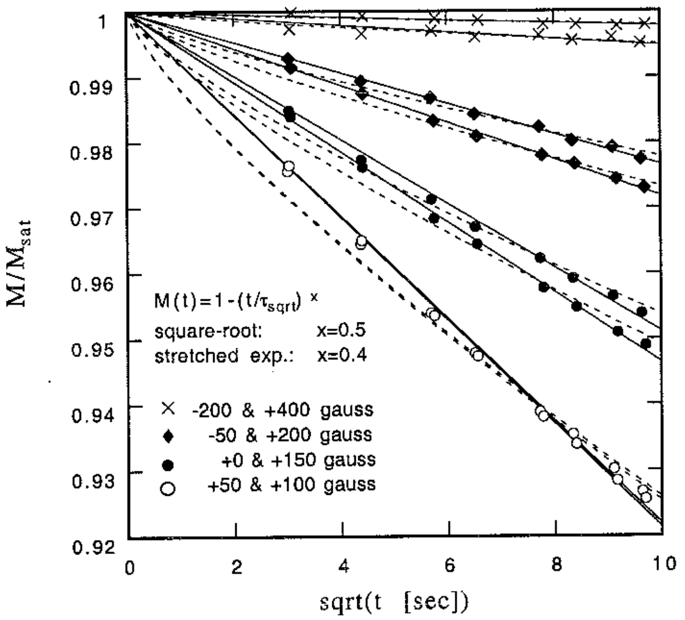

Figure V.2.1.2: The relaxation curves (longl) in different external fields as function of the square-root of the time.

The inverse square-root relaxation rates τ_{sqrt}^{-1} are plotted as a function of the field in figure [V.2.1.3]. The fastest relaxation rate is found at a field of $H = +80$ Oe and is of the order of $\tau_{sqrt}^{-1}(H = +80\text{ Oe}) = 2 \times 10^{-5}$ sec. The field value of the center of the first resonance is the same as observed be other methods (long relaxation curves, hysteresis curves, and Multi-Relaxation-Scans). It is remarkable that the square-root relaxation time is of the same order of magnitude as the relaxation time obtained by a stretched exponential fit $\tau \sim 10^4$ sec.

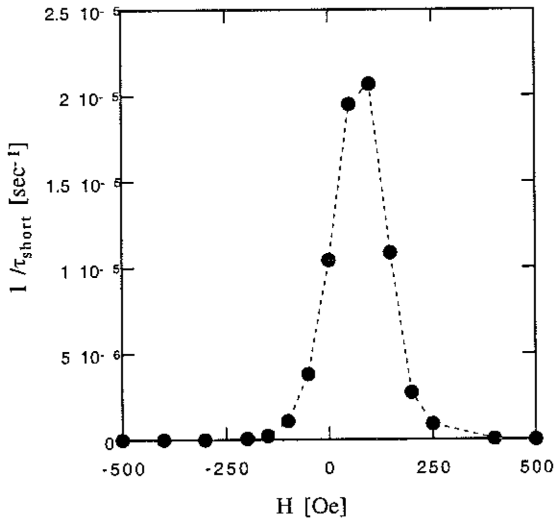

Figure V.2.1.3: Inverse square-root relaxation times (longl) as function of the external field.

The results for a second long sample (long2) are shown in figure [V.2.1.4] and [V.2.1.5]. The square-root behavior is about the same as for the other sample except that the fastest relaxation here is at a field value of +20 Oe and the relaxation time is three times faster compared to the sample (long1).

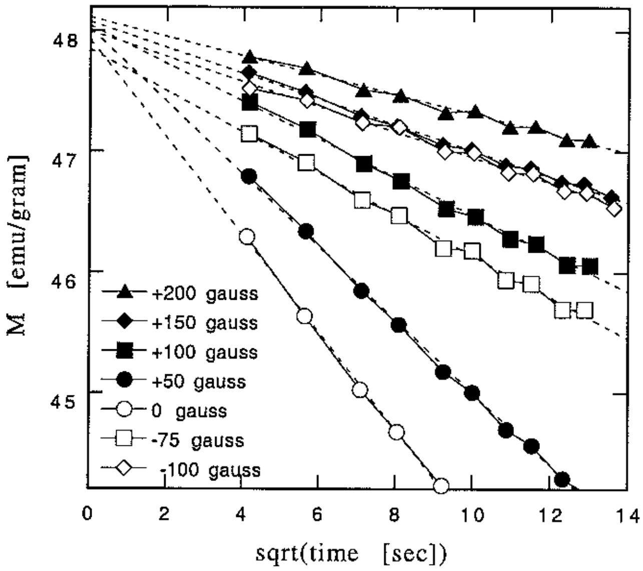

Figure V.2.1.4: Relaxation curves as function of the square-root of the time in different external fields for another long sample (long2).

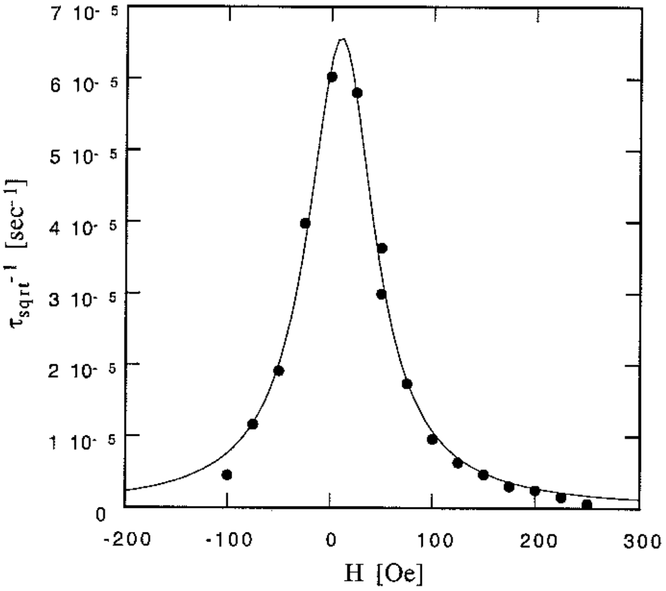

Figure V.2.1.5: Inverse square-root time (long2) as function of the external field.

In figure [V.2.1.6] the field dependence of the relaxation rate for 4 different sample shapes are presented. This figure contains the data of the 2 long samples (long1) and (long2) and of the spherical and the flat sample. The resonances have all about the same width of 100 Oe and the square-root relaxation time are also of about the same order $\tau \sim 10^4$ sec. The positions of the resonance centers are at +80 Oe (long1), +20 Oe (long2), +300 Oe (sphere and flat). These values correspond roughly to what we have seen before from hysteresis measurements and Multi-Relaxation-Scans.

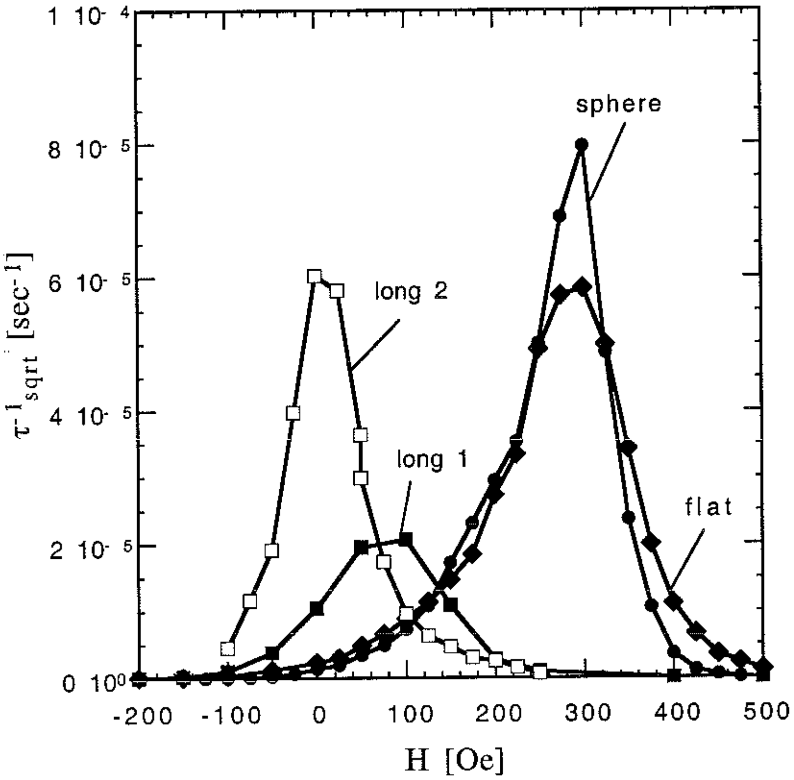

Figure V.2.1.6: Inverse square-root relaxation time for different sample shapes as function of the external field. The width of the resonances are about the same for all sample shapes ~100 Oe. The center of the resonances varies significantly with the sample shape.

The inverse square-root relaxation time $\tau^{-1}_{sqrt}(H)$ should be proportional to the initial local field distribution according to the theory of P&S. If we compare the experimental curves with our numerical calculations for the initial state, figure [V.1.2.1], we find no agreement! These calculations were done on samples with a similar aspect ratio as the sample we have measured. According to our calculations only the flat sample should have a resonance at a positive field. (For a comparison we have to change the sign of the field values for the numerical calculations). The long and the spherical sample should have their first resonance at negative (applied) fields. The spherical sample should have a much smaller resonance width than the other samples and the resonance of the long and flat samples should be skewed. The fact that the resonance of the spherical sample has the same width as the other samples might come from the rough surface of the sample. Due to the milling process to produce a spherical sample the surface has many defects.

V.2.2) Phenomenological model

Dipole interactions between molecules strongly influence the relaxation behavior in the quantum regime. In this chapter we will discuss how the local field distribution affects the relaxation dynamics. We will present a simple phenomenological model that fits the relaxation curve well and can indicates why the relaxation curves resembles a stretched exponential behavior in an intermediate time range. The model can also explain why the measured relaxation rate $\tau_{effective}^{-1}$ is orders of magnitude slower than the theoretical predicted tunneling rate τ_0^{-1} of a single molecule. Their ratio $\tau_{effective}/\tau_0$ is of the same order as the ratio between the strength of the dipole interaction E_D and the resonance width of a single molecule σ_{tunnel}: $\tau_{effective}/\tau_0 \sim E_D/\sigma_{tunnel}$.

The tunneling of the spin in a single molecule has an extremely narrow resonance width. The resonance width between the ground states $m = \pm 10$ is given by the tunnel splitting between these states Δ_{10}. The exact value of Δ_{10} is not known but theoretical estimates indicate that Δ_{10} should not exceed 10^{-8}K. This energy corresponds to a magnetic field of about 10^{-5} gauss acting on a spin of $S = 10$ [Prokof'ev 98]. If we include hyperfine effects as proposed by P&S this resonance is broadening up to a estimated value of $\xi_0 \sim 10^{-5}$ K corresponding to a field of 10^{-2} gauss. We can thus assume that the resonance of a single molecule is roughly of the order of say $\sigma_{tunnel} \sim 10^{-2}$ gauss. Within a sample the molecules will all experience a different field. This local field distribution might be due to an inhomogeneous demagnetization field but also that during the course of a relaxation more and more spins are turning. This also gives rise to a broadening of the local field distribution, see in the annex IV or the section on the numerical calculation of randomly orientated spins. The typical local field distribution is of the order of $E_D \sim 100$ gauss. In consequence only a small fraction of the molecules are in resonance. A schematic picture of this situation is shown in figure [V.2.2.1].

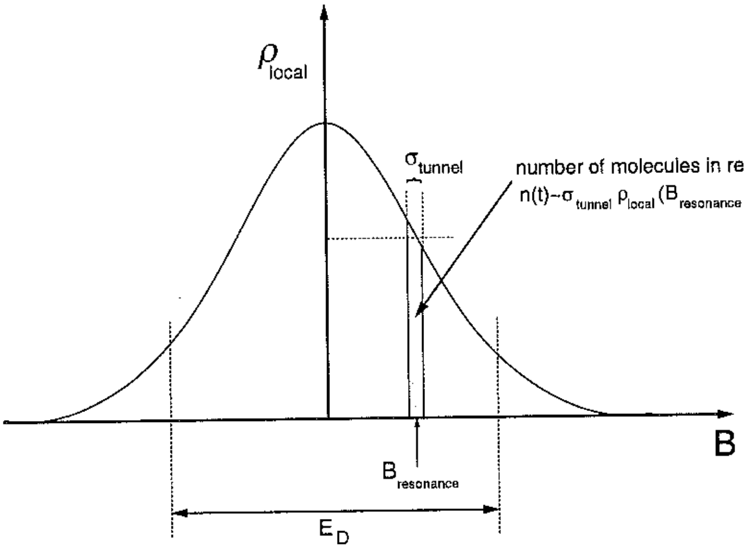
ρ_{local}
σ_{tunnel}
number of molecules in resonance
$n(t) \sim \sigma_{tunnel}\,\rho_{local}(B_{resonance};t)$
B
$B_{resonance}$
E_D

Figure V.2.2.1: Schematic picture of the effect of the local field distribution on the relaxation. The local field distribution is much larger than the resonance width of the molecules. Therefore only a small fraction of the molecules are in resonance (shaded bar) and can take part in the relaxation, the other molecules are blocked and can't tunnel.

Only the molecules of the local field distribution that are at the resonance field $B_{resonance}$ and in a small surrounding range of σ_{tunnel} may flip. All other molecules are off resonance and blocked. The number of molecules that are in resonance is depicted in the figure [V.2.2.1] by the shadowed bar. Since the local field distribution is much broader than the resonance of a single molecule $E_D >> \sigma_{tunnel}$ we can assume that the resonance of a single molecule as function of the field is given by

$$\rho_{resonance}(B) \approx \sigma_{tunnel}\delta(B) \qquad (1, \text{V.2.2})$$

where $\delta(B)$ is the Dirac delta function.

During the course of the relaxation the local field distribution evolves in time t, schematically shown in figure [V.2.2.2].

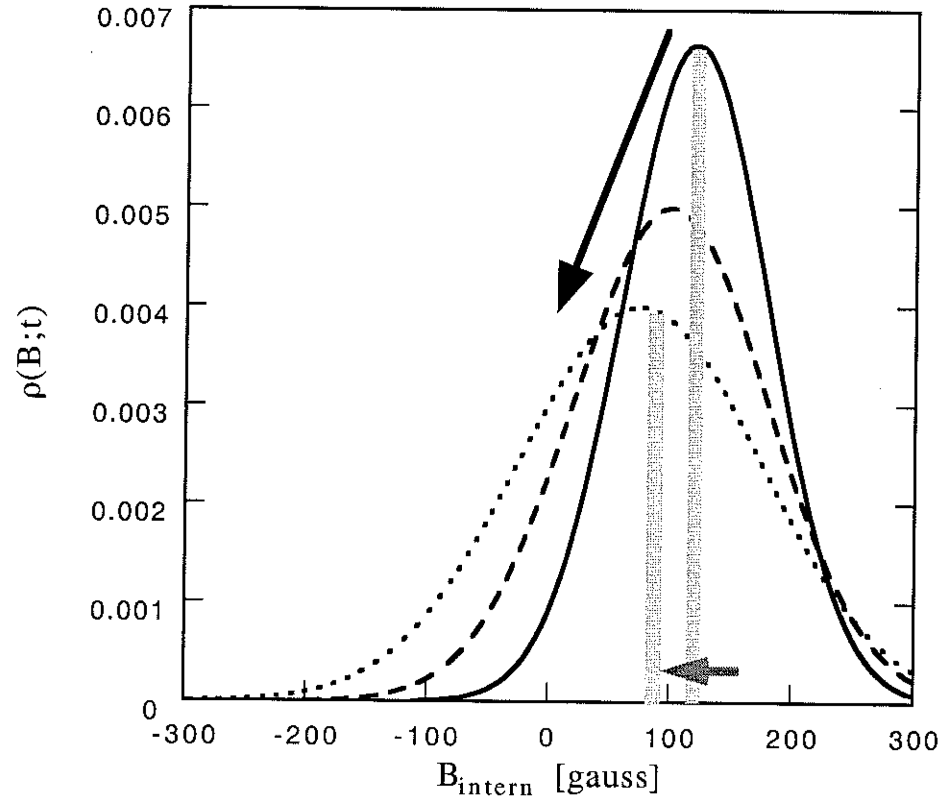

Figure V.2.2.2: During the course of the relaxation the local field distribution is evolving. The center shifts from the initial value to zero and the distribution width increases continuously. The small arrows at the bottom indicates that the resonance is shifting relative to the internal field B_{intern} due to the change of the demagnetization field $H_D = NM$ while changing the magnetization M.

The local field distribution $\rho_{local}(B;t)$ shifts towards zero from the starting value and broadens at the same time. During this evolution the resonance of the molecules will stay at the same value. Experimentally we can shift the local field distribution by an external field H_{extern}. The resulting local field distribution is then $\rho_{local}(B - B_{extern};t)$. The number of molecules in resonance will also evolve with the local field distribution. The fraction of molecules in resonance $n(t)$ is given by

$$n(t) = \int \rho_{resonance}(B)\rho_{local}(B - B_{extern};t)\, dB = \sigma_{tunnel}\rho_{local}(-B_{extern};t). \qquad (2, \text{V.2.2})$$

We can simple write

$$n(M(t)) = \sigma_{tunnel}\rho_{local}(B_{extern};M(t)). \qquad (3, \text{V.2.2})$$

where $\rho_{local}(B - B_{extern};M)$ signifies this time no field distribution but the value of the local field distribution at the fixed value B_{extern}. Figure [V.2.2.3] shows an example of how the local field distribution changes for a fixed value of B_{extern} as a function of the changing the magnetization M.

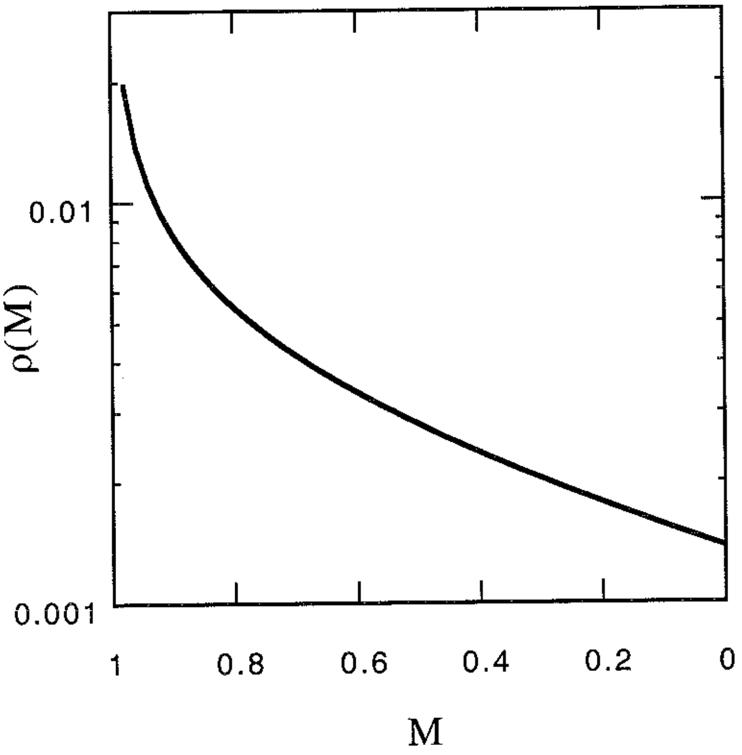

Figure V.2.2.3: As $M(t)$ decreases during a relaxation measurement, the fraction of molecules in resonance $n(M(t))$ decreases also. That means less and less molecules are in resonance and the relaxation becomes slower.

The dynamic model

For a phenomenological model of the relaxation we use the rate equation

$$\frac{dM(t)}{dt} = -\tau^{-1}(t)M(t) \quad (4, \text{V.2.2})$$

where we allow the relaxation rate to change with time during the course of the relaxation and we neglect correlation effects between the spins, i.e. two particle effects, see [Prokof'ev 98]. As mentioned, at any given time only a small fraction of the molecules are free to tunnel and most of the molecules are blocked. All molecules in resonance are assumed to have the same relaxation rate τ_0^{-1}. The relaxation rate will therefore be proportional to the fraction of molecules in resonance hence

$$\tau^{-1}(t) = \tau_0^{-1}n(t). \qquad (5, \text{V.2.2})$$

Using equation (3, V.2.2) the relaxation is given by the differential equation

$$\frac{dM}{dt} = -\tau_0^{-1}\sigma_{tunnel}\rho_{local}(B_{extern};M)M. \quad (6, \text{V.2.2})$$

To solve this differential equation we need to know how the local field distribution evolves during the course of the relaxation. A priori we cannot say what form the local field distrbution has. However, it has been demonstrated that in the thermal activated regime for a growing number of randomly placed spins the local field distribution evolves from a Lorentzian form to a gaussian distribution, see annex IV and [Berkov 96]

$$\rho_{local}(B,M)=\frac{1}{\sqrt{2\pi}\sigma(M)}\exp\left(-\frac{(B-\mu(M))^2}{2\sigma^2(M)}\right). \qquad (7, V.2.2)$$

The center and the width of this Gaussian distribution is given by

$$\mu(M)=\mu_0 M \quad (8, V.2.2)$$

where μ_0 has the dimensions *[field / magnetization]*, and describes the linear shift of the peak with changing *M*.

$$\sigma^2(M)=\sigma_0^2(1-M) \ (9, V.2.2)$$

as we have discussed in the chapter V.1.3, see also annex IV. Finally we assume that we apply an external field that shifts the center of the local field distribution into resonance thus

$$H_{extern}=\mu_0 M_{sat} \qquad (10, V.2.2)$$

in this units $M_{sat}=1$. Substituting this into the differential equation we get

$$\frac{dM}{dt}=-\tau_{effective}^{-1}\frac{\exp(-b(1-M))}{\sqrt{1-M}} \qquad (11, V.2.2)$$

with

$$b=\frac{\mu_0^2}{2\sigma_0^2} \qquad (12, V.2.2)$$

and

$$\tau_{effective}^{-1}=\frac{1}{\sqrt{2\pi}}\tau_0^{-1}\frac{\sigma_{tunnel}}{\sigma_0}. \qquad (13, V.2.2)$$

We can now solve equation (11, V.2.2) and fit the resulting curve to the data of a relaxation experiment. The fitting parameters are $\tau_{effective}^{-1}$ and *b*. We can't solve the equation analytically thus we used numerical methods. We studied the solution of equation (11, V.2.2) with various values of the parameters $\tau_{effective}^{-1}$ and *b* and found that the resulting curve is somehow determined independently by these parameters. The parameter *b* determines mainly the curvature while $\tau_{effective}^{-1}$ determines mainly the time scale. The resulting curve of equation (11, V.2.2) can be well fit by a stretched exponential function with its fitting parameters $\tau_{stretch}$ and β. The parameter $\tau_{effective}$ is almost identical to the fitted relaxation time $\tau_{stretch}$ and the parameter *b* influences mainly the exponent β of the stretched exponential function but in a way we can't exactly quantify.

The result of this fit is shown in figure [V.2.2.4]. The figure shows that a fit of this model matches the data as well as a stretched exponential in an intermediate time regime (200 sec – 10^5 sec). The obtained fitting parameters are $\tau_{effective}^{-1}=1.5\times10^{-5}$ sec and $b=7.95$. Although this equation has also 2 fitting parameters as the stretched exponential the relaxation process is now better understood along with the evolving local field distribution.

From equation (13, V.2.2) we can now estimate the tunneling rate of a single molecule τ_0^{-1}. Using the observed values for $\sigma_0\sim100$ gauss and taking for the resonance width the estimated value of $\sigma_{tunnel}\sim10^{-3}$ gauss we find that the tunneling time for a single molecule is of the order of $\tau_0\sim1$ sec in agreement with the theoretical value, see (3, V.2.1).

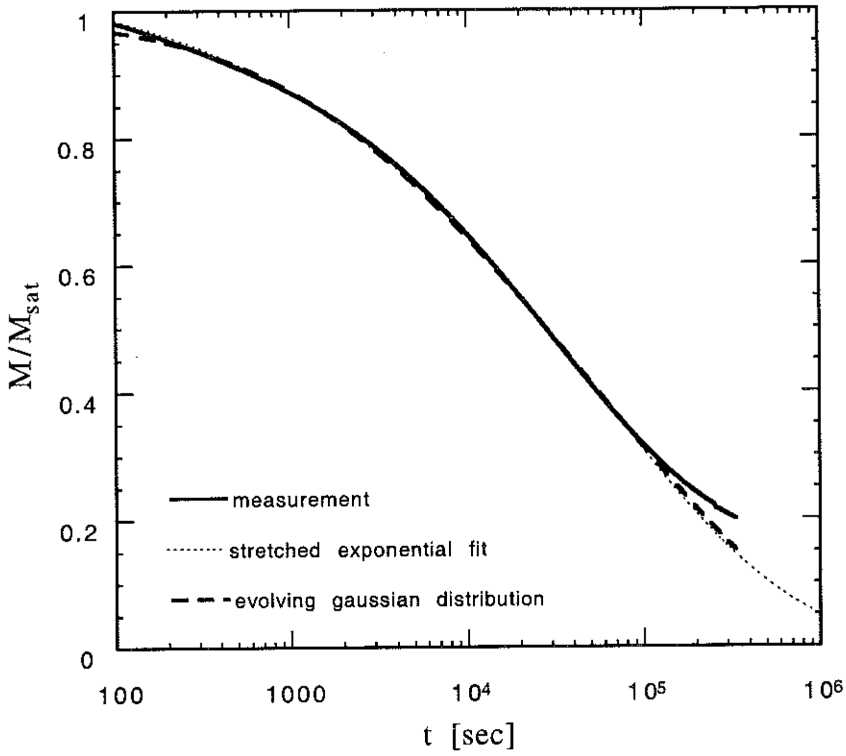

Figure V.2.2.4: The fit of a model curve (dashed line) to a measured relaxation curve (solid line). In addition a fit to a stretched exponential is shown (point line). The model curve has the same shape as a stretched exponential function.

Obviously this fit doesn't match the data at very long times and at short times (square root relaxation). It is surprising that this model matches the data at all since we used a local field distribution that is justified only for a thermal activated regime and we use it for a fit in the pure quantum regime. We therefore recall the main assumptions:

1) All molecules in resonance tunnel at the same rate

2) The number of molecules in resonance is decreasing continuously during the course of a relaxation

We can thus use equation (4, V.2.2) and (5, V.2.2) to measure or calculate the fraction of spins in resonance

$$\tau_0^{-1} n(t) = -\frac{d \ln M(t)}{dt}. \qquad (14, V.2.2)$$

For a stretched exponential relaxation this function reads

$$\tau_0^{-1} n(t) = \beta \tau_{stretch}^{-\beta} t^{\beta-1}. \quad (15, V.2.2)$$

the decrease of molecules in resonance follows a power law in time. An evolving gaussian distribution give rise to a function

$$\tau_0^{-1} n(t) = \tau_{effective}^{-1} \frac{\exp(-b(1-M))}{M\sqrt{1-M}}. \qquad (16, V.2.2)$$

It is not obvious that equation (15, V.2.2) and (16, V.2.2) result in the same relaxation. In figure [V.2.2.5] we plot these functions and the data (using equation (14, V.2.2)).

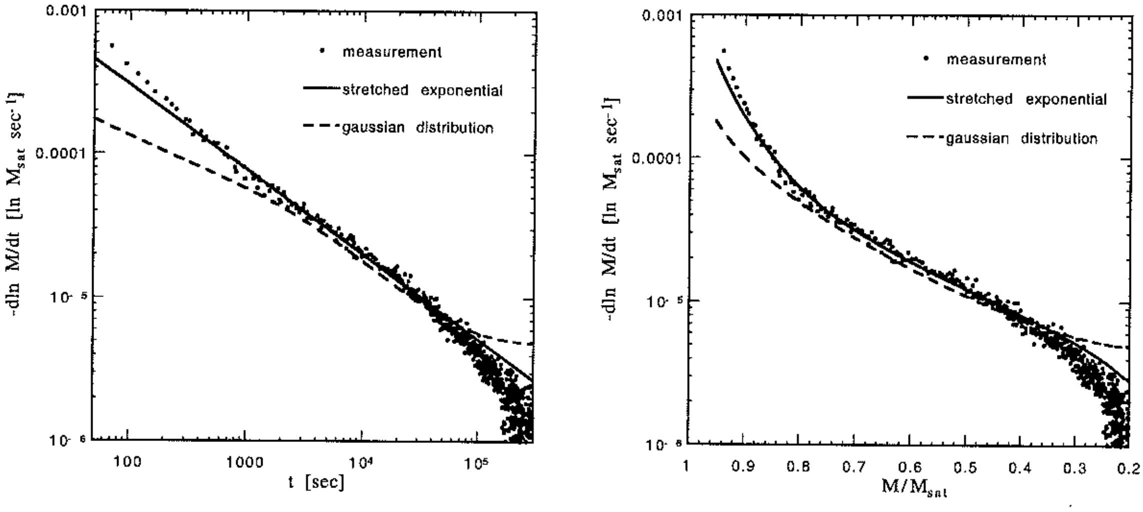

Figure V.2.2.5: dlnM/dt of a measurement (relaxation at 70mK) and the corresponding functions for a stretched exponential or the gaussian distribution versus the time or the magnetization.

It is now clear that the fact that an evolving gaussian distribution leads to a decrease of the number of spins in resonance similar to a power law is the main ingredient allowing us to fit the data in an intermediate time range by this model.

Due to the discussion above we can now give an interpretation of the parameter β of a stretched exponential fit. Assuming the relaxation of the isolated molecules in resonance τ_0 is constant then the number of molecules in resonance decreases proportional to a power law in time $n(t) \propto t^{\beta-1}$ (equation 15, V.2.2).

We will discuss in the next section that the field sensitivity of the tunnel effect gives rise to correlations in the spin configuration. We will also show that these correlations strongly influence the local field distribution and that in fact the shape of this distribution is not at all gaussian. Thus an open question remains why this model is in such good agreement with the data over a long period of time. This question merits further investigation.

V.3.1) Correlation effects

We have demonstrated that dipole interactions between molecules influence strongly the relaxation behavior in the quantum regime. So far we have only discussed this effect in terms of a local field distribution over the sample. The different local field values at the molecules corresponds to a 'local' energy shift at each molecule. If the energy shift is larger than $|\Delta_{tunnel}|$ the molecule is blocked and cannot flip. If the energy shift is smaller than $|\Delta_{tunnel}|$ the molecule is free to flip by quantum tunneling. We have shown that the local field distribution is evolving during the course of a relaxation and will change the number of spins in resonance. This number in turn is governing the relaxation behavior. For the evolution of the local field distribution we have use results as discussed in the annex IV and in the chapter on the numerical calculation V.1. What we have neglected so far is how spins may develop correlations via the dipole fields and thus the energy shift. We emphasize that the correlations are not caused by exchange interactions or magnetic dipole *forces* between the molecules that would try to align or anti-align the spins. The actual orientation of a spin is not determined by these correlation effects because (at the first resonance $H_{local} = 0$ gauss) the up and down state are degenerate and thus neither is energetically favorable. The correlation effects govern wether a spin is free to flip, or if it is blocked.

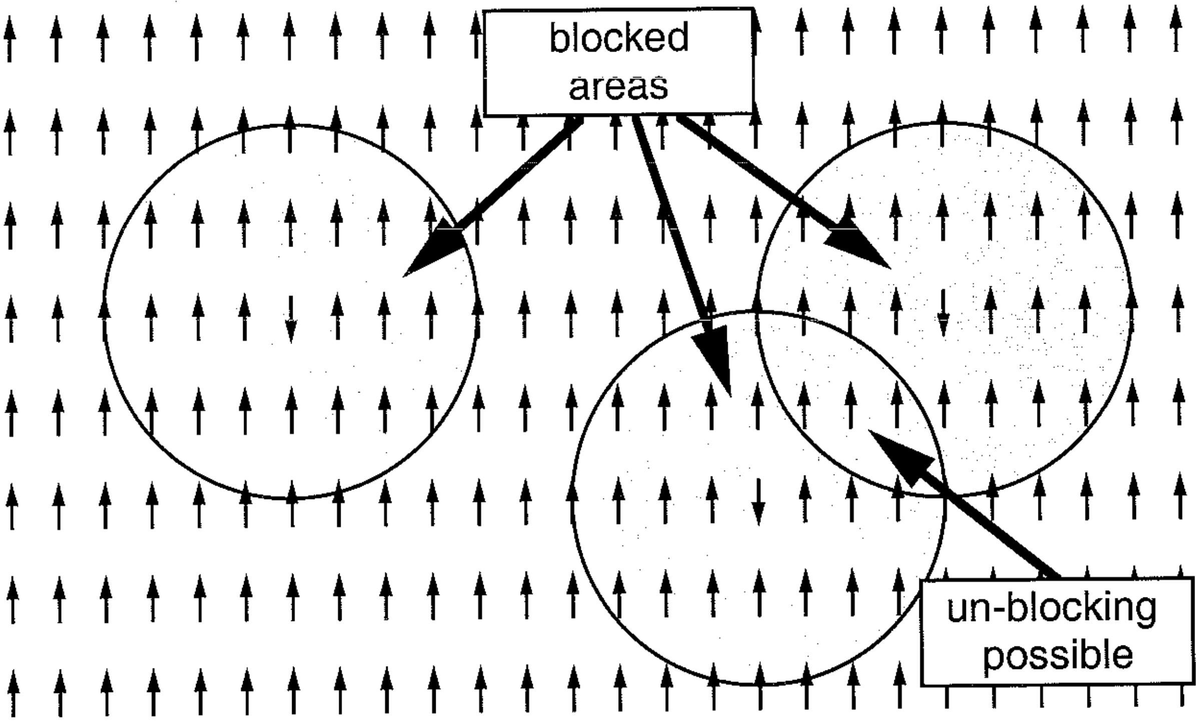

Figure V.3.1.1: Schematic 2-dimensional figure on the occurrence of correlations in a quantum tunneling system. Assuming all spins are initially in resonance. If one spin turns it will block about 10^5–10^6 neighboring spins. If another spin turns in the vicinity of a blocked are it will block other spins but might un-block some spins in an overlapping area.

A spin can only flip via tunneling if the initial and the final states are degenerate, i.e. the local field is zero within $|\Delta_{tunnel}|$, and therefore the Zeeman energy of the spin does not change. Correlations come about because the weak dipole field of a spin that has tunneled can nevertheless lift the degeneracy and remove from resonance a large number of neighboring spins. These spins become effectively blocked or frozen and most wait until some new configuration of spins results in a field close to zero. As an illustration, consider the ideal case of a spherical sample, with all spins aligned after saturation. If a small external field is applied in order to compensate for the demagnetization field, the internal field $H_{local} = 0$ and all spins may be brought into resonance at once. However, as the first few spins begin to tunnel, the now uncompensated dipole fields of each one will remove from resonance all other spins within a radius r, where its dipole field $\sim 1/r^3$ is greater $|\Delta_{tunnel}|$, see figure [V.3.1.1] left hand side (for simplicity we ignor the vector nature of the dipole field). For $S = 10$, and a resonance width of 10^{-3} gauss, this corresponds to approximately 10^5–10^6 spins that are pushed off resonance for each spin that tunnels! Thus very quickly most spins will be blocked and only a small fraction 10^{-6}–10^{-5} of the relaxation occurs with this natural rate. Nevertheless, the relaxation does not stop completely because some spins in the vicinity of blocked regions may still be free to flip. These spins can in turn un-block spins in some overlapping volumes by compensating the internal field such that once again $H_{local} < |\Delta_{tunnel}|$ in those regions, see figure [V.3.1.1] right hand side. Then spins in these 'newly liberated' volumes may flip, blocking and un-blocking other parts, and so on. For very long times, the blocked areas are so close that very few spins remain in resonance. These may still tunnel back and forth, but do not change M unless multiple flipping occurs, which we have neglected in phenomenological model.

Note that the resulting spin configuration due to the correlation effects is strongly influenced by the anisotropy of the dipole interaction. The z-component of dipole field of a single spin is given by

$$H = E_D \frac{3\cos^2(\theta) - 1}{r^3} \quad (1, \text{V.3.1})$$

where θ is the angle between the orientation of the spin (the a-axis) and the direction pointing to the position of the neighboring spin, r is the distance between the spins, and E_D the strength of the interaction. Thus the sign of the dipole field depends of the relative position of the neighboring spin. To give an example lets assume all spins are up and the local field is exactly zero. If one spin turns all neighboring spins within a cone along the a-axis will experience a positive energy shift and the spins outside the cone will experience a negative energy shift, see figure [V.3.1.2]. The spins within a radius r_{block} will be blocked. To un-block a neighboring spin **a** with a positive energy shift another spin **b** outside the blocked area has to turn. The spin **a** can only be un-blocked if the change in the local field due to the spin **b** is negative and can counterbalance the former energy shift up to $|\Delta_{tunnel}|$.

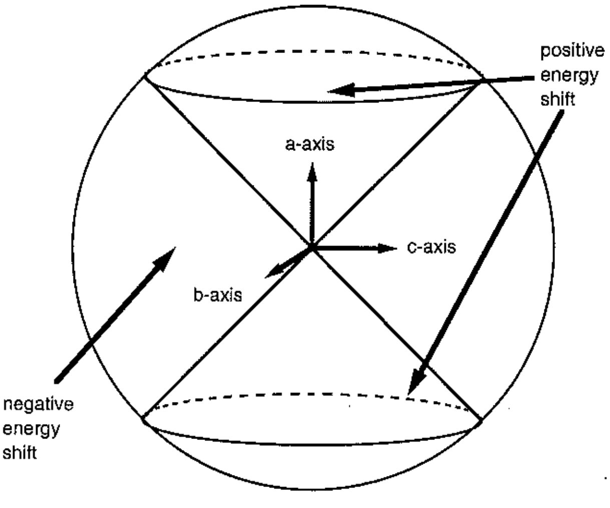

Figure V.3.1.2: Angular variation of the dipole field. If the spin at the origin is up the dipole field (and the energy shift) within a cone along the a-axis is positive and negative outside.

V.3.2) Monte-Carlo Simulation

To study the correlation effects in this system we did Monte-Carlo (MC) simulation of the relaxation in the quantum regime[1]. We found that the local field distribution shows remarkable differences between a thermal activated process and a quantum tunneling process. In the calculations we have made before, chapter [V.1.3], we turned the spins randomly. This corresponds to a thermal activated process in an Ising-system. In such a process the spins are free to turn independently of the local field they experience[2]. In the quantum regime a spin is only free to tunnel if the local field value is within a range of about $\Delta_{tunnel} \sim 10^{-3}$ gauss. The MC-distribution is depleted at the resonance field, i.e. less spins remain in resonance compared to a random-distribution.

We employed a MC algorithm to simulate the relaxation via quantum tunneling. The algorithm works at follows:

1) First we chose a molecule by random
2) The local field of the molecule is calculated
3) If the field value is within the resonance the spin may flip with a certain probability p_0 if the molecule is off resonance nothing is changed.

These steps are continuously repeated. The numerical simulations were made using a VOLVOX multiprocessor system at the CRTBT. This computer consists of 12 processors that work independently. We were thus able to run up to 12 independent MC-relaxation simulations in parallel and test a large variety of parameter sets. We preformed MC simulation on cubic and spherical samples in the range from 20 x 20 x 20 sites up to 50 x 50 x 50 sites. Since the dipole interaction is long range we have to re-calculate the local field distribution after every spin that turns. To improve the computing performance we used a look-up table. Before starting the MC-simulation an array **H** was initialized where we stored the local field contribution of a molecule/spin at a site distance of (0,0,1), (0,1,0), (1,0,0), (0,0,2) etc. After this initialization the calculation of the local field at one site due to all molecules/spins in the sample is reduced to a simple addition in the working memory of the processor.

Two different criteria were used to determine if a given spin can flip, i.e. if the spin is in resonance:

a) We can use a step-function, i.e. if the field is within a range H_0 of the resonance field H_{res}, the molecule may flip with a probability p_0 otherwise it is blocked.
b) We can use a resonance function as proposed in [Prokof'ev 98] where hyperfine effects are take into account. For a molecule experiencing a local field H, the flipping probability is given by $p(H) = p_0 \exp\left(-|H - H_{res}|/H_0\right)$.

The parameter H_{res} allows us to bring the maximum of the initial local field distribution into resonance and corresponds to an external field in an experiment. We found that both criteria give about the same results. Usually we used the method b). For the calculations of the local field we used the ion-model because we believe the 3 well separated peaks in the local field distribution of the spin-10-model are rather artificial and will lead to spurious results. We tried various parameter sets for p_0, H_{res}, and H_0 and found that the result is very sensitive to their choice but nonetheless have common features. Usually we use $p_0 = 0.1$. For a spherical sample $H_{res} = 122$ gauss and $H_0 = 0.3$ gauss and for the cubic sample $H_{res} = 80$ gauss and $H_0 = 1$ gauss. H_{res} was chosen so that the resonance is in the maximum of the initial local field distribution. For H_0 we have used larger values than the theoretically predicted (~ 10^{-3} gauss) due to restriction in size for the numerical simulation. If the resonance is too small the whole sample will be blocked if the first spin is turned or worse due to finite size effects not even one spin might be initially in resonance. A spin at a distance of 10 sites has a dipole field that is 1000 times smaller than the dipole field of the nearest neighbor. Thus since the dipole field of the nearest neighbors is of the order of ~100 gauss, such a distant spin still has a dipole field contribution of 0.1 gauss, i.e. of the order of the resonance!

---

[1] I acknowledge the help of Nikolai Prokof'ev

[2] The dipole field effect on the barrier height is negligible. An energy barrier of 24K corresponds to a field of $H_S = 1.8$ tesla. The change in the barrier height due to the Stoner-Wohlfarth model is given by $\Delta(H) = \Delta\left(1 - (H/H_S)^2\right)$. A dipole field of 100 gauss will change the barrier height only by $\varepsilon(H) = (H/H_S)^2 \sim 10^{-5}$. Although the barrier height effects the relaxation time $\tau(T,H)$ exponentially, for such a small change we can do an expansion of the exponential function $\tau(T,H) = \tau(T,H=0)(1+\varepsilon(H))$.

The overall local field distribution for a spherical sample after a relaxation to $M = 0.8$ is shown in figure [V.3.2.1]. In this figure we compare the overall field distribution obtained by the MC simulation (solid line) with the distribution that is obtain if we turn the same number of spins by random (dashed line). The peaked shape of the distribution is due to the triclinic lattice of Fe8 as we have discussed before, chapter [V.1.3], and is of no further importance for the discussion here. It is remarkable that the overall local field distribution is almost the same, regardless if we have turned the spins randomly or by the MC rules.

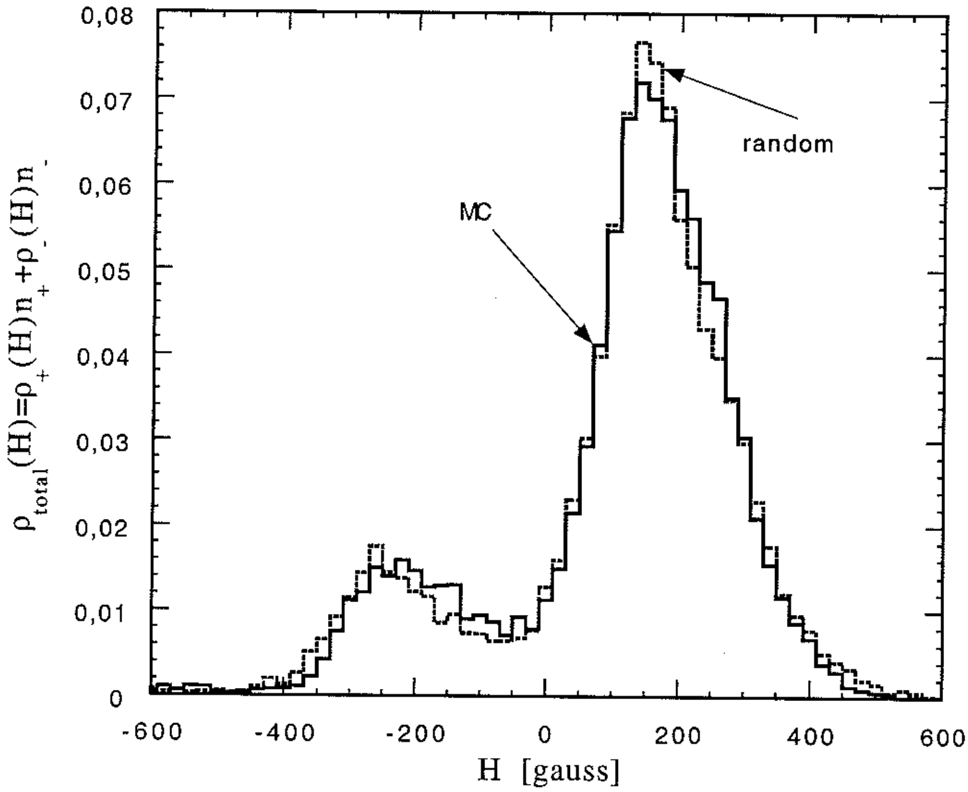

Figure V.3.2.1: Overall local field distribution of a spherical Fe8-sample with 20% of the spins turned. The random- and the MC-distribution are almost identical.

A difference in the local field distribution due to the to relaxation processes only occurs if we distinguish between the local field distribution over all up spins in the sample $\rho_+(H)$ and the distribution over all down spins $\rho_-(H)$. A comparison of the $\rho_+(H)$-distribution between the MC and random calculation is shown in figure [V.3.2.2]. The figure shows that the MC-distribution is reduced near the resonance (vertical dashed line) compared to the random-distribution. About 200 gauss away from the resonance the MC-distribution is larger than the random-distribution. Beside this difference both distribution are similar, i.e. they both have a peaked shape due to the triclinic lattice.

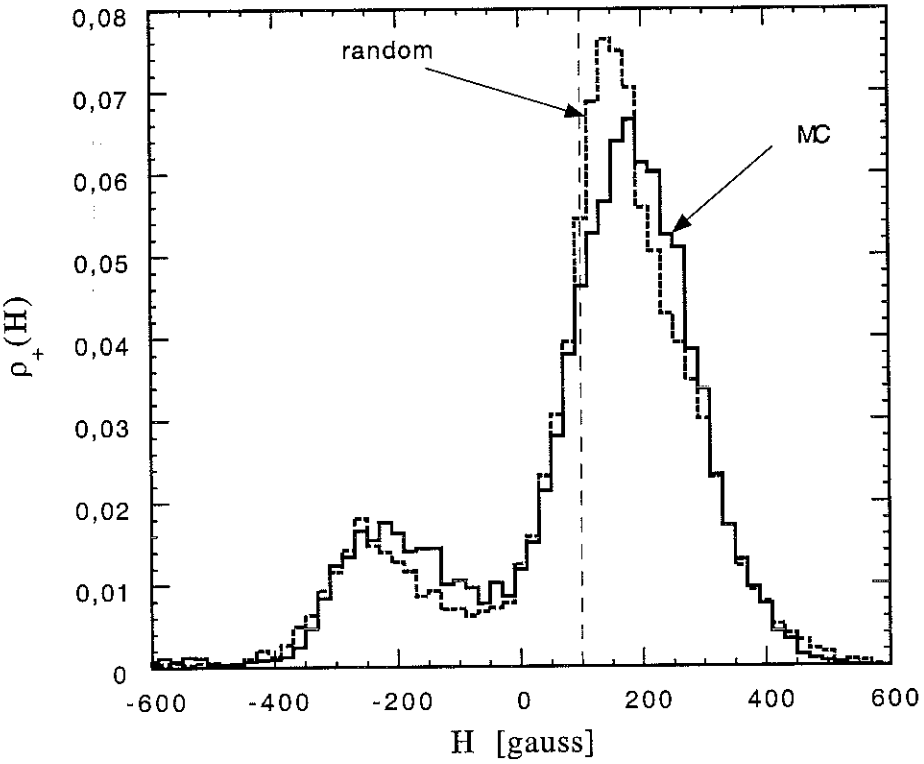

Figure V.3.2.2: The local field distribution over all up-spins for a spherical Fe8-sample with 20% spins turned. The MC-distribution is depleted at the resonance compared to the random-distribution.

The difference between the $\rho_-(H)$-distributions is more pronounced, figure [V.3.2.3]. Again the random-distribution has a similar shape as before, i.e. as for $\rho_+(H)$ and $\rho_{overall}(H)$. However, the MC-distribution is very different. This distribution has no second peak, is much narrower than the corresponding peak of the random-distribution, has a much larger peak value, and is centered exactly at the resonance.

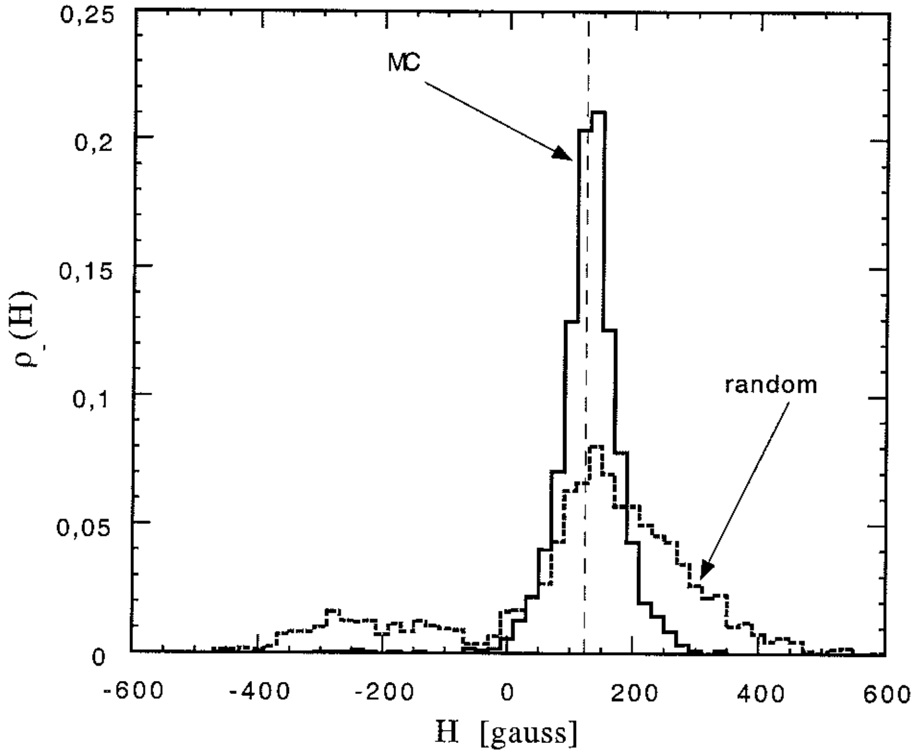

Figure V.3.2.3: Local field distribution over the down spins for a spherical sample with 20% spins turned. The MC-distribution is centered at the resonance and has only one peak. The random distribution resembles the overall random-distribution.

We have seen that the overall distribution is identically for the random process and the MC process while the $\rho_-(H)$-distribution evolves in a very different way. Since the weighted sum of the $\rho_+(H)$- and the $\rho_-(H)$-distribution gives $\rho_{overall}(H)$ the large difference in the $\rho_-(H)$-distribution has to have an effect on $\rho_+(H)$. In the range where $\rho_-(H)$ is larger than the equivalent random distribution $\rho_+(H)$ has to be smaller and vice versa.

In figure [V.3.2.4] we present the corresponding distributions for a cubic sample. The distributions of the cubic sample have the advantage that the initial distribution is much broader than for a spherical sample due to inhomogenities in the demagnetization field. Though the effects are the same, the differences in the distributions are easier to recognize since the peaks due to the triclinic lattice are smeared out and much less pronounced. In the figure we present the $\rho_+(H)$-, the $\rho_-(H)$-, and the $\rho_{overall}(H)$-distribution of a cube with 25 x 25 x 25 sites for a magnetization of $M = 0.8$. Again the $\rho_-(H)$-distribution has only one peak and is centered exactly at the resonance. In this figure it can easily be seen that the $\rho_-(H)$-distribution is exactly the amount by which the $\rho_+(H)$-distribution is depleted at the resonance.

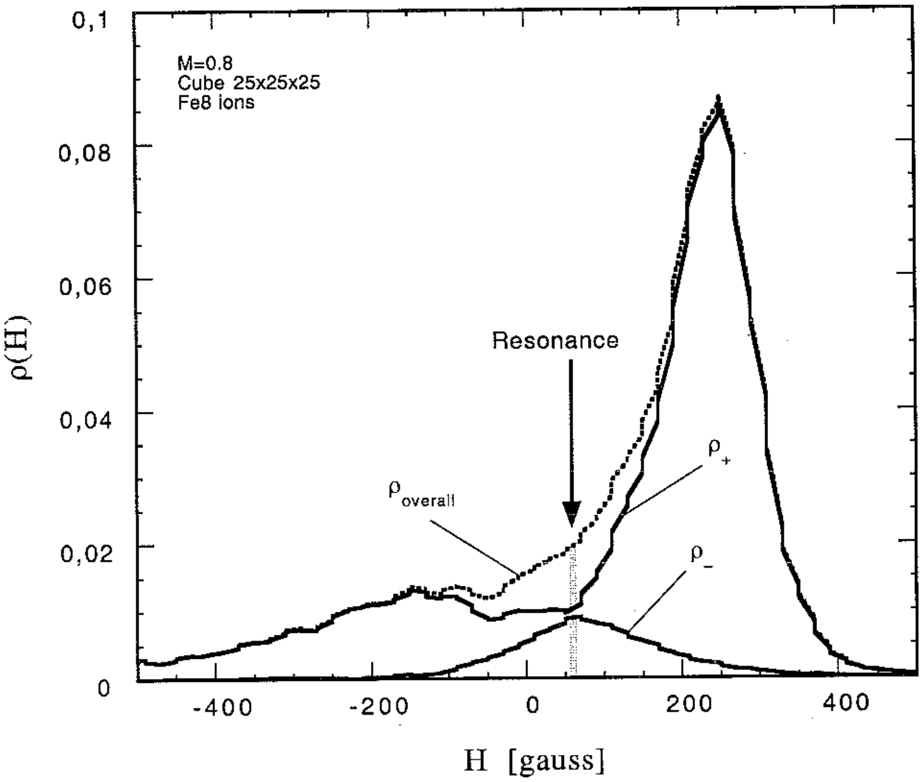

Figure V.3.2.4: Comparison of the MC local field distributions for a cubic sample with 10% of the spins turned. The depletion of the up-spin distribution corresponds to the increase in the down-spin distribution.

The spins of the $\rho_-(H)$-distribution and the $\rho_+(H)$-distribution have different effects on the quantum relaxation. The spins of the $\rho_+(H)$-distribution are up. If one tunnels the magnetization decreases, i.e. the sample relaxes. The spins of the $\rho_-(H)$-distribution are down thus if one flips, the magnetization increases. At the resonancce $\rho_-(H)$ is smaller than $\rho_+(H)$, and the net effect is that the magnetization decreases but at a slower rate, i.e. the relaxation time is strongly influence by the difference between these distributions. We therefore introduce the definition of a depletion-distribution

$$d(H) = \rho_+(H) - \rho_-(H). \qquad (1, \text{V}.3.2)$$

A comparison for the cubic sample between the overall distribution and the depletion distribution is shown in figure [V.3.2.5]. It shows that the depletion effect at the resonance is very pronounced in the depletion distribution *d(H)*.

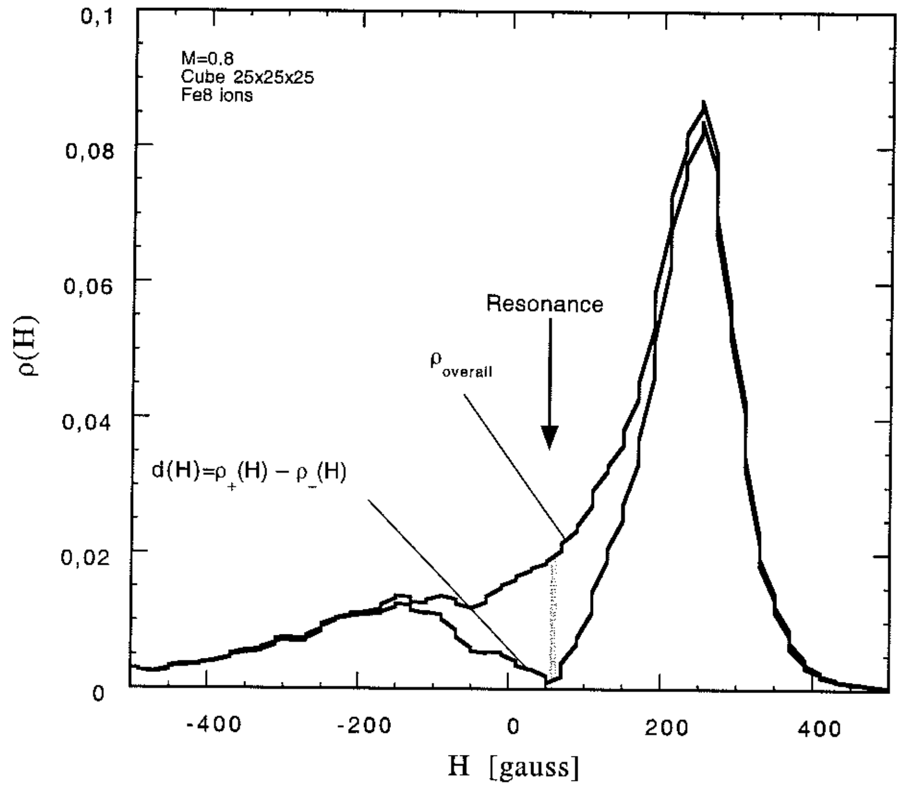

Figure V.3.2.5: The depletion distribution *d(H)* compared to the overall distribution. The depletion distribution should govern the relaxation process.

V.3.3) Measurement of the local field distribution

In this chapter we want to discuss the depletion of the local field distribution near the resonance due to the correlations in the system which develop during the course of a relaxation in the quantum regime. Finally we will present an experiment that measures qualitatively the depletion effect.

First we will show how correlation effects enter the phenomenological model as we have proposed in, chapter [V.2.2]. We have seen that we have to distinguish between the local field distribution of the up spins $\rho_+(H)$ and of the down spins $\rho_-(H)$. The number of molecules in resonance is not simply give by the overall distribution $\rho_{overall}(H)$ but the relaxation is governed by the depletion distribution *d(H;t)*. This distribution evolves almost like the other distribution during the course of a relaxation along with the shifting center and the broadening. We use again the rate equation but this time not for overall magnetization *M* but for the fraction of down spins *n₋*:

$$\frac{dn_-(t)}{dt} = -\left[p_-(t)n_-(t) - p_+(t)n_+(t)\right] \qquad (1, \text{V.3.3})$$

where $p_\pm(t)$ are the flipping probabilities from up to down (+) and down to up (–). The flipping probabilities are proportional to number of molecules (up or down) in resonance.

$$p_\pm(t) = \tau_0^{-1}\Delta_{tunnel}\rho_\pm(-H_{extern};t) \qquad (2, \text{V.3.3})$$

where $\rho_\pm(H;t)$ are the normalized local field distribution over the up (+) and down (–) spins. The differential equation that governs the relaxation is thus

$$\frac{dn_-(t)}{dt} = -\tau_0^{-1}\Delta_{tunnel}d(-H_{extern};t) \qquad (3, \text{V.3.3})$$

but we can't give any expression for *d(H;t)*.

Measurements

We have measured the effects of quantum tunneling on the distribution of relaxation times as shown in figure [V.3.3.3]. Our numerical simulations can be qualitatively compared to these measurements. All three measurements were made at 80mK on an approximately spherical single crystal. However, the sample was prepared in different ways, as we shall explain below.

The sharp peaked 'initial distribution' (τ_{sqrt}^{-1} vs. field) was made with the magnetization always close to the saturation value ($1 - M/M_{sat} << 1$) and was obtained by using the same procedure as used in chapter V.2.1 on the square-root behavior, i.e. for each point the sample was first saturated, the field was then rapidly decreased to a given target field, and the relaxation of the magnetization was measured. Because the sample was close to saturation, a fit to $\sqrt{t}$ is appropriate. The peak in the distribution for this sample was approximately +230 Oe with a width of ~ 120 Oe. This sharp peak corresponds roughly to the initial distribution of our computer simulations.

The other two distribution curves were made at the half demagnetized state $M \approx M_{sat}/2$. However, there is a tremendous difference in the two distributions curves depending on how we arrive at $M_{sat}/2$.

– Thermal distribution

The 'thermal distribution' was made by rapidly quenching the sample from 1K to 80 mK in a field of 800 Oe, (i.e. field cooled magnetization). At 1K and 800 Oe, M has an equilibrium value of $M \approx M_{sat}/2$. During the rapid cooling to 80 mK ($t < 30$ seconds), the sample does not have time to change its state, either by thermal activation or tunneling (if present), and thus the thermal distribution is frozen. The distribution was then measured by sweeping the field at a fixed ramping rate, and measuring the relaxation for 20 minutes at each field as shown in figure [V.3.3.1]. A $\tau_{stretch}$ at each field was obtained by a fit to a stretched exponential with $\beta = 1/2$.

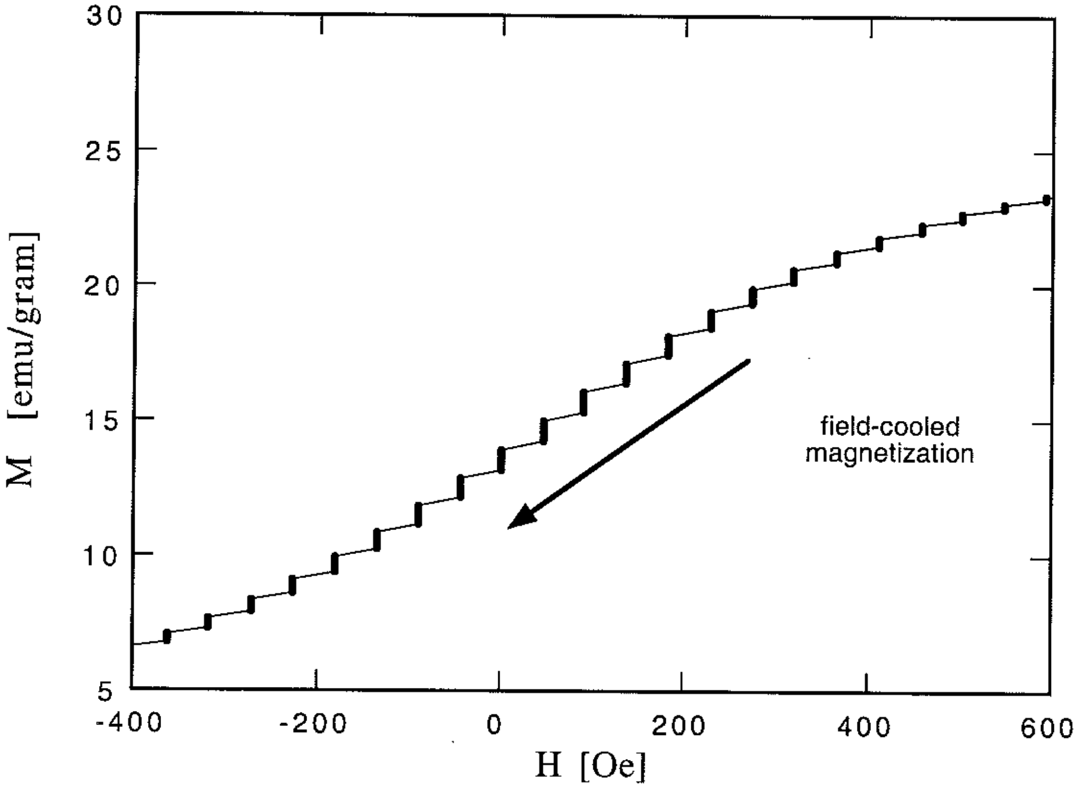

Figure V.3.3.1: Measurement of the thermal distribution. The sample is field cooled to have a magnetization of $M = 0.5$. Afterwards we step through the field and perform a sequence of relaxation measurements.

– *Quantum tunneling distribution*

The 'tunneling distribution' was made by first saturating the sample in a high field, and then letting the sample relax in an applied field of +230 Oe (i.e. at the peak of the initial distribution). During this time correlations between the spins develop. After a period of 4 hours, the magnetization decreases to $M = M_{sat}/2$. At this point we then swept the field up to 800 Oe as shown in the inset, again measuring the relaxation for 20 minutes at each field, and obtaining $\tau_{stretch}$ from stretched exponential fits with $\beta = 1/2$. The entire procedure was repeated for the decreasing field sweep, see figure [V.3.3.2].

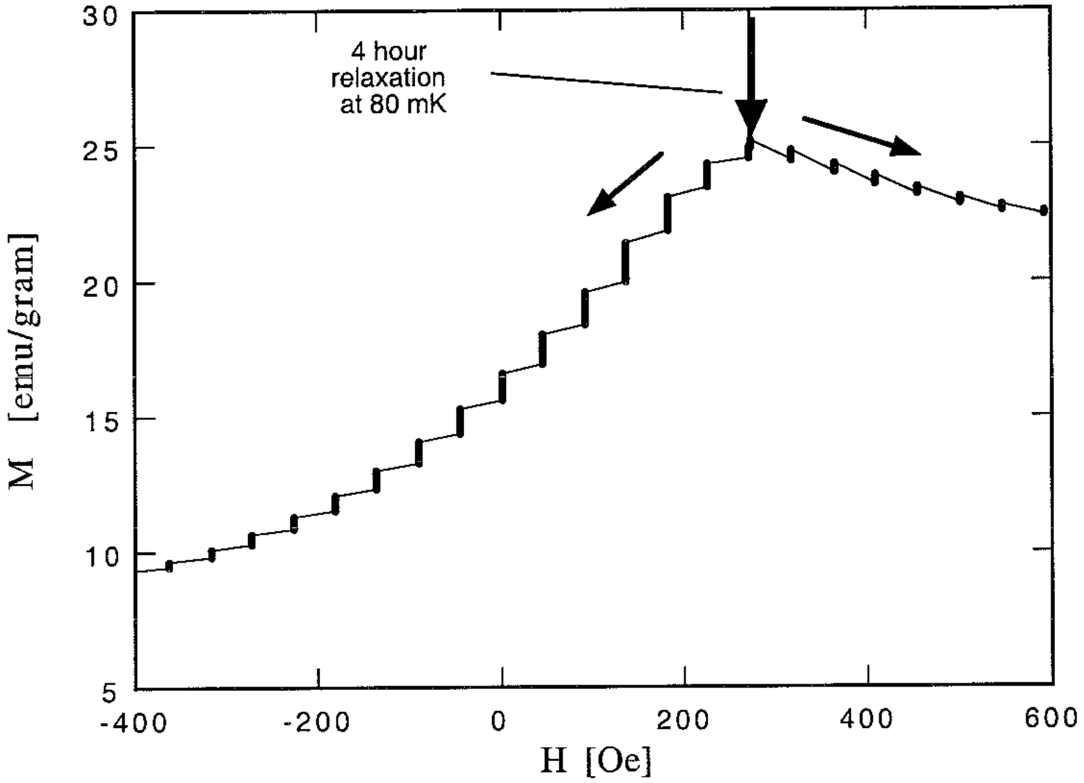

Figure V.3.3.2: Measurement of the quantum distribution. We let a staturated sample relax for 4 hours at the center of the initial distribution to a magnetization value of $M = 0.5$. Afterwards we step through the field and perform a sequence of relaxation measurements.

The difference between the thermal and quantum tunneling distributions is striking, figure [V.3.3.3]. The former is broad, and well fit by a Gaussian distribution (solid line) of width ~ 400 Oe indicating the random nature of the distribution similar to the random simulations. The tunneling distribution is distorted, similar to the Monte-Carlo results, figure [V.3.2.5], showing a depletion of the spins at the initial resonance which we believe are due the growth of correlation effects in the quantum regime. This gradual distortion results in the breakdown of the 'intermediate time model', because less spins stay in resonance as predicted, and the relaxation becomes slower than the calculated curve

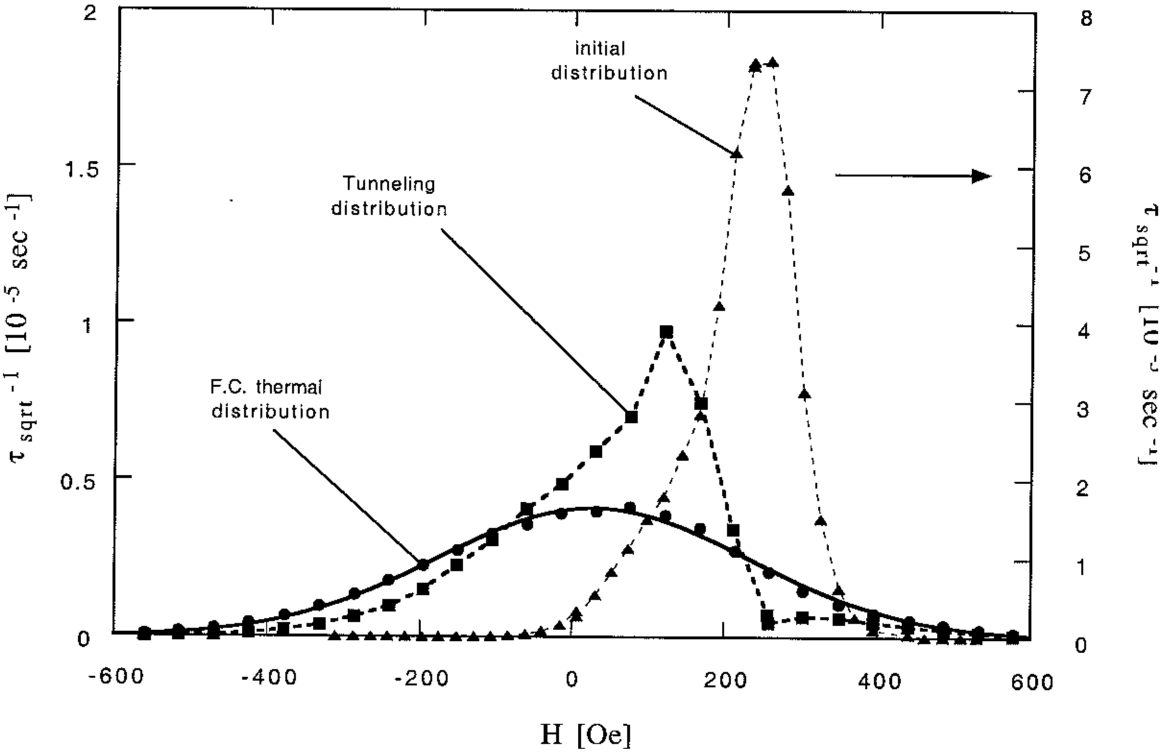

Figure V.3.3.3: Three inverse relaxation time distributions. The initial distribution was measured for a saturated sample $M = 1$. The thermal distribution was done on field cooled sample that was half-demagnetized $M = 0.5$. Finally the tunneling distribution was also done on a half-demagnetized sample. For this measurement we let a saturated sample relax for 4 hours at the center of the initial distribution (+230 Oe). The thermal distribution is smooth and regular reflecting the randomness of the thermal activated spin flipping. The tunneling distribution is very irregular with a sharp peak and a minimum at the former relaxation field of +230 Oe. This irregularity reflects the depletion of the local field distribution due to correlations that build up during the course of the initial relaxation of 4 hours.

Conclusion Générale

Nous avons étudié l'effet tunnel d'aimantation dans des aimants moléculaires à très basse température. Les systèmes que nous avons étudiés se composent de molécules magnétiques entourées par un cristal organique non-magnétique. Il s'agit donc d'un réseau régulier d'aimants nanoscopiques. A basse température, les molécules apparaissent comme ayant un seul spin géant. La majorité des expériences sont consacrées à l'aimant moléculaire Fe8. Les molécules de Fe8 portent un spin 10 et ont une interaction négligeable. Le système Fe8 montre des effets tunnels résonants à basse température au-dessous de 0,4 K. A haute température, au-dessus de 1K, Fe8 se comporte comme un système superparamagnétique.

Les expériences sont faites en utilisant des magnétomètres à SQUID aux performances uniques. Ces magnétomètres permettent des mesures de haute sensibilité en champ fort, jusqu'à 8 tesla, et aux très basses températures (> 50mK). Nous avons mesuré l'aimantation en fonction de la température et du champ et la susceptibilité en fonction de la fréquence et de la température.

A haute température la courbe d'aimantation de Fe8 ne suit pas la fonction de Brillouin d'un système paramagnétique simple, mais une fonction qui prend en compte la barrière d'anisotropie. La constante de Curie de la susceptibilité en champ faible est plus élevée que pour un système paramagnétique. Elle correspond également à la valeur que nous avons calculée pour un système superparamagnétique. La partie imaginaire de la susceptibilité satisfait au modèle de Debye et le système est donc géré par un seul temps de relaxation. La courbe de relaxation vers 1 K est exponentielle, comme prévu pour un système régulier et sans interaction. Le temps de relaxation à haute température suit la loi d'Arrhenius avec une hauteur de barriére de 24 K et un préfacteur $\tau_0 \sim 10^{-7}$ sec, bien plus grand que pour un spin libre. Dans cette gamme de température, Fe8 relaxe donc par activation thermique. Nous avons obtenu les mêmes temps de relaxation pour un échantillon en poudre et un monocristal.

Au-dessous d'une température de 0,4 K la relaxation est indépendante de la température. La courbe de relaxation est non-exponentielle, et bien décrite par une loi exponentielle étirée. Le temps de relaxation varie fortement avec le champ externe. La variation n'est pas monotone et présente un effet résonant : le temps de relaxation est plus court à des valeurs de champ équidistantes, séparées par 2 kOe. Dans la première résonance, le temps de relaxation a une valeur de $\tau \sim 10^4$ s et hors résonance une valeur de 10^8 s. La courbe d'hystérésis présente des sauts aux valeurs du champ résonant et l'aimantation reste presque constante hors résonance. La première résonance a une largeur d'environ 100 Oe et la deuxième résonance une largeur de 500 Oe. Comme dans le régime superparamagnétique, nous avons mesuré les mêmes temps de relaxation pour un échantillon en poudre et un monocristal. Cependant nous avons observé d'influence de la forme d'un monocristal. Nous avons fait des mesures sur des échantillons en forme allongée, sphérique et aplatie. La courbe de relaxation varie avec la forme, mais les paramètres de l'exponentielle étirée ont presque la même valeur. Nous avons observé par contre que la position de la première résonance change beaucoup avec la forme d'échantillon. Pour l'échantillon long, après la saturation dans un champ positif, la première résonance se trouve à une valeur de +80 Oe à +100 Oe. L'échantillon sphérique a sa première résonance à +230 Oe et l'échantillon plat à une valeur de +200 Oe, également après une saturation en champ positif.

Nous avons démontré que les champs dipolaires entre les molécules ont une forte influence sur la relaxation. Ces champs n'agissent pas comme une force entre les spins qui alignerait les spins parallèlement ou antiparallèlement. Les champs dipolaires permettent ou suppriment l'effet tunnel quantique dans les molécules. Dans Fe8 les états de spin sont bien séparés et le système traverse par effet tunnel la barrière entre un état discret à un autre état discret. L'effet tunnel est permis seulement si les deux états ont la même énergie ou si le décalage d'énergie est plus petit que l'amplitude tunnel, Δ_{tunnel}. En présence d'un champ magnétique les états de spin vont bouger et changer le décalage entre les états. Si ce décalage est plus grand que Δ_{tunnel}, l'effet tunnel est supprimé et le spin est bloqué. Nous avons observé une relaxation en racine carrée du temps pour le début de la relaxation, comme prévu par une théorie qui prend en compte les effets de champ local.

Nous présentons un modèle phénoménologique simple qui décrit bien la courbe de relaxation sur 4 décades en temps. Dans ce modèle, nous supposons que la résonance quantique d'une molécule est très étroite, de 4 à 5 ordres de grandeur plus petite que la largeur de la distribution du champ local. En conséquence, seulement une petite fraction de spins est en résonance. La plupart des molécules sont hors résonance et ne peuvent pas participer à la relaxation. Nous supposons que la distribution du champ local évolue pendant la relaxation. Le nombre de molécules en résonance diminue au cours du temps avec pour effet que la relaxation se ralentit. Pour cette raison, la courbe de relaxation ressemble à une fonction exponentielle étirée. Une autre conséquence de cet effet dans les expériences, est que nous n'observons pas le taux d'effet tunnel quantique τ_{tunnel}, mais un temps de relaxation effectif $\tau_{effectif}$. Le rapport entre le taux effectif de relaxation et le taux d'effet tunnel quantique $\tau_{effectif} / \tau_{tunnel} \sim \sigma / \Delta_{tunnel}$ a le même ordre de grandeur que le rapport entre la largeur de la distribution du champ local σ et la résonance quantique d'une seule molécule Δ_{tunnel} : $\sigma / \Delta_{tunnel} \sim 10^4 - 10^5$. De cette façon nous pouvons également comprendre pourquoi nous observons dans les expériences une résonance avec une largeur de 100 Oe et plus.

Pour mieux comprendre l'effet du champ local nous avons fait des calculs numériques. Dans ceux-ci nous faisons une distinction entre le champ dipolaire et le champ local. Le champ dipolaire est le champ magnétique créé par tous les spins dans un échantillon, et varie de position à position et même à l'intérieur d'une molécule. Le champ local est directement lié au décalage d'énergie d'un spin géant. Ce champ est seulement défini par rapport à une molécule et les positions de ses spins ioniques.

Nous avons calculé la distribution du champ local pour un échantillon dont tous les spins sont parallèles, ce qui correspond à la distribution initiale d'une expérience de relaxation. Ensuite nous avons étudié la distribution dans un cas où les spins sont retournés de manière aléatoire. Nous observons une forte influence du réseau triclinique sur la distribution du champ local. Pour réaliser une simulation de la relaxation dans le régime quantique nous utilisons une méthode de Monte-Carlo. L'effet tunnel quantique crée des corrélations inhabituelles dans la configuration de spin. Autour de la résonance moléculaire, ces corrélations changent la distribution du champ local. Dans cette région ils diminuent l'amplitude de la distribution (comparée à celle d'une distribution aléatoire) et encore moins de molécules sont en résonance que dans un modèle statistique. Un spin qui tourne change le champ local dans son environnement proche. Dans une certaine région le changement dans le champ local est plus grand que la résonance moléculaire et les molécules de cette région sont bloquées. Un autre spin qui tourne dans la proximité d'une telle région va bloquer également des spins voisins, mais dans une région en commun quelques molécules vont peut-être se débloquer. Donc le champ local ne détermine pas l'orientation d'un spin, il permet ou supprime le retournement d'un spin par effet tunnel quantique. A la fin du mémoire nous présentons une expérience qui montre clairement les effets de corrélations sur le champ local.

En résumé nous avons étudié un échantillon, Fe8, montrant clairement l'effet tunnel quantique résonant. Pour la première fois il a été possible d'étudier avec soin et de manière très détaillée le comportement magnétique dans le régime quantique. Nous avons montré que le champ dipolaire entre les molécules influence fortement la dynamique des spins. L'effet tunnel quantique crée des corrélations inhabituelles dans un tel système. Nous croyons que nos arguments sont très généraux et s'appliquent également aux autres systèmes tunnels résonants, comme Mn12ac.

Annexes

Annexe I) Etats du Spin de Fe8 153

Annexe II) Courbe d'Aimantation de Fe8 155

Annexe III) Champ Démagnétisation 159

Annexe IV) Théorie Statistique sur la Distribution du Champ Local 163

Annexe V) Relaxation Non-Exponentielle 167

Annex I

AI) Energy levels of Fe8

In this annex we given some technical details used to calculate the energy levels of the Fe8-Hamiltonian and their field dependence. The energy level scheme is interesting in itself and can be used to calculate thermodynamically properties such as the magnetization curve, see annex II.

To calculate the energy levels of the spin states we have to diagonalize the Hamiltonian. In the case of Fe8 the diagonalization can be done numerically. The Fe8 Hamiltonian reads

$$\hat{H} = -D\hat{S}_z^2 + E\left(\hat{S}_x^2 - \hat{S}_y^2\right) + g\mu_B\hat{S}_z H \quad (1, \mathrm{AI})$$

The first term is the anisotropy barrier, the second is due to the transverse anisotropy and gives the tunneling term, and the last term gives the Zeemann energy shift due to a magnetic field H. The parameters D and E have been first measured by EPR-measurement [Barra 96] and later confirmed by inelastic neutron scattering [Caciuffo 98]. We used the values from the EPR-measurement, D = 0.27K and E = 0.046K. Instead of using the transversal spin components $\hat{S}_x$ and $\hat{S}_y$ we can express equation (1, AI) in terms of the spin raising and lowering operator $\hat{S}_\pm = \hat{S}_x \pm i\hat{S}_y$. Thus

$$\hat{H} = -D\hat{S}_z^2 + E/2\left(\hat{S}_+^2 + \hat{S}_-^2\right) + g\mu_B\hat{S}_z H. \qquad (2, \mathrm{AI})$$

If a spin S is in the state $|S,m\rangle$ with $m = -S, \ldots, +S$ then the z-component operator of the spin acts as

$$\hat{S}_z^n|S,m\rangle = m^n|S,m\rangle \quad (3, \mathrm{AI})$$

The raising/lowering spin operator gives

$$\hat{S}_\pm|S,m\rangle = \sqrt{S(S+1) - m(m\pm 1)}\,|S,m\pm 1\rangle. \quad (4, \mathrm{AI})$$

and the square of this operator

$$\hat{S}_\pm^2|S,m\rangle = \sqrt{[S(S+1) - m(m\pm 1)][S(S+1) - (m\pm 1)(m\pm 2)]}\,|S,m\pm 2\rangle. \qquad (5, \mathrm{AI})$$

Using these equations we can now write the Hamiltonian as a matrix in the Heisenberg picture. The diagonal elements are given by

$$\alpha_m = -Dm^2 + g\mu_B Hm$$

where $m = -10, \ldots, +10$. The raising and lowering spin operators give two off-diagonal lines in the matrix and all the other elements are zero. We will write the matrix elements as H_{ij} where the index i is over the rows and j over the columns. The off-diagonal elements are placed where $i+1 = j-1$ and $i-1 = j+1$. Their values are

$$\gamma_m = E/2\sqrt{[S(S+1) - m(m+1)][S(S+1) - m(m-1)]} \qquad (6, \mathrm{AI})$$

where $m = i+1$ if $i+1 = j-1$ and $m = i-1$ if $i-1 = j+1$, respectively. Thus

$$H_{ij} = \begin{cases} \alpha_m & \text{for } i = j \equiv m \\ \gamma_m & \text{for } i-1 = j+1 \equiv m \text{ or } i+1 = j-1 \equiv m. \\ 0 & \text{else} \end{cases} \qquad (7, \mathrm{AI})$$

In a matrix form this looks like

$$\mathbf{H} = \begin{pmatrix} \alpha_{+10} & 0 & \gamma_{+9} & & & & & & & \\ 0 & \alpha_{+9} & 0 & \gamma_{+8} & & & & & & \\ \gamma_{+9} & 0 & \cdot & \cdot & \cdot & & & 0 & & \\ & \gamma_{+8} & \cdot & \cdot & \cdot & \cdot & & & & \\ & & \cdot & \cdot & \cdot & \cdot & \cdot & & & \\ & & & \cdot & \cdot & \cdot & \cdot & \cdot & & \\ & & & & \cdot & \cdot & \cdot & \cdot & \gamma_{-8} & \\ & & 0 & & & \cdot & \cdot & \cdot & 0 & \gamma_{-9} \\ & & & & & & \gamma_{-8} & 0 & \alpha_{-9} & 0 \\ & & & & & & & \gamma_{-9} & 0 & \alpha_{-10} \end{pmatrix} \qquad (8, \mathrm{AI})$$

The diagonalization of the matrix can in principle be solved analytically but it is a very tedious task. We therefore preferred a numerical method to solve this problem and used the eigenvalue finder of MATHEMATICA. The result is shown in figure [AI.1].

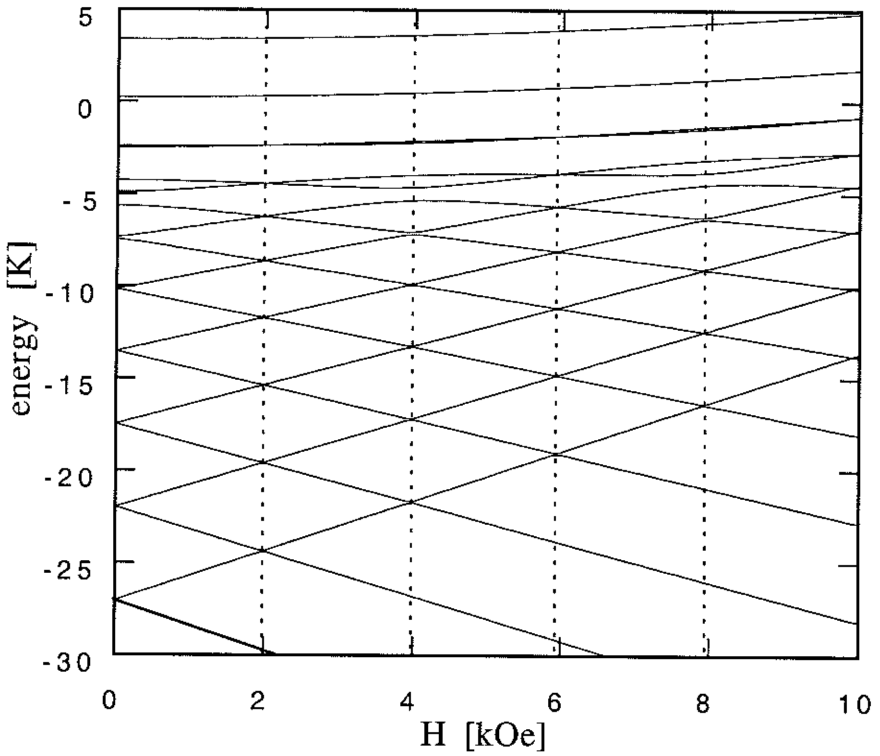

Figure AI.1: Fe8 energy levels as function of the magnetic field.

Annex II

AII) Magnetization curve of Fe8

The magnetization curve of a paramagnet at a temperature of T and in a small field H obeys the Curie law

$$M(H,T) = \frac{C}{T}H \qquad (1, \text{AII})$$

where C is the Curie constant. If the orbital moment is zero then we need only take the spin S into account and the Curie constant is given by $C = N_A g^2 \mu_B^2 / 3kS(S+1)$. $g = 2$ the g-factor of the spin, μ_B the Bohr magneton, and k the Boltzman constant. N_A is the Avogadro's number and the Curie constant is expressed in units of emu/mole, but it may also be expressed as emu/mass or emu/volume.

For high enough fields H a saturation effect will occur and the magnetization deviates from the Curie law. Statistical thermodynamics tells us that the magnetization results from the partition function

$$Z(H,T) = \sum_{m=-S}^{+S} \exp\left(\frac{E_m(H)}{kT}\right) \quad (2, \text{AII})$$

where $E_m(H)$ are the energy level of a spin in a state $m = -S, \ldots, +S$ in a magnetic field H. The magnetization M in the thermodynamic equilibrium is given by

$$M(H,T) = NkT\frac{d\ln Z(H,T)}{dH}.(3. \text{AII})$$

For a paramagnet of free spins the energy levels are

$$E_m(H) = g\mu_B Hm \qquad (4, \text{AII})$$

and the magnetization can be given analytically

$$M(H,T) = Ng\mu_B SB_S(y) \qquad (5, \text{AII})$$

where $y = g\mu_B SH/kT$ and

$$B_S(y) = \frac{2S+1}{2S}\coth\left(\frac{2S+1}{2S}y\right) - \frac{1}{2S}\coth\left(\frac{y}{2S}\right) \qquad (6, \text{AII})$$

is the Brillouin function. For free electrons $S = 1/2$ this result simplifies further to

$$B_{1/2}(y) = \tanh(y). \qquad (7, \text{AII})$$

Note that so far in all case the magnetization is scaling with H / T.

This scaling no longer holds for superparamagnets. In the case of a uni-axial, quadratic anisotropy barrier as in first approximation in Fe8 and Mn12ac the energy levels are

$$E_m(H) = -Dm^2 + g\mu_B Hm \qquad (8, \text{AII})$$

where the height of the energy barrier is given by DS^2. The magnetization can by calculated directly by equation (3, AII) which becomes now

$$M(H,T) = NkT\frac{g\mu_B \sum_{m=-S}^{+S} m\exp\left(\frac{E_m(H)}{kT}\right)}{\sum_{m=-S}^{+S}\exp\left(\frac{E_m(H)}{kT}\right)}. \qquad (9, \text{AII})$$

We have calculated this magnetization curve and compare it to the Brillouin function and more important to the measured data.

Including the off-diagonal, tunneling term the Hamiltonian of Fe8 reads

$$\hat{H} = -D\hat{S}_z^2 + E/2\left(\hat{S}_+^2 + \hat{S}_-^2\right) - g\mu_B\hat{S}_z H. \qquad (10, \text{AII})$$

First we have to calculate the energy levels $E_m(H)$, see annex I, then we can simply use equation (9, AII) again and calculate the magnetization as a function of the field and the temperature. The resulting magnetization curve deviates only slightly from the magnetization curve where we have neglected the off-diagonal terms in the Hamiltonian, see the figures [AII.1] to [AII.3].

If we want to fit these plots to a measured curve we have to take into account that the external field is not the same as the field experienced by a molecule. We will discuss this in detail in the following annex. For a fit we don't have to take account every detail. Some parameters can't be given and to match these calculated curves to measured data it is sufficient to assume that the internal field is proportional to the external field H_{ext} and the magnetization of the sample M hence

$$H = H_{ext} - NM \qquad (11, \text{AII})$$

where N is the demagnetization factor, see the presentation of the experimental results on Fe8 in chapter IV.2.1.

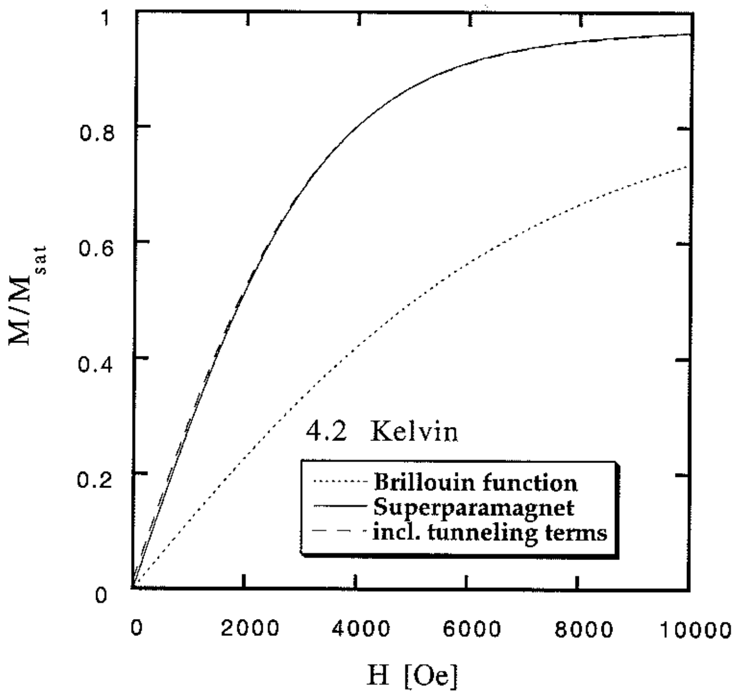

Figure AII.1: Calculated magnetization curve of Fe8 at 4.2K.

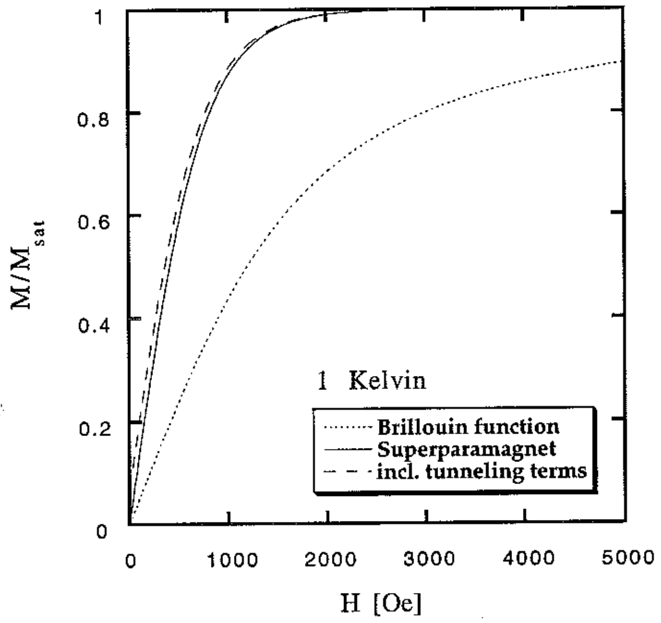

Figure AII.2: Calculated magnetization curve of Fe8 at 1K.

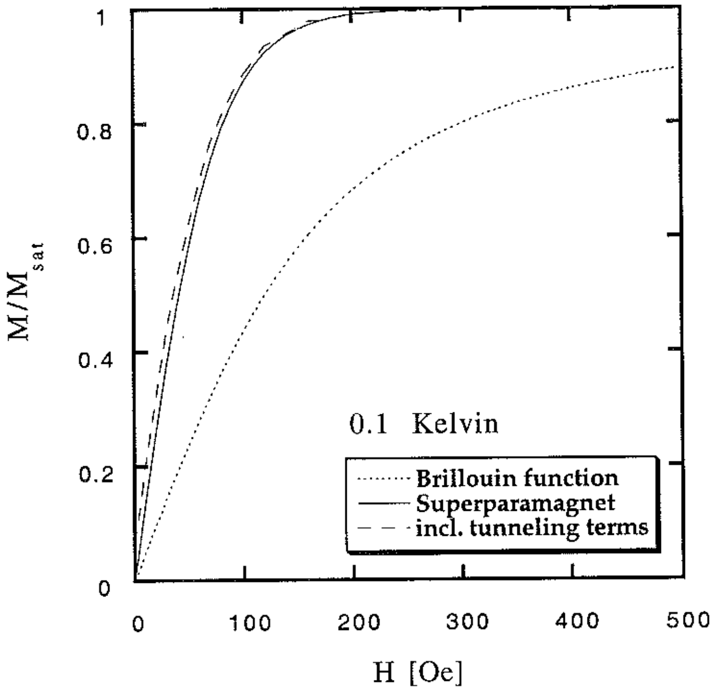

Figure AII.3: Calculated magnetization curve of Fe8 at 0.1K.

Comparison of the susceptibility, d*M*/d*H* at the origin ($H = 0$) for different temperatures and different models:

Temperature	Brillouin fn.	Superparamagnet	Incl. tunneling terms
4.2K	0.000117	0.000282	0.000279
1K	0.000487	0.00128	0.00124
0.1K	0.00482	0.0123	0.0113

Table AII.1: Susceptibility, d*M*/d*H* for small fields. The units are M/M_{sat}/K.

Annex III

AIII) Demagnetization field

The demagnetization field H_D is an effect of uncompensated magnetic dipole moments on the surface of a sample. These dipole moments give rise to a magnetic field, the demagnetization field, in the opposite direction of the dipole moments, see figure [AIII.1]. For simple sample shapes as a ellipsoid, a long cylinder, and a flat disk the demagnetization field is homogeneous and proportional to the magnetization M of the sample $H_D = -NM$ where N is the demagnetization factor. Here, we only take one component of the magnetic field into account (along the axis of the cylinder or perpendicular to the disk). In general the demagnetization factor is a tensor **N** thus $\vec{H}_D = -\mathbf{N}\vec{M}$. It can be shown that the coordinate system can always be chosen in such a way that the tensor has only diagonal elements.

$$\mathbf{N} = \begin{pmatrix} N_x & 0 & 0 \\ 0 & N_y & 0 \\ 0 & 0 & N_z \end{pmatrix} \quad 1, \mathrm{AIII})$$

The trace of the matrix is constant and the sum of the diagonal elements is $N_x + N_y + N_z = 4\pi$ in cgs units and $N_x + N_y + N_z = 1$ in SI units. For a sphere the diagonal elements are $N_x + N_y + N_z = 4\pi/3$, for a long cylinder $N_x = N_y = 2\pi$, $N_z = 0$, and for the flat disk $N_x = N_y = 0$, $N_z = 4\pi$. The demagnetization elements for a ellipsoid can be given analytically in the form of an integral. Say, the ellipsoid has the diameters a_x, a_y, a_z along its three axes. The demagnetization factors in SI units along these axes are

$$N_i = \frac{a_x a_y a_z}{2} \int_0^\infty \frac{ds}{(s + a_i^2)\sqrt{(s + a_x^2)(s + a_y^2)(s + a_z^2)}} \qquad (1, \mathrm{AIII})$$

where the index i stands for x, y, or z [Stratton 61]. In cgs units the demagnetization factors are $4\pi N_i$.

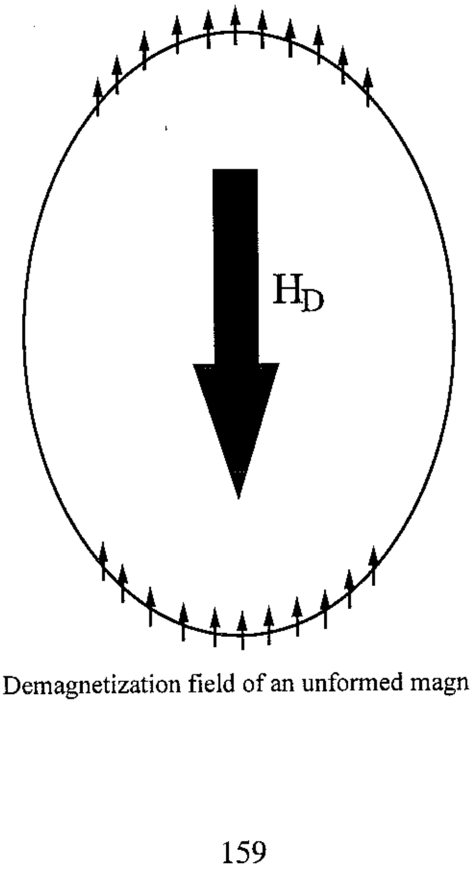

Figure AIII.1: Demagnetization field of an unformed magnetized ellipsoid.

For any other sample shape the demagnetization field is inhomogeneous and will vary spatially. Formally we could write $\vec{H}_D = -\mathrm{N}(\vec{r})\vec{M}$ but we cannot give any expression for the demagnetization factors $N_i(\vec{r})$. What we can do is to calculate the magnetic field within a sample numerically. For this calculation we place the dipole moments $\vec{m}$ on the sites of the 3-dimensional lattice and calculate the magnetic field due to all dipole moments in the sample as we have done for Fe8.

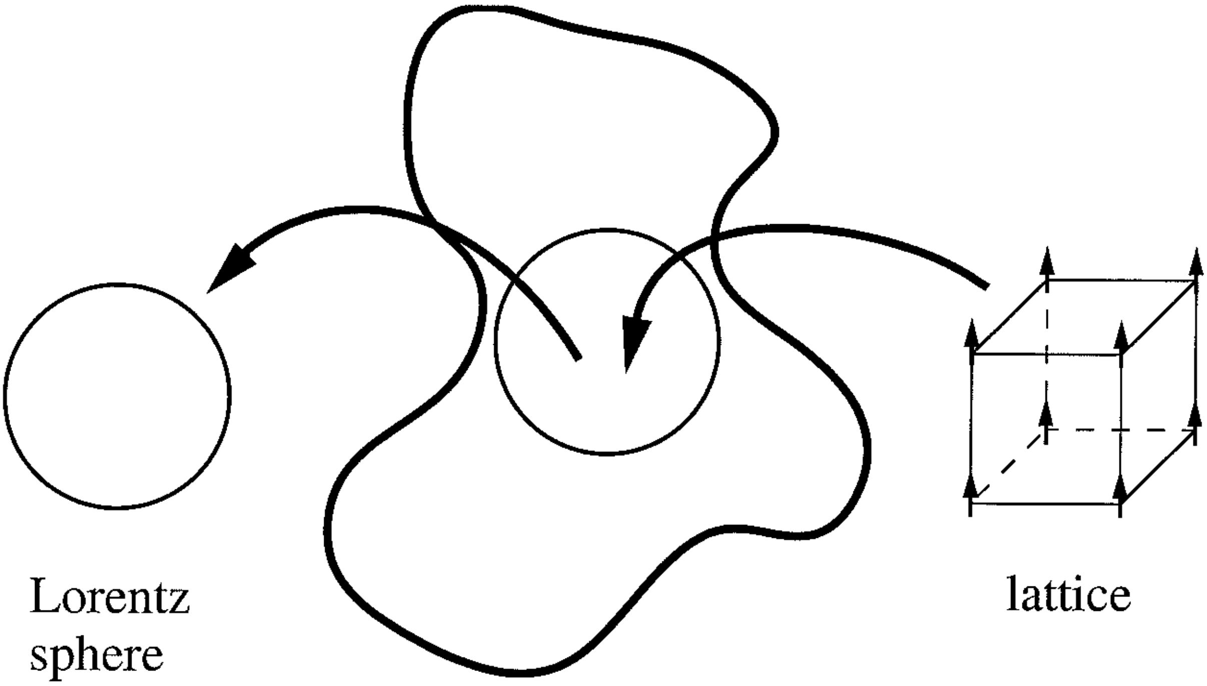

Figure AIII.2: Lorentz sphere construction: Within an arbitrary sample shape a spherical sub-volume is replaced by point dipoles on a crystal lattice.

The numerical calculation can only be done over an relatively small sub-volume of a real sample that contains a few thousand magnetic moments. The overall magnetic field is give by

$$\vec{H} = \vec{H}_{outer} + \vec{H}_{inner}. \quad (2, \text{AIII})$$

We thus have to distinguish an outer component $\vec{H}_{outer}$ where we can for simplicity assume that the magnetization is uniformly distributed and an inner component $\vec{H}_{inner}$ that includes the calculated field value. The outer component is simply the sum of a facultative external field $\vec{H}_{extern}$ and the demagnetization field $\vec{H}_D = -\mathrm{N}(\vec{r})\vec{M}$ thus

$$\vec{H}_{outer} = \vec{H}_{extern} - \mathrm{N}(\vec{r})\vec{M}. \quad (3, \text{AIII})$$

To evaluate the inner component $\vec{H}_{inner}$ we use the technique of a Lorentz sphere. That means we subtract a small uniformly magnetized sphere, the Lorentz sphere, from the interior of the sample and replace it with an array of dipole moments on a crystal lattice, see the schema in figure [AIII.2]. The field of the Lorentz sphere is $\vec{H}_{Lorentz} = +4\pi/3\vec{M}$. The factor $4\pi/3$ is the demagnetization factor of a sphere but this time with an opposite sign since we are subtracting the sphere and leave a cavity in the sample. The numerically calculated field of the moments in the small sphere is $\vec{H}_{near}$. Thus the inner field is given by

$$\vec{H}_{inner} = \frac{4\pi}{3}\vec{M} + \vec{H}_{near}. (4, \text{AIII})$$

Summing these components up we get the expression for the magnetic field inside a sample

$$\vec{H} = \vec{H}_{extern} + \left(\frac{4\pi}{3} - \mathrm{N}(\vec{r})\right)\vec{M} + \vec{H}_{near}. \text{(5, AIII)}$$

Recall that this expression is only true if the near field is calculated for a spherical sub-volume, in any other cases the numerically calculated field itself will include a inhomogeneous demagnetization field! In the case of a spherical sample the expression in the brackets is zero and in the absent of an external field the magnetic field inside the sample will only be determined by possible lattice effects in $\vec{H}_{near}$. For example the near field H_{near} of a simple cubic (sc) lattice is zero. A somehow simplified argument goes as follows: The two next neighbors in z-direction each give a field of $H = +2m/r^3$ while the four next neighbors in x- and y-direction each give a field of $H = -m/r^3$. Thus the field of the six next neighbors of a molecule sum up to a zero field. A more elaborate explanation is given e.g. in [Jackson 75]. Thus even though the demagnetization field is non-zero ($\vec{H}_D = -4\pi/3\vec{M}$) the magnetic field experienced by the molecule inside the sample is zero.

We have calculated that the triclinic lattice of Fe8 give a easy axis-component of the near field of $H_{near} = +122$ gauss if all spins are parallel. This value is changing if some spins are turning. We also discussed that while the spins are turning a broadening of the local field distribution occurs. Therefore is the near field over the sample not only varying with the magnetization but also with place $\vec{H}_{near}(M,\vec{r})$. This function is not known the only thing we can say is that the spatial variation is small for M near 1 and $\langle H_{near}\rangle_{\vec{r}}$ not zero. For $M = 0$ the spatial variation is large and $\langle H_{near}\rangle_{\vec{r}} = 0$.

We can now introduce some major simplifications. We might neglect any spatial distribution and assume that the near field is also proportional to the magnetization

$$\vec{H}_{near}(M) = \mathbf{N}_{near}\vec{M}. \quad \text{(6, AIII)}$$

Then the whole demagnetization effects reduces to the simple formula

$$\vec{H} = \vec{H}_{extern} - \mathbf{N}_{total}\vec{M}. \text{ (7, AIII)}$$

where of course all the complication is hidden in the total demagnetization factor

$$\mathbf{N}_{total} = \mathbf{N} - \frac{4\pi}{3} - \mathbf{N}_{near}. \qquad \text{(8, AIII)}$$

We use this expression for simplicity equation (7,AIII) in the analysis in the experiments. It is now clear that even for a spherical sample the demagnetization field might differ from zero if the lattice is not simple cubic.

Annex IV

AIV) Statistical theory of the dipole field distribution

In this chapter we will review some results on statistical properties of the local field distribution. We discuss what kind of shape the local field distribution will have for a increasing number of randomly placed magnetic moments. We use these results in our situation, i.e. the number of the spins in the sample is fixed and during the course of a relaxation the spins are changing their orientation.

Randomly placed spins

It has been pointed out, that the dipole field distribution for randomly placed spins in the dilute limit is Lorentzian [Anderson 51, Abragam 70] and that for a larger number of spins the dipole field distribution becomes Gaussian. A discussion of the crossover from a Lorentzian to a Gaussian distribution shape is discussed in [Berkov 96]. In this publication the dipole field distribution is analyzed for a system of aligned spins and randomly orientated spins. In this model, a number N of uniformly magnetized spheres of a volume V_m is randomly placed in the total volume V of the system. The parameter for the transition of the distribution shape is $\eta = NV_m / V$. This is the ratio between the volume occupied by the magnetic spheres NV_m and the volume of the total system V.

– Dilute limit

If the number of spins is small the dipole field distribution $\rho(H)$ is Lorentzian

$$\rho_L(H) = \frac{\Gamma/\pi}{(H-\mu)^2 + \Gamma^2} \qquad (1, \text{AIV})$$

where H is the field value, μ the center of the distribution, and Γ the width of the distribution. Berkov found that the distribution is Lorentzian as long as $\eta < 0.03$. The width of the distribution changes linearly with η

$$\Gamma = \Gamma_0 \eta, \qquad (2, \text{AIV})$$

see also [Anderson 51].

– Large number of spins

For a larger number of spins $\eta \geq 0.2$ the dipole field distribution becomes Gaussian

$$\rho_G(H) = \frac{1}{\sqrt{2\pi}\sigma} \exp\left(-\frac{(H-\mu)^2}{2\sigma^2} \right) \qquad (2, \text{AIV})$$

where μ is the center of the distribution and σ is the width, i.e. σ^2 is the variance of the dipole field values. For the Gaussian distribution the variance changes linearly with the number of spins

$$\sigma^2 = \sigma_0^2 \eta. \qquad (3, \text{AIV})$$

Dipole field distribution in a paramagnet

In the systems we are studying the number of spins are fixed and we cannot apply these results directly. We found that the dipole fields have a tremendous effect on the quantum tunneling and we are therefore mainly interested in the dipole distribution at low temperatures. For Fe8 the quantum regime starts at a temperature of 0.4K. Since the level spacing between the spin states $m = \pm 10$ and $m = \pm 9$ is about 5K we can assume that only the lowest energy states $m = \pm 10$ are occupied. The system is Ising-like in this temperature range.

If we saturate the sample in a high positive field, all are spins are aligned and pointing up. We will call this the initial distribution. To discuss this system we introduce the notation:

- n_+ the fraction of up spins
- n_- the fraction of down spins.

These variables are so normalize that $n_+ + n_- = 1$ and $M = n_+ - n_-$ is the normalized magnetization of the sample. The variables n_+ and n_- range from 0 to +1. The above mentioned parameter η is equivalent to $1-M$, i.e. $\eta = 2n_-$. For the further discussion we introduce the following definitions:

- $\rho_{total}(H)$ the overall dipole field distribution for all spins
- $\rho_N^+(H)$ the normalized dipole field distribution of only the up spins
- $\rho_N^-(H)$ the normalized dipole field distribution of only the down spins

The distribution are normalized such that

$$\int \rho_{total}(H)\, dH = 1 \qquad (4, \text{AIV})$$

and

$$\int \rho_N^\pm(H)\, dH = 1 \qquad (5, \text{AIV})$$

hence

$$\rho_{total}(H) = n_+ \rho_N^+(H) + n_- \rho_N^-(H). \qquad (6, \text{AIV})$$

For the initial distribution, all spins up, $\rho_{total}(H) = \rho_N^+(H)$. In the ideal case of a spherical sample with a simple cubic lattice and all spins up the initial dipole field distribution is given by

$$\rho_{total}^{sc,sphere}(H) = \delta(H) \qquad (7, \text{AIV})$$

where $\delta(H)$ is the Dirac delta-function. In general the sample can have a non-homogeneous demagnetization field and depending of the crystal lattice the center μ_0 of the initial distribution may be different from zero, i.e. $\delta(H) \rightarrow \delta(H-\mu_0)$ in equation (7, AIV).

If the spins are flipped *randomly* all three dipole field distribution should be equivalent:

$$\rho_{total}(H) \approx \rho_N^+(H) \approx \rho_N^-(H). \quad (8, \text{AIV})$$

We can now argue that the dipole field distribution $\rho_N^-(H)$ will change in a spherical sample with the number of turned spin n_- as discussed above for randomly placed spins. At the beginning the $\rho_N^-(H)$-distribution contains no spins. If we flip spins by random the number of spins in the $\rho_N^-(H)$-distribution will increase. We thus expect that the $\rho_N^-(H)$-distribution will be Lorentzian if only a few spins are turned and will become Gaussian if a larger number of spins are turned.

If the lattice is not simple cubic the dipole field distribution even for the initial state will be centered at a value different from zero $\mu_0 \neq 0$. Further more, the center of the distribution will shift with the magnetization field as

$$\mu = \mu_0 M. \qquad (9, \text{AIV})$$

Including the magnetization M as a parameter the dipole field distribution will have the form

– *Dilute limit*

$$\rho_L(H) = \frac{\Gamma(M)/\pi}{(H-\mu(M))^2 + \Gamma^2(M)} \qquad (10, \text{AIV})$$

with

$$\mu(M) = \mu_0 M \qquad (11, \text{AIV})$$

and

$$\Gamma(M) = \Gamma_0(1 - M). \qquad (12, \text{AIV})$$

– Many spins turned

$$\rho_G(H) = \frac{1}{\sqrt{2\pi M}} \exp\left(-\frac{(H - \mu(M))^2}{2\sigma^2(M)} \right) \qquad (13, \text{AIV})$$

with

$$\mu(M) = \mu_0 M \quad (14, \text{AIV})$$

and

$$\sigma^2(M) = \sigma_0^2(1 - M). \quad (15, \text{AIV})$$

The linear dependence of $\sigma^2(M)$ on M (equation 15, AV) breaks down as the magnetization approaches zero. If 50% of the spins are turned the width of the distribution will have a maximum and if more spins are turned the width will decrease. This comes because for more than 50% of turned spins the order in the system is increasing and if all spins are turned there will be no distribution at all. In this case the $\rho_N^-(H)$-distribution will for a spherical sample be a Dirac delta-function as mention in equation (7, AIV) for the initial case. The only difference might be that the delta-function will be shifted by $-\mu_0$ for a lattice that is not simple cubic. We therefore expect that the width of the Gaussian distribution will gradually change from equation (15, AIV) if we approach M = 0 and will becomes inverse for a negative magnetization, i.e. more than 50% of spins are turned, see figure [V.1.3.6] in the chapter [V.1.3] on the numerical calculations.

Annex V

AV) Non-Exponential Relaxation

In a perfect paramagnet the relaxation obeys the Debye-model and the relaxation curve is single exponential

$$M(t) = M_0 \exp(-t/\tau). \qquad (1, \text{AV})$$

In the presence of disorder or interactions the relaxation behavior will change. To better fit the data, phenomenological models include an additional parameter (in fact often two parameters)

$$\exp(-t/\tau) \rightarrow a \exp\left(-(t/\tau)^{\beta}\right). \qquad (2, \text{AV})$$

This relaxation law is call the Kohlrausch function or a stretched exponential function. For short times an expansion of the stretched exponential function

$$\lim_{t \to 0} \exp\left(-(t/\tau)^{\beta}\right) \approx 1 - (t/\tau)^{\beta} \qquad (3, \text{AV})$$

can fit the data often only with a change in the parameter β. Thus the relaxation starts off as a power law for short times and change to a relaxation on a roughly logarithmic scale for longer times. Taking this into account, the original exponential function is often replaced by

$$\exp(-t/\tau) \rightarrow a t^{-\alpha} \exp\left(-(t/\tau)^{\beta}\right). \qquad (4, \text{AV})$$

In general the parameters are temperature dependent ($\alpha(T), \beta(T)$).

A stretched exponential behavior is ubiquitous in physics and many phenomenological theories try to explain its appearance. This kind of behavior was extensively studied in the context of spin glasses, e.g. [Ogielski 85]. One major shortcoming of these phenomenological relaxation laws is that the underlying physical process remains unclear. One can imagine that such a complicated function as in equation (4, AV) with 2 extra parameters will fit a large variety of relaxation curves. Many phenomenological theories exists that try to give a justification for these laws. Some theories are deterministic while others use statistical arguments. In the following we will shortly review some theories on non-exponential relaxation. In these theories a distribution of relaxation times of subsystems in the sample is a priori assumed. In detail we might also distinguish between theories in which these relaxation times act in *parallel*, thus the many subsystem are essentially independent from each other, and theories where the relaxation times act in a *serial* manner, i.e. the relaxation times depend on certain conditions that evolve during the course of the relaxation.

In a disordered system each subsystem might have a different relaxation time and over the whole sample a certain distribution of relaxation times is present $p(\tau)$. In this case the bulk relaxation is given by

$$M(t) = M_0 \int_0^{\infty} p(\tau) \exp(-t/\tau)\, d\tau. \qquad (5, \text{AV})$$

Often a rather broad distribution is assumed and over a certain time range a logarithmic relaxation can describe sufficiently the measured data

$$\frac{dM(t)}{d\ln t} = S \sim const. \qquad (6, \text{AV})$$

where τ_0 is an additional parameter that determines the time scale.

A more specific assumption is to postulate a gaussian $g(\Delta)$ distribution of the barrier heights Δ in an ensemble of superparamagnets.

If the Arrhenius law is valid

$$\tau(T)=\tau_0\exp(\Delta/T)\quad (7,\mathrm{AV})$$

this distribution corresponds to a gaussian distribution on the logarithm of the relaxation times $g(\ln\tau)$. If we integrate equation (5, AIV) the exponential function in the integrand "$\exp(-t/\tau)$" result in a sharp cut-off in the integration range thus

$$M(t)\sim\int_0^{\ln t} g(\ln\tau)\,d\ln\tau \qquad (8,\mathrm{AV})$$

which results in an error function on the ln$t$-scale that is for most real cases indistinguishable from a stretched exponential relaxation.

A class of theories studying serial processes in the relaxation behavior establish a hierarchy of subsystems. Each subsystem has its own relaxation time that depends on the relaxation time of a subsystem that is one step higher in the hierarchy. The spin degrees of freedom on each level n in the hierarchy is

$$p_n=N_n/N\quad (9,\mathrm{AV})$$

and the relaxation time for each level is given by

$$\tau_{n+1}=2^{\mu_n}\tau_n.\quad (10,\mathrm{AV})$$

In [Palmer 84] a variety of assumptions on p_n and μ_n have been discussed. The authors found a stretched exponential behavior for a geometric series in $p_{n+1}=p_n/\lambda$ and a power law $\mu_n=\mu_0 n^{-p}$ with $p\geq 1$. These postulates are deterministic and in contrast Souletie and Castaing following Montroll, e.g. [Montroll 84, Souletie 94] use a statistical argument. Equation (10, AV) can be expressed as

$$\ln\tau_{n+1}=\sum_n \mu_n\ln 2+\ln\tau_0.\quad (11,\mathrm{AV})$$

They argue that one can assume a random distribution of the exponents μ_n, thus we get a gaussian distribution on the logarithm of the relaxation times $g(\ln\tau_n)$. We can thus return to the arguments used for the equation (8, AV) and find again a stretched exponential relaxation. A consequence of this approach is that a relationship $\ln\tau\sim 1/\beta^2$ is estavlished, see figure [IV.2.2.9].

A somehow different theory on stretched exponential relaxation in a ordered system is given by Lottis and Dahlberg [Lottis 91, Dahlberg 94]. They assume an ordered system of non-interacting superparamagnets. The relaxation rate of these superparamagnets obey the Arrhenius law, equation (7, AV), where they explicitly take the field dependence into account via the energy barrier $\Delta(H)$. In extension to the Debye model, flipping of the magnetic moment in both directions is allowed, i.e. up to down with a probability $p_+(H, T)$ and down to up $p_-(H, T)$, thus

$$\frac{dM}{dt}=-\tau_0^{-1}\left[\frac{M-1}{2}\exp\left(-\Delta_+(H)/T\right)-\frac{1-M}{2}\exp\left(-\Delta_-(H)/T\right)\right]\qquad (12,\mathrm{AV})$$

where $\Delta_\pm(H)$ is the field dependence of the energy barrier due to the Stoner-Wohlfarth model

$$\Delta_\pm(H)=\Delta(1\mp(H/H_S)^2).\quad (13,\mathrm{AV})$$

H_S is the switching field of the energy barrier. They argue that the demagnetization field $H_D=NM$ is continuously diminishing during the course of the relaxation and will in consequence change the barrier height at the same time. They solved the equation (12, AV) numerically and found that the relaxation curve resembles very much a stretched exponential function.

Références

[Abragam 70] A. Abragam and A. Bleaney, "*Electron Paramagnetic Resonance of Transition Ions*", (Clarendon 1970)

[Aharoni 96] A. Aharoni, "*Introduction to the Theory of Ferromagnetism*", (Clarendon Press 1996)

[Anderson 51] P. W. Anderson, Phys. Rev., **82**, 342 (1951)

[Ashcroft 76] N. W. Ashcroft and N. D. Mermin, "*Solid State Physics*", (Saunders College 1976)

[Awschalom 89] D. D. Awschalom, J. R. Rozen, M. B. Ketchen, W. J. Gallagher, A. W. Kleinsasser, R. L. Sandstrom, and B. Bumble, Appl. Phys. Lett., **53**, 2108 (1989)

[Awschalom 92a] D. D. Awschalom, J. F. Smith, G. Grinstein, D. P. DiVincenzo, and D. Loss, Phys. Rev. Lett., **68**, 3092 (1992)

[Awschalom 92b] D. D. Awschalom, *et al.*, Science, **258**, 414 (1992)

[Barbara 95] B. Barbara *et al.*, JMMM, **140-144**, 1825 (1995)

[Barra 96] A. L. Barra, P. Debrunner, D. Gattschi, C. E. Schulz, and R. Sessoli, Europhys. Lett., **35**, 133 (1996)

[Barra 97] A. L. Barra, D. Gatteschi, and R. Sessoli, Phys. Rev. B, **56**, 8192 (1997)

[Berkov 96] D. V. Berkov, Phys. Rev. B, **53**, 731 (1996)

[Brailsford 66] E. Brailsford, "*Physical Princliples of Magnetism*", (D. Van Nostrand Company, 1966)

[Brown 63] W. F. Brown, Phys. Rev. **130**, 1677 (1963)

[Burrin 96] A. L. Burin, N. V. Prokof'ev, and P. C. E. Stamp, Phys. Rev. Lett., **76**, 3040 (1996)

[Caciuffo 98] R. Caciuffo, G. Amoretti, A. Murami, R. Sessoli, A. Caneschi, and D. Gatteschi, to be published

[Caldeira 81] A. O. Caldeira and A. J. Leggett, Phys. Rev. Lett., **46**, 211 (1981)

[Caldeira 83] A. O. Caldeira and A. J. Leggett, Annals of Physics, **149**, 374 (1983)

[Chamberlin 84] R. V. Chamberlin, G. Mozurkewich et R. Orbach, PRL **53**, 867 (1984)

[Caneschi 98] A. Canschi, D. Gatteschi, R. Sessoli, and J. Schweizer, Physica B, **241-243**, 600 (1998)

[Chudnovski 88] E. M. Chudnovski and L. Gunther, Phys. Rev. Lett., **60**, 661 (1988)

[Chudnovski 88] E. M. Chudnovsky p. 77 in [QTM 94]

[Chudnovski 97a] E. M. Chudnovsky and D. A. Garanin, Phys. Rev. Lett., **79**, 4469, (1997)

[Chudnovski 97b] E. M. Chudnovsky and D. A. Garanin, Phys. Rev. B, **56**, 11102, (1997)

[Dahlberg 94] E. D. Dahlberg, D. K. Lottis, R. M. White, M. Matson et E. Engle J. Appl. Phys. **76**, 6396 (1994)

[Delfs 93] C. Delfs, D. Gatteschi, L. Pardi, R. Sessoli, K. Wieghardt, and D. Hanke, Inorg. Chem, **32**, 3099 (1993)

[Dobrovitski 97] V. V. Dobrovitski and A. K. Zvezdin, Europhys. Lett., **38**, 377 (1997)

[Dormann 88] J. L. Dormann, L. Bessais, and D. Fiorani, J. Phys: C, **21**, 2015 (1988)

[Enz 86] M. Enz and R. Schilling, J. Phys. C, **19**, 1765 (1986)

[Feynman 66] R. P. Feynman, R. B. Leighton, and M. Sands, "*The Feynman Lectures on Physics III*" (Addison–Wesley 1966)

[Feynman 63] R. P. Feynman and F. L. Vernon, Ann. Phys., **24**, 118 (1963)

[Fiorani 86] D. Fiorani, J. L. Tholence, and J. L. Dormann, J. Phys. C, **19**, 5495 (1986)

[Fominaya 97] F. Fominaya, J. Villain, P. Gandit, J. Chaussy, and A. Caneschi, Phys. Rev. Lett., **79**, 1126 (1997)

[Fort 98] A. Fort, A. Rettori, J. Villain, D. Gatteschi, and R. Sessoli, Phys. Rev. Lett., **80**, 612 (1998)

[Friedman 96] J. R. Friedman, M. P. Sarachik, J. Tejada, J. Maciejewski, and R. Ziolo, Phys. Rev. Lett., **76**, 3830 (1996)

[Gallop 91] J. C. Gallop, "*SQUIDs, the Josephson Effects and Superconducting Electronics*" (Adam Hilger 1991)

[Garanin 91] D. A. Garanin, J. Phys. A, **24**, L61 (1991)

[Garg 93a] A. Garg, Phys. Rev. Lett., **70**, C2198 (1993)

[Garg 93b] A. Garg, Phys. Rev. Lett., **71**, 4241 (1993)

[Garg 95] A. Garg, Phys. Rev. Lett., **74**, 1458 (1995)

[Garg 96] A. Garg, Science, **272**, 425 (1996)

[Gatteschi 94] D. Gatteschi, A. Caneschi, L. Pardi, and R. Sessoli, Science **265**, 1054 (1994)

[Gatteschi 96] D. Gatteschi, A. Canschi, R. Sessoli, and A. Cornia, Chem. Soc. Rev., 101 (1996)

[Cernicchiaro 97] G. R. C. Cernicchiaro, thèse, CRTBT CNRS, 1997

[Goldberg 95] D. P. Goldberg, A. Caneschi, C. D. Delfs, R. Sessoli, and S. J. Lippard, J. Am. Chem. Soc., **117**, 5789 (1995)

[Gunther 90] L. Gunther, Physics World, p. 28, December 1990

[Hartmann 96] F. Hartmann–Boutron, P. Politi, and J. Villain, Int. J. of Mod. Phys. B, **10**, 2577 (1996)

[Hemmen 86a] L. van Hemmen and A. Sütö, Europhys. Lett., **1**, 481 (1986)

[Hemmen 86b] L. van Hemmen and A. Sütö, Physica B, **141**, 37 (1986)

[Hemmen 88] L. van Hemmen and W. F. Wreszinski, Commun. Math. Phys. **199**, 213 (1988)

[Hemmen 88] L. van Hemmen and W. F. Wreszinski, Phys. Rev. B, **57**, 1007 (1998)

[Hemmen 94] L. van Hemmen and A. Sütö, p. 19, in [QTM 94]

[Hernandez 96] J. M. Hernandez, X. X. Zhang, F. Luis, J. Bartolome, J. Tejada, and R. Ziolo, Europhys. Lett., **35**, 301 (1996)

[Hernandez 97] J. M. Hernandez, X. X. Zhang, F. Luis, J. Tejada, J. R. Friedman, M. P. Sarachik, and R. Ziolo, Phys. Rev. B, **55**, 5858 (1997)

[Ioselevich 87] A. M. Ioselevich, JETP Lett., **45**, 571 (1987)

[Jackson 75] J. D. Jackson, “Classical Electrondynamics”, (John Wiley & Sons 1975)

[Kahn 93] O. Kahn, "*Molecular Magnetism*" (VCH Publishers 1993)

[Korenblit 78] I. Y. Korenblit and E. F. Shender, JETP, **46**, 937 (1978)

[Leggett 80] A. J. Leggett, Supp. of the Prog. Of Theo. Phys., **69**, 80 (1980)

[Leggett 83] A. J. Leggett, Phys. Rev. B, **30**, 1208 (1983)

[Leggett 87a] A. J. Leggett, *et al.*, Rev. of Mod. Phys., **59**, 1 (1987)

[Leggett 87b] A. J. Leggett, Jap. Journ. of Appl. Phys., **27**, 1986 (1987)

[Lionti 97] F. Lionti, L. Thomas, R. Ballou, B. Barbara, A. Sulpice, R. Sessoli, and D. Gatteschi, J. Appl. Phys., **81**, 1 (1997)

[Lis 80] T. Lis, Acta Cryst. B, **36**, 2042 (1980)

[Lottis 91] D. K. Lottis, R. M. White et E. D. Dahlberg, Phys. Rev. Lett., **67**, 362 (1991)

[Montroll 84] E. W. Montroll and J. T. Bendler, J. Stat. Phys., **34**, 129 (1984)

[Morrish 65] Morrish, “*The Physical Principles of Magnetism*”, (John Wiley & Sons 1965)

[Néel 49] L. Néel, Annales de Géophysique, **5**, 99 (1949)

[Néel 61] L. Néel, Cours de Physique Théorique, Les Houches, p. 412, Presses Universitaires de France1961

[Novak 95a] M. Novak and R. Sessoli, p.171 in [QTM 94]

[Novak 95b] M. Novak, R. Sessoli, A. Caneschi, and D. Gatteschi, JMMM, **146**, 211 (1995)

[Ogielski 85] A. T. Ogielski, Phys. Rev. B, **32**, 7384 (1985)

[Palmer 84] R. G. Palmer, D. L. Stein, E. Abrahams et P. W. Anderson, Phys. Rev. Lett., **53**, 958 (1984)

[Paulsen 95a] C. Paulsen and J. G. Park, p.189 in [QTM 94]

[Paulsen 95b] C. Paulsen, J. G. Park, B. Barbara, R. Sessoli, and A. Caneschi, JMMM, **140-144**, 1891 (1995)

[Politi 95] P. Politi, A. Rettori, F. Hartmann–Boutron, and J. Villain, Phys. Rev. Lett., **75**, 537 (1995)

[Prokof’ev 93a] N. V. Prokof'ev and P. C. E. Stamp, J. Phys. **CM5**, L663 (1993)

[Prokof’ev 93b] N. V. Prokof'ev and P. C. E. Stamp, Proc. **LT20**, Aug (1993)

[Prokof’ev 94] N. V. Prokof'ev and P. C. E. Stamp, in pp. 347–371 [QTM 94]

[Prokof’ev 96] N. V. Prokof'ev and P. C. E. Stamp, J. Low Temp. Phys. **104**, 143 (1996)

[Prokof’ev 97] N. V. Prokof'ev and P. C. E. Stamp, UBC preprint, march 1997

[Prokof’ev 98] N. V. Prokof'ev and P. C. E. Stamp, Phys. Rev. Lett., **80**, 5794 (1998)

[QTM 94] "*Quantum Tunneling of Magnetisation-QTM'94*", (ed. L. Gunther and B. Barbara, Kluwer Publishing 1995)

[Sampaio 94] L. C. Sampaio Lima, thèse, Lab. louis Néel, 1994

[Sangregorio 97] C. Sangregorio, T. Ohm, C. Paulsen, R. Sessoli, and D. Gatteschi, Phys. Rev. Lett., **78**, 4645 (1997)

[Sangregorio 98] C. Sangregorio, thèse, Université Florence, 1998

[Scharf 87] G. Scharf, W. F. Wreszinski, and J. L. van Hemmen, J. Phys. A, **20**, 4309 (1987)

[Schwarzschild 97] B. Schwarzschild, Physics Today, p. 17, January 1997

[Sessoli 93] R. Sessoli, D. Gatteschi, A. Caneschi, and M. A. Novak, Nature **365**, 141 (1993)

[Souletie 94] J. Souletie, J. Appl. Phys., **75**, 5512 (1994)

[Stamp 92a] P. C. E. Stamp, E. M. Chudonovsky, and B. Barbara, Int. J. of. Mod. Phys. B, **6**, 1335 (1992)

[Stamp 92b] P. C. E. Stamp, Nature **359**, 365 (1992)

[Stamp 92c] P. C. E. Stamp, UBC preprint, Sept. 1992, unpublished

[Stamp 96] P. C. E. Stamp, Nature **383**, 125 (1996)

[Stamp 98] P. C. E. Stamp pp.101-197 in "*Tunneling in Complex Systems*", ed. Tomsovic (World Scientific 1998)

[Stratton 61] J. A. Stratton, “*Théorie de l’électromagnétisme*”, p292, Dunod 1961.

[Thomas 96] L. Thomas, F. Lionti, R. Ballou, D. Gatteschi, R. Sessoli, and B. Barbara, Nature **383**, 145 (1996)

[Thomas 97] L. Thomas, thèse, Louis–Néel CNRS, Grenoble, 1997

[Tupitsyn 97] I. S. Tupitsyn, N. V. Prokof'ev, P. C. E. Stamp, Int. J. of. Mod. Phys. B, **11**, 2901 (1997)

[Villain 94] J. Villain, F. Hartman-Boutron, R. Sessoli, and A. Rettori, Europhys. Lett., **27**, 159 (1994)

[Wernsdorfer 96] W. Wernsdorfer, thèse, Louis–Nèel CRTBT CNRS, 1996

[Wieghardt 84] K. Wieghardt, K. Pohl, I. Jibril, and G. Huttner, Angew. Chem. Int. Ed. Engl. **22** ,727 (1984)

Publications

- T. Ohm, C. Sangregorio, C. Paulsen
  Non-exponential relaxation in a Resonant Quantum Tunneling System of Magnetic Molecules
  (accepted for publication by Jour. of Low Temp. Phys.)

- T. Ohm, C. Sangregorio, C. Paulsen
  Local-Field Dynamics in a Resonant Quantum Tunneling System of Magnetic Molecules
  (accepted for publication by EPJ B)

- C. Sangregorio, T. Ohm, C. Paulsen, R. Sessoli, D. Gatteschi,
  Quantum Tunnelling of Magnetisation in an Iron Ion Cluster Nanomagnet.
  PRL, **78**, 4645 (1997)

- A. Caneschi, T. Ohm, C. Paulsen, D. Rovai, C. Sangregorio, R. Sessoli,
  Quantum tunnelling of the magnetic moment in manganese and iron molecular clusters
  JMMM, **177-181**, 1330 (1998) invited paper

- T. Ohm, C. Paulsen, C. Sangregori, R. Sessoli, D. Gatteschi,
  L'effet tunnel magnetique dans un agregat moleculaire Fe8,
  Proceedings of the 5th Colloque Louis Néel, Banyuls sur Mer, France, 1997.

- K. Fegy, D. Luneau, T. Ohm, C. Paulsen, and P. Rey
  Two-Dimensional Nitroxide-Based Molecular Magnetic Materials
  Angew. Chem. Int. Ed. **37**, 1270 (1998)

- K. Fegy, D. Luneau, T. Ohm, C. Paulsen, J.-L. Tholence, M, Novak, P. Rey,
  One-dimensional Nitroxide Based Molecular Magnetic Materials
  (accepted for publication by JACS).

- C. Hess, C. Schlenker, G. Bonfait, T. Ohm, C. Paulsen, D. Dumas,
  Z. Teweldemedhin, M. Greenblatt, J. Marcus, and M. Almeida
  CDW State and Superconductivity in the Quasi-Two-Dimensional Monophosphate Tungsten Bronze $P_4W_{14}O_{50}$,
  Solid State Comm., **104**, 663 (1997)

- C. Hess, C. Schlenker, G. Bonfait, J. Marcus, T. Ohm, C. Paulsen, J. Dumas,
  J.-L. Tholence, M. Greenblatt, and M. Almeida,
  Superconductivity in the charge density wave state of the quasi-two-dimensional monophosphate tungsten bronze $P_4W_{14}O_{50}$.,
  Physica C, **282-287**, 955 (1997)

Quantum Tunneling of the Magnetization in the Molecular Magnet Fe8

We have studied quantum tunneling of the magnetization in molecular magnets at very low temperatures. Our experiments give clear evidence of resonant quantum tunneling in the iron-ion compound Fe8. This system can be thought of as an ensemble of identical, iso-oriented nanomagnets each with a net spin of $S = 10$.

Measurements of the relaxation of the magnetization were made using unique SQUID-magnetometers that can operate in strong fields (up to 8 tesla) and at temperatures down to 50mK. At high temperatures, above 1K, the Fe8-system behaves as a superparamagnet and relaxes via thermal activation over an anisotropy barrier of approximately 24K. Below 0.4K the relaxation is temperature independent indicating that the giant molecular spin tunnels through the anisotropy barrier. The relaxation time varies strongly with the external magnetic field and shows resonant effects at equidistant field values. In this quantum regime the relaxation curve is non-exponential and can be well fit by a stretched exponential. However, the very beginning of the relaxation follows a square root behavior.

We give evidence that the dipole fields between the molecular spins strongly influence the relaxation behavior. The dipole fields do not act like a force between the molecules but permit or suppress quantum tunneling by shifting molecules into or away from resonance. We present a simple phenomenological model that explains the stretched exponential relaxation behavior. The model is based on a very narrow tunneling resonance along with an evolving local field distribution during the course of a relaxation.

In addition, we calculated numerically the initial local field distribution and its time evolution. Comparison with measurements of the distribution of relaxation times and with Monte-Carlo simulation of the quantum relaxation indicates that unusual correlations develop between spins.

Résumé

Nous avons étudié les retournements d'aimantation par effet tunnel quantique dans des aimants moléculaires. Nos expériences montrent clairement l'effet tunnel quantique dans l'aimant moléculaire Fe8. Ce système se compose d'un ensemble d'aimants nanoscopiques identiques et orientés parallèlement. Chacune des molécules porte un spin $S = 10$.

Les mesures de relaxation sont faites en utilisant des magnétomètres à SQUID aux performances uniques. Ces magnétomètres permettent des mesures de haute sensibilité en champ fort, jusqu'à 8 tesla, et aux très basses températures (> 50 mK). A haute température le système Fe8 se comporte comme un système superparamagnétique qui relaxe par activation thermique au-dessus d'une barrière de 24 K. Au-dessous de 0,4 K la relaxation est indépendante de la température ce qui est le signe d'un effet tunnel quantique du spin moléculaire à travers la barrière. Le temps de relaxation varie fortement avec le champ externe et montre des effets résonants. Dans le régime quantique la courbe de relaxation est non-exponentielle et bien décrite par une exponentielle étirée. Le début de la courbe de relaxation suit une loi en racine carrée du temps.

Nous montrons que le champ dipolaire entre les molécules a une forte influence sur la relaxation mais le champ dipolaire n'agit pas comme une force : il permet ou empêche l'effet tunnel quantique dans une molécule. Nous présentons un modèle phénoménologique simple qui explique pourquoi la courbe de relaxation ressemble à une exponentielle étirée. Dans ce modèle nous supposons que chaque molécule a une résonance très étroite et que la distribution du champ local évolue pendant la relaxation.

De plus, nous présentons un calcul numérique sur l'évolution de la distribution du champ local. Un calcul de Monte-Carlo avec des distributions réalistes montre lui aussi l'existence de corrélations inhabituelles en accord qualitatif avec nos observations.

Mots-clés

aimants moléculaires
magnétisme à très basse température
effet tunnel d'aimantation
effet tunnel résonant
Fe8
physique mésoscopique
relaxation non-exponentielle
champ interne